Magnetische hysteretische karakterisering
van ferromagnetische materialen met het oog
op het niet-destructief evalueren van materiaaldegradatie

Magnetic Hysteretic Characterization
of Ferromagnetic Materials with Objectives
towards Non-Destructive Evaluation of Material Degradation

Lode Vandenbossche

Promotoren: prof. dr. ir. L. Dupré, prof. dr. ir. J. Melkebeek
Proefschrift ingediend tot het behalen van de graad van
Doctor in de Ingenieurswetenschappen: Werktuigkunde-Elektrotechniek

Vakgroep Elektrische Energie, Systemen en Automatisering
Voorzitter: prof. dr. ir. J. Melkebeek
Faculteit Ingenieurswetenschappen
Academiejaar 2008 - 2009

UNIVERSITEIT
GENT

ISBN 978-90-8578-276-6
NUR 959, 971
Wettelijk depot: D/2009/10.500/35

Universiteit Gent
Faculteit Ingenieurswetenschappen
Vakgroep Elektrische Energie, Systemen en Automatisering
Laboratorium voor Elektrische Energietechniek
Sint-Pietersnieuwstraat 41, B-9000 Gent, Belgium

UNIVERSITEIT GENT

Magnetische hysteretische karakterisering van ferromagnetische materialen met het oog op het niet-destructief evalueren van materiaaldegradatie

Magnetic Hysteretic Characterization of Ferromagnetic Materials with Objectives towards Non-Destructive Evaluation of Material Degradation

Lode Vandenbossche

Promotoren:

Prof. dr. ir. Luc Dupré
Prof. dr. ir. Jan Melkebeek

Leden van de examencommissie:

Prof. dr. ir. Rik Van de Walle, voorzitter
Prof. dr. ir. Patricia Verleysen, secretaris
Dr. Ivan Tomáš (Academy of Sciences, Prague, Czech Republic)
Prof. dr. ir. Christophe Geuzaine (Université de Liège)
Dr. Milan Konstantinović (SCK·CEN, Mol)
Prof. ir. Leo Broekaert

EELAB

Dankwoord

Eerst en vooral dank ik de promotoren van mijn onderzoekswerk, Prof. Luc Dupré en Prof. Jan Melkebeek.

De sterke dynamiek, het onvermoeibare enthousiasme en de kritische geest van Prof. Luc Dupré hebben me continu vooruitgestuwd tijdens de voorbije jaren. Zijn constructieve inbreng en grote interesse was en is substantieel bij mijn onderzoek en bij het tot stand komen van dit proefschrift. Wat ik verder ten zeerste wist te appreciëren was de strategische visie van Prof. Dupré over het onderzoek binnen zijn onderzoeksgroep op de langere termijn.

Ik dank Prof. Dupré verder ook voor de geboden hoge graad van onderzoeksvrijheid en de mogelijkheid om een brede waaier aan technieken en probleemstellingen te kunnen onderzoeken. Ook de samenwerking in verschillende dienstverlenings- en onderzoeksprojecten wist ik ten zeerste te appreciëren: deze zijprojecten met industriële partners en met andere onderzoeksinstellingen waren een aangename en welkome afwisseling, maar bovendien ook een extra motivatie voor het meer fundamentele onderzoek in het kader van mijn doctoraat.

Mijn dank gaat uit naar Prof. Jan Melkebeek voor de feedback over het proefschrift. Zijn opmerkingen en suggesties tijdens het grondig nalezen van de tekst hebben de kwaliteit van dit werk merkbaar verbeterd.

Ik dank alle collega's aan het Laboratorium voor Elektrische Energietechniek, in het bijzonder mijn bureau-buddies Ben Van de Wiele, Tom Hilgert en partner-in-crime Guillaume Crevecoeur: ik voelde me gesterkt door de joviale en constructieve werksfeer. Bij jullie kon ik mijn ei kwijt en kon ik mezelf zijn, dikke merci.

Verder waardeer ik ten zeerste de inbreng van Ingrid Dubois als de spilfiguur en mater familias van ons labo, voor de ondersteuning in oneindig veel administratieve taken, en misschien nog meer voor de subtiele, schijnbaar onzichtbare maar o zo belangrijke dagdagelijkse zaken.

Vele medewerkers en ex-medewerkers van het laboratorium droegen een sterk geapprecieerd steentje bij tot dit onderzoekswerk. De "mannen-van-boven" Christiaan Vervust, Tony Boone, Fernand De Boever, Stefaan Dhondt en Tom Dekeyser

dank ik voor de vele kleine en grote technische verwezenlijkingen die van essentieel belang zijn geweest bij het uitbouwen van de verschillende meetopstellingen in het kader van mijn onderzoek.

Verschillende mensen zowel binnen als buiten de muren van het labo verdienen een welgemeende dankuwel voor de aangename en interessante samenwerking, zoals Peter Sergeant en Ahmed Abou-Elyazied Abdallh, maar ook Ivan Garshelis, Stijn Tollens en Ryan Kari, en dan vergeet ik ongetwijfeld nog enkele anderen...

Tijdens mijn onderzoek heb ik de sterk geapprecieerde mogelijkheid gehad om samen te werken met vele mensen op het Studiecentrum voor Kernenergie te Mol. In de eerste plaats dank ik Milan Konstantinović voor de energieke samenwerking, de collegiale sfeer en de leerrijke kruisbestuiving tussen de visie van een wetenschapper en een ingenieur. Samen met Boris Minov timmeren we verder aan het gezamenlijke project. Leo Van Houdt en Paul Wouters dank ik verder voor de nauwgezette assistentie aan de hot cell. De warme mentaliteit van de Kempen doet me keer op keer deugd.

Speciale dank gaat uit naar mijn ouders, mijn familie en in het bijzonder naar Ilse voor de onvoorwaardelijke steun, het oneindig vele geduld en voor het scheppen van een ideale mix tussen werklust en ontspanning, tussen motivatie en verstrooiing. Wat betreft die verstrooiing deelt Emiel natuurlijk ook in de bloemen...

Lode Vandenbossche
15 Maart 2009

Samenvatting

In onze industriële samenleving worden structurele componenten en machineonderdelen vervaardigd uit staal vaak onder veeleisende omstandigheden uitgebaat, en dit dikwijls voor tijdspannes van meerdere jaren. Dergelijke uitbatingsomstandigheden kunnen microstructurele materiaaldegradatieprocessen induceren en zodoende de materiaalintegriteit aantasten. Bijvoorbeeld, cyclische mechanische spanning leidt tot metaalvermoeiing; het samengaan van voldoend hoge spanning met voldoend hoge temperatuur kan aanleiding geven tot vervorming door thermische kruip; bestraling met neutronen induceert verbrossing en verharding. In de meeste gevallen evolueren deze materiaaldegradatieprocessen relatief traag, maar desalniettemin is de bijhorende verslechtering van de mechanische eigenschappen een cumulatief en verraderlijk fenomeen, aangezien dergelijke materiaaldegradatieprocessen kunnen leiden tot scheurgroei en uiteindelijk tot het falen van componenten, iets wat verstrekkende gevolgen kan hebben. Daarom is de inschatting van de materiaalintegriteit van groot belang, zowel voor veiligheids- als economische redenen. Typisch kan deze beoordeling van de materiaalintegriteit worden uitgevoerd met behulp van niet-destructieve evaluatietechnieken (NDE).

In een dergelijke context is de belangrijkste doelstelling van het gepresenteerde onderzoek het exploreren van de mogelijkheden, de beperkingen en de sensitiviteit van magnetische hysteretische karakteriseringstechnieken met het oog op het niet-destructief evalueren van toenemende microstructurele materiaaldegradatie. Een dergelijke aanpak is gemotiveerd door de kennis dat het macroscopisch magnetisch hysteretisch gedrag van ferromagnetische materialen beïnvloed is door de microstructurele eigenschappen van het materiaal, en omdat degradatieprocessen veranderingen kunnen veroorzaken in de microstructuur, kunnen dergelijke processen ook repercussies hebben op het magnetisch hysteretisch gedrag. De onderliggende fundamentele principes betreffende deze relatie tussen microstructurele eigenschappen en de magnetisatieprocessen is een cruciaal punt in ons onderzoek: tijdens het magnetisatieproces wordt de mobiliteit van de magnetische domeinmuren alsook de magnetische domeinstructuur beïnvloed door de microstructuur. Bijvoorbeeld, een hoge defectdensiteit in het kristalrooster resulteert in een hoge graad van hindering van de domeinmuurbewegingen.

Omgekeerd reflecteert de verandering in de vorm van de magnetische hysteresislussen de verandering in de microstructurele eigenschappen van het materiaal. In principe kunnen we deze microstructurele veranderingen identificeren en de degradatie van de mechanische eigenschappen monitoren op een niet-destructieve manier, met behulp van de karakterisering en de evaluatie van het magnetisch hysteretisch gedrag.

Deze gepostuleerde methode, namelijk de karakterisering van het magnetisch hysteretisch gedrag, beperkt onmiskenbaar de toepassing ervan tot ferromagnetische materialen. Desalniettemin is het toepassingsgebied nog steeds zeer breed, omdat het merendeel van de commercieel geproduceerde ijzerlegeringen en laaggelegeerde staalsoorten een ruimtelijk gecentreerd kubisch (ferritisch) kristalrooster hebben, en dergelijke materialen zijn ferromagnetisch.

De aanpak van dit onderzoek is grotendeels experimenteel, en de ontwikkeling van magnetische karakteriseringsmethodes is dan ook een belangrijk onderdeel van dit onderzoek. Veelzijdige experimentele meetopstellingen en veldmetrische meettechnieken zijn ontwikkeld, in combinatie met geavanceerde analysetechnieken ter interpretatie van de experimentele data, om de karakterisering van de vele deelaspecten gerelateerd aan zowel het magnetisch alsook het magneto-mechanisch hysteretisch gedrag mogelijk te maken.

Echter, in ons experimenteel onderzoek van gedegradeerde materialen zijn de monsters vaak beperkt tot veel kleinere dimensies dan de afmetingen die voorgeschreven zijn in internationale normen. Verder is in ons onderzoek de vorm van de proefstukken in veel gevallen beperkt tot staven met vierkante of cirkelvormige dwarsdoorsneden. Ook voor dergelijke proefstukken met beperkingen qua grootte en vorm, slaagden we erin aangepaste en geminiaturiseerde meetopstellingen te ontwikkelen – geïnspireerd door, en zo dicht als mogelijk aanleunend bij de gestandaardiseerde single sheet tester – resulterend in een goede herhaalbaarheid voor de magnetische karakterisering van de verschillende samples onder test.

Betreffende de magnetische hysteretische karakteriseringstechnieken voor NDE doelstellingen, is de kerntaak het definiëren van magnetische parameters die gevoelig genoeg zijn om de veranderingen in microstructurele eigenschappen te kunnen identificeren. Als een eerste stap kunnen de klassieke parameters gebruikt worden die de magnetische hysteresislus bij saturatie karakteriseren, zoals het coercitief veld, de remanente inductie en de permeabiliteit. In dit onderzoekswerk wordt gestreefd naar een uitbreiding en verbetering van de magnetische hysteretische niet-destructieve evaluatiemethode door de input van experimentele data te verhogen. Bovendien is het nuttig hierbij een hysteresismodel zoals het Preisach-model te gebruiken, aangezien een dergelijk model het gehele magnetische hysteresisgedrag in rekening brengt.

Gebaseerd op een aantal experimentele studies van verscheidene materiaaldegradatieprocessen, worden de mogelijkheden en de beperkingen onderzocht voor

zowel de ***magnetische*** en de ***magnetomechanische*** hysteretische karakterisering.

Een van de belangrijkste onderzochte onderwerpen betreffende het effect van microstructurele veranderingen op het ***magnetisch hysteretisch gedrag,*** is de verbrossing en verharding van ferritisch staal omwille van neutronenbestraling. In de nucleaire industrie kan dit effect schadelijk zijn voor het staal waaruit het drukvat van de nucleaire reactor (RPV) is vervaardigd. De onderliggende reden voor dergelijk materiaaldegradatieproces is de vorming van defecten van nanometergrootte geïnduceerd door neutronenbestraling, namelijk de door de bestraling versterkte precipitatie van koper en de geïnduceerde schade aan de Fe-matrix (clusters van puntdefecten).

Conventioneel wordt de status van het materiaal betreffende de verbrossing, de verharding en de breuktaaiheid geëvalueerd aan de hand van destructieve mechanische testen op zogenaamde surveillance proefstukken, die gemaakt zijn uit hetzelfde materiaal als het drukvat. Teneinde een verlengde levensduur van nucleaire reactoren mogelijk te maken (bijvoorbeeld om economische redenen) en gezien het gelimiteerde aantal proefstukken (voor de destructieve testen) dat oorspronkelijk is ingebracht in de reactor is er een tendens tot het ontwikkelen van niet-destructieve evaluatietechnieken. Dergelijke technieken kunnen beschouwd worden als bijkomende en/of mogelijke alternatieve technieken teneinde de materiaalstatus te beoordelen, met als bijkomend voordeel dat de surveillance proefstukken herbruikt kunnen worden.

Ten eerste zijn tijdens dit onderzoek de verhardings- en verbrossingsfenomenen veroorzaakt door Cu-precipitatie onderzocht, afzonderlijk van de door neutronenbestraling geïnduceerde schade aan de Fe-matrix, en dit aan de hand van thermische veroudering van Fe-Cu modellegeringen. De vorming en groei van Cu-precipitaten tijdens het thermische verouderingsproces aan 500°C leidt tot veranderingen in de bestudeerde magnetische hysteretische eigenschappen, zoals remanente inductie, maximum permeabiliteit, en de breedte en de piekwaarde van de Preisach-gerelateerde distributie van het lokale interactieveld. De verschillende regimes die aangeduid kunnen worden in de relatie van de magnetische parameters met de verouderingstijd corresponderen met de mechanische verhardings- en verzachtingsregimes, zoals waargenomen in de verandering van de vloeigrens. Wanneer de initiële en de extremale waardes (corresponderend met de grootste mechanische hardheid) van de bestudeerde magnetische parameters worden vergeleken, dan kan een verandering van ongeveer 50% (en meer, afhankelijk van de beschouwde magnetische parameter) worden vastgesteld. Deze uitgesproken sensitiviteit geeft het potentieel aan van magnetisch NDE voor de evaluatie van verharding en verzachting geïnduceerd door Cu-precipitatie.

Ten tweede is de verbrossing en verharding omwille van de neutronenbestraling bestudeerd. De microstructurele veranderingen die veroorzaakt worden door de neutronenbestraling beïnvloeden niet alleen het mechanische gedrag, maar leiden ook tot variaties in het magnetische hysteretische gedrag van alle bestudeerde

materialen, namelijk nominaal puur Fe, Fe-Cu modellegeringen, en RPV ferritisch staal. De laatste categorie omvat zowel een referentiekwaliteit van RPV staal, 'JRQ' (Japanese Reference Quality), alsook een set surveillance proefstukken behorende bij het drukvat van een eigenlijke nucleaire reactor, 'BSP' (Belgian Surveillance Program). De twee belangrijkste parameters gerelateerd aan de vorm van de magnetische hysteresislus die in deze context worden bestudeerd zijn het maximum van de relatieve differentiële permeabiliteit en de piekintensiteit van de Preisach-gerelateerde distributie van het lokale interactieveld. Beide parameters dalen met stijgende neutronendosis en met stijgende vloeigrens, en dit voor alle bestudeerde materialen.

Het magnetisch gedrag is gevoelig voor beide door neutronenbestraling geïnduceerde verhardeningsmechanismen: een dalende trend in de hierboven vermelde magnetische parameters tijdens de mechanische verharding is merkbaar, ongeacht de verhardingsoorzaak: ofwel enkel Cu-precipitatie (thermische veroudering van Fe-Cu modellegeringen), ofwel enkel schade aan de Fe-matrix (bestraling van puur ijzer), ofwel beide mechanismen (bestraling van Fe-Cu modellegeringen of ferritische staalsoorten). Deze resultaten kunnen verklaard worden door het feit dat de beweging van de magnetische domeinmuren gehinderd wordt door defecten van nanometer-grootte, die geïnduceerd zijn door neutronenbestraling. De grootte van de verandering van de magnetische parameters is hierbij typisch 40%, hetgeen de sensitiviteit en het potentieel aangeeft van de magnetische hysteretische karakterisering voor de evaluatie van door neutronenbestraling geïnduceerde materiaalverharding en -verbrossing.

Verder hebben we een magnetomechanische meetopstelling ontworpen en gebouwd voor de studie van het ***magnetomechanisch gedrag***. Deze opstelling is in principe de integratie van een magnetische meetopstelling in een mechanische testbank. Met deze meetopstelling wordt het mogelijk het magnetomechanisch effect te bestuderen, een effect dat kan beschreven worden als het gecombineerde effect op de magnetisatie van een aangelegde elastische mechanische spanning en een aangelegd magnetisch veld. Magnetomechanische experimenten zijn uitgevoerd voor verschillende omstandigheden betreffende elastische spanning en magnetisch veld (beide grootheden kunnen hierbij zowel statisch als dynamisch zijn). In het geval van constant aangelegd magnetisch veld en cyclisch variërende mechanische spanning, vertoont de magnetisatie als functie van spanning voor laag-koolstof ferritisch staal typisch een hysteretisch, asymmetrisch, niet-lineair en niet-monotoon gedrag. Een zekere overeenkomst in de niet-lineariteit van dergelijk hysteretisch magnetomechanisch gedrag is merkbaar in vergelijking met het anhysteretisch magnetomechanisch gedrag.

Dergelijke experimentele studie van het magnetomechanisch gedrag is uitgevoerd met als doelstelling magnetische NDE-methodes te ontwikkelen voor het continu monitoren van metaalvermoeiing. Wegens het abrupte finale karakter van metaalvermoeiing is het moeilijk voorspellingen te maken over de aanvang van het

vermoeiingsfalen, wanneer dit enkel gebaseerd is op experimentele data verworven tijdens een beperkt aantal onderbrekingen van de cyclische belasting. Daarom verkennen we in dit werk de mogelijkheid tot het onderzoeken van het vermoeiingsproces tijdens de cyclische mechanische belasting zelf, en zodoende ook experimentele data te verwerven voor elke mechanische belastingscyclus. Voor dergelijke doelstelling kan van het magnetomechanisch effect gebruik gemaakt worden: tijdens de cyclische mechanische belasting wordt een magnetisch veld aangelegd, en de variatie van de magnetisatie (omwille van zowel de aangelegde cyclische mechanische spanning en het aangelegde veld) kan continu opgemeten worden tijdens de gehele cyclische mechanische vermoeiingstest.

Twee magnetomechanische methodes worden vooropgesteld, methodes die enkel verschillend zijn wat betreft het magnetisch veld dat continu aangelegd wordt aan het proefstuk tijdens de cyclische mechanische belasting: i.e. een constant of een tijdsafhankelijk magnetisch veld. In beide methodes wordt tijdens elke spanningscyclus de magnetisatieverandering veroorzaakt door het magnetomechanisch effect continu opgemeten. Beide magnetomechanische methodes resulteren in informatie over de verschillende vermoeiingsstadia, alsook over het finale vermoeiingsstadium, en dit is het geval voor alle drie de bestudeerde ferritische staalsoorten. De kenmerkende eigenschappen betreffende de magnetomechanische monitoring parameters in het stabiele (tweede) stadium, vertonen potentieel om een stop-criterium te definiëren voor het stopzetten van de werking van stalen componenten onder cyclische belasting. Deze methode van continu monitoren van veranderingen in het magnetomechanisch gedrag tijdens de cyclische mechanische belasting is gevalideerd door het vergelijken met de continue evaluatie van veranderingen in het mechanische rek-versus-spanningsgedrag: de verschillende vermoeiingsstadia in het inelastische rek-versus-spanningsgedrag corresponderen volledig met de overeenkomstige vermoeiingsstadia gedefinieerd aan de hand van het magnetomechanisch gedrag.

Als algemene conclusie, veranderingen in de microstructurele eigenschappen betreffende de kristalroosterdefecten beïnvloeden de dynamica van dislocaties, maar hebben ook een impact op de beweging van de magnetische domeinmuren in ferromagnetische materialen; dit leidt respectievelijk tot veranderde mechanische en magnetische macroscopische eigenschappen. Hoewel de onderliggende mechanismen van het magnetische en mechanische gedrag verschillend zijn, bestaat er een zekere interrelatie tussen het macroscopische magnetische gedrag, het magnetische mechanische gedrag en de onderliggende microstructurele eigenschappen van het materiaal. De ontwikkelde magnetische en magnetomechanische karakteriseringstechnieken kunnen gebruikt worden voor de niet-destructieve evaluatie van macroscopische mechanische eigenschappen en microstructurele kenmerken, met als doelstelling de beoordeling van de ferromagnetische materiaalintegriteit tijdens hun werking en/of voor de kwaliteitscontrole tijdens materiaalproductieprocessen.

Summary

In our modern industrial world, components of structures or machines manufactured from steels are often operating under very demanding service conditions and frequently for time spans of many years. Such service conditions can impair the material integrity since they induce material degradation processes, manifested as changes in the microstructure of the material. For instance, cyclic mechanical stress gives rise to fatigue damage progression; the combination of both elevated stress levels and high temperatures can induce creep deformation; neutron irradiation can lead to embrittlement. In most cases these material degradation processes are slow processes, but nevertheless the material degradation and the associated deterioration of the mechanical properties is a cumulative and insidious process. Finally, this can lead to nucleation and growth of cracks and even to component failure, which can have disastrous consequences. Therefore, the assessment of the material integrity is of high importance, both for safety and economical reasons. Such integrity assessment on the material level is typically performed by non-destructive evaluation techniques.

In such context of non-destructive assessment of material degradation, the general aim of the presented research is to explore the possibilities, the limitations and the sensitivity of magnetic hysteretic characterization techniques in order to evaluate non-destructively the progression of microstructural degradation phenomena. Such approach is motivated by the knowledge that the macroscopic magnetic hysteretic behaviour of ferromagnetic materials is influenced by the microstructural features of the material, and since the material degradation processes can alter microstructural features, hence these material degradation processes can have repercussions on the magnetic hysteretic behaviour. The underlying fundamental principle of this relation between microstructural features and magnetization processes is one of the crucial points in our research: during the magnetization process, the mobility of the magnetic domain walls, and the structure of the magnetic domains, is influenced by the microstructural features: for instance a high crystal defect density results in a high degree of obstruction to the motion of magnetic domain walls.

Conversely, the change in the shape of the magnetic hysteretic loop reflects the

variation in the microstructural features in the material. In principle, we may identify the microstructural changes and monitor the degradation of the mechanical material properties in a non-destructive fashion, by the characterization and evaluation of the magnetic hysteretic behaviour.

This method postulation, i.e. the characterization of the magnetic hysteretic behaviour, obviously restricts the application of the method to ferromagnetic materials. Nevertheless, the range of application is still very broad, since most of the tonnage of commercially produced iron alloys and low-alloyed steels have a body-centered cubic ferritic crystalline structure, which is ferromagnetic.

The approach of this research work is merely experimental, therefore the development of magnetic characterization methods is a primordial and important issue. We developed versatile experimental setups and field-metric measuring techniques, in combination with advanced analyzing techniques of the experimental data, in order to facilitate and enhance the characterization of the many features related to both the magnetic and the magnetomechanical hysteretic behaviour.

In our experimental investigations on mechanically degraded materials, the sample dimensions are however constrained to much smaller dimensions than the dimensions prescribed in international standards. Also the sample shape is in many cases constrained to bars with square or circular cross sections. Even for such samples with constrained size and shape we succeeded to design modified and miniaturized single sheet tester (SST) configurations, inspired by and as close as possible to the standardized SST, resulting in reasonable accuracy and good repeatability for the magnetic characterization of the different samples under investigation.

Concerning the magnetic hysteretic characterization techniques for NDE purposes, the core issue is to define magnetic parameters that are sensitive enough to identify the changes of microstructural properties under investigation. As a first step, the classical magnetic hysteresis parameters characterizing the saturation magnetization loop, such as coercive field, remanent induction, permeability, can be used. In this research work, the magnetic hysteretic non-destructive evaluation method is extended by increasing the input of experimental data. Moreover a hysteresis model such as the Preisach model that takes the overall magnetic hysteresis behaviour into account is shown to be useful for non-destructive evaluation of microstructural changes.

Based on a number of experimental case studies for several material degradation processes, the possibilities and limitations of both the magnetic hysteretic and magnetomechanical characterization are investigated.

Concerning the effect of microstructural changes on the ***magnetic hysteretic behaviour,*** one of the main topics that is investigated in this research work, is the irradiation-induced embrittlement and hardening of iron-based materials. In the

nuclear industry this effect can be detrimental for reactor pressure vessel (RPV) steels. The underlying reason of such material degradation process is the formation of nano-size defects during neutron irradiation, i.e. the irradiation-assisted Cu-precipitation, accompanied with matrix damage.

Conventionally, the material status concerning embrittlement, hardening and fracture toughness is evaluated destructively on the basis of surveillance specimens, made of exactly the same material as the pressure vessel. In order to cope with extending the life time of nuclear power plants and considering the limited number of specimens originally inserted into the reactor in order to perform such destructive mechanical tests, there is a tendency to develop non-destructive evaluation techniques. Such techniques can be considered as additional and/or possible replacement techniques to assess the material condition, having also the advantage that the surveillance specimens can be reused.

Firstly, the hardening and embrittlement processes due to Cu-precipitation, separately from the effects of the irradiation-induced matrix damage, is investigated during this research work by thermal aging of Fe-Cu model alloys. The formation and growth of Cu-precipitates during the thermal aging process at 500°C lead to variations of the investigated magnetic hysteretic properties, such as remanence, maximum permeability, width and peak value of the Preisach-based local interaction field distribution. The regimes that can be indicated in their relation to the aging time correspond with the mechanical hardening and softening regimes, in other words the magnetic parameters fully mimic the yield stress variation. When compared to the initial case, the peak hardening values of the magnetic parameters, such as remanence, maximum permeability, width and peak value of the local interaction field distribution, change with approximately 50% (or more, depending on the considerered magnetic parameter). This pronounced sensitivity indicates the potential of magnetic NDE for the evaluation of hardening and softening phenomena induced by Cu-precipitation.

Secondly, the irradiation-induced embrittlement and hardening is studied. The irradiation-induced microstructural changes not only affect the mechanical behaviour, but also lead to variations in the magnetic hysteretic behaviour for all investigated materials, i.e. nominally pure Fe, Fe-Cu model alloys, and RPV steels, both for a reference quality of RPV steel, 'JRQ' (Japanese Reference Quality), and for the surveillance samples of the reactor pressure vessel of an actual nuclear reactor, 'BSP' (Belgian Surveillance Program). The main two parameters related to the magnetization loop shape that are investigated are the maximum relative differential permeability, and the peak intensity of the Preisach-based local interaction field distribution. Both parameters decrease with increasing neutron fluence and with increasing yield stress, and this for all investigated materials.

The magnetic behaviour is sensitive to both irradiation-induced hardening mechanisms: a decreasing trend in the above-mentioned magnetic parameters during

the mechanical hardening is noticeable, regardless the origin of hardening, which can be either Cu-precipitation (thermal aging of Fe-Cu model alloys), only matrix damage (irradiation of pure Fe), or both mechanisms (irradiation of Fe-Cu model alloys or ferritic RPV steels). These results suggest that the magnetic domain wall movement is hindered by the nano-sized defects induced by irradiation. The change of the magnetic parameters is found to be up to 40%, which indicates the sensitivity and the potential of magnetic hysteretic characterization for the assessment of irradiation-induced material hardening and embrittlement.

Concerning the ***magnetomechanical behaviour,*** we designed and constructed a magnetomechanical experimental setup, which is in principle the incorporation of a magnetic measurement setup inside a mechanical testing apparatus. With this setup it becomes possible to investigate the magnetomechanical effect, which can be considered as the combined effect of elastic mechanical stress and magnetic field on the magnetization. Magnetomechanical experiments are conducted for different conditions of elastic stress and magnetic field (both as static or dynamic quantities). In case of constant applied magnetic field and cyclic varying mechanical stress, for low-carbon ferritic steels the magnetization-stress behaviour shows hysteretic, asymmetric, non-linear and non-monotonic features. A fair correspondence in the non-linearity of such hysteretic stress-magnetization behaviour and of the anhysteretic stress-magnetization behaviour is observed.

Such an experimental study of the magnetomechanical behaviour is performed with as aim to develop magnetic non-destructive evaluation methods for the continuous monitoring of the metal fatigue damage process. Due to the abrupt character of metal fatigue it can be difficult to make predictions about the onset of fatigue failure based on experimental data obtained at only a limited number of load interruptions. Therefore we explore in this research work the possibility to examine the fatigue process during the cyclic mechanical loading itself, in order to experimentally obtain information for every single mechanical loading cycle. For this purpose the magnetomechanical effect can be exploited: during the cyclic mechanical loading the application of a magnetic field can be considered, and the magnetization variation resulting from both the applied mechanical stress and the enforced magnetic field can be continuously monitored throughout the cyclic mechanical loading test.

Two magnetomechanical examination methods are investigated, differing only in the magnetic field that is continuously applied to the sample during the stress-controlled cyclic mechanical loading: i.e. a constant magnetic field, or a time-varying magnetic field. In both methods the magnetization variation during each stress cycle due to the magnetomechanical effect, is continuously measured. Both magnetomechanical methods provide information about the different stages in the fatigue lifetime and also about the final fatigue stage. This is the case for the three investigated ferritic steels. The finer-scale features of the magnetomechanical monitoring parameters in the steady-state stage, show potential to be used in

order to define and evaluate a stop criterion for the cyclic load operation of steel components. This method of continuously monitoring the changes in the magnetomechanical behaviour during the cyclic mechanical loading is validated by comparing with the continuous examination of changes in the mechanical stress-strain behaviour: the different fatigue stages in the inelastic strain-stress behaviour fully mimic the corresponding fatigue stages in the magnetomechanical behaviour.

As a general conclusion, changes in the microstructural features of the crystal lattice defects influence the dislocation dynamics, but also affect the magnetic domain wall motion in ferromagnetic materials, which lead to altered mechanical and magnetic macroscopic properties, respectively. Although the underlying mechanisms of magnetic and mechanical behaviour are different, there exists a certain interrelation between the macroscopic magnetic behaviour, the macroscopic mechanical behaviour and the underlying microstructural features of the material. The developed magnetic characterization techniques can be exploited for the non-destructive evaluation of macroscopic mechanical properties and/or microstructural features, aiming for the assessment of ferromagnetic material integrity during their operation or for the quality control during material processing.

Contents

List of notations, symbols and abbreviations

General notations

- scalar quantities: V (voltage), r (distance), f (frequency)
- units: V (Volt), m (meter), Hz (Hertz)
- spatial unity vectors (cartesian coordinate system): $\mathbf{e}_x$, $\mathbf{e}_y$, $\mathbf{e}_z$ (or $\mathbf{e}_1$, $\mathbf{e}_2$, $\mathbf{e}_3$)
- spatial vectors in the time domain: $\mathbf{H}(x, y, z, t) = H_x(x, y, z, t)\ \mathbf{e}_x + H_y(x, y, z, t)\ \mathbf{e}_y + H_z(x, y, z, t)\ \mathbf{e}_z$
- tensors: $\overline{\mathbf{c}}$ (stiffness), $\overline{\sigma}$ (stress), $\overline{\epsilon}$ (strain)
- operators and functions: $\mathrm{d}r$, $\partial/\partial x$, $\sin(x)$
- indices of crystallographic direction: $[100]$
- indices of family of crystallographic directions: $\langle 100 \rangle$
- indices of crystallographic plane: (100)
- indices of family of crystallographic planes: $\{100\}$
- proportional to: $\sim$
- approximated as: $\approx$

Abbreviations

AC	alternating current
b.c.c.	body centered cubic (crystal lattice)
DAQ	data acquisition
DBTT	ductile-to-brittle transition temperature
DC	direct current
EELAB	Electrical Energy Laboratory (Ghent University)
f.c.c.	face centered cubic (crystal lattice)
FEM	finite element method
FWHM	full width at half maximum
GMR	giant magneto-impedance effect

NDE	non-destructive evaluation
PC	personal computer
PDF	Preisach distribution function
PhD	Doctor of Philosophy
PM	permanent magnet
ppm	parts per million
SCK	Studiecentrum voor Kernenergie (Belgian research center for nuclear energy)
SUT	sample under test
SST	single sheet tester
TEM	transmission electron microscope
USE	upper shelf energy
wt%	weight percentage (chemical composition)

Quantity symbols - Greek letters

α_i	direction cosines of magnetization $\mathbf{M}$, relative to the three cubic crystal axes $(i = 1..3)$ [-]
γ	specific domain wall energy [J/m^2] (domain wall energy per unit area)
δ	domain wall width [m]
$\overline{\varepsilon}$, ε	mechanical strain (tensor) [-]
θ	angle [rad]
λ	magnetostriction [-]
λ_s	saturation magnetostriction [-]
λ_{100}	saturation magnetostriction of a cubic single crystal, magnetized along a (100) direction [-]
λ_{111}	saturation magnetostriction of a cubic single crystal, magnetized along a (111) direction [-]
μ_0	magnetic permeability of vacuum [H/m]
μ_r	relative permeability [-]
μ_{rd}	relative differential permeability [-]
μ_{ri}	relative initial permeability [-]
$\overline{\sigma}$, σ	mechanical stress (tensor) [MPa] $\sigma > 0$: tensile stress $\sigma < 0$: compressive stress
σ_y	yield stress [MPa]
φ	angle [rad]
ϕ	physical magnetic flux [Wb]
ψ	coupled magnetic flux [Vs]
χ	magnetic susceptibility [H/m]
ω	angular velocity [rad/s]
Ω	volume [m^3]

Quantity symbols - Roman letters

a	cubic lattice spacing [m] (cube edge length of a cubic crystal lattice)
A	exchange stiffness [J/m]
$\mathbf{A}$	magnetic vector potential [Vs/m]
$\mathbf{B}$, B	magnetic induction (magnetic flux density) [T]
B_r	remanent induction [T]
$\overline{\mathbf{c}}$	mechanical stiffness tensor [MPa]
C	capacitance [F]
d	geometrical quantity, thickness, diameter [m]
$\mathbf{E}$, E	electric field strength [V/m]
f	frequency [Hz]
$\mathbf{F}$, F	force [N]
h	geometrical quantity, height [m]
$\mathbf{H}$, H	magnetic field [A/m]
H_c	coercive field [A/m]
h_c	Preisach elementary loop local coercive field [A/m]
h_m	Preisach elementary loop local mean (interaction) field [A/m]
I	current [A]
$\mathbf{J}$, J	magnetic polarization [T]
K_1	anisotropy constant [J/m^3]
l	geometrical quantity, length [m]
L	inductance [H]
$\mathbf{m}$, m	(atomic) magnetic moment [Am^2]
$\mathbf{M}$, M	magnetization [A/m]
$\mathbf{M}_{loc}$	local magnetization [A/m]
M_s	spontaneous magnetization [A/m]
P	Preisach distribution function [H/A]
Q_c	Preisach-based local coercive field distribution [H/m]
Q_m	Preisach-based local interaction field distribution [H/m]
$\mathbf{r}$	position vector [m]
r	geometrical quantity, distance, radius [m]
R	electrical resistance [Ω]
$\mathcal{R}$	magnetic reluctance [H^{-1}]
s	mechanical compliance [MPa^{-1}]
S	cross section [m^2]
t	time [s]
T	temperature [K],[^{o}C]
v	velocity [m/s]
V	voltage [V]
w	energy density [J/m^3]
W	energy, energy loss [J]
Z	electrical impedance [Ω]

Chapter 1

Introduction

In our modern industrial world, there are components of structures or machines manufactured from steels which are often operating under very demanding service conditions and frequently for time spans of many years. For instance, there are steel constructions which are subjected over the years to a high number of mechanical loading cycles of considerable stress amplitude. Other examples are components in power plants that are intended to operate under the application of considerable mechanical stress levels and at high service temperatures, such as boiler tubes. In nuclear applications there are also components such as reactor pressure vessels that are exposed to considerable neutron irradiation fluences.

Concerning the integrity of the material from which the machine or structural component is manufactured, these demanding in-service conditions can induce small scale **material degradation** processes, which are manifested as changes in the microstructure of the material. These material degradation processes are in most cases slow processes, but nevertheless the degradation of the mechanical properties is a cumulative and insidious process. For instance, cyclic mechanical stress can give rise to fatigue damage progression; the combination of both elevated stress levels and high temperatures can induce creep deformation; thermal ageing can give rise to precipitation hardening; neutron irradiation can lead to embrittlement.

The above-mentioned material degradation processes can lead to a deterioration of the macroscopic mechanical properties and/or to the nucleation of cracks. Finally, this can lead to component failure. Failure of critical components in a construction or machine can have disastrous consequences. Therefore, the assessment of the material integrity is of high importance, both for safety and economical reasons. Such assessment of the component integrity on the material property level can typically be performed by **non-destructive evaluation** techniques.

In such context of non-destructive assessment of material degradation, the general aim of our presented research is to explore the possibilities, the limitations and the sensitivity of **magnetic hysteretic characterization techniques** in order to evaluate non-destructively the progression of microstructural degradation phenomena. Such approach is motivated by the knowledge that the macroscopic magnetic hysteretic behaviour of ferromagnetic materials is influenced by the microstructural features of the material, and since the material degradation processes can alter microstructural features, hence these material degradation processes have repercussions on the magnetic hysteretic behaviour.

Numerous experiments have shown that the shape of the magnetization loop is affected by crystal defects, such as for instance dislocations or impurity precipitates. The underlying fundamental principle of this relation between microstructural features and magnetization processes is one of the crucial points in our research, and therefore a complete chapter is devoted to treat it in more detail (chapter 2). Qualitatively we can say that during the magnetization process, the mobility of the magnetic domain walls, and the structure of the magnetic domains, is influenced by the microstructural properties: for instance a high crystal defect density results in a high degree of obstruction to the motion of magnetic domain walls.

Conversely, the change in shape of the magnetic hysteretic loop reflects the variation in the microstructural features in the material. In principle, we may identify the microstructural changes and monitor the degradation of the mechanical material properties in a non-destructive fashion, by the characterization and evaluation of the magnetic hysteretic behaviour. Moreover, the same techniques can also be implemented as quality control monitoring during material production procedures such as mechanical processing and/or thermal treatments.

This method postulation, i.e. the characterization of the magnetic hysteretic behaviour, obviously restricts the application of the method to **ferromagnetic materials**. Therefore, in the following we will confine our investigation to ferromagnetic, mostly iron-based, materials. Nevertheless, the range of application is still very broad, since most of the tonnage of commercially produced iron alloys and low-alloyed steels have a body-centered cubic (b.c.c.) ferritic crystalline structure, which is ferromagnetic. Low-alloyed ferritic steels provide a good strength-to-cost ratio, which explains why they are so widely used as commercial construction steels.

1.1 Contextual framework

In the following section, a brief survey is given to introduce the most relevant topics related to this research work, such as magnetic hysteresis, microstructure, material degradation and non-destructive evaluation.

1.1.1 Magnetic hysteretic behaviour of ferromagnetic materials

Ferromagnetic materials, such as iron or ferritic steels, can be magnetized by an externally imposed time-varying magnetic field. In general, on the macroscopic scale, the relation between the applied magnetic field H (input) and the resulting magnetic induction B (output) is not single-valued, but instead a magnetization loop or hysteresis loop is described, as shown for example in figure 1.1. Other typical features of the $B(H)$ relation are the non-linearity and the saturation property.

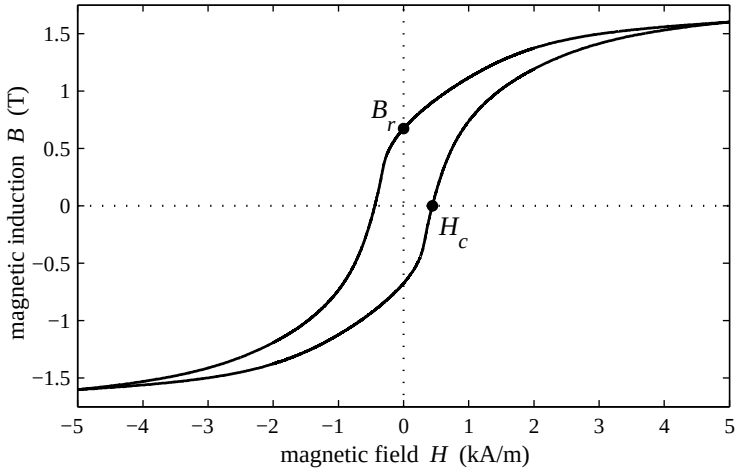

Figure 1.1. Experimentally obtained hysteresis loop $B(H)$ of a sample of low-carbon steel. The hysteresis loop parameters coercive field H_c and the remanent induction B_r are also indicated on the figure.

The indicated parameters coercive field H_c and the remanent induction B_r are only a few of the possible parameters to characterize the hysteresis loop shape, see section 2.1 and chapter 4 for more about the characterization of magnetic hysteresis.

Since the study of the magnetic hysteretic behaviour is the core business of our research, the complete next chapter 2 is devoted to treat the ferromagnetic behaviour in much more detail.

1.1.2 Microstructure, crystal defects and residual stresses

The material behaviour that is apparent on the macroscopic level, such as the magnetic but also the mechanical properties, depends on small scale structural features of the material. Some knowledge about the different possible constituents of the fine structure of the material - also generally termed as the *microstructure*

of the material - is therefore a prerequisite to fully understand the macroscopic behaviour, whether dealing with magnetic or mechanical macroscopic properties.

Therefore the most important aspects - relevant to the present research - of the microstructure of polycrystalline iron-based materials are introduced in this paragraph.

Crystal lattice

The ferromagnetic materials under investigation in this work, such as iron and low-alloyed ferritic steels (with typically about 99 weight-% of iron), have a crystalline structure, which means that the arrangement of atoms is according to a regular and strictly periodic three dimensional pattern. Such periodic arrangement in three dimensions is called the crystal lattice, and the smallest entity of such lattice is called the unit cell.

Ferritic iron and steels have a body-centered cubic (b.c.c.) crystal lattice[1]. In a b.c.c. lattice, the atoms are located on the corners and in the center of a cubic unit cell, as is shown schematically in figure 2.10.

Polycrystalline materials

In commercial metallic materials, such regular arrangement of the crystal lattice typically does not extend to the overall size of the material piece, but instead such materials consist of a very large number of small individual crystals or *grains*. Such materials are called polycrystalline materials. All grains which constitute a polycrystalline material, have the same crystal lattice structure, only the lattice orientation from grain to grain is different.

The ferromagnetic materials under investigation in this work, such as iron and steels, are polycrystalline materials. Figure 1.2 shows a typical grain structure of a low-carbon steel.

One of the parameters to characterize the grain structure is the grain size d_g, defined as the average grain diameter. To give an impression about the different scales involved: for ferritic low-carbon steels, the order of magnitude of grain size is 10^{-4} m to 10^{-6} m, whereas the crystal lattice parameter of Fe is about 3 10^{-10} m.

[1] Up to 1180 K, iron atoms are arranged in a body-centered cubic pattern. The b.c.c. phase is known as the *ferrite* phase of iron, and is ferromagnetic. Above this temperature a phase transition occurs to a face-centered cubic lattice. The f.c.c. phase of iron is known as the *austenite* phase, and is non-magnetic.

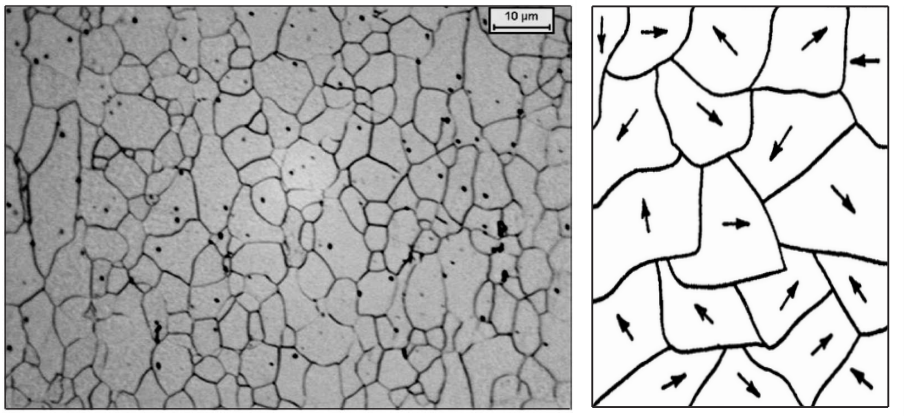

Figure 1.2. (a) Optical micrograph of a polished and chemically etched piece of low-carbon steel, showing several crystal grains separated by grain boundaries. (b) Schematic representation of the difference in crystal lattice orientation for a sub-set of grains.

Evaluated on the macroscopic level, the lattice orientation of the various grains in polycrystalline materials can be random, meaning that all lattice orientations occur in more or less equal quantities. This results in practically isotropic macroscopic properties (no significant property differences when measured in different directions). If on the other hand there are some preferred grain orientations (for instance introduced by the cold rolling of sheets), then we speak about a material with a certain crystallographic texture, which may result in anisotropy of the macroscopic material properties.

Crystal lattice defects

It is an unavoidable reality that commercial polycrystalline materials such as low-alloyed steels are never free from a certain degree of crystal lattice defects. This is a fundamental consequence of equilibrium thermodynamics and is due to the lack of mechanisms to establish thermal equilibrium [Gottstein2004].

Crystal lattice defects can be introduced during the thermal and mechanical processes of the material production process, or they can be developed during the in-service operation of the material. Also, impurity alloying elements disturb the perfect crystal lattice of the dominant ferritic phase (also called the matrix).

Moreover, and maybe this sounds somewhat odd, but it is the existence and the extent of these crystal defects which determines many of the macroscopic properties (the so-called structure-sensitive properties). In other words, the most interesting

features of materials are their imperfections...

Crystal lattice defects can be classified according to their dimensions:

Point defects or atomic size defects are irregularities in the crystal lattice consisting of one missing or additional atom, such as a *vacancy* (missing atom in the matrix), a *substitutional* atom (an impurity atom at a regular crystal lattice site, replacing a matrix atom) or an *interstitial* atom (extra atom, in between the matrix lattice, from an impurity element or from the matrix itself). In figure 1.3 such point defects are depicted schematically. Most prominent are vacancies and impurity interstitials. In reality, agglomerates of point defects can occur, and also so-called extended point defects, where more than one regular site of the perfect crystal lattice is disturbed.

Linear defects or dislocations. A *dislocation* is a one-dimensional defect because the perfect crystal lattice is only disturbed along a line, the so-called dislocation line. The easiest way to visualize the concept of dislocations is by introducing the edge-type dislocation, which can be regarded as an extra crystallographic half plane ending in the actual defect, the dislocation line. Figures 1.3(b) and 1.4 show such an edge dislocation for the simple case of a cubic primitive crystal lattice (in a b.c.c. lattice the exact structure of the dislocation will be more complicated). There exist also other kinds of dislocations (such as screw dislocations, mixed (edge-screw) dislocations) and combinations of dislocations (dislocation dipoles, dislocation loops, see figure 1.3, f and g).

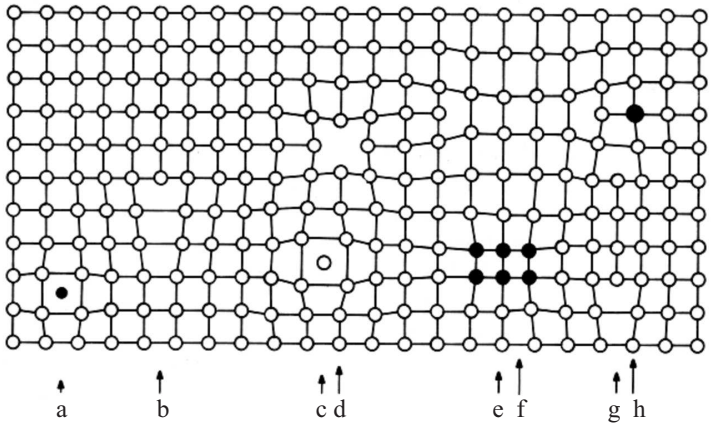

Figure 1.3. Schematic overview of several types of crystal lattice defects (white circles represent the Fe atoms, black circles the impurity atoms of alloying elements): (a) interstitial impurity atom, (b) edge dislocation, (c) self interstitial atom, (d) vacancy, (e) precipitate of impurity atoms, (f) vacancy type dislocation loop, (g) interstitial type dislocation loop, (h) substitutional impurity atom. Credit for this drawing goes to [Föll2006].

More important than the particular classification of dislocation types however, is the fundamental notion that dislocations of any kind are responsible for crystal deformations, since plastic deformation of crystals actually proceeds by the generation and movement of dislocations through the crystal [Gottstein2004].

One of the parameters to characterize the dislocation structure, is the dislocation density ρ_d, defined as the overall dislocation line length per unit volume (typically expressed in cm^{-2} units). To give an rough impression about the dislocation density range for iron and steels [Dieter1988]: even well-annealed materials are never free from dislocations, a dislocation density of about 10^6 cm^{-2} is observed in well-annealed iron which can be regarded as a lower limit. On the other hand, as a practical upper limit, heavily cold-worked steel samples have dislocation densities of about 10^{11} cm^{-2}.

Planar defects such as grain boundaries and phase boundaries, are the interfaces between homogeneous regions of material.

Grain boundaries: neighbouring grains are at an arbitrary crystal lattice orientation to one another, therefore at the grain boundaries there occurs an abrupt and discontinuous change in lattice orientation. The lattice disturbance itself is only a few lattice parameters wide.

Phase boundaries: second phases (such as austenite or martensite) that are present in the matrix or parent phase (e.g. ferrite phase), give rise to discontinuous interfaces in between the different phases. Between two neighbouring phases, both the crystal lattice itself, as well as its orientation can be different.

Volume defects, such as micro-cracks, voids (3D-clusters of vacancies), particle inclusions or precipitates (3D-clusters of impurity atoms). If their volume fraction is small, they can be envisaged as distortions of the matrix. The most important features of such volume defects are their spatial distribution in the matrix and their average size.

Residual stresses

Each of the above-described crystal lattice defects (such as point defects, dislocations, precipitates and so on) can be envisaged as a perturbation of elastic displacement field at the crystal lattice scale, and therefore as a source of local internal stress fields. For instance, figure 1.4 is an illustration of the micro stress distribution around an edge dislocation.

This consideration is in fact part of a broader framework, viz. the concept of *residual stresses* [Mura1987, Kandil2001, Withers2007].

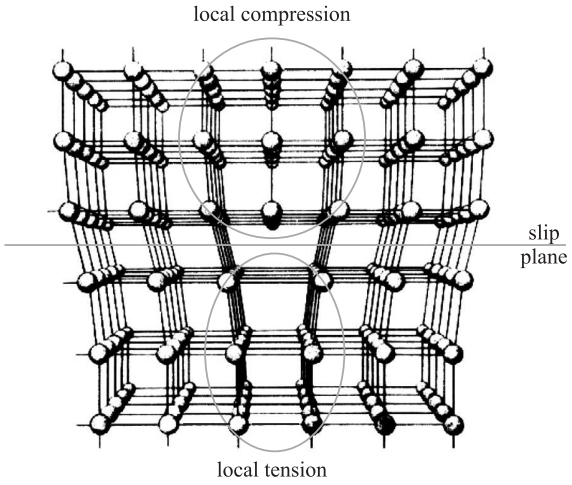

Figure 1.4. Around an edge dislocation, both local compressive and local tensile residual stress fields are present, as indicated in the figure.

Residual stress fields are the stress fields caused by all kinds of incompatibilities or misfits of the crystal lattice. Residual stress fields remain in the material, even in absence of their cause, which can be externally applied forces, thermal gradients or surface constraints. Hence, residual stresses are self-equilibrated: material regions with compressive residual stress are always compensated by other regions in the material having a tensile residual stress, resulting in a zero average stress for the entire material.

Residual stresses originate during the material's manufacturing processes which introduce non-uniform plastic deformation into the material, such as mechanical machining processes, forming, bending, surface treatments (shot peening), heat treatments (quenching), joining by welding... Residual stresses can also be introduced by localized volume changes associated with the precipitation of solute atoms, or with phase transformations. The residual stress state can also continue to develop during the in-service operational life of the material, due to material degradation processes under elevated stress and/or temperature levels.

Classically, three different types of residual stress are defined [Withers2007], depending on the scale at which the material is analyzed for residual stresses, and according to the characteristic length scale over which they self-equilibrate. These three types are shown schematically in figure 1.5.

Macro residual stresses (Type I). This type of residual stresses represents the macroscopic picture of the resulting residual stress distribution due to non-uniform plastic deformation processes, when the underlying microstructure is completely ignored, in order words when the material is characterized at the continuum level.

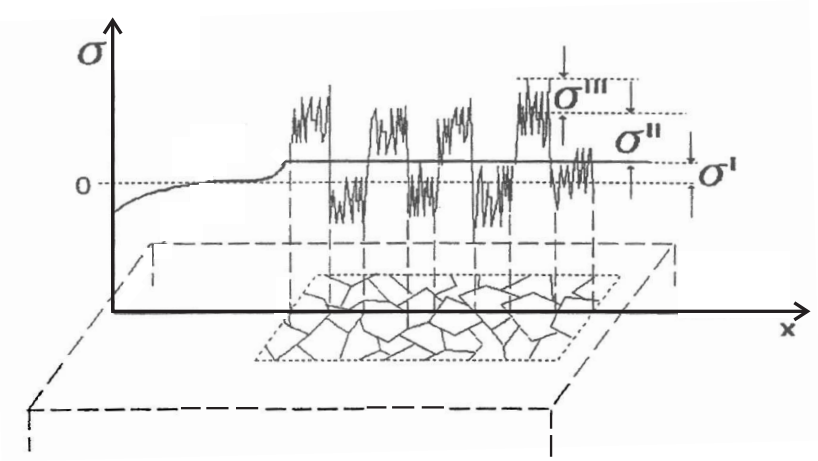

Figure 1.5. Schematic representation of the concept of macro residual stress (type I), intergranular micro residual stress (type II) and atomic-scale micro residual stress (type III) [Kandil2001].

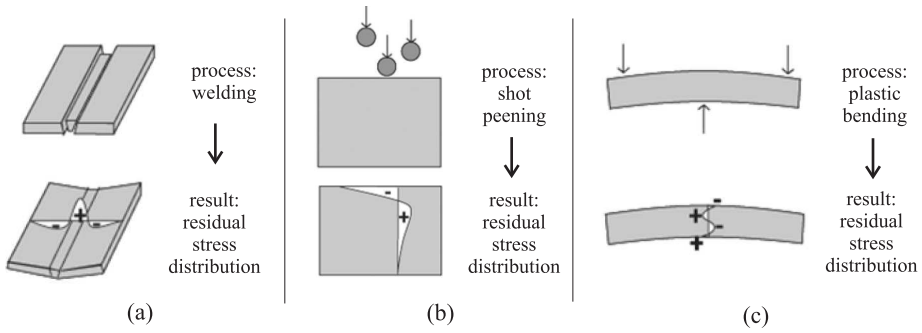

Figure 1.6. Three examples of macro residual stress distributions (type I) along the material's cross section (convention: tensile stress is positive, compressive stress is negative): (a) **Welding** typically produces large tensile stresses in the weld itself, which are balanced by compressive residual stresses in the joined pieces of material, due to localized thermal expansion and non-uniform cooling. (b) **Shot peening** surface treatment: balls are projected with a high speed to the material's surface. This leads to plastic deformation of the surface layers, leading to compressive residual stresses in these outer layers, compensated by tensile residual stresses in the bulk of the sample. (c) In case of **bending**, four different regions of residual stress can be distinguished: during the bending process the outer layers are plastically deformed: the top outer layer is plastically deformed in tension (resulting in compressive residual stress), whereas the bottom outer layer is plastically deformed in compression (so tensile residual stress). The center part is only elastically deformed during bending (top middle layer in elastic tension, bottom middle layer in elastic compression) and when the externally applied stress is removed, the outer regions which have been plastically deformed prevent the inner elastic regions from undergoing complete elastic recovery to the unstrained condition. Credit for these drawings goes to [Withers2007].

Here, the characteristic length over which the residual stresses self-equilibrate, is the size of the considered material piece. Figure 1.6 gives some examples of macro residual stresses (type I).

A more realistic picture of the residual stress distribution is of course obtained when the actual crystal defects and the associated micro residual stresses are also taken into account. Two types of micro residual stresses are distinguished:

Intergranular micro residual stresses (Type II). These residual stresses reflect the anisotropy in the behaviour of each individual grain. Differences in slip behaviour between differently oriented grains result in inhomogeneous deformation at the intergranular level. Consequently the characteristic length for type II residual stresses is of the order of (several times) the grain size. Another origin of Type II residual stresses can be the occurrence of multiple phases in the material, where the different phases have different material properties.

Atomic-scale micro residual stresses (Type III). The origin of such residual stresses are the actual crystal defects, such as dislocations (as depicted in figure 1.4), point defects, inclusions. Such lattice imperfections result in incompatible permanent strains, the so-called eigen-strains [Mura1987]. The characteristic length is much smaller than the grain size, i.e. several crystal lattice parameters.

The effects of the combined residual stresses (types I, II, and III) on the mechanical material behaviour may be either beneficial or detrimental, depending on the sign of the residual stress. For instance, if the residual stress is tensile, it adds to a tensile applied stress and hence the total stresses can become sufficiently large to cause local plastic deformation. In other words the applied stress at which failure occurs can become lower than in the hypothetic case without residual stresses.

Conclusion about crystal defects and residual stresses (section 1.1.2)

Such an alternative view on crystal defects, namely by the concept of residual stress fields, is very convenient for the treatment of the effect of microstructural features on the magnetic properties. As we will see later in chapter 2, the central concept in this relation between microstructure and ferromagnetic behaviour is the *magnetoelastic coupling*, i.e. the influence of mechanical stresses (of any kind: micro residual, macro residual or applied) on the magnetic domain structure[2].

[2] Qualitatively speaking, in case of tensile residual stresses for instance, due to the magnetoelastic coupling it becomes energetically favourable for the magnetic moment vectors to change their orientation, so that in positive magnetostrictive materials for example, the magnetic moment direction approaches more the tensile stress direction. Consequently, the corresponding stress-induced changes of the magnetic domain distribution have an effect on the macroscopic magnetic hysteretic behaviour. But now we are really running ahead, the concept of magnetoelastic coupling is treated in more detail further in chapters 2 and 6.

1.1.3 Effect of microstructure on the magnetic and mechanical macroscopic properties

Crucial in this research is the interrelation between the macroscopic magnetic behaviour, the macroscopic mechanical behaviour and the underlying microstructural features of the material. In this section some examples are given to illustrate the effect of the microstructure on both the magnetic and the mechanical macroscopic behaviour.

Effect of microstructure on magnetic properties

Magnetic hysteretic properties depend on microstructural features. Qualitatively speaking, the magnetic domain walls have to overcome various types of microstructural obstacles during their movement, a process which is responsible for the magnetic hysteretic behaviour. Here, two illustrative examples are given: the effect of grain size and the effect of dislocation density on the coercive field.

(a) Grain size. Above a certain value for the grain size (of the order of 1 μm [Herzer1990]), the coercive field of iron and ferritic steels is found to decrease with increasing grain size. As explained later in chapter 2, grain boundaries obstruct the domain wall motion and act as pinning sites for the domain walls. With increasing grain size, the overall surface of all grain boundaries decreases and hence domain wall pinning decreases. Qualitatively speaking the coercive field H_c is associated with the strength of domain wall pinning, therefore H_c decreases with increasing grain size. Based on experimental and theoretical data, an inverse dependency of coercivity H_c on grain size d_g is often given as an empirical relation in the literature [Mikheev1981, Sablik2001]:

$$H_c = c_1 + \frac{c_2}{d_g}, \tag{1.1}$$

with c_1 and c_2 constants, which however can depend on microstructural features other than grain size.

(b) Dislocation density. The coercive field of iron and ferritic steels is found to increase with increasing dislocation density. Qualitatively speaking, as dislocation density increases, dislocations begin to get clustered or entangled, and as explained later in chapter 2, this results in stronger pinning sites for the magnetic domain walls. Hence the coercive field H_c, which reflects the pinning strength, increases with increasing dislocation density ρ_d. Kronmüller systematically studied the effect of dislocations on magnetic properties of single crystals [Kronmüller1972], a study which is based on theoretical micromagnetic considerations (see section 2.3) and which results in the following relation:

$$H_c \sim \sqrt{\rho_d}. \tag{1.2}$$

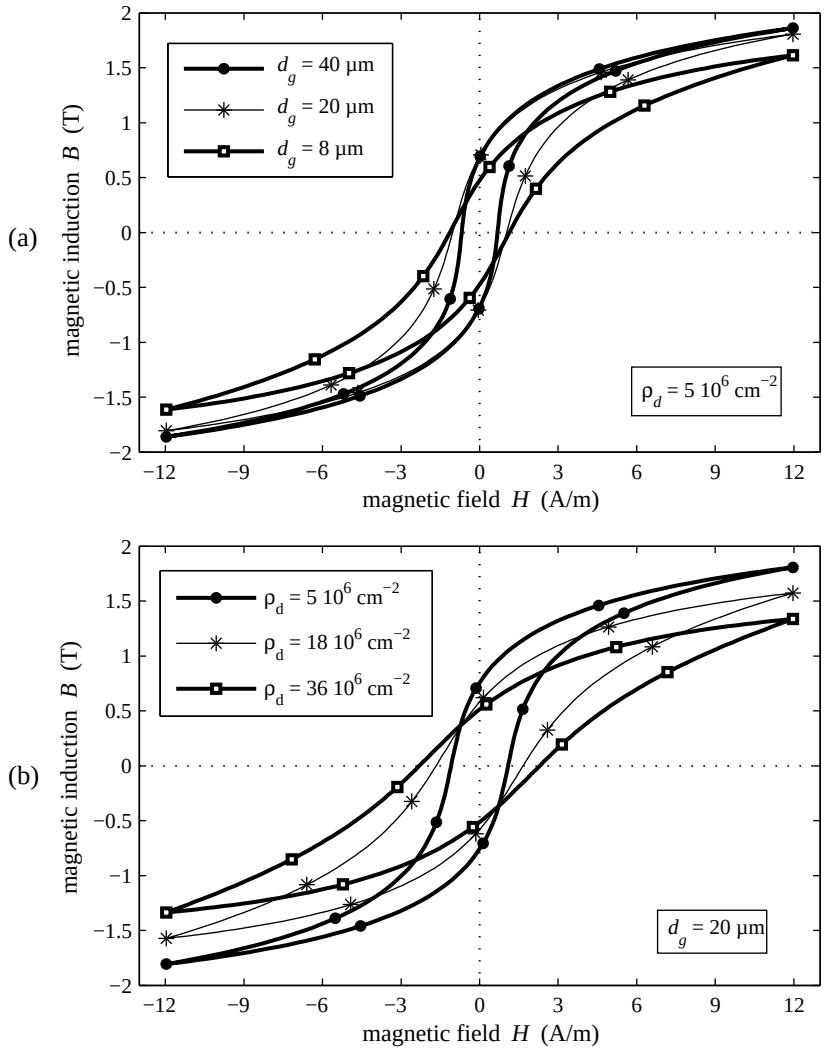

Figure 1.7. (a) Effect of grain size on the magnetic hysteresis loop shape, for several grain size values (notice that $1/d_g$ is more or less equidistant). Dislocation density has a constant value, as indicated. (b) Effect of dislocation density on the magnetic hysteresis loop shape, for several dislocation density values (notice that $\sqrt{\rho_d}$ is more or less equidistant). Grain size has a constant value, as indicated. All hysteresis loops in (a) and (b) are the result of simulations dealing with 3 wt% Si non-oriented electrical steels [Dupré2002].

This theoretical prediction is also confirmed with experimental data [Lubitz1974, Sternberk1983].

Grain size and dislocation density do not only have an effect on the coercive field, but also on the entire magnetic hysteresis loop shape, as illustrated in figure 1.7. The remanent induction B_r and the maximum differential permeability $\mu_{d,max}$ (with $\mu_d = \mathrm{d}B/\mathrm{d}H$) both decrease with increasing dislocation density ρ_d or with decreasing grain size d_g.

Effect of microstructure on mechanical properties

Generally speaking, crystal lattice imperfections have a mechanical strengthening effect, since the lattice defects act as obstacles to the movement of dislocations when a mechanical stress is applied. For instance, in absence of other lattice defects a dislocation can move easily when a small stress is applied to the material and therefore plastic deformation occurs already at quite low stress values, hence the yield stress in such case is low. On the other hand, the more the dislocations are hindered by lattice defects during their movement, the larger is the stress necessary to yield the material macroscopically.

Different strengthening mechanisms can be distinguished depending on the type of lattice defect contributing to the obstruction of moving dislocations:

- Solid-solution strengthening (interstitial/substitutional impurity atoms)
- Strengthening from point defects (due to vacancies)
- Work-hardening or strain-hardening (due to other dislocations)
- Grain boundary strengthening
- Martensite strengthening (phase transformation)
- Strengthening from fine particles (due to precipitates/inclusions)

Here, not all strengthening mechanisms are treated, just the same two examples as in the preceding paragraph on magnetic properties are given: the effect of grain size d_g and the effect dislocation density ρ_d on the yield strength σ_y, so the strengthening effect of grain boundaries and the work hardening effect, respectively.

(a) Grain size. The yield strength of iron and ferritic steels is found to increase with decreasing ferrite grain size. This mechanism is known as grain boundary strengthening. Qualitatively speaking, it is difficult for a dislocation to move from one grain to another, especially if the neighbouring grain directions make large angles. Grain size reduction results in larger grain boundary surface area per unit volume, and therefore this results in more obstruction to dislocation movement at the grain boundaries, resulting in dislocations that pile up against the grain boundary. All this leads to higher yield strength with decreasing grain size. The

general relationship describing the effect of grain size on yield strength is given by the Hall-Petch relation:

$$\sigma_y = \sigma_f + \frac{k}{\sqrt{d_g}}, \tag{1.3}$$

with σ_f and k material-dependent constants; typical values for e.g. low-carbon steel are σ_f = 70 MPa and k = 0.74 MPa$\sqrt{\text{m}}$ [Gottstein2004]. The friction stress σ_f is the stress required to move a dislocation in a single crystal, or in other words the overall resistance of the crystal lattice to dislocation motion. This Hall-Petch relation has been experimentally confirmed on many iron-based materials, and for grain sizes from 0.1 to 250 μm [Gottstein2004].

(b) Dislocation density. The yield strength of iron and ferritic steels is found to increase with increasing dislocation density. Qualitatively speaking, the more dislocations present in the material volume, the more they get entangled and the more obstruction to the dislocation movement, due to the high density of other dislocations acting as pinning sites. This mechanism is also known as work hardening: the dislocation density increases with plastic deformation (cold work) due to dislocation generation, and the dislocations start blocking the motion of each other. This leads to higher yield strength with increasing dislocation density. The general relationship describing the effect of dislocation density on yield strength is given by the Bailey-Hirsch relation:

$$\sigma_y = \sigma_0 + \alpha G b \sqrt{\rho_d}, \tag{1.4}$$

with G the shear modulus, b the crystal lattice parameter (base length of cubic unit cell), and α a constant equal to 0.4, approximately. Typical values for steels are σ_0 = 100 MPa, G = 80 GPa, b = 0.3 nm [Takaki2005] [3].

Conclusion about the effect of microstructure on magnetic and mechanical macroscopic properties (section 1.1.3)

In section 1.1.3 we illustrated that the changes in the microstructural features of the crystal lattice defects influence the dislocation dynamics, but also affect the magnetic domain wall motion in ferromagnetic materials, which leads to altered mechanical and magnetic macroscopic properties, respectively.

Although the underlying mechanisms of magnetic and mechanical behaviour are different, the preceding examples indicate a certain interrelation between the macroscopic magnetic behaviour, the macroscopic mechanical behaviour and the underlying microstructural features of the material.

[3] When inserting the minimum and maximum dislocation density values (see page 7), viz. ρ_d = 10^6 cm^{-2} and 10^{11} cm^{-2}, this formula results in $\sigma_y = 101$ MPa and 404 MPa respectively.

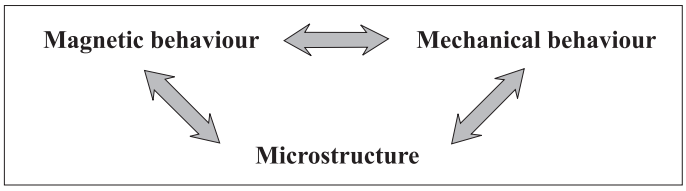

Figure 1.8. The core business of our research can be situated in this triangular relation between 'Magnetic properties' – 'Microstructure' – 'Mechanical properties'.

In the preceding examples related to the effects of grain size and dislocation density on yield strength and coercivity, some qualitative trends become apparent: increasing the dislocation density or decreasing the grain size leads to mechanical hardening (increased yield strength), but also leads to increased coercivity, in other words leads to magnetic 'hardening'. Generally speaking, such a trend - an increase of coercivity with increasing hardness - is also often found experimentally [Devine1992].

However, one should be careful in interpreting such experimental results. In reality it is difficult to change only one of the microstructural features and to keep the other features constant. For instance, a lower grain size (i.e. more grain boundaries per unit volume) inherently leads to more dislocations located at the border of the grain boundaries. Therefore, during experiments the changes in macroscopic properties can be influenced by more than one microstructural feature. When aiming at experimentally investigating the effect of a certain microstructural feature, great care should be taken to estimate or to minimize the possible effect of other microstructural properties, for instance by working with stress-relief annealed samples, or by studying separate effects on binary model alloys.

1.1.4 Material degradation

The microstructural features of materials and the associated crystal lattice defects, which determine the macroscopic mechanical and magnetic behaviour, can be introduced and modified during the material's manufacturing processes, but moreover, these microstructural defect structures can also develop further during in-service operation. Such service-induced microstructural changes can lead to gradual deterioration of the mechanical properties of the material, therefore the underlying mechanisms are termed as material degradation processes.

Steel components of structures or machines are often operating under very demanding **service conditions** (conditions dealing with stress, temperature and/or irradiation), and are frequently operating for time spans of many years. To give some examples:

- Components, such as crankshafts, are subjected during the years to a high number of mechanical loading cycles of considerable stress amplitude;
- Components in power plants, such as boiler tubes and steam turbine blades, operate under the application of considerable mechanical stress levels and at high service temperatures;
- Components in nuclear applications, such as reactor pressure vessels, are exposed to considerable neutron irradiation fluences.

Concerning the integrity of the material from which the machine or structural component is manufactured, these demanding in-service conditions can induce small scale **material degradation** processes, which are manifested as changes in the microstructure of the material. These material degradation processes are in most cases slow processes, but nevertheless the associated degradation of the mechanical properties is a cumulative and insidious process. To give some examples of material degradation processes, starting from the above-mentioned examples of service conditions:

- cyclic mechanical stress at constant temperature can give rise to **isothermal fatigue** damage progression: fatigue is a cumulative damage process under the application of cyclic mechanical loading, which starts with modifications in the dislocation density and dislocations substructure, followed by the initiation and growth of micro-cracks, and the development of a dominant macroscopic crack, a process which can end in fatigue fracture;
- the combination of both elevated stress levels and high service temperatures can induce **creep deformation**: creep is a continuous deformation process at constant load and elevated temperature, associated with dislocations overcoming obstacles by thermally assisted mechanisms such as vacancy diffusion, a process which can end in creep fracture;
- the combination of both time-varying stresses and time-varying temperatures – most frequently found in start-up and shut-down cycles of high temperature components e.g. in power plants – can lead to **thermomechanical fatigue**, which can be regarded as the interaction of several material degradation processes such as fatigue, creep and oxidation;
- neutron irradiation can lead to **irradiation-induced embrittlement** which is a decrease of toughness, due to the irradiation-induced increase of point defect density and due to the irradiation-induced precipitation of solute atoms, a process which can lead to brittle fracture.

The above-mentioned material degradation processes can lead to a deterioration of the macroscopic mechanical properties and/or to the nucleation of cracks. Finally, this can lead to component failure, which can have disastrous consequences in critical components. Hence, in order to avoid that material degradation processes such as metal fatigue, embrittlement, creep... eventually lead to fracture or failure, material condition monitoring is vital, both for safety and for economical reasons.

The assessment of the material integrity is treated in the following sections 1.1.5 to 1.1.7.

Firstly, two of the material degradation processes that are treated further in this research, i.e. neutron irradiation embrittlement and isothermal metal fatigue, are introduced in more detail.

Example 1: embrittlement due to neutron irradiation

Neutron irradiation is known to cause embrittlement during long-term service of iron-based materials. In the nuclear industry, such a material degradation process can be detrimental for the reactor pressure vessel. To assure safe operation of a nuclear power plant, the integrity of the reactor must be guaranteed for the entire lifetime of the plant. The irradiation-induced embrittlement of the reactor pressure vessel steels is therefore a main concern in order to cope with extended life times of nuclear power plants.

The reactor pressure vessel (RPV) is part of the primary closed loop of a nuclear plant, and contains the nuclear reactor core, see figure 1.9. Typical dimensions of the RPV are a height of 15 m, a diameter of 5 m and a wall thickness of 0.2 m [Odette1998]. Typical operational conditions of a pressurized water reactor (PWR) are $300\,^{\circ}\mathrm{C}$ and 150 bar.

The RPV is made of a low-carbon Cu-alloyed[4] ferritic steel. First types of RPVs were constructed with welded steel plates or rings (with a typical average Cu-content of 0.2 wt$\%$ Cu [Chaouadi2005]), resulting in even higher copper concentrations at the location of the welds. As explained later on, the precipitation of Cu (for instance at the welds) is one of the causes for embrittlement, therefore the latest generation of RPVs are 'one-piece' constructions with ferritic steels having a lower average Cu-content (typically 0.1 wt$\%$ Cu [Chaouadi2005]). At the surface of the ferritic reactor pressure vessel, typically an austenitic steel cladding is added (typically 5 mm thick), mainly for anti-corrosive purposes.

In commercial reactors a neutron flux of 10^{10} neutrons/cm^2/s typically reaches the reactor pressure wall, which leads to the irradiation-induced embrittlement of the ferritic steel of the RPV wall. Due to its size, its position at the heart of the reactor, and the high degree of contamination, such a RPV is quasi-irreplaceable in a cost-effective way.

Dealing with the material degradation process itself, on the microstructural level, the neutron irradiation enhances the creation of nano-size defects, such as the

[4]Cu is commonly used as alloying element for reactor pressure vessel steels in nuclear power plants, mainly because Cu-alloyed steels exhibit an improved strength at the elevated reactor operating temperatures ($\approx 300^{\circ}$C).

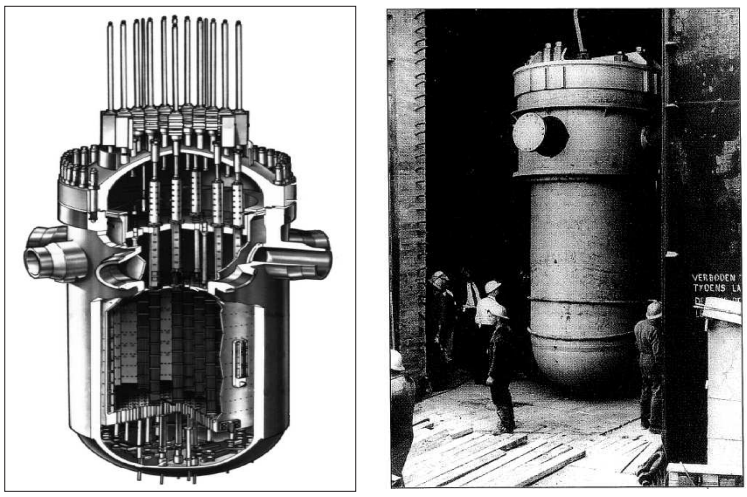

(a) (b)

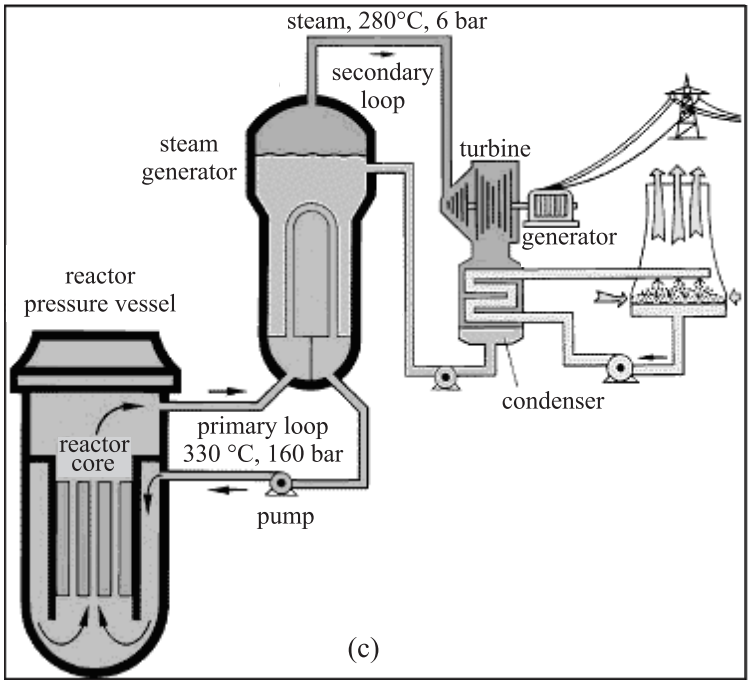

Figure 1.9. (a) illustration of a section of the reactor pressure vessel; (b) photograph of the mounting of the reactor pressure vessel into the BR3 test reactor building (1962, SCK-CEN, Mol, Belgium) to give an impression about its size; (c) simplified overview of the main components in a PWR nuclear power plant.

increase of matrix damage (e.g. point defects, vacancy-interstitial clusters) and the formation of Cu-rich precipitates. Both types of defects (matrix damage and Cu-precipitates) act as obstacles impeding the dislocation motion, resulting in undesired changes of the mechanical material properties, such as a decrease of toughness and ductility.

Conventionally, the embrittlement status is evaluated on the basis of destructive tests on surveillance specimens made of the same material as the vessel. Such surveillance samples have been originally inserted in the nuclear reactor, in such a way that the surveillance samples become irradiated faster than the RPV wall itself (typically a three times higher neutron flux reaches the surveillance samples). These surveillance specimens are periodically retrieved and Charpy impact and tensile tests are performed on them, to assess the integrity of the actual reactor pressure vessel. Some typical observations of varying mechanical properties due to irradiation are the increase of yield strength and ductile-to-brittle transition temperature (DBTT), and the decrease of the strain hardening capacity, the ductility

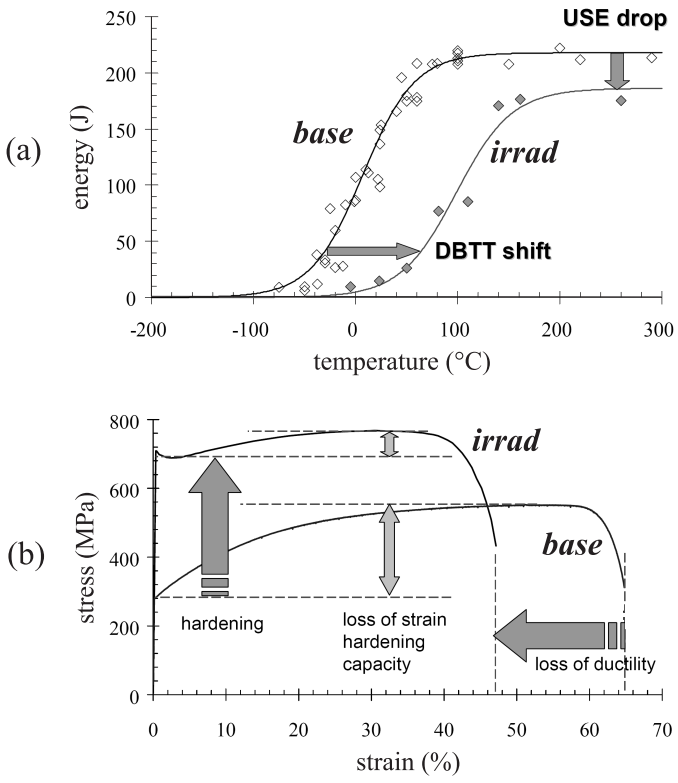

Figure 1.10. Charpy impact and tensile test parameters: typical trends between non-irradiated (base) and irradiated samples.

and the upper shelf energy (USE) [Fisher1985], as is shown in figure 1.10.

However, in order to cope with extended life times of nuclear power plants and considering the limited number of specimens originally inserted into the reactor in order to perform such destructive mechanical tests, there is a tendency to develop non-destructive evaluation (NDE) techniques. Such NDE techniques can be considered as additional and/or possible replacement techniques to assess the material condition. Their advantage is that the surveillance specimens can be reused, so without losing precious surveillance material.

In such context, also magnetic non-destructive evaluation techniques can be considered to assess the embrittlement status, because the development of irradiation-induced microstructural defects – more precisely the variation of the micro-stress distribution around those defects – influences the magnetic domain wall motion, and hence leads to altered macroscopic magnetic properties, such as the magnetic hysteretic behaviour. In this research work, such an approach is studied in more detail in section 5.1.

Example 2: metal fatigue of ferritic steels

Subjecting a material to a high number of mechanical loading cycles can lead to failure, even at cyclic stress levels in the macroscopically elastic regime, so much lower than the stress required to cause fracture by a single application of continuously increasing tensile load. Generally speaking, such failures under cyclic mechanical loading occur after a considerable period of service (i.e. after a high number of loading cycles), which explains why they are called *fatigue* failures. Fatigue is a material degradation process that consists of a progressive cycle-by-cycle accumulation of damage, a degradation process which can insidiously end in a sudden fracture, occurring without any obvious previous warning. Because of its abrupt character, fatigue is responsible for a majority of failures and fractures in industrial components and constructions [Dieter1988].

Here, we focus further on the metal fatigue of ferritic structural steels. The fatigue damage progression can be divided into different (partially overlapping) stages, based on studies of the basic structural changes [Dieter1988, Cui2002, Socha2003]:

(a) Fatigue damage initiation. Even at cyclic stress amplitudes below the macroscopic yield stress, the cyclic mechanical loading can plastically deform the material locally on a microscopically small scale: such micro-plastic flow first occurs in the grains that are stressed with the highest shear stress amplitude, and near inherent material imperfections (inclusions, scratches, voids). Indeed, tensile residual stress concentrations associated with such imperfections, lower the actual applied stress at which the material starts to plastically deform locally in

some individual grains. The initiation of damage due to cyclic deformation therefore consists of microstructural changes associated with localized micro-plastic deformation in some individual grains, i.e. the development of slip bands, the generation of dislocations (increase of dislocation density), and the rearrangement of dislocations into dislocation tangles, dislocation walls and persistent slip bands. These persistent slip bands can be envisaged as embryonic fatigue cracks.
Result: Nucleation of micro-sized cracks along the developed slip bands in a number of grains.

(b) Slip-band (stage-I) crack growth. Consider a micro-crack that is initiated inside an individual grain of a polycrystalline material. Such micro-crack can grow further under sufficiently applied cyclic stress, along slip planes of high shear stress. Then, to develop further, the crack must propagate into the neighbouring grains, which have different lattice orientations and therefore different slip systems. For small micro-cracks to propagate, the crack needs to reorientate at the grain boundary towards a particular slip direction of the surrounding grain. Typically, the majority of lifetime corresponds with micro-crack (nucleation and) growth, which is moreover a regime of stable damage progression.
Result: Formation of dominant crack(s) (with dimensions of typically a few to ten grain diameters wide [Cui2002]).

(c) Transgranular (stage-II) crack growth. As the micro-crack propagates, the plastic zone around the crack tip increases and the resistance to crack growth diminishes. The crack becomes insensitive to grain boundary obstacles and to the particular slip systems of individual grains: the crack now develops in the plane normal to the tensile stress direction, and at much faster rates per loading cycle

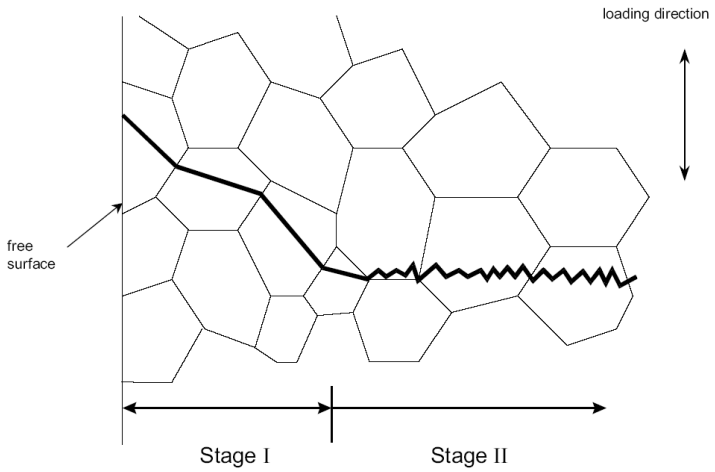

Figure 1.11. Illustration of stage I and stage II crack growth.

compared to stage-I crack growth.
Result: Growth of a well-defined crack, along the plane normal to the applied stress direction, and coalescence of micro-cracks towards a macro-crack with such critical macroscopic dimensions, that the remaining cross-sectional area of the material can no longer support the maximum applied load, and the material fails by ultimate fracture during the last stress cycle.

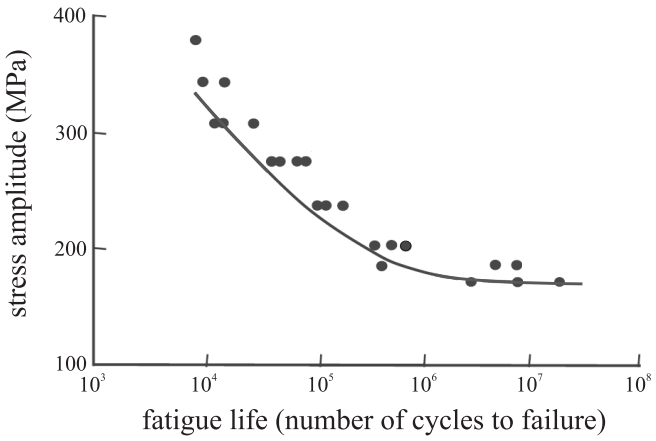

Figure 1.12. A typical S-N curve for a low-carbon steel.

The material's performance concerning the fatigue damage process is typically characterized by a **S-N curve**, also known as a Wöhler curve, which gives the cyclic stress amplitude (σ_a) as a function of the number of cycles to failure (n_f), the latter in a logarithmic scale.

Such a curve is obtained by numerous destructive fatigue tests on a set of macroscopically seemingly identical samples, and with an accurate reproduction of the fatique test conditions. Different levels of cyclic stress amplitude are applied to the individual test specimens (the mean stress remains constant for all samples) and the stress-controlled fatigue test results in the number of cycles to failure.

As illustrated in figure 1.12, the fatigue damage process inherently shows considerable scatter, in spite of the precautions concerning sample preparation and test conditions (for a certain value of σ_a, up to a factor 10 difference in n_f is possible, especially for high-cycle fatigue [Dieter1988]). This scatter is typical for fatigue and indicates that initial differences in microstructural inhomogeneities between macroscopically identical samples, before the start of the fatigue tests, have a considerable impact on the fatigue damage progression of the individual samples.

Another feature that is typical for low-carbon steels becomes apparent in S-N curves: there appears to be a limiting stress amplitude which may be applied indefinitely without failure. This stress amplitude is called the fatigue limit or en-

durance limit of the steel under test. Roughly speaking, the fatigue limit of a certain steel is usually about 40% to 60% of its ultimate tensile strength [Forrest1962]. For applied stresses lower than the fatigue limit, it is observed that micro-cracks nucleate, but that they don't grow through the first microstructural barrier (typically the grain boundary) [Dieter1988].

Detection of fatigue damage is crucial to avoid failure of constructions and machines, because its consequences can be catastrophic both for human lives and equipment. To detect the onset of fatigue failure and to predict the remaining life of a component or structure, evaluation techniques sensitive to the different above-mentioned stages of fatigue damage progression should be used.

Due to the abrupt character of the fatigue failure, and concerning the considerable scatter on the individual fatigue behaviour, the continuous monitoring of the fatigue damage progression is recommended, preferably based on NDE methods. Several of such techniques are able to discover fatigue damage before fracture, but most of these methods are based on the detection of cracks and their growth.

Concerning ferromagnetic materials, magnetic properties are known to be sensitive to both cracks and microstructural changes, because such structural features affect the mobility of the domain walls. This makes magnetic features suitable for the early fatigue damage evaluation, in particular before a crack can be identified by conventional methods. In this research, the continuous monitoring of the magnetization during the cyclic mechanical loading itself, based on the magnetomechanical effect, is studied in more detail as magnetic NDE method in chapter 6.

1.1.5 What can we do about material degradation?

The above-mentioned material degradation processes can lead to a deterioration of the macroscopic mechanical properties and/or to the nucleation of cracks. Finally, this can lead to failure of critical components in a construction or machine, which can have disastrous consequences.

Knowing all this, the first aim would be to try to minimize the possibility for material degradation to occur, by taking accurate measures before taking the materials and components into operational service. This can be achieved for example by: accurate *materials choice* (e.g. 9-12wt%Cr steels have an improved resistance to creep deformation and corrosion at elevated temperatures, compared to conventional steels [Fujita1992, Matijasevic2008]); *conservative design*, in order to accommodate the effects of microstructural heterogeneity and variation in the operational service conditions; *careful manufacturing* (e.g. avoiding improper heat treatment, inaccurate welding or faulty machining); *quality control* during and after the production process, before taking the material into service.

In spite of such precautions, materials degradation processes will nevertheless still occur during operation under harsh service conditions, which highlights the need for the *assessment of the material integrity*, so that adequate operational safety margins can be maintained in a reliable way without economical repercussions.

Moreover, sometimes exceptional and unforeseen operational conditions can occur, which can dramatically shorten the lifetime of certain components. Also of topical interest is the need for prolonged service of gas pipelines and power plants. Both considerations demand for the continuous assessment of the material integrity during operation, in order to be able to evaluate the likelihood of failure throughout the entire service life and to estimate the remaining lifetime.

Within this context our research focusses on non-destructive inspection methods during the operational lifetime aiming at *condition monitoring and lifetime assessment*, to tackle the inevitable material degradation problems due to operational and environmental in-service conditions. Worth mentioning is that similar non-destructive techniques can be used also for the inspection during production and fabrication processes aiming at *quality control* of materials.

Dealing with materials evaluation, apart from the already made distinction between the in-service material integrity assessment and the quality control during production, also a distinction can be made between destructive and non-destructive evaluation methods. Moreover, a further distinction is possible between continuous (on-line / in-service) monitoring, and discontinuous (intermittent) evaluation at process interruptions.

In this research work we predominantly treat (magnetic) non-destructive evaluation techniques for material integrity assessment, both by continuous and discontinuous methods.

1.1.6 Non-destructive evaluation

Within the context of the assessment of material integrity against material degradation processes, non-destructive evaluation (NDE) involves all inspection and characterization techniques to evaluate the material performance and the integrity of engineering structures or machine components, without damaging it, or without having impact on its future usability. Most of the NDE methods lean upon analyzing the manner how the material under investigation reacts on enforcing a certain form of energy, which can be electromagnetic, radiative, mechanical, acoustic, thermal, optical energy, and so on. This energy interacts with the imperfections and microstructural features of the material. The underlying relationship between the energy input and the resulting energy output is determined by the actual material condition. Therefore by studying this relation between energy input and output, the material condition can be deduced.

Non-destructive techniques are of course opposed to destructive techniques. Examples of destructive techniques are the tensile test, the Charpy impact test, the hardness indentation test, the fatigue test, and so on. Compared to destructive tests, the non-destructive tests have the following advantages:

- the biggest advantage is of course the *non-destructive nature* of the test, meaning that the sample is not destroyed and can be reused;
- this non-destructive nature implies that the evaluation can be performed on the *actual product itself*, rather than on a representative sample, which is of high importance for such properties that can differ remarkably between different samples of the same material batch, properties such as the fatigue strength (see for instance the scatter on different destructive fatigue tests on figure 1.12);
- another implication is that in principle non-destructive evaluation can be performed on *all involved material*, whereas with destructive tests typically only a subset of samples can be tested up to destruction, and it is then assumed that the result obtained by the destructive test is representative for the remaining (not tested) material from the same piece;
- non-destructive evaluation opens perspectives towards *in-service assessment* and on-line condition monitoring, compared with destructive tests which only can be performed at interruptions of operational service or production.

Non-destructive evaluation methods are however indirect evaluation methods, so there is a need for calibration, laboratory tests and comparison with destructive or other tests in order to be able to correlate the measured properties obtained by the NDE methods with the actual property of interest, which is typically a certain mechanical or microstructural feature.

For the assessment of material integrity, the choice for a particular NDE method depends on the size and distribution of the inhomogeneities under investigation. Material degradation mechanisms can be classified in the following categories:

- degradation mechanisms that affect the microstructural features of the material, and therefore change the intrinsic material properties (examples of such mechanisms are embrittlement, thermal aging, metal fatigue, creep);
- degradation mechanisms that impose some macroscopic physical damage, either by metal loss (e.g. corrosion) or by the initiation of cracks (e.g. stress-corrosion, metal fatigue).

Hence, because of the differences in defect size (micro- or macroscopic size) and differences in the distribution of defects (localized or uniformly distributed; only at the surface or also in the volume of the material), appropriate NDE techniques should be put forward.

As been said, several physical phenomena can be employed for non-destructive evaluation, giving rise to a broad variety of methods based on for instance ultrasonic, radiographic, optical and also electromagnetic phenomena. Well known and frequently utilized are [Halmshaw1987, Raj2003, Jiles2008]:

- Visual inspection techniques, possibly assisted by a colored liquid penetrant, to make more contrast for the detection of small surface cracks;
- Ultrasonic techniques, which evaluate changes in acoustic impedance, due to defects and/or cracks;
- X-ray diffraction techniques, to obtain insight into the material;
- Eddy current inspection of conducting materials;
- Magnetic flux leakage (MFL) and magnetic particle visual inspection (MPI) on ferromagnetic materials: the material under test is magnetized and the flux leakage that occurs locally at places where there are discontinuities on or near the surface of the material (cracks or inclusions) are detected by measuring the magnetic leakage field with field sensors (MFL method) or detected visually by using magnetic particles (MPI method).

1.1.7 Magnetic hysteretic non-destructive evaluation

Apart from the NDE techniques listed in the previous paragraph, which are widely used in industrial environments, the characterization of the magnetic hysteretic behaviour also shows potential NDE purposes. The subtle interplay between magnetic hysteretic behaviour and the microstructural features, residual stresses, small localized defects,... inspired investigators to develop magnetic hysteretic non-destructive evaluation techniques, especially for the evaluation of material degradation processes that lead to changes in microstructure and crystal defect densities, hence affecting the intrinsic material properties.

As been said, most of the NDE methods lean upon analyzing the manner how the material under investigation reacts on enforcing a certain form of energy. The enforcement of electromagnetic energy is a good candidate for NDE. Magnetic hysteretic NDE techniques are generally based on the knowledge that the development of microstructural defects and the variations of the internal micro stress distributions around those defects influence the magnetic domain wall motion, leading to altered macroscopic magnetic hysteretic properties. In principle, we may identify microstructural changes, even before the initiation of cracks, and evaluate the deterioration of mechanical properties of ferromagnetic materials in a non-destructive manner by the characterization of the electromagnetic behaviour.

The core issue in relation to magnetic hysteretic NDE techniques is to define magnetic parameters that are sensitive enough to identify the changes of microstructural properties under investigation. As a first step, the classical magnetic hysteresis parameters characterizing the saturation magnetization loop such as coercive

field, remanent induction, permeability, and electromagnetic losses can be used for NDE purposes [Bose1986, Lo2000].

In this research, the magnetic hysteresis non-destructive evaluation method is extended by increasing the input of experimental data for the evaluation technique. This is done by considering a whole set of magnetization loops from low to high magnetic induction levels, instead of taking into account only the saturation magnetization loop. A hysteresis model such as the Preisach model [Bertotti1998] that takes the overall magnetic hysteresis behaviour into account (the Preisach hysteresis model is introduced in section 4.2) can be useful for non-destructive evaluation purposes: the Preisach distribution function is shown to be dependent on microstructure [Basso1995, Dupré1999, Melikhov2001].

1.2 General aim and motivation

The general aim of the proposed research is the development of magnetic characterization techniques in order to advance the fundamental study of the interrelation between the macroscopic magnetic behaviour, the macroscopic mechanical properties and the underlying microstructure of ferromagnetic materials. Such magnetic techniques can be employed for the non-destructive evaluation of macroscopic mechanical properties, microstructural features and/or localized flaws, aiming for the assessment of ferromagnetic material integrity during their operation (or for the quality control during material processing).

Indeed, during long-term operation the effects of mechanical elastic stress (static or cyclic), elevated temperature and/or neutron irradiation, induce slow but nevertheless insidious microstructural degradation processes which gradually impair the intrinsic mechanical properties of the utilized materials, and which can also lead to the nucleation of localized cracks, flaws and/or other inhomogeneities. Hence, in order to avoid that material degradation processes such as metal fatigue, embrittlement, creep eventually lead to fracture or failure, material condition monitoring is vital, both for safety and for economical reasons. Such assessment of the material integrity during operational service is typically performed by one or multiple non-destructive evaluation (NDE) methods.

Due to the always increasing concern for improved safety in industrial environments and engineering structures, but also in the society in general, there remains a continuous need for the development of alternative and improved NDE technologies, which can offer greater capability when used in combination with already existing non-destructive and/or destructive techniques. Indeed, the sensitivity of the material integrity assessment can be enhanced by using a combination of multiple methods for the same materials evaluation task.

Most of the NDE methods lean upon analyzing the manner how the material under investigation reacts on enforcing a certain form of energy. The enforcement of electromagnetic energy is a good candidate for NDE. Indeed, it is generally known that the development of defect structures and the underlying microstructural changes influence the dislocation dynamics, but also affect the magnetic domain wall motion in ferromagnetic materials, leading to altered mechanical and magnetic macroscopic properties, respectively, as is also shown in the examples treated in section 1.1.3. The underlying fundamental principles of this relation between microstructural features and magnetization processes is at the heart of this research work and will be treated in much more detail in chapter 2.

Conversely, changes in the ferromagnetic behaviour reflect the variation in the microstructural features in the material and/or the change of the mechanical stress state. In principle, we may identify the microstructural changes and monitor the degradation of the material's mechanical properties in a non-destructive fashion, by the characterization and evaluation of the magnetic and magnetomechanical hysteretic behaviour.

In this research, we explore and investigate the possibilities, the limitations and the sensitivity of the macroscopic magnetic and magnetomechanical hysteretic characterization of ferromagnetic materials to non-destructively evaluate the progression of microstructural degradation phenomena. The main goal is to deliver a proof of concept of magnetic hysteretic NDE methods by experimental sensitivity studies in a laboratory environment, for several material degradation processes. In a further stadium which can be part of future research, the results of such investigations can serve as the necessary knowledge to develop prototype experimental systems for the in-situ material integrity inspection of critical components of actual engineering structures and industrial installations.

1.3 Research strategy and outline of following chapters

The general aim of this research is to explore the possibilities and the sensitivity of the magnetic and magnetomechanical hysteretic characterization to non-destructively evaluate the progression of microstructural degradation phenomena in ferromagnetic materials.

This main objective is subdivided in the following subtasks:

1. The fundamental principles dealing with the relation between the magnetization processes and the microstructural features of iron-based materials are elucidated first. The ferromagnetic behaviour and its relation with the microstructure of the material is treated on a merely theoretical basis in **chapter 2**. The general aspects of ferromagnetic behaviour are introduced, both on the macroscopic and the microscopic level. The internal mecha-

nisms and the underlying origin for ferromagnetic behaviour are discussed, with special emphasis on the influence of the microstructural features. To gain an in-depth knowledge about this topic, the general framework of the micromagnetic theory is very useful. The micromagnetic theory is based on the minimization of the free energy of a ferromagnetic system of interacting magnetic moments, and is a comprehensive formalism to fundamentally describe ferromagnetic behaviour and its internal mechanisms.

2. Another subtask is the development of magnetic characterization methods i.e. (a) versatile experimental setups and measuring techniques, in combination with (b) advanced analyzing techniques of the experimental data, in order to facilitate and enhance the precise characterization of the manifold features related to both magnetic and magnetomechanical hysteretic behaviour. In **chapter 3** the experimental magnetic and magnetomechanical setups are described, with special attention to the general principles and the necessary experimental tools, and to the actual interpretation of the obtained experimental results. In **chapter 4** the advanced analysis and characterization of the magnetic hysteretic behaviour is treated. The Preisach hysteresis model is introduced, a model which can serve as an instrument for magnetic NDE.
3. Next, a sensitivity study of the magnetic characterization methods is carried out for the non-destructive evaluation of microstructural changes, such as the changes induced during material degradation processes. Based on a number of experimental case studies for several material degradation processes, carried out inside a laboratory environment during this research, the possibilities and limitations of the field-metric magnetic hysteresis characterization are investigated. In **chapter 5** the magnetic hysteresis behaviour is characterized to evaluate the material in case of irradiation-induced embrittlement, plastic deformation and non-homogeneous residual stress distribution, whereas in **chapter 6** the magnetomechanical behaviour is exploited to evaluate the material during fatigue damage progression.

Chapter 2

Ferromagnetic behaviour

In this chapter, the internal mechanisms and the underlying origin for ferromagnetic behaviour are discussed, with special emphasis on the influence of the microstructural features, as introduced in section 1.1.2.

The general aspects of ferromagnetic behaviour are introduced, both on the macroscopic and the microscopic level. In section 2.1 typical macroscopic magnetic observations are highlighted, such as the non-linearity, saturation and hysteresis features of the magnetic constitutive law (i.e. the magnetization as a function of the magnetic field), but also the macroscopic magnetoelastic coupling is introduced, which manifests itself through the magnetostrictive effect and the magnetomechanical effect. Next, section 2.2 introduces the underlying (microscopic) basic concepts leading to such typical ferromagnetic behaviour, concepts such as atomic magnetic moments, spontaneous magnetization and magnetic domains.

Section 2.3 deals with the micromagnetic theory, a general and comprehensive formalism to fundamentally describe ferromagnetic behaviour and its internal mechanisms. In essence, the micromagnetic theory is based on the minimization of the free energy of a ferromagnetic system of interacting magnetic moments, taking into account all energy terms that are relevant for ferromagnetic behaviour: both the short-range atomic scale contributions (such as exchange energy, magnetocrystalline anisotropy energy, and magnetoelastic energy) and also the long-range contributions (magnetostatic energy and externally applied field energy).

Micromagnetism provides a theoretical framework for the interaction of microstructural defects and inhomogeneities on the one hand and the equilibrium magnetic domain configuration on the other hand, since the defects and inhomogeneities slip into the micromagnetic equations via the magnetoelastic energy term as a residual internal stress distribution. Therefore the magnetoelastic energy plays a central part in this present study.

Making use of the micromagnetic energy concepts, section 2.4 treats the typical magnetization processes occurring when a time-varying magnetic field is applied to a bulk ferromagnetic sample, again with special attention to the influence of microstructural defects on these magnetization processes. A domain wall model is derived giving some qualitative results about the influence of defect density and pinning strength on macroscopic magnetic parameters such as coercive field and initial permeability.

2.1 Ferromagnetic behaviour on a macroscopic scale

2.1.1 Maxwell equations and constitutive law $B(H)$

To provide some general context, let us start with introducing some basic principles of electromagnetism, valid on a macroscopic scale. To describe the combination of electrical and magnetic phenomena, both for static and dynamic conditions, Maxwell postulated a set of equations carrying his name [Maxwell1873]. In our present study, a magnetostatic subset of Maxwell's treatment will turn out to be satisfactory.

Maxwell introduced several types of magnetic fields defined by the *magnetic constitutive law* (a general formula, true for all circumstances):

$$\mathbf{B}(\mathbf{H}) = \mu_0\mathbf{H} + \mu_0\mathbf{M}(\mathbf{H}), \tag{2.1}$$

with the magnetic field $\mathbf{H}$ and the magnetic induction $\mathbf{B}$ defined in each point of space, and with the magnetization $\mathbf{M}$ only defined for magnetizable material. Therefore the relation $\mathbf{B}(\mathbf{H})$ depends on the considered medium: for vacuum for instance, $\mathbf{M} = 0$ and the relation $\mathbf{B} = \mu_0\mathbf{H}$ is valid, with μ_0 the magnetic permeability of vacuum, $\mu_0 = 4\pi\ 10^{-7}$ Vs/Am (or H/m). If however a magnetic material is present then an externally imposed magnetic field strength $\mathbf{H}(t)$ magnetizes the material, giving rise to the magnetization $\mathbf{M}(t)$ in every point of the magnetic material volume, with $\mathbf{M}$ depending on $\mathbf{H}$.

The thus defined fields $\mathbf{H}(t)$ and $\mathbf{B}(t)$ have to fulfil the following – low frequency magnetic or 'magnetostatic' – subset of Maxwell's equations, with $\mathbf{j}(t)$ representing the current density and $\mathbf{E}(t)$ the electrical field strength:

$$\begin{aligned} \nabla \times \mathbf{H} &= \mathbf{j} \\ \nabla \times \mathbf{E} &= -\frac{\mathrm{d}\mathbf{B}}{\mathrm{d}t} \\ \nabla \cdot \mathbf{B} &= 0 \end{aligned} \tag{2.2}$$

Alternatively, these basic (macroscopic) electromagnetic equations can be envisaged as follows. A current $I(t)$ flowing through a conductor generates a magnetic field strength vector $\mathbf{H}(x, y, z, t)$, in each point of space (x, y, z). In turn, the magnetic field strength gives rise to the magnetic flux density or magnetic induction $\mathbf{B}(x, y, z, t)$, again in each point of space but dependent on the present medium or material. The change in time of the magnetic flux ϕ coupled with a winding having a cross section S, defined as $\phi = \int_S \mathbf{B} \cdot \mathrm{d}\mathbf{S}$, induces a voltage $V(t)$ in this winding.

As will be outlined further in chapter 3, these electromagnetic principles provide the general framework to perform magnetic measurements, more precisely to measure – independently from each other – the macroscopic quantities magnetic field strength $\mathbf{H}(t)$ and magnetic induction $\mathbf{B}(t)$. As a matter of fact, the principal aim to perform such magnetic measurements is actually to determine experimentally the magnetic constitutive law, in other words the macroscopic relation between $\mathbf{H}$ and $\mathbf{B}$.

In the following treatment and also throughout this work, only ***unidirectional*** conditions are considered. This means that the magnetic field is applied along one particular direction, $\mathbf{H}(t) = H(t)\mathbf{e}_H$, and the macroscopic magnetization and magnetic induction are considered along the same direction $\mathbf{e}_H$, also leading to scalar quantities for the macroscopic magnetic induction and magnetization, respectively $B(t) = \mathbf{B}(t) \cdot \mathbf{e}_H$ and $M(t) = \mathbf{M}(t) \cdot \mathbf{e}_H$. The scalar unidirectional constitutive law is then written as follows:

$$B(H) = \mu_0 H + \mu_0 M(H). \tag{2.3}$$

For so-called paramagnetic and diamagnetic materials, the relation between M and H is linear for a large range of magnetic field strengths: $M = \chi H$, with χ the (constant) magnetic susceptibility ($\chi < 0$ for diamagnetics and $\chi > 0$ for paramagnetics). Alternatively, B versus H is also linear for such materials: $B = \mu_0 \mu_r H$, with μ_r the (constant) relative permeability, defined as $\mu_r = 1 + \chi$. For diamagnetic and paramagnetic materials the magnitude of the magnetic susceptibility $|\chi|$ is roughly of the order 10^{-5}, so $\mu_r \approx 1$ is a good first approximation.

On the other hand, when a ***ferromagnetic*** substance is subjected to a unidirectional magnetic field $H(t)$, it becomes strongly magnetized, giving rise to much higher susceptibilities, of the order of 10^3. Moreover, the macroscopic constitutive law $B(H)$ for ferromagnetic materials has the typical features of *non-linearity*, *saturation* and *hysteresis*. The non-linearity and the saturation features are illustrated in figure 2.1(a), showing the single-valued initial or virgin magnetization curve for a sample of pure iron; an initial magnetization curve is the B versus H trajectory that is traversed by increasing the magnetic field from $H = 0$ to H_{max}, starting from the demagnetized state (see further, section 2.2.3). The saturation feature is due to the fact that there is a maximum possible value for

the magnetization, the saturation magnetization M_{sat} (see further, section 2.2). The non-linearity and the saturation features of the constitutive law can be described, in case of the single-valued initial magnetization curve, by making the relative permeability field dependent, i.e. $\mu_r = \mu_r(H)$, and thus the constitutive law describing the virgin magnetization curve reads:

$$B(H) = \mu_0 \mu_r(H) H. \tag{2.4}$$

The third characteristic feature for ferromagnetic materials is the hysteretic behaviour of the constitutive law, as illustrated in figure 2.2. When a time-dependent magnetic field waveform $H(t)$ is applied, there exists no unique relation between the magnetization of the material and the applied magnetic field. For instance when a periodical magnetic field waveform $H(t)$ is applied and once the initial magnetization curve is traversed, no single valued magnetization curve is described, but instead a *magnetization loop* (or a *hysteresis loop*) is followed periodically. As a specific example of the more general magnetic hysteretic behaviour, a quasi-static symmetric first order saturation magnetization loop is shown in figure 2.2. Moreover there is energy dissipation associated with the hysteretic behaviour, denoted by the hysteresis loss W_{hyst}:

$$W_{hyst} = \int_{\Omega_m} \left(\oint H \mathrm{d}B \right) \ \mathrm{d}V, \tag{2.5}$$

with Ω_m the volume of magnetized material. This energy dissipation corresponds with the counter-clockwise traversal of the hysteresis loop. On figure 2.2(a) also two characteristic quantities of the saturation hysteresis loop are introduced, the coercivity H_c defined as $H(B = 0)$, and the remanence $B_r = B(H = 0)$.

More generally, the hysteretic behaviour can be envisaged as follows. When starting from a certain condition $(H(t_0), B(t_0))$ at time t_0, the point (H, B) at time $t_1 > t_0$ not only depends on the present value of the magnetic field $H(t_1)$, but also on its history. As a matter of fact, in practice all internal (H, B) points inside a saturation magnetization loop can be reached, depending on the past and present magnetic field values. It is obvious that the general hysteretic behaviour cannot be described by a single-valued function as (2.4), but that instead a more complicated description for the hysteretic constitutive law $B(H)$ is necessary. Therefore, a more systematic approach is needed to model the general hysteretic behaviour. One of the possibilities to describe the hysteretic features and to take its characteristic memory properties into account, is by making use of the Preisach formalism. Further on, in section 4.2 the Preisach hysteresis model is introduced, since it is one of our basic tools for the characterization of the magnetic hysteretic behaviour in order to evaluate material degradation.

It is evident that the relative permeability is an important quantity for ferromagnetic materials, both related to the hysteresis loop and the initial magnetization

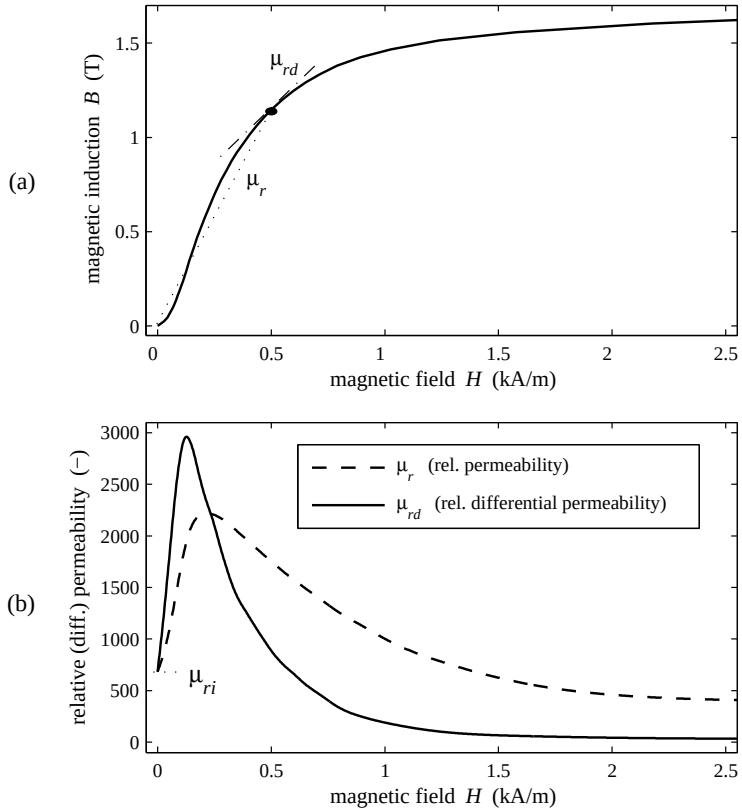

Figure 2.1. (a) Initial (or virgin) magnetization curve for a sample of pure iron, illustrating the features non-linearity and approach to saturation. A graphical interpretation of the permeability definitions (see formula's (2.6) and (2.7)) is also indicated: the slope of the dotted/dashed lines is proportional to the labelled permeability variable at the considered magnetic field value (H = 500 A/m, depicted by the black dot). (b) Relative permeability μ_r and relative differential permeability μ_{rd}, both as a function of magnetic field H, associated with the single-valued initial magnetization curve shown in part (a) of this figure. Also indicated is the initial relative permeability μ_{ri}.

curve. As been said before, the permeability depends non-linearly on H and this relation is not single-valued due to magnetic hysteresis. In this context, it is necessary to make distinction between the relative permeability μ_r and the relative *differential* permeability μ_{rd}:

$$\mu_r(H) = \frac{1}{\mu_0}\frac{B(H)}{H} \tag{2.6}$$

$$\mu_{rd}(H) = \frac{1}{\mu_0}\frac{\mathrm{d}B(H)}{\mathrm{d}H} \tag{2.7}$$

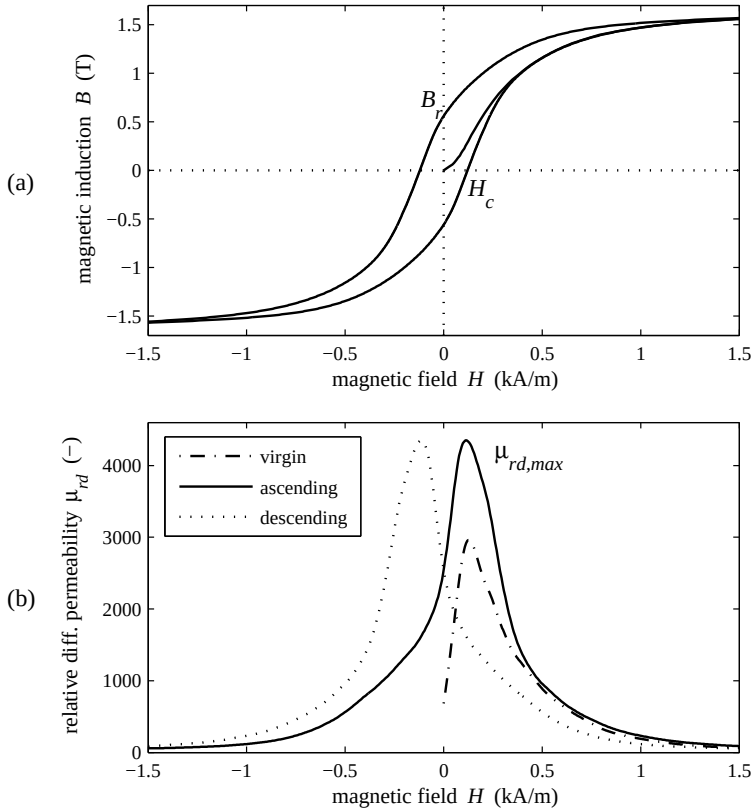

Figure 2.2. (a) Symmetric first-order hysteresis loop, corresponding to the same sample of pure iron as in figure 2.1. This quasi-static hysteresis loop is obtained by applying a periodical magnetic field $H(t)$ with 0.5 Hz excitation frequency, starting from the demagnetized state. First the initial magnetization curve is traversed (H from 0 to maximum) and then the hysteresis loop is cycled periodically. The coercive field H_c and the remanent induction B_r are also indicated on the figure. (b) Relative differential permeability μ_{rd} as a function of magnetic field H, corresponding to the initial magnetization curve and to the descending and ascending branch of the hysteresis loop. Note that the maximum relative differential permeability $\mu_{rd,max}$ occurs at $|H| \approx H_c$.

Figure 2.1 illustrates both definitions by showing the two different permeabilities as a function of magnetic field H, corresponding to the single-valued initial magnetization curve. On the other hand for hysteresis loops, the relative permeability μ_r can become zero or infinite along the hysteresis loop respectively at the points B_r and H_c. Therefore the differential relative permeability μ_{rd} is a more convenient property dealing with hysteresis loops, as shown in figure 2.2(b).

Throughout this work we will utilize predominantly the relative differential permeability μ_{rd} and especially its maximum value, $\mu_{rd,max}$.

The initial relative permeability μ_{ri} is defined as $\lim_{(H\to 0, B\to 0)}\mu_r$, and equals $\mu_{rd}(H = 0, B = 0)$ as shown in figure 2.1(b), with μ_r and μ_{rd} both corresponding to the initial magnetization curve.

A final remark: in this section we discussed the constitutive law for ferromagnetic substances as the hysteretic relation between the magnetic induction B and the magnetic field H, since these two properties lead to the definition of the (relative) permeability. Alternatively, the introduced concepts can also be applied towards a description of the constitutive law in terms of magnetization $M(H)$ or magnetic polarization $J(H) = \mu_0 M(H)$. This is justified when dealing with soft magnetic materials (as is the case in this study) and as long as the material is not strongly saturated. Under these conditions $H \ll M$, and according to (2.3) the following approximation is valid: $B(H) \approx \mu_0 M(H) = J(H)$.

2.1.2 Magnetostriction and the magnetomechanical effect

Apart from the constitutive law $B(H)$ or $M(H)$, there is a second class of macroscopic observations that needs to be introduced. On the one hand, it is observed that when a ferromagnetic specimen is subjected to a magnetic field, its magnetization as well as its length change. On the other hand, when a ferromagnetic specimen is subjected to a mechanical stress, both its length as well as its magnetization change.

Both macroscopic phenomena indicate that there is an interaction between the magnetic behaviour and the elastic mechanical behaviour. These two phenomena are termed *magnetostriction* and *magnetomechanical effect* respectively, and are the macroscopic outcome of what is called magnetoelastic interaction.

Magnetoelastic interactions are the underlying reason for the influence of the externally applied stress and/or the localized stress distribution around microstructural defects on the magnetization of a ferromagnet. The magnetoelastic interaction will be discussed in detail in the general context of the micromagnetic theory, see section 2.3.4.

Magnetostriction

When a bulk ferromagnetic sample is exposed to a magnetic field, it becomes magnetized but also its macroscopic dimensions change. This effect is called magnetostriction. The change in length Δl is often considered in the direction parallel to the magnetization vector $\mathbf{M}$, and the associated (magnetically induced)

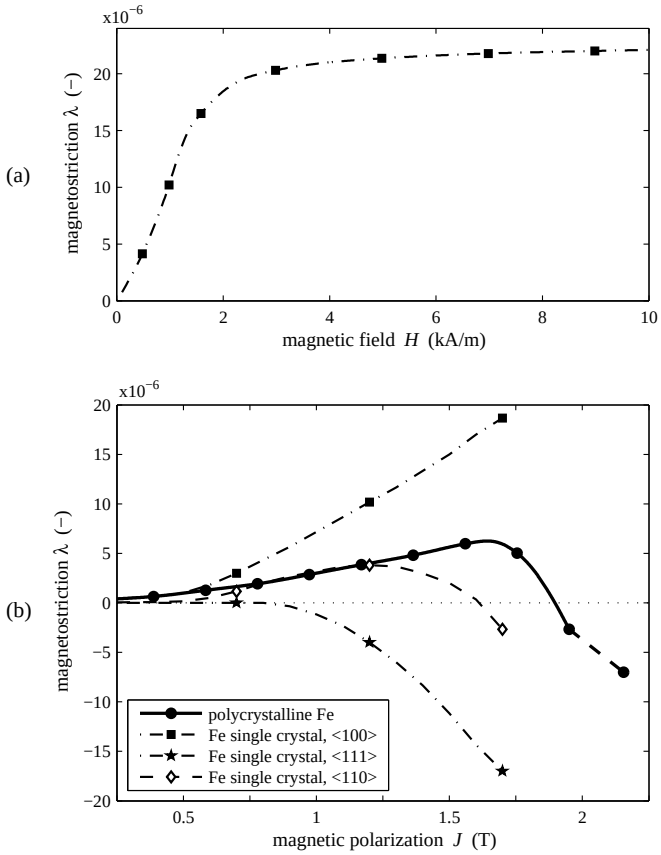

Figure 2.3. (a) Magnetostrictive behaviour of a Fe single crystal, magnetized in a $\langle 100 \rangle$ direction, illustrated by the single-valued relationship $\lambda(H)$ between the applied magnetic field H and the longitudinal magnetostriction λ in the direction of the applied field. (b) Magnetostrictive behaviour of polycrystalline iron, magnetized along an arbitrary direction, illustrated by the single-valued relationship $\lambda(J)$ between the magnetic polarization $J = \mu_0 M$ and the longitudinal magnetostriction λ. Also shown as reference in (b) is the anisotropic magnetostrictive behaviour of an iron single crystal, magnetized along a $\langle 100 \rangle$, a $\langle 111 \rangle$ and a $\langle 110 \rangle$ direction. Saturation magnetostriction (at $J_s = 2.15$ T): $\lambda_{s,poly} \approx -7\ 10^{-6}$; $\lambda_{100} = 22\ 10^{-6}$; and $\lambda_{111} = -21\ 10^{-6}$. Single crystal data from [Webster1930]; polycrystal data from [Bozorth1951].

strain is referred to as 'longitudinal magnetostriction', defined as:

$$\lambda = \frac{\Delta l}{l_0} = \frac{l - l_0}{l_0}, \tag{2.8}$$

with l_0 the original length of the demagnetized sample. According to this definition, positive magnetostriction means that the material elongates parallel to

the magnetization direction. The magnetostriction λ depends non-linearly on the magnetic field H and exhibits saturation (and hysteresis [Bozorth1951]). The non-linearity and the saturation of $\lambda(H)$ are illustrated in figure 2.3(a). The saturation magnetostriction λ_s is defined as the value of λ corresponding with the technical saturation magnetization, i.e. the magnetization corresponding to a single domain structure. The relative change in dimensions is usually quite small, typically $|\lambda_s|$ is of the order of 10^{-5} for iron and ferritic steels[1].

For a large range of applied magnetic fields, the material volume remains approximately equal, therefore a longitudinal elongation corresponds with a contraction in the transverse direction: $\lambda_t = -\lambda/2$.

For polycrystalline iron and ferritic steels, and within the magnetic polarization range of practical interest (i.e. $J = \mu_0 M$ from zero to 1.7 T), the longitudinal magnetostriction λ is positive, see figure 2.3(b). However, at even higher J, the magnetostriction becomes negative, and finally the saturation magnetostriction of polycrystalline Fe appears to be about $\lambda_s \approx -7\ 10^{-6}$ (experimentally determined on a polycrystalline Fe sample [Cullity1972]). The polycrystalline magnetostrictive behaviour depends on the magnetostriction of the different crystal grains, on the crystallographic texture, and on the localized internal strain distribution between the different grains [Cullity1972]. As an illustration, in figure 2.3(b) the anisotropic longitudinal magnetostrictive behaviour of an iron single crystal is shown, magnetized along different cubic crystallographic directions.

Magnetostriction is perhaps known best as one of the causes for the humming noise of electrical power transformers: when an alternating magnetic field is applied, the transformer's ferromagnetic core vibrates due to the magnetostriction and sends out a sound wave.

Magnetomechanical effect

Although the magnetostrictive effect is rather small, on the macroscopic level there exists also an inverse effect with more substantial outcome. This effect is called the *inverse magnetostrictive effect* or the *magnetomechanical effect*.

Consider a material with positive magnetostriction. This material will elongate when being magnetized. On the other hand, applying a tensile[2] stress ($\sigma > 0$) elongates the material and therefore it will increase the magnetization (if the initial $M \neq 0$, see section 6.1). For infinitesimal and reversible changes in magnetic field and mechanical stress, these coupled effects can be described conceptually

[1] To appreciate the magnitude of the magnetostrictive strain: for iron $|\lambda_s| \sim 10^{-5}$ and with an elasticity modulus E equal to 210 GPa, the corresponding elastic stress is of the order of 2 MPa.

[2] The following convention is valid throughout this work: tensile stress is positive ($\sigma > 0$), compressive stress is negative ($\sigma < 0$).

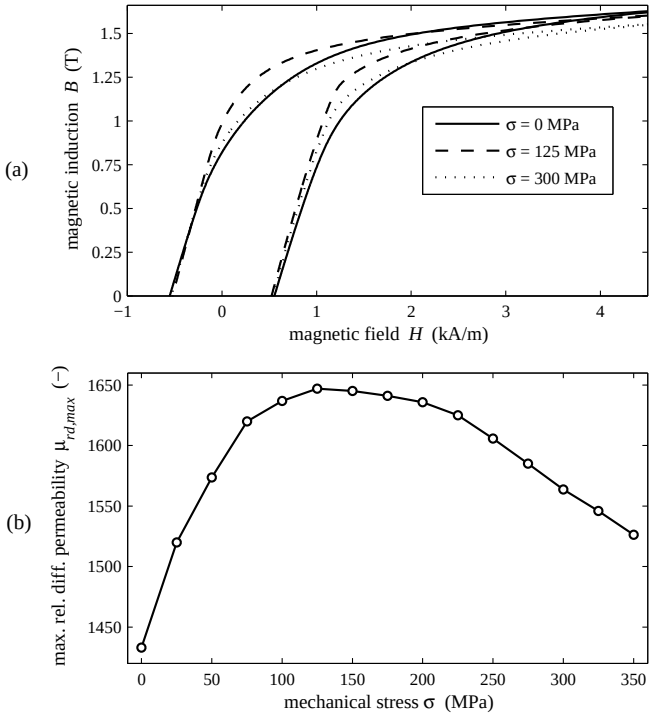

Figure 2.4. (a) Quasi-static magnetization loops measured on a hot-rolled low-carbon steel sample for several constant applied tensile stresses, within the elastic region (yield stress σ_y = 390 MPa). For clarity, only the loops at 0, 125 and 300 MPa are shown here. (b) Maximum of the relative differential permeability, as a function of constant applied elastic tensile stress, obtained from the same experimental data as (a). In (a) also the effect of tensile elastic stress on the remanent induction and the coercive field is visible.

as follows [Bozorth1951]:

$$\left.\frac{\mathrm{d}M}{\mathrm{d}\sigma}(\sigma, H_0)\right|_{\sigma=\sigma_0} \sim \left.\frac{\mathrm{d}\lambda}{\mathrm{d}H}(\sigma_0, H)\right|_{H=H_0}, \tag{2.9}$$

with σ_0 and H_0 constant stress and constant field, respectively. One of the typical macroscopic features of this inverse magnetostrictive effect is that it causes the permeability to be dependent on applied elastic stress, see figure 2.4.

Notice in figure 2.3(b) that the magnetostriction of polycrystalline iron (and by extension of ferritic steels) is positive and increasing at low magnetic fields, but starts to decrease and even becomes negative at high H. Accordingly, the magnetic behaviour under stress of iron and ferritic steels is also complex and shows two tendencies, see figure 2.4: the permeability first increases but then decreases with applied tensile elastic stress. The magnetomechanical effect is treated in more detail in chapter 6.

Macroscopic magnetoelastic coupling

In the two previous paragraphs the magnetostriction and the magnetomechanical effect are introduced. As a matter of fact, both phenomena can be considered as specific cases within a more general conceptual framework termed as *macroscopic magnetoelastic coupling*, as shown schematically in figure 2.5.

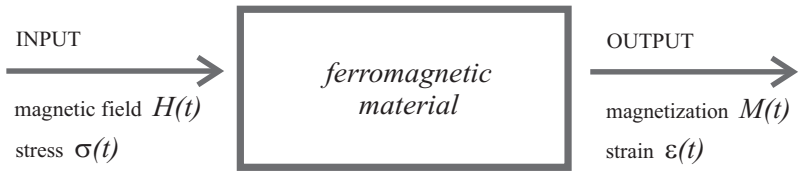

Figure 2.5. Concept of macroscopic magnetoelastic coupling, shown schematically as an input-output system with the applied magnetic field and the applied mechanical stress as inputs and the resulting bulk magnetization and longitudinal strain as outputs.

In the most general case the ferromagnetic material under test is subjected to both a time-dependent applied magnetic field and a time-dependent applied mechanical stress. During the experiments in the frame of this research, both inputs are uniform and uniaxial, and moreover parallel to each other. On the other hand, the resulting bulk magnetization and also the elongation are examined simultaneously along the same direction as the magnetic field. In other words, all four examined macroscopic properties can be considered along the same direction and can be expressed as scalar properties.

The general relations between the considered macroscopic properties magnetic field H, magnetization M, stress σ and strain ε can then be written in this conceptual framework as follows:

$$\begin{bmatrix} M \\ \varepsilon \end{bmatrix} = \begin{bmatrix} F_1(H,\sigma) \\ F_2(H,\sigma) \end{bmatrix} = \begin{bmatrix} \chi(H,\sigma) & f_1(H,\sigma) \\ f_2(H,\sigma) & s(H,\sigma) \end{bmatrix} \begin{bmatrix} H \\ \sigma \end{bmatrix} \tag{2.10}$$

with χ the magnetic susceptibility, s the mechanical compliance, and with the cross terms f_1 and f_2 representing the macroscopic magnetoelastic coupling.

Within this general framework the *magnetostriction*, illustrated in figure 2.3, can be written conceptually as follows:

$$\varepsilon = F_2(H, \sigma = 0), \tag{2.11}$$

whereas a specific aspect of the *magnetomechanical effect*, namely the change in magnetic hysteretic behaviour for different constant elastic stress values σ_k, as shown in figure 2.4, can be written as:

$$M = F_1(H, \sigma = \sigma_k). \tag{2.12}$$

In order to investigate experimentally the magnetomechanical effect, a combined mechanical and magnetic setup is being built at EELAB. In section 3.3 this magnetomechanical setup is described (see figure 3.24 for a schematic overview within the conceptual framework of figure 2.5). Making use of this setup, in chapter 6 the magnetomechanical effect is investigated in more detail, for the cases where only one of the inputs (H or σ) is periodically changing with time, whereas the other input is kept constant. In case of constant mechanical stress and cyclic magnetic field not only the effect of tension but also of compression on the magnetization loops is examined (section 6.1.3), whereas in section 6.1.4 also the hysteretic behaviour of magnetization as a function of time-dependent applied mechanical stress is investigated for constant values of applied magnetic field. Finally in section 6.1.5 the case is treated where both inputs H and σ are periodically changing with time.

As has been said, the general framework of figure 2.5 and (2.10) is merely conceptual for the magnetoelastic coupling phenomena on the macroscopic level: an explanation for the magnetoelastic coupling has to be found on a micro-scale level. As a matter of fact, the underlying basic principles for this magnetoelastic coupling observed on a macroscopic level, are the micro-scale interactions between the magnetization and the mechanical strain in the crystal lattice – which are termed as *magnetoelastic interactions* – and which are treated further in this chapter in section 2.3.4 as the *magnetoelastic energy* contribution within the micromagnetic formalism.

2.2 Ferromagnetism on a microscopic scale

The typical hysteretic behaviour of ferromagnetic materials, accompanied by relative permeabilities of the order of 10^3 (as shown for instance in section 2.1.1, figures 2.1 and 2.2 for pure iron), and also the typical magnetoelastic behaviour of ferromagnetic materials (section 2.1.2), are the macroscopic outcome of magnetization processes on a microscopic scale. On the microscopic level the following three basic concepts are essential to understand why a particular material shows ferromagnetic behaviour, briefly:

1. the existence and permanent nature of the *atomic magnetic dipole moments*,
2. the *parallel alignment* of neighbouring atomic magnetic moments due to strong *mutual interaction between the atomic magnetic moments*, leading to *spontaneous magnetization*, and
3. the organization of all the atomic magnetic moments into a structure of *magnetic domains*.

Possessing a magnetic dipole moment per atom (basic concept 1) is a necessary condition for ferromagnetic behaviour, but however it is not a sufficient one. For instance, **paramagnetic** substances also have a net magnetic moment per atom. However, the atomic magnetic moments of a paramagnetic substance are randomly aligned in absence of applied magnetic field, in other words there are no significant mutual interactions between the individual magnetic moments (basic concept 2 not fulfilled). When a magnetic field is applied in a certain direction, the magnetization process consists of aligning some of the magnetic dipole moments into the field direction. Macroscopically this results in a single-valued magnetization curve $M(H)$, so without hysteresis. However for paramagnetic substances, thermal agitation plays a major role, opposing the rotation of the magnetic moments towards the applied field. Therefore very large magnetic fields and/or near-zero absolute temperatures ($\approx$ 0 K) are necessary for paramagnetic substances to align the majority of the magnetic moments towards the applied magnetic field, in other words to approach saturation. At room temperature and for a large range of magnetic field strengths, the thermal agitation dominates the field energy resulting in a constant magnetic susceptibility value for paramagnetic materials roughly of the order 10^{-5}.

On the contrary, **ferromagnetic** substances typically have 10^8 times higher magnetic susceptibilities, exhibit a non-linear and hysteretic $M(H)$ relationship, and moreover approach technical saturation at 'relatively low' magnetic fields, when compared to paramagnetic behaviour. These macroscopic observations illustrate the huge differences between ferromagnetic and paramagnetic behaviour, and can be explained by making use of to the basic concepts (2) and (3) stated above. Actually, these two concepts correspond qualitatively with the two original postulations initiated by Weiss to understand the particular ferromagnetic behaviour, when compared to paramagnetic behaviour [Weiss1907]. These concepts can be described as follows: in absence of an externally applied magnetic field, a ferromagnetic substance is divided into a number of subregions called magnetic domains (postulation 1), and a magnetic domain itself is a magnetically ordered region for which all atomic magnetic moments are aligned parallel to each other (postulation 2). Hence a magnetic domain is spontaneously magnetized, even in absence of an externally applied magnetic field. For ferromagnetic materials, the total magnetization $\mathbf{M}$ on the macroscopic level can then be envisaged as the vector sum of the local spontaneous magnetization vectors $\mathbf{M_s}$ of all magnetic domains in the considered material volume.

Furthermore, as we will see later on, a change of the externally applied magnetic field leads to a rearrangement of these magnetic domains, which in turn results in a modified macroscopic magnetization. The magnetization processes involved with these rearrangements of magnetic domains lead to the typical ferromagnetic features such as high susceptibility at low magnetic fields, hysteresis, non-linearity and saturation.

In the following paragraphs the underlying basic concepts of ferromagnetism (atomic magnetic moments, spontaneous magnetization and magnetic domains) are treated in more detail.

2.2.1 Atomic magnetic dipole moments [Cullity1972]

Macroscopic ferromagnetic behaviour originates from the presence of magnetic dipole moments on the atomic scale: bulk ferromagnetic materials can be fundamentally described as a collection of magnetic dipole moments per unit volume, which can also be represented as a net magnetic moment per individual atom. This assumption of associating a magnetic moment locally to each atom is denoted as the *localized moment theory*[3].

The basic principles of the localized moment theory are summarized in this section, starting from more substantial treatments in [Cullity1972, Dauwe2004].

In general, the magnetic dipole moment per atom is determined principally by the electrons (since the magnetic moment of the nucleus is negligibly small and moreover it does not affect the macroscopic magnetic properties). There are two contributions to the electron magnetic moment, related to (1) the orbital angular momentum of the electron, and to (2) the intrinsic spin of the electron. The orbital motion of an electron around a nucleus, with orbital angular momentum $\mathbf{L}$, may be regarded – in a classical view – as a microscopic current loop which results in the orbital magnetic moment $\mathbf{m_L} = -\frac{e}{2m_e}\mathbf{L}$, where m_e is the electron mass and e is the electron charge. Additionally, an electron possesses an intrinsic spin with the properties of an angular momentum, i.e. the spin angular momentum $\mathbf{S}$: the electron behaves as if it is spinning around its own axis. In a quantum mechanical view there is an intrinsic magnetic moment $\mathbf{m_S}$ associated with this electron spin. Quantum theory learns us that both the orbital and spin magnetic moments $\mathbf{m_L}$ and $\mathbf{m_S}$ are constrained to discrete values.

For crystalline materials, the ferromagnetic behaviour as a function of applied magnetic field can be considered to originate from rearrangements of spin magnetic moments, rather than of orbital magnetic moments [Cullity1972]. This is explained as follows: generally speaking, when a (macroscopic) magnetic dipole moment $\mathbf{m}$ is placed in an externally applied magnetic field $\mathbf{H}$, the magnetic

[3] There is also a different viewpoint to fundamentally explain ferromagnetism, called *collective electron theory* or *band theory*. The basic assumption there is that the outer shell electrons are more or less free to move around in the crystal lattice [Cullity1972, Herring1960]. In the context of our study the localized moment concept is more convenient, since it permits a simpler treatment of a central ferromagnetic concept, namely the exchange interaction (see further in section 2.2.2 and section 2.3.1). Also, dealing with the domain wall thickness and energy (see section 2.3.9), the theoretical results based on localized moments are in good agreement with experimentally obtained values [Kittel1949].

moment tends to be aligned parallel to the field, which can be described by the potential energy W_p [J]:

$$W_p = -\mu_0 \mathbf{m} \cdot \mathbf{H}. \tag{2.13}$$

This is also expected to occur with the electronic magnetic moments of crystalline materials, when an external magnetic field is imposed along an arbitrary direction in the crystal lattice. However, the orientations of the orbital moments are strongly bound to the crystal lattice orientations ('orbit-lattice' coupling), whereas on the other hand, the spin moments are only weakly coupled to the orbital moments ('spin-orbit' coupling). Hence, the strong orbit-lattice coupling impedes the orbital moment to change its direction, whereas due to the weak spin-orbit coupling, the spins are more or less free to rotate towards the magnetic field. As a consequence, the spin moments contribute predominantly to the magnetization process, rather than the orbital moments.

To summarize, the spin magnetic moments of the electrons contribute to the net magnetic dipole moment per atom. Depending on the electronic structure of a particular atom there are two possibilities: (1) all electron moments cancel each other out, resulting in no atomic magnetic moment; or (2) most electron moments cancel out whereas the uncompensated spin moments give rise to a certain net atomic magnetic moment. These atomic magnetic moments have a fixed amplitude and a variable orientation. For ferromagnetic materials, such as Fe in its body-centered cubic (b.c.c.) crystalline state and below 770 °C (Curie temperature of Fe, see section 2.2.4), there is such a resulting net atomic magnetic dipole moment.

We can estimate the order of magnitude of the atomic magnetic dipole moment as follows: $|\mathbf{m}| = M_s V_{atom}$, with M_s the spontaneous magnetization and V_{atom} the equivalent volume of one atom. A b.c.c. unit cell (with lattice edge length a) contains two atoms (one atom at the center of the cube, plus 8 times 1/8 of the atoms at the corner points), thus $V_{atom} = (a^3)/2$. For b.c.c. Fe (α-Fe) with $a = 0.286$ nm, this gives $V_{atom} = 1.170 \cdot 10^{-29}$ m^3. Thus for b.c.c. Fe (M_s = $1.745 \cdot 10^6$ A/m) the atomic magnetic moment is of the order of $|\mathbf{m}| = 2 \cdot 10^{-23}$ Am^2. Alternatively expressed as a number of Bohr magnetons (which is a quantummechanical measure of a single spin magnetic moment, $\mu_{Bohr} = 9.274 \cdot 10^{-24}$ Am^2), this gives $|\mathbf{m}|/\mu_{Bohr} = 2.2$, which roughly corresponds with Fe having two uncompensated spin magnetic moments, i.e. 5 out of the 8 electrons of the $3d$ electronic shell of Fe having spin up, and 3 out of 8 having spin down.

2.2.2 Interacting magnetic moments: exchange coupling

In the previous paragraph we have seen that some substances can have a net magnetic moment per atom. Moreover, for a part of such substances there exists a mutual interaction between these individual atomic magnetic moments. In case of

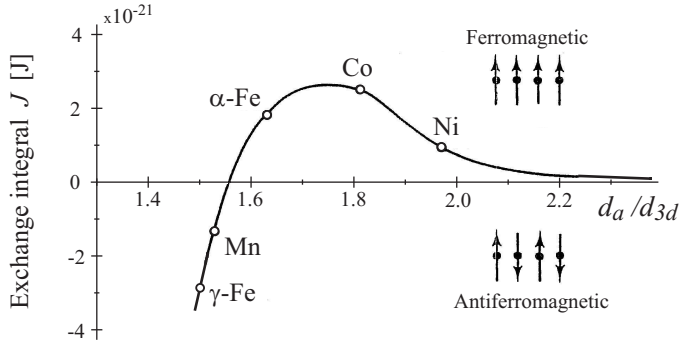

Figure 2.6. Schematic representation of the so-called Bethe-Slater curve (taken from [Cullity1972, Bozorth1951]), depicting the exchange integral as a function of d_a/d_{3d} with d_a the interatomic distance between two neighbouring atoms, and d_{3d} the diameter of the incomplete $3d$ shell. The values are marked for some transition metals with incompletely filled $3d$ electronic shell (namely Mn, Fe, Co and Ni, which respectively have 5, 6, 7 and 8 electrons in the $3d$ shell). This figure is the result of approximative calculations with varying d_a and fixed d_{3d} by [Slater1930, Sommerfeld1933]. α-Fe has a body centered cubic lattice and is ferromagnetic, whereas γ-Fe has a face centered cubic lattice and is not ferromagnetic.

the ferromagnetic substances this interaction leads to a strong tendency for neighbouring atomic magnetic moments to align parallel to each other, whereas for the anti-ferromagnetic substances, anti-parallel alignment is favoured.

The underlying reason for this mutual interaction can be explained by the quantum-mechanical concept of *exchange coupling* between the spin angular moments of electrons belonging to adjacent atoms [Heisenberg1928]. The associated exchange force is a non-classical quantum-mechanical force which depends on the relative orientation of the spin angular moments of neighbouring atoms and also on the interatomic distance d_a. The coupling between spin angular moments caused by this quantum-mechanical exchange effect can be described by the Heisenberg Hamiltonian or energy function:

$$\mathcal{H} = -2\sum_{j\neq i} \mathcal{J}_{ij}(d_{ij})\mathcal{S}_i(\mathbf{r}_i)\cdot\mathcal{S}_j(\mathbf{r}_j), \tag{2.14}$$

with $\mathcal{J}_{ij}$ the quantum-mechanical exchange integral corresponding to two atoms i and j, with $\mathcal{S}_i$ the spin angular momentum of atom i and with d_{ij} the distance between the two considered atoms. The exchange integral $\mathcal{J}_{ij}$ for atom pairs of αFe–αFe, Ni–Ni and Co–Co appears to be positive, as shown schematically in figure 2.6, and hence parallel spin alignment results in minimum energy (according to (2.14)) for these three ferromagnetic substances.

2.2.3 Spontaneous magnetization and magnetic domains

In the previous paragraphs we have seen that ferromagnetic substances have a net magnetic moment per atom, and that there is a strong tendency to parallel alignment of the atomic magnetic moments. However, to obtain the typical – hysteretic and non-linear – ferromagnetic behaviour on the macroscopic level, the concept of a magnetic domain structure [Weiss1907] is a *conditio sine qua non*.

In ferromagnetic materials, the atomic magnetic moments are ordered in certain regions, called *magnetic domains*. In each such ferromagnetic domain, all atomic magnetic moments $\mathbf{m}$ are aligned parallel to each other, due to the exchange interaction discussed above. As a consequence of the parallel alignment of the magnetic moments, these magnetic domains exhibit a *spontaneous magnetization*,

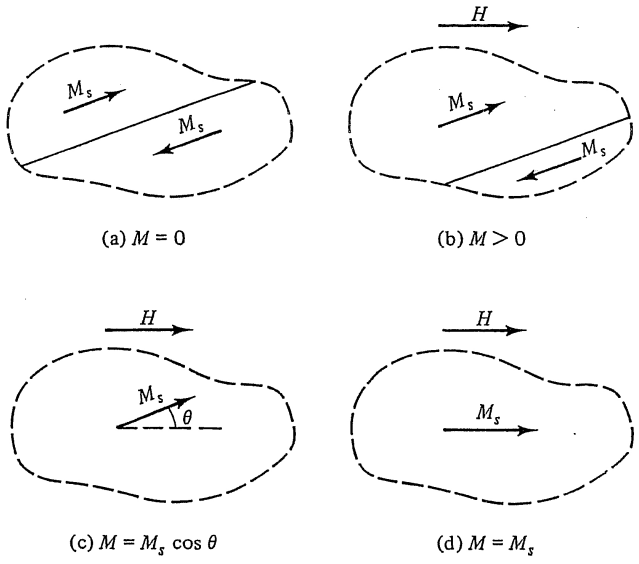

Figure 2.7. Simplified schematic view of the magnetization process at the magnetic domain level under the application of an increasing external magnetic field. Only a portion of a single crystal is considered (enclosed by a dashed line), in which initially (with applied magnetic field $H = 0$, and magnetization $M = 0$) there are portions of two domains magnetized spontaneously in opposite directions, see (a). The magnetic domain wall is the boundary between the domains (depicted by a straight line in the schematic view). Subplot (b) shows the domain wall motion under the application of a magnetic field, leading to an increase of the magnetic domain volume for which the angle between its magnetization vector $\mathbf{M_s}$ and the applied field $\mathbf{H}$ is lowest, until in (c) the domain wall has moved out of the considered region. At still higher externally applied fields, the spontaneous magnetization of the single domain rotates towards the magnetic field direction, resulting finally in magnetic saturation in the field direction, see (d).

$\mathbf{M_s}$, even in absence of an external magnetic field. In other words, even when the applied magnetic field is removed, the atomic magnetic moments composing a magnetic domain remain aligned parallel (the domains are 'self-saturated'), and with this zero-field situation there still corresponds a certain magnetic domain structure. The orientation of the spontaneous magnetization is different from domain to domain, whereas their magnitude equals the same value M_s for each domain (see also section 2.2.4). The interface region between two neighbouring magnetic domains, where the magnetic moments have to change orientation from one domain orientation to another, is termed a *magnetic domain wall*. Figure 2.7(a) illustrates the concepts magnetic domain, spontaneous magnetization and magnetic domain wall.

For a given magnetic domain configuration, the total macroscopic magnetization $\mathbf{M}$ of a ferromagnetic sample can be determined as the vector sum of the local spontaneous magnetization vectors $\mathbf{M_s}$ of all magnetic domains in the considered material volume, provided that the sample consists of a large number of magnetic domains. The macroscopic magnetization is thus dependent on the relative orientations and the volumes of all magnetic domains inside the considered macroscopic volume of the material sample. Furthermore, a change of the externally applied magnetic field leads to a rearrangement of the magnetic domains, which in turn results in a modified total magnetization $\mathbf{M}$. Figure 2.7 introduces some of the different magnetization processes involved on the scale of magnetic domains (see also section 2.4.1), when an increasing magnetic field is applied to the material.

Several questions still remain unanswered for the moment, for instance why multiple magnetic domains are formed. The formation of a particular magnetic domain structure and the changes of the domain configuration due to the application of an external magnetic field can be explained best in the framework of a micromagnetic formalism, which is a general comprehensive theory based on the different energy contributions that are involved in ferromagnetic systems, see further in section 2.3.

2.2.4 Curie temperature

The alignment of the neighbouring atomic magnetic moments constituting a ferromagnetic domain is only perfectly parallel at zero absolute temperature. For $T > 0$ K, the thermal energy of the individual magnetic moments causes a precession of the atomic magnetic moment around the local magnetic field direction. Moreover, the precession becomes more significant as temperature increases. Therefore, the thermal agitation of the atomic magnetic moments partially counteracts/disturbs the parallel alignment of the magnetic moments constituting the magnetic domains, causing the spontaneous magnetization $M_s(T)$ to decrease

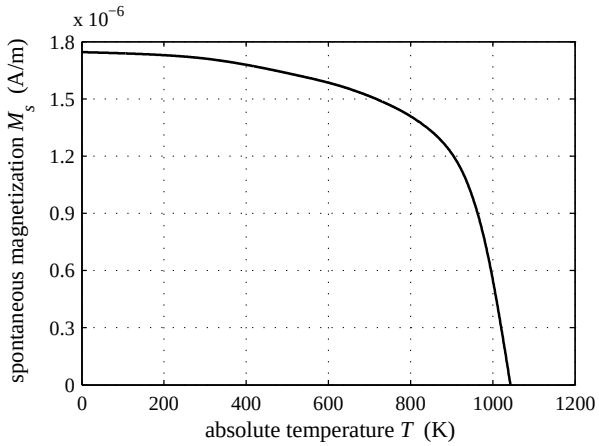

Figure 2.8. Spontaneous magnetization M_s as a function of temperature T, in case of iron (Curie temperature T_c = 1043 K; spontaneous magnetization at zero absolute temperature $M_{s,0} = 1.745 \cdot 10^6$ A/m).

with increasing temperature, as can be seen in figure 2.8, in case of iron.

However, for moderate temperatures ($T < 300$ K) the thermal effect is rather insignificant: for instance at room temperature (293 K) the spontaneous magnetization of Fe is only 1.7% less than its maximum value $M_{s,0}$ at zero absolute temperature, corresponding with complete parallel alignment. At sufficiently high temperatures however the thermal agitation becomes dominant, and finally above a certain temperature, which is called the *Curie temperature*, the material loses its ferromagnetic order. The Curie temperature T_C is a material dependent property, e.g. for pure iron its value is 1043 K (770 °C). Above the Curie temperature, the net magnetic moment per atom still exists in iron and iron-based materials, but the individual atomic magnetic moments are now randomly oriented in the absence of a magnetic field. This leads to paramagnetic behaviour for such materials above T_C. Therefore, the Curie temperature marks the transition from the ferromagnetic ordered phase to the paramagnetic disordered phase of iron.

2.2.5 Magnetostriction

In section 2.1.2 we introduced magnetostriction on the macroscopic – experimental – level. Now that the basic ferromagnetic concepts are introduced, such as spontaneous magnetization and magnetic domains, we are capable to give an interpretation of magnetostriction on the magnetic domain level [Lee1955]. Experiments on an iron single crystal, magnetized to saturation in a $\langle 100 \rangle$ direction, show that the length of the crystal in that direction is increased. An explanation is found

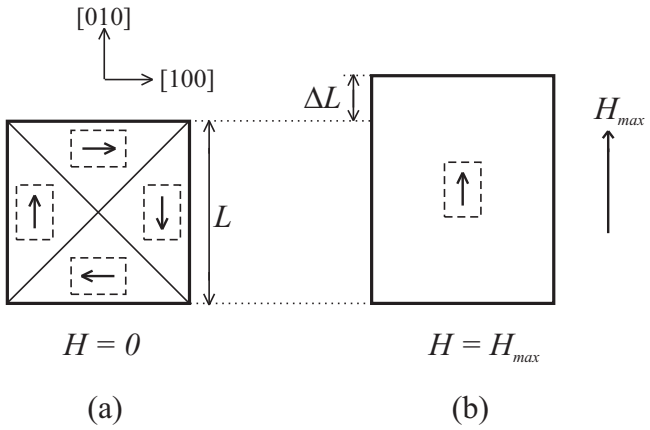

Figure 2.9. Field-induced magnetostriction of a iron single crystal, shown schematically on a simple domain structure. The spontaneous magnetostriction is depicted by the – exaggerated – elongation of the crystal lattice, as a matter of fact in reality $\Delta L/L$ is of the order of 10^{-5} (from [Cullity1972]).

in the fact that the unit cell of ferromagnetic iron is not exactly cubic but slightly tetragonal, which means that the lattice consists still of three orthogonal axes, but one axis, the one parallel to the local spontaneous magnetization, is slightly longer ($\approx$ 1.00001 times longer) than the other two axes. Accordingly, a magnetic domain of a single crystal in the demagnetized state, spontaneously magnetized in a $\langle 100 \rangle$ direction, is also spontaneously elongated in the same $\langle 100 \rangle$ direction.

We can distinguish two types of magnetostriction: spontaneous magnetostriction and field-induced magnetostriction. Spontaneous magnetostriction corresponds with the magnetic ordering transition that occurs when cooling down the material below Curie temperature: above T_C the lattice of paramagnetic b.c.c. iron is perfectly cubic, below T_C the ferromagnetic lattice becomes body-centered tetragonal, elongated in the direction of local spontaneous magnetization. The field-induced magnetostriction, as illustrated in figure 2.9, can be regarded as follows: increasing the uniaxial magnetic field corresponds with the conversion of the demagnetized sample (with several domains that are strained spontaneously in different directions), into finally a saturated single-domain specimen, which is now spontaneously strained (elongated) in one direction, namely the magnetic field direction.

2.2.6 Reference magnetic states

In section 2.1 and section 2.2 the macroscopic observations and the underlying basic concepts of ferromagnetic behaviour are introduced. Before continuing, the

proper treatment of the ferromagnetic hysteretic behaviour demands for some kind of reference magnetic state, which connects the macro-level to the micro-level. For such a reference magnetic state, the link between the macroscopic magnetization and the underlying magnetic domain structure should be known a priori. This reference magnetic state then serves as a starting point to traverse the macroscopic magnetic hysteresis trajectories. Two possibilities of reference conditions are the saturated magnetic state and the demagnetized state.

The ***saturated magnetic state*** corresponds with the highest achievable macroscopic magnetization. On the magnetic domain level, the saturated state corresponds to the material consisting of one single magnetic domain with its spontaneous magnetization vector $\mathbf{M_s}$ parallel to the applied magnetic field $\mathbf{H}$, as already explained in figure 2.7. Hence the resulting macroscopic magnetization is equal to the spontaneous magnetization of the magnetic domain, $M = M_s$. However, figure 2.8 shows that the spontaneous magnetization is temperature dependent, and that the maximum spontaneous magnetization value $M_{s,0}$ is reached at $T = 0$ K. This value can be considered as the *absolute saturation* magnetization, $M_{sat,abs} = M_{s,0}$. Due to thermal agitation of the magnetic moments (as explained in section 2.2.4), the spontaneous magnetization M_s at room temperature is somewhat lower than this upper limit. For temperatures higher than 0 K, the magnetization value corresponding to the single domain configuration with $\mathbf{M_s}$ parallel to $\mathbf{H}$, is called the *technical saturation* magnetization, $M_{sat,tech} = M_s(T) < M_{sat,abs} = M_{s,0}$ [Jiles1998]. Remember that the difference between M_s at room temperature and $M_{s,0}$ is small, only 1.7%. Starting from such domain configuration, further increasing the magnetic field counteracts the thermal agitation of the magnetic moments. This is called forced magnetization and brings the saturation magnetization closer to the absolute saturation magnetization. However, to obtain absolute saturation, the required magnetic field needs to be very large.

Starting from the saturated reference magnetic state, and when decreasing the magnetic field, a unique trajectory is followed, which is the descending branch of the saturation magnetization loop.

The ***demagnetized state*** corresponds to a particular magnetic domain structure for which the averaged macroscopic magnetization turns out to be zero $(M = 0)$, under the condition that the applied field is zero $(H = 0)$. This reference state is reached when an alternating magnetic field is externally applied with a slowly decreasing field amplitude, beginning at a sufficiently high field amplitude corresponding to (technical) saturation and ending at zero field amplitude. This procedure is called *demagnetizing* the material.

Starting from the demagnetized reference magnetic state, and when increasing the magnetic field, the initial or virgin magnetization curve is followed.

2.3 Micromagnetic theory

Of primary interest in our study is the relation between the macroscopic magnetic hysteresis properties of bulk ferromagnetic samples (having typical dimensions in the range of 10^{-3} m to 10^{-2} m), and the material's microstructural features. Therefore we search for a general physical framework that can give insight in the underlying phenomena giving rise to this relation between the microstructural features introduced in section 1.1.2, and the macroscopic magnetic properties.

In previous paragraphs (see sections 2.2.1–2.2.2) we have seen that ferromagnetism is inseparably associated with ***quantum mechanical concepts*** like electron spin, giving rise to *discrete* atomic magnetic moments, and also the exchange interaction between these atomic magnetic moments. However, in order to describe macroscopic features of samples with dimensions of the order of 10^{-2} m, the use of a pure quantum mechanical numerical model on an *interatomic scale* (10^{-10} m), starting from all separate quantum mechanical magnetic moments and their interactions, is practically impossible with today's computing capabilities.

At the other end of the spatial spectrum, the ***Maxwell equations*** describe electric and magnetic fields on a *macroscopic length scale* and in a *classical continuum* framework. In the Maxwell formulation the macroscopic magnetic features are taken into account by making use of a constitutive law between the magnetic field $\mathbf{H}$ and the magnetic induction $\mathbf{B}$ (see section 2.1): $\mathbf{B} = \mu_0(\mathbf{H} + \mathbf{M}) = \mu_0\mu_r\mathbf{H}$. In this equation the magnetization $\mathbf{M}$ is the volumetric 'macroscopic average' over the considered material volume (the entire material sample) of all atomic magnetic moments. Also μ_r is a global property for the macroscopic specimen. Due to this implicit volumetric averaging, the Maxwell formulation can of course not explain the magnetization processes on the magnetic domain level.

In this section 2.3, we introduce the ***micromagnetic model*** which bridges the gap between the macroscopic and the quantum mechanical theories. Within the micromagnetic framework, the quantum mechanical nature of the magnetic moments is ignored and the local magnetization is approximated as a *continuous classical* quantity. Moreover, the micromagnetic model can be positioned at an *intermediate scale* between the atomic resolution and the magnetic domain scale, see further. The basic features of the micromagnetic formalism are the following [Brown1963, Fidler2000, VandeWiele2005]:

- The main micromagnetic variable describing the magnetic state of the ferromagnetic crystal, is the ***local magnetization vector*** $\mathbf{M}_{loc}(\mathbf{r})$. This property varies continuously with position $\mathbf{r}$ in the crystal. In essence, this local magnetization represents the atomic magnetic moment per unit volume: $\mathbf{M}_{loc}$ can be considered as the 'microscopic average' of atomic magnetic moments. A conventional theoretical assumption, following Landau and Lifshitz [Landau1935, Landau1960], is that the local magnetization vector

has a constant amplitude, equal to the spontaneous magnetization M_s of the considered (homogeneous) material[4], whereas the direction varies continuously with position. Therefore the local magnetization can be written as:

$$\mathbf{M}_{loc}(\mathbf{r}) = M_s \left[\alpha_1(\mathbf{r})\ \mathbf{e}_1 + \alpha_2(\mathbf{r})\ \mathbf{e}_2 + \alpha_3(\mathbf{r})\ \mathbf{e}_3\right], \tag{2.15}$$

with $\mathbf{e}_k$ the unit vectors of an arbitrary chosen Cartesian coordinate system, for instance parallel to the three orthogonal cube edges of the iron crystal lattice $\langle 100 \rangle$, and with $\alpha_k(\mathbf{r})$ the corresponding direction cosines.

- In order to perform micromagnetic simulations, a ***spatial discretization*** of all considered continuous quantities is necessary. Therefore the ferromagnetic sample under consideration is divided into a number of basic cells of equal volume $(\Delta_s)^3$, with Δ_s the spatial discretization length. The chosen spatial discretization length Δ_s is the result of a compromise. On the one hand, in order to still describe all relevant interactions between the magnetic moments, Δ_s should be sufficiently small. Consider that due to the strong exchange interaction of iron the change in orientation of neighbouring atomic magnetic moments always remains small (maximum variation is typically less than 1 degree, inside magnetic domain walls, see section 2.3.9). Therefore Δ_s can be taken as approximately one order of magnitude larger than the atomic resolution a (lattice edge length for b.c.c. iron: a = 0.286 nm). On the other hand to describe macroscopic magnetic behaviour on 'large' samples (typical dimensions of 10^{-2} m), an enormous number of basic cells is needed; to speed up the computation time, we therefore aim at Δ_s to be as high as possible. Increasing Δ_s from 1 nm up to 10 nm results in the achievement of more or less identical magnetic equilibrium states [VandeWiele2007], identical on the level of magnetic domain structures, so $\Delta_s = 10$ nm is a good compromise, also with respect to the width of a domain wall (about 200 nm for a 180° domain wall in iron, see further in section 2.3.9).

- The total energy of a bulk ferromagnetic sample is given by the Gibbs free energy. In particular, we are interested in all contributions of the Gibbs free energy which depend on the local magnetization vector $\mathbf{M}_{loc}$. In the following paragraphs 2.3.1–2.3.5, the different ***magnetic free energy contributions*** are treated separately in more detail, and are expressed as a function of the local magnetization directions. The Gibbs free energy has the following free independent (input) variables: the magnetic field $\mathbf{H}$, the elastic stress tensor $\overline{\sigma}(\mathbf{r})$, and the temperature T (the latter is kept constant throughout this work).

[4]Remark: for a fixed temperature, $|\mathbf{M}_{loc}|$ is considered to be constant, equal to M_s. Moreover, the temperature dependence of M_s can be ignored for temperatures far below the Curie temperature of the material, see figure 2.8.

- The core problem is then to find the equilibrium local magnetization direction as a function of position, that correspond to the lowest total free magnetic energy. A common approach to the ***minimization of the magnetic free energy*** is by utilizing the Landau-Lifshitz equation, see further in section 2.3.7.

- The result of the minimization leads to the existence of regions of parallel $\mathbf{M}_{loc}$, and of regions in which the direction of $\mathbf{M}_{loc}$ changes rapidly with position $\mathbf{r}$. Hence, the ***magnetic domains and domain walls*** are the natural outcome of the micromagnetic simulations. In other words, the existence of domains and domain walls are not an assumption or postulation in the micromagnetic theory [Brown1963]. Domain walls are treated in more detail in section 2.3.9.

In sections 2.3.1 to 2.3.5 the magnetic free energy contributions of different origin are introduced separately. We will see that each magnetic free energy contribution (exchange, magnetocrystalline anisotropy, magnetostatic, magnetoelastic or external field energy) is in favour for a different local magnetization configuration (for a summary see section 2.3.6). The combination of all contributions then leads to an equilibrium local magnetization configuration, see sections 2.3.7 to 2.3.9.

2.3.1 Exchange energy

The exchange energy forms the physical basis for a central concept in ferromagnetism i.e. the mutual interaction of the individual atomic magnetic moments, which in ferromagnetic substances leads to a strong tendency to the adjacent atomic magnetic moments to align parallel to each other. As been mentioned before in section 2.2, this mutual interaction between neighbouring magnetic moments can be explained by the quantum-mechanical concept of exchange interaction, as expressed by the Heisenberg Hamiltonian, see equation (2.14).

In the micromagnetic formalism we need however a continuum expression of the quantum-mechanical exchange concept. Since it turns out that the angles between neighbouring spins are small (e.g. for the spins that constitute the magnetic domain walls of iron-based ferromagnetic materials, the angle is typically less than 1 degree, see also section 2.3.9) a semi-classical approximation of the quantum theory can be used [Kronmüller2003]. In this context, we may represent the quantum-mechanical spin momentum by a classical vector. The energy corresponding with the exchange interaction can then be written as:

$$W_{exch}(\mathbf{r}_i) = -2\sum_{j\neq i} J_{ij}(r_{ij})\ \mathbf{S}_i \cdot \mathbf{S}_j = -2S^2 \sum_{j\neq i} J_{ij}(r_{ij}) \cos\theta_{ij} \qquad (2.16)$$

with $\mathbf{S}_i$ the spin angular momentum at position $\mathbf{r}_i$, and J_{ij} the exchange integral depending on the distance r_{ij} between the two considered atoms. The angle between the spin vectors $\mathbf{S}_i$ and $\mathbf{S}_j$ is denoted by θ_{ij}, and the net spin angular momentum per atom is S. Exchange forces are short range forces, meaning that they decrease rapidly with distance r_{ij}. Hence restricting the summation to the nearest neighbours j of atom i is justified. Assuming additionally that all such nearest neighbour interactions are equal (in other words the exchange energy is isotropic), then J_{ij} can be replaced by J, the exchange integral between two neighbouring spins. Both assumptions together give:

$$W_{exch}(\mathbf{r}_i) = -2JS^2 \sum_{j \neq i}^{N} \cos\theta_{ij} \tag{2.17}$$

with the summation over all (N) nearest-neighbour pairs i and j. For ferromagnetic substances the exchange integral J is positive, in other words the exchange energy of the parallel spin alignment between nearest neighbours is lowest, and therefore parallel alignment is favoured.

Alternatively, for a micromagnetic continuum description in terms of the local magnetization vector $\mathbf{M}_{loc}$, the following expression of the exchange energy can be used [Herring1951]:

$$w_{exch}(\mathbf{r}) = \frac{A}{M_s^2} \sum_{i=1}^{3} |\nabla M_{loc,i}(\mathbf{r})|^2 = A \sum_{i=1}^{3} |\nabla \alpha_i(\mathbf{r})|^2 \tag{2.18}$$

$$W_{exch} = \int_{\Omega_m} w_{exch}(\mathbf{r})\ \mathrm{d}V \tag{2.19}$$

with $M_{loc,i}$ representing the component of $\mathbf{M}_{loc}$ along axis i of a Cartesian coordinate system, and with α_i the direction cosines of $\mathbf{M}_{loc}$ relative to this Cartesian coordinate system. In the following the three cubic crystallographic axes $\langle 100 \rangle$ are chosen as Cartesian coordinate system, hence $\alpha_1 = \cos(\mathbf{M}_{loc}; [100])$, $\alpha_2 = \cos(\mathbf{M}_{loc}; [010])$ and $\alpha_3 = \cos(\mathbf{M}_{loc}; [001])$. Ω_m is the material volume and M_s is the spontaneous magnetization. Material parameter A is called the exchange stiffness and characterizes the strength of the exchange interaction. A is positive in ferromagnetic materials, giving minimum W_{exch} when magnetic moments are parallel.

To conclude, when hypothetically taking into account only the exchange energy, the complete parallel alignment of all atomic magnetic moments in the ferromagnetic material sample should be favoured. This exchange energy term is isotropic, which means that it is independent of the spatial direction in which the crystal is magnetized. However, in reality ferromagnetic crystals are not isotropic, which is described by the magnetocrystalline anisotropy energy term.

2.3.2 Magnetocrystalline anisotropy energy

Generally speaking, anisotropy indicates that material properties depend on the direction along which they are measured. Magnetic properties of ferromagnetic single crystals show anisotropy with respect to the crystallographic axes: it appears that spontaneous magnetization vectors tend to align along certain definite crystallographic directions. For obvious reasons this is called magnetocrystalline anisotropy[5].

Consider the following experiment of unidirectional magnetic measurements on a single crystal of body-centered cubic (b.c.c.) iron. When a magnetic field is applied parallel to one of the $\langle 100 \rangle$ crystallographic directions (which are the directions along the cube edges of the unit cell), the experiment shows that saturation can be achieved easily with quite low magnetic field strengths, see figure 2.10. For b.c.c. iron these $\langle 100 \rangle$ directions are therefore denoted as crystallographic directions of 'easy' magnetization. On the other hand, when the experiment is performed with a magnetic field along one of the $\langle 111 \rangle$ crystallographic directions (which are parallel to the cube diagonals of the unit cell), much higher magnetic field strengths are necessary to bring the single crystal to saturation, in other words the single crystal is hard to magnetize in that direction. Therefore for b.c.c. iron the $\langle 111 \rangle$ directions are termed 'hard' crystallographic directions for the magnetization.

In this context, *magnetocrystalline anisotropy* means that the atomic magnetic moments preferably align with one of the 'easy' crystallographic directions. Other directions are energetically unfavourable: the magnetocrystalline anisotropy energy is the extra energy that arises when the atomic magnetic moments are not aligned along one of the easy crystallographic axes. The magnetocrystalline anisotropy energy per unit volume for a material with a cubic crystal lattice can be expressed as an even function of the three direction cosines α_i of the local magnetization relative to the three cubic (orthogonal) crystallographic axes $\langle 100 \rangle$. Denoting the direction cosines as $\alpha_1 = \cos(\mathbf{M}_{loc}; [100])$, $\alpha_2 = \cos(\mathbf{M}_{loc}; [010])$ and $\alpha_3 = \cos(\mathbf{M}_{loc}; [001])$, the magnetocrystalline anisotropy energy per unit volume is described approximately as a function of fourth and sixth order α_i terms:

$$\begin{aligned} w_{anis}(\mathbf{r}) &= K_1(\alpha_1^2(\mathbf{r})\alpha_2^2(\mathbf{r}) + \alpha_2^2(\mathbf{r})\alpha_3^2(\mathbf{r}) + \alpha_1(\mathbf{r})^2\alpha_3^2(\mathbf{r})) \\ &+ K_2(\alpha_1^2(\mathbf{r})\alpha_2^2(\mathbf{r})\alpha_3^2(\mathbf{r})), \end{aligned} \tag{2.20}$$

[5] In case of macroscopic ferromagnetic properties, also other anisotropies can be defined, e.g. (a) *shape anisotropy*: due to the specific geometry of the specimen, generally speaking the geometrically longest axis is easiest to magnetize, its origin is found in the magnetostatic energy contribution (see further, section 2.3.3); (b) *stress anisotropy*: for a material with positive magnetostriction, the direction of a tensile applied stress is easier to magnetize (or harder, for a compressive applied stress), its origin is found in the magnetoelastic energy contribution (see further, section 2.3.4).

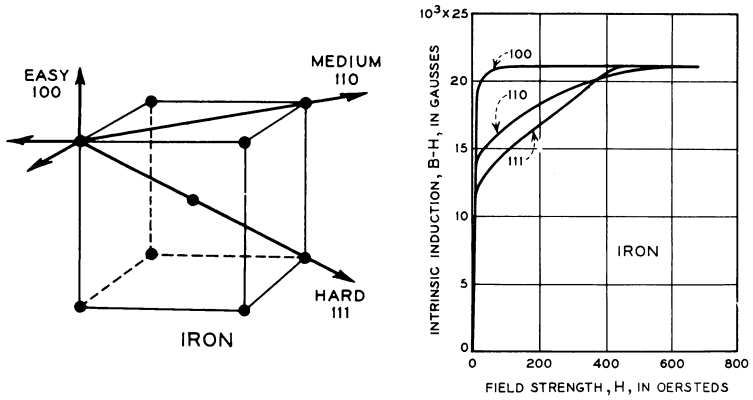

Figure 2.10. (a) Body centered cubic unit cell, with indication for b.c.c. iron of easy, medium, and hard magnetization directions; (b) magnetization curves for a b.c.c. iron single crystal as a function of different crystallographic directions in the cubic lattice (from [Bozorth1951], original data from [Honda1926]). 1 Gauss $= 10^{-4}$ T; 1 Oersted ≈ 80 A/m.

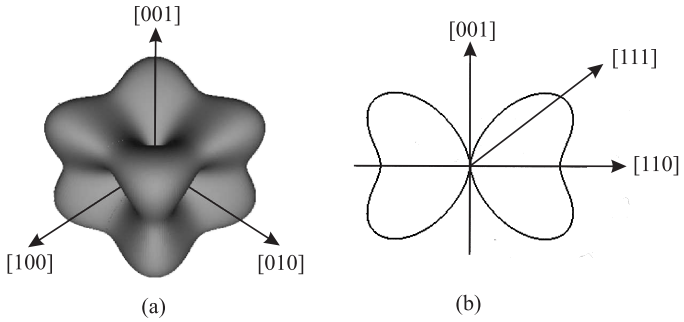

Figure 2.11. Visualization of the magnetocrystalline anisotropy energy of iron as a function of the direction of the magnetic moment, relative to the cubic unit cell directions.

$$W_{anis} = \int_{\Omega_m} w_{anis}(\mathbf{r})\ \mathrm{d}V \tag{2.21}$$

with K_1 and K_2 the first and second magnetocrystalline anisotropy constant. For b.c.c. iron at room temperature [O'Handley2000]: K_1 = 48 kJ/m^3 and K_2 = 5 kJ/m^3. In figure 2.11, $w_{anis}(\mathbf{r})$ is visualized for b.c.c. iron, when only taking into account the most important fourth order (K_1) terms.

To conclude, when hypothetically taking into account only the magnetocrystalline anisotropy energy and the exchange energy terms, the complete alignment of all atomic moments parallel to a direction of easy magnetization is favoured. The exchange interaction tends to align all magnetic moments parallel, no matter in which direction, whereas the actual direction of magnetization is determined by

the magnetocrystalline anisotropy. This parallel alignment should lead to macroscopic saturation magnetization of the single crystal, in other words to the existence of one single magnetic domain. Therefore, an explanation is needed why a configuration with multiple domains arise. The driving term for multiple domain formation is the magnetostatic energy.

2.3.3 Magnetostatic energy

The concept of magnetostatic energy was proposed by Landau and Lifshitz and explains the formation of a multiple magnetic domain structure [Landau1935].

The magnetostatic energy arises from the classical interaction of an individual magnetic moment with the magnetic field produced by all other magnetic dipole moments, called the magnetostatic field $\mathbf{H}_{ms}$. Therefore the magnetostatic energy is a long-range effect of dipole-dipole interactions, in contradiction to the anisotropy energy and the exchange energy, which are short-range effects. Due to its classical nature, the derivation of the magnetostatic field is based on Maxwell's equations, more precisely on the subset for magnetostatic problems, with no current sources present:

$$\nabla \times \mathbf{H}_{ms} = 0 \tag{2.22}$$

$$\nabla \cdot \mathbf{B} = 0 \quad \Rightarrow \quad \nabla \cdot \mathbf{H}_{ms} = -\nabla \cdot \mathbf{M}_{loc} = \rho_m \tag{2.23}$$

with ρ_m the fictitious magnetic charge density, which arises wherever $\mathbf{M}_{loc}$ turns out to be varying in space. For the continuum micromagnetic formalism, the magnetostatic energy can be described in terms of $\mathbf{M}_{loc}$ and $\mathbf{H}_{ms}$ as follows:

$$W_{ms} = -\frac{1}{2}\mu_0 \int_{\Omega_m} \mathbf{M}_{loc} \cdot \mathbf{H}_{ms} \, \mathrm{d}V = \frac{1}{2}\mu_0 \int_{\Omega_t} |\mathbf{H}_{ms}|^2 \, \mathrm{d}V, \tag{2.24}$$

with Ω_m the ferromagnetic material volume, and Ω_t the total volume (ferromagnetic material + surrounding air). So, according to (2.24), W_{ms} is minimum for a domain configuration that leads to a magnetostatic field as small as possible.

To illustrate the concept of the magnetostatic energy as driving force for the formation of magnetic domains, consider a uniformly magnetized single crystal with its spontaneous magnetization aligned to an easy crystallographic direction as depicted in figure 2.12(a). There is a discontinuous change in magnetization at the external surfaces with their outward normal parallel to the magnetization, which can be envisaged as a source of magnetic charges (marked 'N' and 'S' in the figure). This gives rise to the demagnetizing or magnetostatic field, both inside and outside the material (see also figure 3.2 for an alternative representation of the

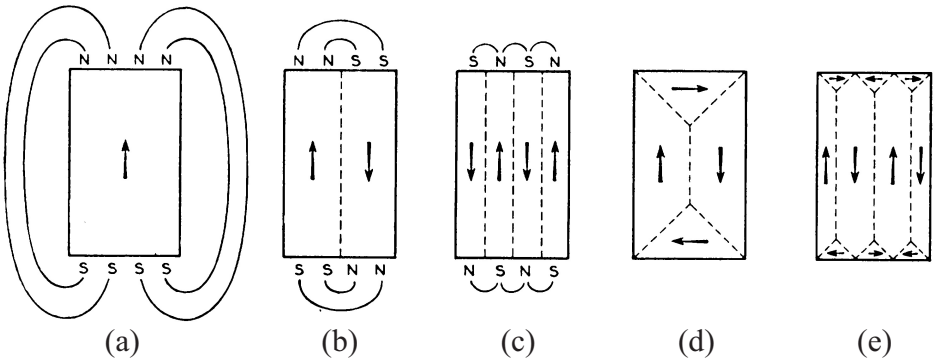

Figure 2.12. Magnetic domain formation, with indication of the magnetostatic field lines and the occurrence of magnetic charges ('N' and 'S', or north and south). Dashed lines are the domain walls, the arrows indicate the orientations of the domains. Only the magnetostatic field lines outside the material are shown. As a matter of fact, the domain configurations shown here from (a) to (e), are ordered from high to low total Gibbs free energy. More explanation is in the accompanying text.

demagnetizing field). For clarity, in figure 2.12 only the stray field lines outside the material are shown. It is clear that the magnetic moment configuration (a) – one single domain – leads to large magnetostatic fields.

The magnetostatic energy can be lowered by assuming a structure with multiple domains having anti-parallel magnetization, as in figure 2.12(b) and (c). Since all domains stay aligned with an easy crystallographic axis, the anisotropy energy of the domains itself stays invariant. In between the domains however, the magnetic moments gradually change their orientation in the so-called magnetic domain walls (see figure 2.15; more about domain walls in section 2.3.9). In such domain walls, the adjacent moments constituting the domain walls are not aligned parallel to each other, and also not aligned parallel to an easy crystallographic axis. Therefore, both w_{exch} and w_{anis} are increased in the domain wall regions. If this additional so-called *domain wall energy* is less than the decrease of the magnetostatic energy, the multiple domain configurations are energetically favoured and finally the domain configuration is set with the minimum sum of domain wall energy and magnetostatic energy.

It is clear that the anisotropy energy of the domains itself should be minimum. In fact, for b.c.c. iron with the three orthogonal $\langle 100 \rangle$ axes as easy crystallographic directions, this leads to two possibilities, both corresponding to minimum anisotropy energy for the domain volumes, i.e. neighbouring domains with anti-parallel or with perpendicular spontaneous magnetization vectors. The domain walls in between such configurations are called 180° and 90° domain walls, respectively.

On the other hand, the magnetostatic energy is minimal if there are no magnetic

charges present at the outer surfaces of the considered material volume. As a matter of fact, for cubic crystals such condition can be achieved, without affecting the anisotropy energy of the domain volumes, by a domain configuration comprising additional so-called closure domains (domains surrounded by the material surface and by 90° domain walls), see figure 2.12(d). Closure domains lead to the closure of the magnetic flux inside the material, therefore their name. Consequently no magnetic charges are present, and the magnetostatic energy is minimum.

As already been said, the domain configurations in figure 2.12 are ordered from high to low total Gibbs free energy. Finally, in order to explain why configuration (e) has a lower total Gibbs free energy than (d), the minimum of the sum of the additional domain wall energy and the so-called magnetoelastic energy has to be considered. In the next paragraph we will first introduce the concept of magnetoelastic energy and then explain why configuration (e) is energetically more favourable than (d), see p. 65.

To conclude, the magnetostatic energy contribution favours a change in the arrangement of the local magnetic moments into a multiple domain structure with main domains and closure domains (in other words domains with in between respectively 180° or 90° domain walls), in such a way that magnetic charges and the corresponding (stray) magnetostatic fields tend to disappear. Nevertheless, a structure with multiple domains inherently leads to an increase of the anisotropy and exchange (and magnetoelastic) energy in the small interface regions between the domains, called magnetic domain walls (see further in section 2.3.9), but as long as this energy increase is smaller than the decrease in magnetostatic energy, the creation of additional domains is favoured. As already been said, in the search for the optimum domain configuration, also the following magnetoelastic energy contribution plays a role.

2.3.4 Magnetoelastic energy

When a magnetic field is applied to a ferromagnetic specimen, its magnetization changes, but also a change of physical dimensions is observed, in response to that change in magnetization. Conversely, when an external mechanical stress is applied to a ferromagnetic specimen, it becomes strained, but also a change of magnetization is observed (if however the ferromagnetic specimen is not in a demagnetized state, see further in section 6.1). These phenomena are termed magnetostriction and magnetomechanical effect respectively (see section 2.1.2), and they both can be considered as the macroscopic outcome of the interaction between magnetic and elastic processes.

The general term for such class of phenomena is *'magnetoelastic interaction'* and the magnetoelastic energy that is treated in this paragraph is that part of the magnetic free energy of a crystal which arises from the interaction between the mag-

netic moments and the mechanical strain of the crystal lattice. The magnetoelastic energy is stored as a distortion of the crystal lattice or as an internal stress in the crystal lattice. For an unstrained lattice the magnetoelastic energy is minimum.

More in particular, as treated in section 1.1.2, also crystal defects induce a characteristic local internal stress distribution in the iron lattice that can be described by a proper elastic stress tensor. The interaction of the local magnetic moments on the one hand and the total elastic stresses introduced in the crystal lattice on the other hand are responsible for the influence of microstructural inhomogeneities (lattice defects) on the microscopic magnetization processes (in the first place domain wall pinning) and accordingly on the resulting macroscopic magnetic properties.

Total elastic strain tensor

In order to derive the magnetoelastic energy, we follow a more general approach [Kronmüller2003, Brown1966]: we start with a general description of the elastic interactions of a ferromagnetic solid, taking into account all possible contributions of both mechanical and magnetic origin, which leads to a total elastic strain tensor:

$$\overline{\varepsilon}_{tot}(\mathbf{r}) = \overline{\varepsilon}_{appl}(\mathbf{r}) + \overline{\varepsilon}_{def}(\mathbf{r}) + \overline{\varepsilon}_{\lambda,sp}(\mathbf{r}) + \overline{\varepsilon}_{\lambda,el}(\mathbf{r}). \tag{2.25}$$

Although these contributions to the total strain tensor have different origins, each contribution is defined within the framework of the linear elastic continuum mechanics theory (see appendix A): between elastic strains and elastic stresses the generalized Hooke's law holds: $\overline{\sigma} = \overline{\mathbf{c}} \cdot\cdot\, \overline{\varepsilon}$, with $\overline{\sigma}$ and $\overline{\varepsilon}$ respectively the symmetric stress and strain tensors of rank two, defined in three dimensions. The material dependent fourth rank elastic stiffness tensor is denoted as $\overline{\mathbf{c}}$, and $'\cdot\cdot'$ corresponds to the double internal product. In appendix A the tensor notation is reviewed with special emphasis on the description of the generalized Hooke's law.

The different contributions to the locally varying total elastic strain tensor (2.25) have the following origins:

- $\overline{\varepsilon}_{appl}$ is the strain caused by externally applied elastic stress $\overline{\sigma}_{appl}$.
- $\overline{\varepsilon}_{def}$ denotes the internal elastic strain due to the stress tensor field $\overline{\sigma}_{def}(\mathbf{r})$ originating from structural defects, such as dislocations or point defects.
- $\overline{\varepsilon}_{\lambda,sp}$ corresponds to the spontaneous magnetostriction due to spin ordering, and is also called the free magnetostrain tensor field. Remember that when iron is cooled down below its Curie temperature, the perfect cubic crystal lattice of the paramagnetic Fe ($T > T_c$) becomes slightly body centered tetragonal in case of ferromagnetic Fe ($T < T_c$), which means that the lattice is slightly longer in the direction of the spontaneous magnetization, see

also section 2.2.5. This elongation of the crystal lattice corresponds to the spontaneous magnetostriction, parallel to the spontaneous magnetization. The spontaneous magnetostriction tensor for a single crystal with cubic lattice can be described as follows [Kronmüller2003]:

$$\overline{\varepsilon}_{\lambda,sp} = \frac{3}{2}\begin{bmatrix} \lambda_{100}\left(\alpha_1^2 - \frac{1}{3}\right) & \lambda_{111}\alpha_1\alpha_2 & \lambda_{111}\alpha_1\alpha_3 \\ \lambda_{111}\alpha_1\alpha_2 & \lambda_{100}\left(\alpha_2^2 - \frac{1}{3}\right) & \lambda_{111}\alpha_2\alpha_3 \\ \lambda_{111}\alpha_1\alpha_3 & \lambda_{111}\alpha_2\alpha_3 & \lambda_{100}\left(\alpha_3^2 - \frac{1}{3}\right) \end{bmatrix} \quad (2.26)$$

with α_i the direction cosines of the magnetization relative to the three cubic crystal axes, and with λ_{100} and λ_{111} the magnetostriction constants, corresponding to the saturation magnetostriction of a single crystal in the $\langle 100 \rangle$ and $\langle 111 \rangle$ direction, respectively.

- $\overline{\varepsilon}_{\lambda,el}$ describes the elastic strain tensor related to inhomogeneous spontaneous magnetostrictive deformation. The total strain tensor due to magnetostriction, $\overline{\varepsilon}_{\lambda} = \overline{\varepsilon}_{\lambda,sp} + \overline{\varepsilon}_{\lambda,el}$, should describe a compatible deformation state, without any abrupt changes in displacement. This strain compatibility condition can be written as follows $\nabla \times (\nabla \times \overline{\varepsilon}_{\lambda}) = 0$. Once the spontaneous magnetostrictive strain $\overline{\varepsilon}_{\lambda,sp}$ is known, the corresponding elastic magnetostrictive strain $\overline{\varepsilon}_{\lambda,el}$ can be calculated in order to obtain strain compatibility. In case of homogeneous spontaneous magnetostrictive strain tensor $\overline{\varepsilon}_{\lambda,sp}$ (for instance a single domain), the strain compatibility is fulfilled and therefore $\overline{\varepsilon}_{\lambda,el} = 0$, whereas for an inhomogeneous spontaneous magnetostrictive strain tensor, $\overline{\varepsilon}_{\lambda,el} \neq 0$.

In the following, it is shown that the magnetostrictive terms $\overline{\varepsilon}_{\lambda,sp}$ and $\overline{\varepsilon}_{\lambda,el}$ are responsible for the interaction between on the one hand the externally applied and internal residual stresses $\overline{\sigma}_{appl}$ and $\overline{\sigma}_{def}$, and on the other hand the magnetic state.

Magnetoelastic interaction energy

In the previous paragraph we considered all possible contributions of the total elastic strain tensor. In this paragraph we shall derive the magnetoelastic energy density w_{me}, starting from the elastic energy density w_{el}:

$$w_{el} = \frac{1}{2}\left(\overline{\varepsilon}_{tot} \cdot\cdot\, \overline{\mathbf{c}} \cdot\cdot\, \overline{\varepsilon}_{tot}\right) - \left(\overline{\sigma}_{tot} \cdot\cdot\, \overline{\varepsilon}_{tot}\right), \quad (2.27)$$

$$w_{el} = -\frac{1}{2}\left(\overline{\varepsilon}_{tot} \cdot\cdot\, \overline{\mathbf{c}} \cdot\cdot\, \overline{\varepsilon}_{tot}\right), \quad (2.28)$$

with $\overline{\varepsilon}_{tot}$ defined as (2.25). The first term of (2.27) describes the internal elastic self energy density, whereas the second term corresponds with the elastic interaction energy density. For elastic stresses and strains (2.27) can be rewritten as

(2.28) since $\overline{\sigma}_{tot} = \overline{\mathbf{c}} \cdot\cdot\, \overline{\varepsilon}_{tot}$ is valid. Accordingly, the elastic energy can be written as follows:

$$W_{el} = \int_{\Omega_m} w_{el}(\mathbf{r})\, dV = -\frac{1}{2} \int_{\Omega_m} [\, \overline{\varepsilon}_{tot}(\mathbf{r}) \cdot\cdot\, \overline{\mathbf{c}} \cdot\cdot\, \overline{\varepsilon}_{tot}(\mathbf{r}) \,]\; dV. \tag{2.29}$$

Substituting the expression (2.25) for the total strain tensor into (2.28) gives :

$$\begin{aligned} w_{el} \;=\; & -\frac{1}{2}\,(\overline{\varepsilon}_{appl} \cdot\cdot\, \overline{\mathbf{c}} \cdot\cdot\, \overline{\varepsilon}_{appl}) \;-\; \frac{1}{2}\,(\overline{\varepsilon}_{def} \cdot\cdot\, \overline{\mathbf{c}} \cdot\cdot\, \overline{\varepsilon}_{def}) \\ & -\; \frac{1}{2}\,(\overline{\varepsilon}_{\lambda,sp} \cdot\cdot\, \overline{\mathbf{c}} \cdot\cdot\, \overline{\varepsilon}_{\lambda,sp}) \;-\; \frac{1}{2}\,(\overline{\varepsilon}_{\lambda,el} \cdot\cdot\, \overline{\mathbf{c}} \cdot\cdot\, \overline{\varepsilon}_{\lambda,el}) \\ & -\; (\overline{\varepsilon}_{appl} \cdot\cdot\, \overline{\mathbf{c}} \cdot\cdot\, \overline{\varepsilon}_{def}) \;-\; (\overline{\varepsilon}_{appl} \cdot\cdot\, \overline{\mathbf{c}} \cdot\cdot\, \overline{\varepsilon}_{\lambda,sp}) \;-\; (\overline{\varepsilon}_{appl} \cdot\cdot\, \overline{\mathbf{c}} \cdot\cdot\, \overline{\varepsilon}_{\lambda,el}) \\ & -\; (\overline{\varepsilon}_{def} \cdot\cdot\, \overline{\mathbf{c}} \cdot\cdot\, \overline{\varepsilon}_{\lambda,sp}) \;-\; (\overline{\varepsilon}_{def} \cdot\cdot\, \overline{\mathbf{c}} \cdot\cdot\, \overline{\varepsilon}_{\lambda,el}) \;-\; (\overline{\varepsilon}_{\lambda,sp} \cdot\cdot\, \overline{\mathbf{c}} \cdot\cdot\, \overline{\varepsilon}_{\lambda,el}). \end{aligned} \tag{2.30}$$

Since we are in search for the magnetoelastic energy we can now erase all terms which are purely mechanical (term 1, 2 and 5), and keep only the terms of magnetic origin, leading to the following expression for the magnetoelastic energy density:

$$\begin{aligned} w_{me} = -\left[\frac{1}{2}(\overline{\varepsilon}_{\lambda,sp} \cdot\cdot\, \overline{\mathbf{c}} \cdot\cdot\, \overline{\varepsilon}_{\lambda,sp}) + \frac{1}{2}(\overline{\varepsilon}_{\lambda,el} \cdot\cdot\, \overline{\mathbf{c}} \cdot\cdot\, \overline{\varepsilon}_{\lambda,el}) + (\overline{\varepsilon}_{\lambda,sp} \cdot\cdot\, \overline{\mathbf{c}} \cdot\cdot\, \overline{\varepsilon}_{\lambda,el})\right] - \\ [(\overline{\varepsilon}_{appl} \cdot\cdot\, \overline{\mathbf{c}} \cdot\cdot\, \overline{\varepsilon}_{\lambda,sp}) + (\overline{\varepsilon}_{appl} \cdot\cdot\, \overline{\mathbf{c}} \cdot\cdot\, \overline{\varepsilon}_{\lambda,el}) + (\overline{\varepsilon}_{def} \cdot\cdot\, \overline{\mathbf{c}} \cdot\cdot\, \overline{\varepsilon}_{\lambda,sp}) + (\overline{\varepsilon}_{def} \cdot\cdot\, \overline{\mathbf{c}} \cdot\cdot\, \overline{\varepsilon}_{\lambda,el})]\,. \end{aligned} \tag{2.31}$$

The first three terms of (2.31) are only depending on one of the contributions to the total magnetostrictive strain, $\overline{\varepsilon}_{\lambda} = \overline{\varepsilon}_{\lambda,sp} + \overline{\varepsilon}_{\lambda,el}$. Moreover, starting from the compatibility requirement of $\overline{\varepsilon}_{\lambda}$ (i.e. $\nabla \times (\nabla \times \overline{\varepsilon}_{\lambda}) = 0$), it can be shown [Kronmüller2003] that the following identity is valid:

$$\overline{\varepsilon}_{\lambda,sp} \cdot\cdot\, \overline{\mathbf{c}} \cdot\cdot\, \overline{\varepsilon}_{\lambda,el} = -\overline{\varepsilon}_{\lambda,el} \cdot\cdot\, \overline{\mathbf{c}} \cdot\cdot\, \overline{\varepsilon}_{\lambda,el}. \tag{2.32}$$

The last four terms of (2.31) are the magnetoelastic interaction energies, and can be rewritten in a more convenient form, i.e. $-(\overline{\sigma}_{appl} + \overline{\sigma}_{def}) \cdot\cdot\, (\overline{\varepsilon}_{\lambda,sp} + \overline{\varepsilon}_{\lambda,el})$.

Combining all this finally gives the following expression for the magnetoelastic energy density:

$$\begin{aligned} w_{me} = \; & -\; \frac{1}{2}\,\overline{\varepsilon}_{\lambda,sp} \cdot\cdot\, \overline{\mathbf{c}} \cdot\cdot\, \overline{\varepsilon}_{\lambda,sp} \\ & +\; \frac{1}{2}\,\overline{\varepsilon}_{\lambda,el} \cdot\cdot\, \overline{\mathbf{c}} \cdot\cdot\, \overline{\varepsilon}_{\lambda,el} \\ & -\; (\overline{\sigma}_{appl} + \overline{\sigma}_{def}) \cdot\cdot\, (\overline{\varepsilon}_{\lambda,sp} + \overline{\varepsilon}_{\lambda,el}). \end{aligned} \tag{2.33}$$

As a summary, the magnetoelastic energy density w_{me} (2.33) consists of three main terms, each with a different meaning:

- The first term of (2.33), denoted further as w_{me1} depends on the spontaneous magnetostriction strain, and corresponds to a magnetostrictive contribution to the magnetocrystalline anisotropy energy: when inserting (2.26) into this first term of the magnetoelastic energy density w_{me1}, and by making use of the expression (A.12) in appendix A, w_{me1} can be written in Voigt's notation (see Appendix A) as follows:

$$w_{me1} = -\frac{1}{2}\,\overline{\varepsilon}_{\lambda,sp} \cdot\cdot\, \overline{\mathbf{c}} \cdot\cdot\, \overline{\varepsilon}_{\lambda,sp} = K_{\lambda,sp} \sum_{i \neq j} \alpha_i^2 \alpha_j^2 + C_{\lambda,sp}, \qquad (2.34)$$

  with $K_{\lambda,sp} = (9/4)[(c_{11} - c_{12})\lambda_{100}^2 - 2c_{44}\lambda_{111}^2]$, and the constant energy density $C_{\lambda,sp}$ can be further omitted. Notice that (2.34) is proportional to $\sum \alpha_i^2 \alpha_j^2$ and therefore w_{me1} has the same form as the magnetocrystalline anisotropy energy (2.21). Accordingly, $K_{\lambda,sp}$ adds to the anisotropy constant K_1. For iron-based materials however this effect is negligible since $|K_{\lambda,sp}/K_1| \approx 10^{-3}$.

- The second term of (2.33) can be considered as the self energy of the elastic magnetostrictive strains:

$$w_{me2} = \frac{1}{2}\,\overline{\varepsilon}_{\lambda,el} \cdot\cdot\, \overline{\mathbf{c}} \cdot\cdot\, \overline{\varepsilon}_{\lambda,el}. \qquad (2.35)$$

- The third term of (2.33) is called the magnetoelastic coupling energy:

$$w_{me3} = -(\overline{\sigma}_{appl} + \overline{\sigma}_{def}) \cdot\cdot\, (\overline{\varepsilon}_{\lambda,sp} + \overline{\varepsilon}_{\lambda,el}), \qquad (2.36)$$

  and describes the interaction between on the one hand the externally applied and the internal residual stresses, $\overline{\sigma}_{appl}$ and $\overline{\sigma}_{def}$, and on the other hand the magnetic state, via the magnetostrictive strain tensor $\overline{\varepsilon}_{\lambda} = \overline{\varepsilon}_{\lambda,sp} + \overline{\varepsilon}_{\lambda,el}$.

As has been said, since the first term simply adds to the anisotropy and is moreover negligibly small ($w_{me1} \approx 0$), only the second and third term of w_{me} are of practical importance.

Further, a frequently applied practical approach is to consider only the spontaneous magnetostrain $\overline{\varepsilon}_{\lambda,sp}$ and to disregard $\overline{\varepsilon}_{\lambda,el}$ in the second and the third term of w_{me}. Hence $w_{me2} = 0$, and the third term reads: $w_{me3} = -(\overline{\sigma}_{appl} + \overline{\sigma}_{def}) \cdot\cdot\, \overline{\varepsilon}_{\lambda,sp}$. As a matter of fact, this is only correct for homogeneous local magnetization. For the frequently existing inhomogeneous magnetization condition in multi-domain configurations, the elimination of $\overline{\varepsilon}_{\lambda,el}$ is called the *relaxed approach*. It is clear

that such approximation leads to loss of strain compatibility in multi-domain configurations, in contradiction to the general and 'constrained' approach of (2.33). However, for low magnetostrictive materials, as is the case for the iron-based materials in this study, the relaxed approach is acceptable [Shu2004] and hence the total magnetoelastic energy formulation is reduced to:

$$w_{me} \approx w_{me,relax} = -(\overline{\sigma}_{appl} + \overline{\sigma}_{def}) \cdot\cdot\, \overline{\varepsilon}_{\lambda,sp}. \tag{2.37}$$

Substituting (2.26) in (2.37) then leads to:

$$w_{me,relax} = -\frac{3}{2}\lambda_{100} \sum_{i=1}^{3} \sigma_{ii}\alpha_i^2 - \frac{3}{2}\lambda_{111} \sum_{i \neq j} \sigma_{ij}\alpha_i\alpha_j, \tag{2.38}$$

where the stress tensor σ_{ij} may correspond to externally applied stresses $\overline{\sigma}_{appl}$ and/or internal stresses resulting from defect structures $\overline{\sigma}_{def}$. Moreover, when the magnetostriction is assumed to be isotropic, and when σ is an unidirectional stress with θ equal to the angle between the direction of σ and the spontaneous magnetization $\mathbf{M_s}$, then:

$$w_{me,relax} = -\frac{3}{2}\ \lambda_s\ \sigma \cos^2\theta, \tag{2.39}$$

with λ_s the isotropic saturation magnetostriction.

Case: Magnetoelastic energy of closure domains

Now that the magnetoelastic energy is introduced, we can go back to the context of figure 2.12, illustrating the origin of the domain structure based on energetic principles. Open question is why domain configuration (b) of figure 2.13 is energetically more favourable than domain configuration (a).

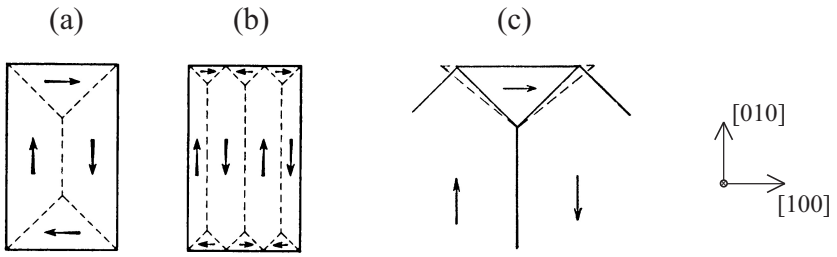

Figure 2.13. (a) and (b) are a repetition of the domain configurations (d) and (e) of figure 2.12. (c) shows the effect of magnetostriction on the closure domains: dotted lines indicate on an exaggerated scale the unconstrained closure domain.

Since for iron $\lambda_{100} > 0$, the $[100]$ closure domain in figure 2.13(c) tends to elongate towards the dotted lines, if it is not constrained by the neighbouring $[010]$ and $[0\bar{1}0]$ main domains. Maintaining the compatibility between the closure domain and the main domains requires that the closure domain is under compressive stress ($\sigma < 0$), giving rise to an increase of magnetoelastic energy according to equation (2.39). The extra magnetoelastic energy stored in the closure domains is proportional to their volume. In order to reduce this additional magnetoelastic energy, the volume fraction of closure domains compared to main domains can be reduced by additional but smaller closure domains and hence also additional but smaller main domains, see configuration (b) versus (a) in figure 2.13. On the other hand, more domains obviously requires more domain walls, which means more domain wall energy (i.e. anisotropy energy and exchange energy in the domain wall regions, see section 2.3.9). Therefore the equilibrium configuration corresponds to the situation where the sum of the magnetoelastic energy of the closure domains and the domain wall energy is minimum.

Case: Magnetoelastic energy of externally applied stresses

The magnetoelastic energy of externally applied *unidirectional* stress σ_{appl} along direction $\mathbf{e}_\sigma$ can be written as follows, when ignoring the intrinsic magnetostrictive stress (thus following the relaxed approach) and under the assumption of isotropic magnetostriction λ_s, according to (2.39):

$$w_{me} \;=\; -\frac{3}{2}\,\lambda_s\,\sigma_{appl}\cos^2\theta, \tag{2.40}$$

with θ equal to the angle between the spontaneous magnetization and the applied uniaxial stress σ_{appl}. This expression has the same format as an uniaxial (magnetocrystalline) anisotropy energy, and is therefore called *stress-induced anisotropy*: the effect of the externally applied stress can be envisaged as the introduction of an extra direction of easy magnetization, in addition to the magnetocrystalline easy directions. This stress-induced easy direction is parallel to the external stress direction $\mathbf{e}_\sigma$ for positive $\lambda_s\sigma_{appl}$ product, and perpendicular to $\mathbf{e}_\sigma$ for negative $\lambda_s\sigma_{appl}$ product. For iron, however, the magnetocrystalline anisotropy remains dominant since $K_1 \gg (3/2)\lambda_s\sigma_{appl}$ for all realistic σ_{appl} and λ_s values[6].

2.3.5 Energy due to externally applied magnetic field

The applied field energy is the energy that arises when a magnetic moment $\mathbf{m}$ or alternatively the local magnetization vector $\mathbf{M}_{loc}(\mathbf{r})$ is placed in an externally im-

[6]For iron $(2K_1)/(3\lambda_s) \approx 3200$ MPa, which is much higher than the yield stress for iron or low carbon steels (typical value: $\sigma_y \approx 300$ MPa).

posed magnetic field. The associated energy density can be described as follows:

$$w_{appl}(\mathbf{r}) = -\mu_0 \mathbf{H}_{appl}(\mathbf{r}) \cdot \mathbf{M}_{loc}(\mathbf{r}). \tag{2.41}$$

When hypothetically taking into account only the applied field energy, this mutual energy between magnetization and applied magnetic field term tends to align all magnetic moments parallel to the applied magnetic field $\mathbf{H}_{appl}$.

2.3.6 Conclusion - Magnetic free energy terms

In the previous paragraphs we treated the different contributions to the total magnetic free energy. As a conclusion:

- the **exchange energy** contribution favours the parallel alignment of neighbouring atomic magnetic dipole moments (short-range dipole-dipole interactions);
- the **anisotropy energy** contribution favours the alignment of all atomic magnetic moments along certain discrete directions, which are fixed to the crystal lattice. For iron, there are 6 directions of easy magnetization: $[001]$, $[00\overline{1}]$, $[010]$, $[0\overline{1}0]$, $[100]$ and $[\overline{1}00]$. The anisotropy energy is caused by those magnetic moments having a different direction compared to the crystallographic easy directions (short-range dipole-lattice interactions);
- the **magnetostatic energy** contribution favours a change in the arrangement of the local magnetic moments into a structure of multiple domains, with domain walls in between (i.e. 180° or 90° domain walls, due to the magnetocrystalline anisotropy energy of b.c.c. iron), in order to minimize the (stray) magnetostatic fields around the ferromagnetic material. The magnetostatic energy is caused by the field that arises from all other magnetic dipoles (long-range dipole-field interactions);
- the **magnetoelastic energy** contribution is due to the presence of mechanical stresses and strains: (1) internal stresses due to crystal defects, (2) externally applied stress leading to stress-induced uniaxial anisotropy (the effect of the applied stress can be envisaged as the introduction of an extra direction of easy magnetization), and (3) stresses and strains due to the magnetostrictive behaviour (short-range magnetoelastic interactions);
- the **externally applied field energy** contribution favours the alignment of all magnetic moments parallel to the applied magnetic field. This energy is caused by the presence of an externally applied field (long-range dipole-field interactions).

Table 2.1. Relevant material parameters at room temperature (293 K), for b.c.c. iron (α–Fe) [Kronmüller2003].

Parameter	Symbol	Value
Lattice edge length	a	0.286 $\cdot 10^{-9}$ m
Spontaneous magnetization	M_s	1.715 $\cdot 10^{6}$ A/m
Exchange stiffness	A	21 $\cdot 10^{-12}$ J/m
First magnetocrystalline anisotropy constant	K_1	48 $\cdot 10^{3}$ J/m^3
Second magnetocrystalline anisotropy constant	K_2	5 $\cdot 10^{3}$ J/m^3
$[100]$ saturation magnetostriction	λ_{100}	22 $\cdot 10^{-6}$
$[111]$ saturation magnetostriction	λ_{111}	-21 $\cdot 10^{-6}$
Stiffness tensor element	c_{11}	241 GPa
Stiffness tensor element	c_{12}	146 GPa
Stiffness tensor element	c_{44}	112 GPa

In the description of the above-mentioned magnetic free energy contributions, only a small number of material dependent parameters are involved. Here, we recapitulate the most important ones in table 2.1. Most of the mentioned material parameters are temperature dependent, such as the spontaneous magnetization M_s (see figure 2.8), the magnetocrystalline anisotropy constants K_1 and K_2, the exchange stiffness A and the saturation magnetostriction constants λ_{100} and λ_{111} [Bozorth1951]. In table 2.1 the room temperature values are given for pure b.c.c. iron. The material parameters are also dependent on chemical composition: to give an example it is known that the anisotropy constant K_1 decreases with increasing Si-content in electrical steels [Bozorth1951].

2.3.7 Minimization of total magnetic free energy

Magnetic systems aim at minimum free magnetic energy. Considering the different energy terms, it is clear that the equilibrium configuration that minimizes the total magnetic free energy is the result of some kind of competition (trade off) between all the different energy contributions. For instance, a magnetic system with additional domains and hence an increased domain wall surface inherently leads to an increase of the anisotropy energy, exchange energy and magnetoelastic energy in the small interface regions between the domains called magnetic domain walls (see further in section 2.3.9), but as long as this energy increase is smaller than the corresponding decrease in magnetostatic energy, the creation of additional domains is favoured.

Firstly, in this paragraph 2.3.7 the minimization of the total magnetic free energy

is the central issue. The minimization technique used in micromagnetics is based on the Landau-Lifshitz equation, which describes the dynamic variation of the local magnetization vector towards its equilibrium. Final result is then the equilibrium configuration of the magnetic domains and domain walls, for a given input (applied magnetic field, applied mechanical stress). Secondly, this micromagnetic approach may be utilized for the simulation of macroscopic magnetic behaviour, see paragraph 2.3.8. Finally, in paragraph 2.3.9 the static equilibrium of a magnetic domain wall is investigated, leading to concepts as domain wall width and domain wall energy per unit area.

The micromagnetic theory considers the total magnetic free energy density of the ferromagnetic material: $w_{tot} = w_{exch} + w_{anis} + w_{me} + w_{ms} + w_{appl}$. Those five contributions are treated already in sections 2.3.1–2.3.5. An equilibrium distribution of the local magnetization vector $\mathbf{M}_{loc}(\mathbf{r})$ corresponds with a minimum of the total magnetic free energy. Aiming at finding the local magnetization at equilibrium, the variational derivative is considered of the total energy density w_{tot}, with respect to the local magnetization [Brown1963]. This variational approach can also be envisaged in terms of the so-called effective magnetic field $\mathbf{H}_{eff}$ at a position $\mathbf{r}$ inside the ferromagnetic material, which is proportional to the variational derivative of w_{tot}:

$$\mathbf{H}_{eff}(\mathbf{r}) = -\frac{1}{\mu_0} \sum_{i=1}^{3} \frac{\partial w_{tot}}{\partial M_{loc,i}} \, \mathbf{e}_i, \tag{2.42}$$

with $\mathbf{e}_i (i = 1...3)$ the unit vectors of a Cartesian coordinate system. Each of the five energy contributions can thus be considered as a contribution to the local effective magnetic field: $\mathbf{H}_{eff} = \mathbf{H}_{exch} + \mathbf{H}_{anis} + \mathbf{H}_{me} + \mathbf{H}_{ms} + \mathbf{H}_{appl}$. Hence the local magnetic field H_{eff} at a certain position $\mathbf{r}$ inside the ferromagnetic material differs from the externally applied magnetic field, due to contributions of magnetic stray fields, and of exchange coupling, magnetocrystalline anisotropy and magnetoelastic interaction energies. The effective magnetic field can be described in more detail as a function of the direction cosines α_i of M_{loc}, as follows [Brown1963]:

$$H_{eff,i} = \frac{2A}{\mu_0 M_s} \nabla^2 \alpha_i - \frac{1}{\mu_0 M_s} \frac{\partial w_{anis}}{\partial \alpha_i} - \frac{1}{\mu_0 M_s} \frac{\partial w_{me}}{\partial \alpha_i} + H_{ms,i} + H_{appl,i}. \tag{2.43}$$

As a matter of fact, (2.42) corresponds with the following expression $w_{tot} = -\mu_0 \mathbf{M}_{loc} \cdot \mathbf{H}_{eff}$. At equilibrium the local magnetization vector is therefore parallel to the local effective magnetic field. This can be envisaged as a torque due to $\mathbf{H}_{eff}$ acting on $\mathbf{M}_{loc}$, which tends to align the local magnetization parallel to the effective field as the system proceeds towards equilibrium:

$$\mathbf{H}_{eff} \times \mathbf{M}_{loc} = 0. \tag{2.44}$$

This equation describes the *static* micromagnetic equilibrium condition.

However, the core problem in micromagnetics – finding the equilibrium directions of the local magnetization – can not be solved in a straight-forward way by static minimization techniques: the energy landscape of a micromagnetic system is usually too complex and contains many local maxima, minima and saddle points, for instance because of the stochastic distribution of microstructural defects such as dislocations, vacancies, precipitates and so on. Moreover, this energy landscape is not invariant: consider a small increase of the externally applied field. Consequently the effective field (and the total free magnetic energy) changes slightly, and the system is no longer in equilibrium: $\mathbf{M}_{loc}$ is not parallel anymore with $\mathbf{H}_{eff}$, and evolves towards a new equilibrium. However, when $\mathbf{M}_{loc}$ changes, the different contributions to the effective field also vary (for instance $\mathbf{H}_{anis}$, $\mathbf{H}_{exch}$, $\mathbf{H}_{me}$ and $\mathbf{H}_{ms}$ are all dependent on $\mathbf{M}_{loc}$), which can be envisaged as a continuously changing energy landscape with possibly modified minima and maxima.

Based on all these considerations, to find the actual equilibrium Landau and Lifshitz suggested to take also into account the particular dynamic approach towards the actual equilibrium, instead of only considering the static equilibrium [Landau1960]. The non-linear dynamics of micromagnetic systems is usually described by the Landau-Lifshitz equation:

$$\frac{\partial \mathbf{M}_{loc}}{\partial t} = \gamma_L \left(\mathbf{H}_{eff} \times \mathbf{M}_{loc}\right) + \frac{\alpha_L \gamma_L}{M_s} \left(\mathbf{M}_{loc} \times \left(\mathbf{H}_{eff} \times \mathbf{M}_{loc}\right)\right) \qquad (2.45)$$

with γ_L the gyromagnetic factor and α_L the damping coefficient. The Landau-Lifshitz formalism results in the damped precession movement of the local magnetization vector around the effective field: the first term at the right hand side of (2.45) causes precession of $\mathbf{M}_{loc}$ around $\mathbf{H}_{eff}$, and the second term represents the damping (see also figure 2.14). The precession corresponds to the typical motion of a spin magnetic moment in a magnetic field, which is mainly governed by

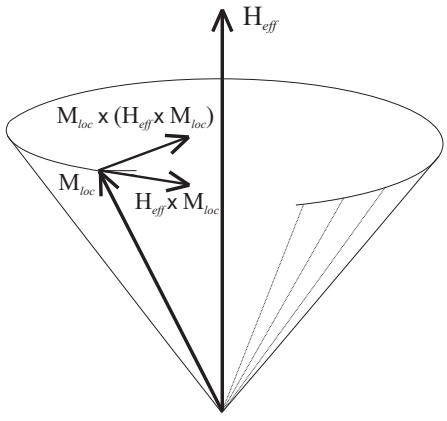

Figure 2.14. Visualization of the precession and damping terms of the Landau-Lifshitz equation (2.45).

its Larmor precession around the magnetic field: the Larmor precession period is typically smaller than a nanosecond, so in order to simulate the damped precession movement of $\mathbf{M}_{loc}$ towards its equilibrium, time steps are required in the order of picoseconds [Kronmüller2003]. The damping mechanism, on the other hand, is a proposition by Landau and Lifshitz, which is generally considered to be a reasonable theoretical hypothesis [Jiles2002].

2.3.8 Micromagnetic simulation of macroscopic behaviour

Micromagnetic simulations are a useful tool for the analysis of ferromagnetic behaviour on small spatial and time scales, for instance for micrometer or submicrometer applications such as magnetic recording (information storage) and magnetic sensors [Fidler2000]. With present computing capabilities it is nowadays possible to apply the micromagnetic theory for the numerical modelling of three-dimensional ferromagnetic crystals with dimensions of the order of 10 μm and larger [VandeWiele2008a].

Moreover, in the micromagnetic theory, microstructural defects can be taken into account as an internal stress tensor field via the magnetoelastic energy, whereas non-magnetic inhomogeneities can be considered via the magnetostatic energy. Therefore, starting from a predefined microstructural state, the micromagnetic model permits to investigate the macroscopic magnetic behaviour of realistic materials. Aiming at the micromagnetic computation of the macroscopic hysteretic behaviour of polycrystalline material samples (with dimensions in the mm and cm range), in order to investigate the influence of the microstructure on the macroscopic magnetic behaviour, is however very complex and challenging. Two of the main difficulties are:

1. *both long-range and short-range interactions are involved.* Especially the long-range magnetostatic energy prevents the treatment of the energy minimization problem as a set of local problems in individual volumes of the material [VandeWiele2007]. This demands for a multi-scale strategy to simulate all relevant features on length scales from the atomistic scale up to the size of the sample;

2. *the distribution of the different microstructural features is stochastic and shows a high degree of structural disorder*. In previous paragraphs we treated the micromagnetic formalism for single crystals of pure iron. Apart from the lattice defects such as dislocations, point defects,impurities and so on, it is clear that for polycrystalline materials also the grain size distribution, the texture, and also secondary phases or precipitates have to be taken into account. Especially grain boundaries and phase boundaries will be locations of additional energy.

Nevertheless, one of the strengths of the numerical micromagnetic approach to investigate macroscopic magnetic behaviour is that it becomes possible to examine in theory the effect of one particular microstructural parameter, which is hard to achieve or to control in case of experimental determination of the magnetic hysteresis loops on samples with different microstructures.

2.3.9 Domain wall energy and domain wall width

The distribution of the individual magnetic moment directions can be envisaged as consisting of a number of regions for which the local magnetization is parallel everywhere ('magnetic domains'), separated by transition regions in which the magnetization direction changes with position ('magnetic domain walls'), as illustrated in figure 2.15. Domain walls were first studied by Bloch [Bloch1932], who derived theoretically that the change of the magnetization direction from one domain to the other is not discontinuous but occurs over a finite width, which is however usually small compared to the magnetic domain dimensions.

The domain wall width is mainly determined by the energy balance between the exchange and magnetocrystalline anisotropy energy (but also the magnetoelastic energy can have a considerable influence, see further). On the one hand the exchange energy decreases if the change in direction between neighbouring magnetic moments is smaller, hence the exchange interaction favours a large domain wall width. On the other hand the anisotropy energy decreases if the individual magnetic moments are aligned more and more with a crystallographic direction of easy magnetization, hence the anisotropy favours a small domain wall width.

The domain wall width can be calculated as the static micromagnetic equilibrium between the different relevant short-range energies (exchange, anisotropy and magnetoelastic energies). As a case study, let's consider a planar $(001)-180°$ Bloch domain wall. In figure 2.16 a Cartesian coordinate system is introduced with unit vectors parallel to the $\langle 100 \rangle$ crystallographic directions, and with $\mathbf{e}_z$

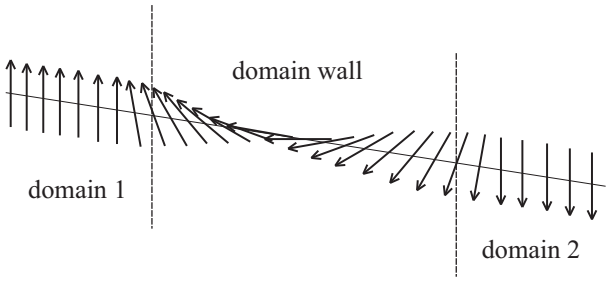

Figure 2.15. Rough sketch of the directional change of the magnetic moments comprising a 180° Bloch domain wall.

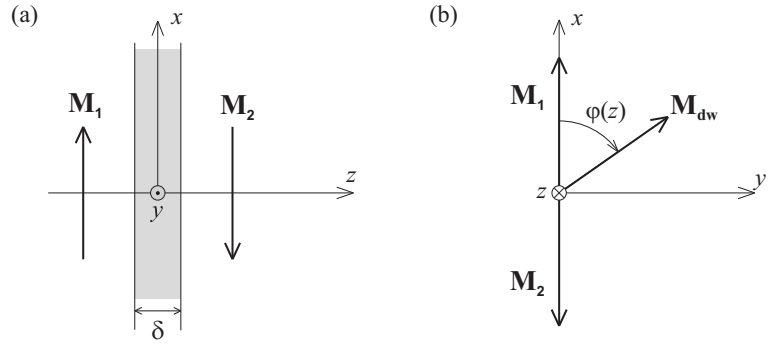

Figure 2.16. Schematic overview of a 180° Bloch domain wall, with its surface normal to $\mathbf{e}_z$. In the figure, the gray-coloured object represents the domain wall, with width δ. The magnetization of the adjacent domains is taken parallel and anti-parallel with $\mathbf{e}_x$, whereas inside the domain wall the magnetization direction changes with position z normal to the domain wall surface.

normal to the domain wall surface. Inside a Bloch wall the magnetization vectors remain parallel with the domain wall surface whereas the magnetization direction changes with position z normal to the domain wall surface. The magnetization $\mathbf{M}_{dw}$ at position z inside the domain wall can be described in terms of the angle $\varphi(z) = \angle(\mathbf{M}_{dw}, \mathbf{e}_x)$:

$$\mathbf{M}_{dw} = M_s \left[\alpha_x(z)\mathbf{e}_x + \alpha_y(z)\mathbf{e}_y\right] = M_s \left[\cos\varphi(z)\mathbf{e}_x + \sin\varphi(z)\mathbf{e}_y\right], \quad (2.46)$$

$$\left[\alpha_x(z),\ \ \alpha_y(z),\ \ \alpha_z(z)\right] = \left[\cos\varphi(z),\ \ \sin\varphi(z),\ \ 0\right]. \quad (2.47)$$

Inside the 180° Bloch domain wall of figure 2.16, the short-range energy density contributions (w_{anis}, w_{me} and w_{exch}) defined for $0 \leq \varphi \leq \pi$, are as follows:

1. The magnetocrystalline anisotropy energy density of the domain wall can be worked out by substituting (2.47) into (2.21):

$$w_{anis}(\varphi) = K_1\alpha_x^2\alpha_y^2 = K_1\cos^2\varphi\sin^2\varphi = \frac{K_1}{4}sin^2 2\varphi. \quad (2.48)$$

   Figure 2.17 gives a visualization of $w_{anis}(\varphi)$: the magnetocrystalline energy density has minima at $\varphi = 0$, $\pi/2$ and π.
2. The determination of the magnetoelastic energy density of the domain wall starts from the general expression (2.33). In case of no externally applied stress and assuming that no internal stress due to defects are present, the third term of (2.33) vanishes and only the first and second term remain. The magnetoelastic energy of the domain wall therefore reads:

$$w_{me} = -\tfrac{1}{2}\,\overline{\varepsilon}_{\lambda,sp} \cdot\cdot\, \overline{\mathbf{c}} \cdot\cdot\, \overline{\varepsilon}_{\lambda,sp} + \tfrac{1}{2}\,\overline{\varepsilon}_{\lambda,el} \cdot\cdot\, \overline{\mathbf{c}} \cdot\cdot\, \overline{\varepsilon}_{\lambda,el}. \quad (2.49)$$

The first term of (2.49) can be written in terms of φ by substituting (2.47) into (2.34):

$$w_{me1}(\varphi) = \left(\frac{9}{4}(c_{11} - c_{12})\lambda_{100}^2 - \frac{9}{2}c_{44}\lambda_{111}^2\right)\sin^2\varphi\cos^2\varphi.$$

On the other hand, the elastic magnetostriction tensor $\overline{\varepsilon}_{\lambda,el}$ for the 180° Bloch domain wall in figure 2.16 can be determined starting from $\overline{\varepsilon}_{\lambda,sp}$ as expressed by equation (2.26) and using equation (2.47) [Kronmüller2003]. Further, the second term of the magnetoelastic energy (2.49) can be elaborated by making use of expression (A.12) of Appendix A, which then gives:

$$w_{me2}(\varphi) = \frac{9}{4}(c_{11} - c_{12})\lambda_{100}^2\sin^4\varphi + \frac{9}{2}c_{44}\lambda_{111}^2\sin^2\varphi\cos^2\varphi.$$

Combining both terms finally results into the magnetoelastic energy of the domain wall:

$$w_{me}(\varphi) = w_{me1}(\varphi) + w_{me2}(\varphi) = K_{\lambda u}\sin^2\varphi, \tag{2.50}$$

with $K_{\lambda u} = \frac{9}{4}\lambda_{100}^2(c_{11} - c_{12}) \approx 103$ J/m^3 for iron. It can be seen that the magnetoelastic energy of a 180° Bloch domain wall shows the features of uniaxial anisotropy. Figure 2.17 gives a visualization of $(w_{anis} + w_{me})$ as a function of φ. The magnetoelastic energy w_{me} has only a small contribution to the energy density $(w_{anis} + w_{me})$, but as a consequence the middle of the domain wall ($\varphi = \pi/2$) becomes energetically less favourable than both ends of the domain wall: $w_{anis} + w_{me}$ has minima at $\varphi = 0$ and $\varphi = \pi$.

3. The exchange energy of the domain wall can be worked out, starting from (2.18) and (2.47):

$$\begin{aligned} w_{exch}(\varphi) &= A\left[\left(\frac{\partial\alpha_x}{\partial z}\right)^2 + \left(\frac{\partial\alpha_y}{\partial z}\right)^2\right] \\ &= A\left[\cos^2\varphi + \sin^2\varphi\right]\left(\frac{\partial\varphi}{\partial z}\right)^2 = A\left(\frac{\partial\varphi}{\partial z}\right)^2. \end{aligned} \tag{2.51}$$

However, the relationship between the magnetization angle φ and the position z is not known a priori. In the following we treat two approaches: in approach (A) a linear $\varphi(z)$ relationship is assumed and the specific domain wall energy is minimized in order to obtain the equilibrium domain wall width, whereas in approach (B) the $\varphi(z)$ relationship is determined by considering the static micromagnetic equilibrium condition.

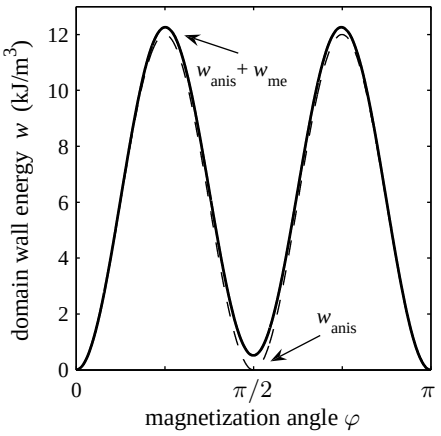

Figure 2.17. Domain wall energy densities w_{anis} (2.48) and $(w_{anis} + w_{me})$, according to (2.48) and (2.50), as a function of φ. The $(w_{anis} + w_{me})$–curve is only qualitatively valid, since for reasons of clarity w_{me} is exaggerated 5 times.

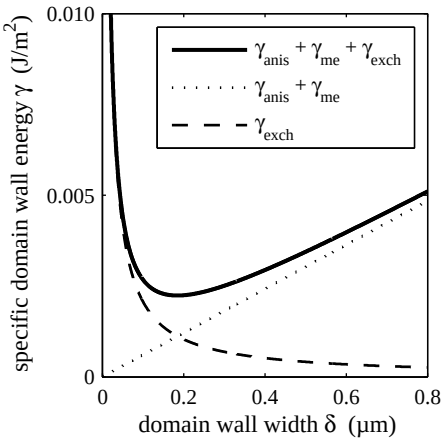

Figure 2.18. Graphical representation of equation (2.54), i.e. the specific domain wall energy γ versus domain wall width δ, as obtained by the postulation of a linear relationship between position z and magnetization angle φ (approach A).

Approach A: assumption of a linear $\varphi(z)$ relationship, and minimization of specific domain wall energy

The specific domain wall energy γ, defined as the domain wall energy per unit area of the domain wall, can be written as follows for a 180° domain wall:

$$\gamma = \int_{-\delta/2}^{\delta/2} w(z)\ \mathrm{d}z = \int_0^{\pi} w(\varphi) \left(\frac{\partial z}{\partial \varphi}\right) \mathrm{d}\varphi, \tag{2.52}$$

with $w = w_{anis} + w_{me} + w_{exch}$ the domain wall energy density. Inserting (2.48), (2.50) and (2.51) into (2.52) then gives:

$$\begin{aligned} \gamma &= \gamma_{anis} + \gamma_{me} + \gamma_{exch} = \frac{K_1}{4} \int_0^{\pi} sin^2 2\varphi \left(\frac{\partial z}{\partial \varphi}\right) \mathrm{d}\varphi \\ &+ K_{\lambda u} \int_0^{\pi} \sin^2 \varphi \left(\frac{\partial z}{\partial \varphi}\right) \mathrm{d}\varphi + A \int_0^{\pi} \left(\frac{\partial \varphi}{\partial z}\right) \mathrm{d}\varphi. \end{aligned} \tag{2.53}$$

Further, when postulating a linear $\varphi(z)$ relationship, $\varphi(z) = \frac{\pi}{2} + \frac{\pi}{\delta} z$, $(-\delta/2 < z < \delta/2)$, the specific wall energy can be worked out in terms of the domain wall width δ:

$$\gamma = \left(\frac{K_1}{8}\right) \delta + \left(\frac{K_{\lambda u}}{2}\right) \delta + \frac{(A\pi^2)}{\delta} = \left(\frac{\tilde{K_1}}{8}\right) \delta + \frac{(A\pi^2)}{\delta}, \tag{2.54}$$

with $\tilde{K_1}$ defined as $\tilde{K_1} = K_1 + 4K_{\lambda u} \approx 1.0086\ K_1$. Minimization of (2.54) results in the following expressions for the equilibrium domain wall width and the equilibrium specific domain wall energy, in case of a 180° Bloch domain wall:

$$\begin{cases} \delta_{180^\circ} = 2\sqrt{2}\pi \sqrt{A/\tilde{K_1}} \\ \gamma_{180^\circ} = \frac{\pi}{\sqrt{2}} \sqrt{A\tilde{K_1}} \end{cases} \tag{2.55}$$

Substituting $\tilde{K_1} \approx 1.0086\ K_1$ into (2.55), and with the room temperature values of K_1 and A in case of pure iron (see table 2.1 on page 68), this finally gives:

$$\begin{cases} \delta_{180^\circ} \approx 185 \text{ nm } (\approx 647\ a) \\ \gamma_{180^\circ} \approx 2.24 \cdot 10^{-3} \text{ J/m}^2 \end{cases}$$

Case: externally applied stress Until now in section 2.3.9, we only considered magnetic domain walls without externally applied stress or internal stress due to defects. We can now consider the effect of an externally applied uniaxial stress on the domain wall width. Assuming only a tensile or compressive elastic stress σ parallel to $\mathbf{e}_x$ and assuming isotropic saturation magnetostriction λ_s, the additional magnetoelastic contribution to the domain wall energy can be written as (2.40):

$$\gamma_{me,\sigma} = \frac{3}{2}\lambda_s\sigma \int_0^\pi \sin^2\varphi \left(\frac{\partial z}{\partial \varphi}\right) \mathrm{d}\varphi. \tag{2.56}$$

This extra energy term has the same form as the already treated magnetoelastic term due to magnetostriction, see (2.53). Therefore this can be treated by an extra uniaxial anisotropy constant adding to $K_{\lambda u}$, therefore:

$$\tilde{K_1} = K_1 + 4(K_{\lambda u} + \frac{3}{2}\lambda_s\sigma). \tag{2.57}$$

With this $\tilde{K_1}$, the equilibrium domain wall width and specific domain wall energy can be calculated by (2.55). It is clear that the effect depends on the sign of the product $\lambda_s\sigma$. Table 2.2 combines some results. Tensile elastic stress along $\mathbf{e}_x$ leads to decreased domain wall width, since $\varphi = \pi/2$ becomes energetically less favourable compared to the stress-free condition.

Approach B: direct determination of equilibrium $\varphi(z)$ relationship

When examining figure 2.17 again, it is clear that for a 180° Bloch domain wall (defined for $0 < \varphi < \pi$), the direction $\varphi = \pi/2$ is energetically favourable, since it corresponds with a crystallographic direction of easy magnetization. The

Table 2.2. Equilibrium domain wall width and equilibrium specific domain wall energy, obtained by approach A, for three cases of uniaxial stress: σ = 0 MPa, 100 MPa and -100 MPa, parallel to $\mathbf{e}_x$. In this calculation the saturation magnetostriction takes the following (positive) value: $\lambda_s = 10^{-5}$.

σ_{appl} (MPa)	$\tilde{K_1}/K_1$ (-)	δ_{dw} (nm)	δ_{dw}/a (-)	γ_{dw} (J/m^2)
-100	0.884	198	691	$2.10 \cdot 10^{-3}$
0	1.0086	185	647	$2.24 \cdot 10^{-3}$
100	1.134	175	610	$2.37 \cdot 10^{-3}$

assumption in previous paragraph of a linear relationship between the magnetization angle φ and the position z is therefore questionable.

The approach in this paragraph is to determine $\varphi(z)$ as a result of the static micromagnetic equilibrium conditions, as outlined in section 2.3.7.

The Bloch domain wall configuration of figure 2.16 can be considered in polar coordinates, with constant polar angle $\theta = \pi/2$ and with azimuthal angle φ depending on position. The static micromagnetic equilibrium conditions (2.44) can be expressed in polar coordinates [Kronmüller2003]. Since the polar angle is constant in our problem, the static micromagnetic equilibrium condition reduces to a single equation depending on φ:

$$2A\ \nabla^2\varphi - \frac{\partial(w_{anis} + w_{me} + w_{ms} + w_{appl})}{\partial\varphi} = 0. \tag{2.58}$$

Considering that φ only depends on z, and that the long-range energy contributions w_{ms} and w_{appl} can be considered to be independent on φ:

$$2A\ \frac{\partial^2\varphi}{\partial z^2} - \frac{\partial(w_{anis} + w_{me})}{\partial\varphi} = 0. \tag{2.59}$$

By integrating twice, this equation becomes:

$$z(\varphi) = \int_0^{\varphi} \frac{\sqrt{A}}{\sqrt{w_{anis}(\varphi') - w_{anis}(0) + w_{me}(\varphi') - w_{me}(0)}}\ \mathrm{d}\varphi', \tag{2.60}$$

with $w_{anis}(\varphi')$ given by (2.48) and $w_{anis}(\varphi' = 0) = 0$. In case of no external stress and no internal stress due to defects, $w_{me}(\varphi')$ is obtained by (2.50) and $w_{me}(\varphi' = 0) = 0$.

The resulting equilibrium $\varphi(z)$ relationship for a $180°$ Bloch domain wall is given in figure 2.19. It is apparent that the domain wall width can not definitely be determined in approach B, since $\varphi = 0$ and $\varphi = \pi$ mathematically correspond to

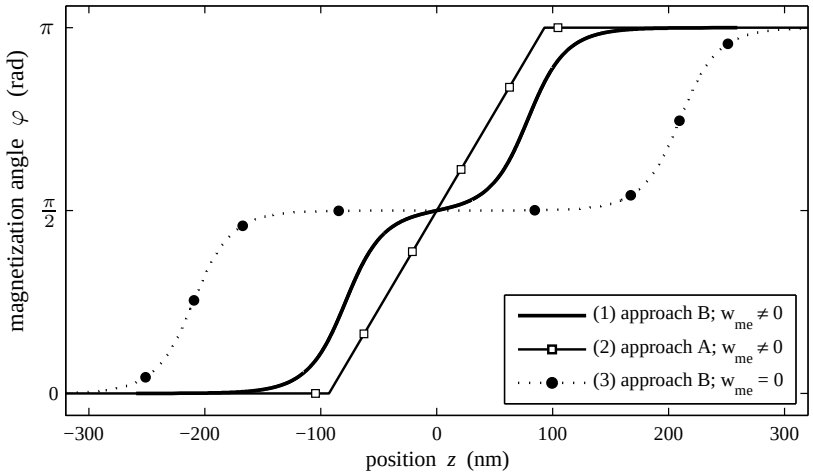

Figure 2.19. Dependence of magnetization angle φ on position z for three cases: (1) equilibrium $\varphi(z)$ obtained by approach B; (2) postulated linear relationship of approach A taking into account the obtained equilibrium δ obtained by approach A; (3) hypothetical case with $w_{me} = 0$ (approach B). Corresponding domain wall widths: $\delta_{(1)} \approx 224$ nm; $\delta_{(2)} \approx 185$ nm; $\delta_{(3)} \approx 480$ nm.

$z \to -\infty$ and $z \to +\infty$ respectively. The following approach is followed: a piecewise linear approximation of $\varphi(z)$ is constructed having as slope the maximum value of $\mathrm{d}\varphi/\mathrm{d}z$, both for $z < 0$ and $z > 0$. The domain wall width is then defined as the difference of the z-values at $\varphi = 0$ and π of such piecewise linear approximation. The equilibrium domain wall width and specific domain wall energy (2.52) then have to following values:

$$\begin{cases} \delta_{180^\circ dw} \approx 224 \text{ nm } (\approx 782\ a) \\ \gamma_{180^\circ dw} \approx 2.03 \cdot 10^{-3} \text{ J/m}^3 \end{cases}$$

Regarding the large conceptual difference between approach A and B, there is a fair correspondence with the results obtained with approach A, both for equilibrium δ and γ.

The magnetoelastic energy w_{me}, which is however low in magnitude compared to w_{anis} (see figure 2.17), has significant consequences on the equilibrium $\varphi(z)$ relationship obtained by approach (B). In figure 2.19 the equilibrium $\varphi(z)$ relationship is also given in case of hypothetically omitting w_{me} into (2.60). This hypothetical result can hardly be considered as a 180° domain wall, but more likely as two separated 90° domain walls ($\delta \approx 60$ nm) with in between a magnetic domain of 360 nm wide (≈ 1260 lattice parameters a).

2.4 Influence of microstructural defects on magnetization processes

In this section we treat the typical magnetization processes that occur under the application of a changing magnetic field, with special attention to the influence of microstructural inhomogeneities (lattice defects) on the magnetization processes.

Figure 2.20 gives a small illustrative example of how variations in microstructural features can alter the magnetic behaviour of bulk ferromagnetic materials. The major magnetic hysteresis loop is shown for two samples with the same dimensions, obtained from the same material (a low-carbon ferritic structural steel). The first sample originates from the as-received material sheet and the second one is taken from a cold-rolled sheet with 10% reduction of thickness. Cold rolling is a plastic deformation process which results in an increase of the dislocation density, see section 5.2.2 for more information and more results concerning cold-rolling. It can be seen that the cold rolled sample has a higher coercive field, a lower remanent induction and a lower maximum differential permeability than the as-received sample.

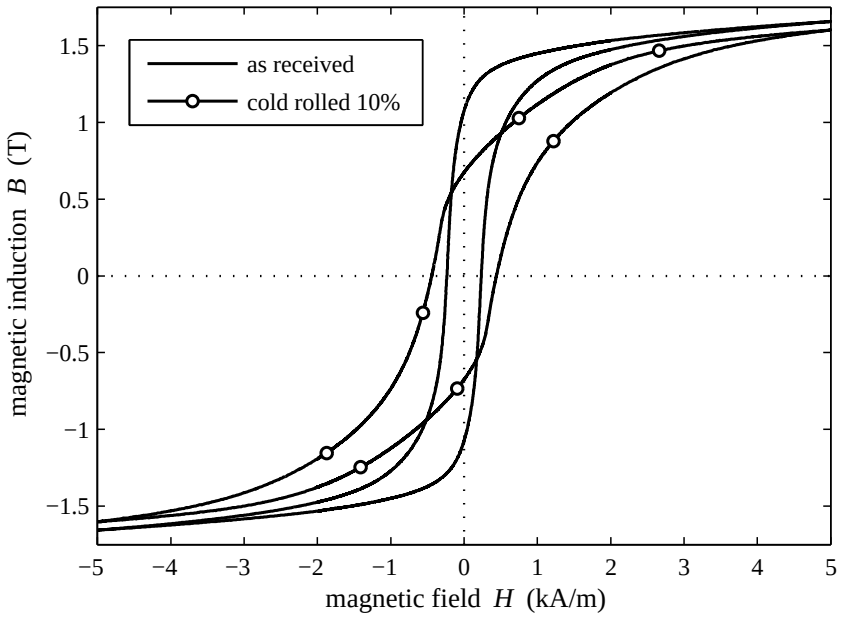

Figure 2.20. Magnetization loop of a cold-rolled sample compared to an as-received sample, as an illustration to what extent microstructural changes (in this case mainly an increase of dislocation density) can affect the magnetization loop shape.

2.4.1 Magnetization processes

When the applied magnetic field is changed, the applied field energy of a ferromagnetic body alters and therefore the equilibrium of the free energy is disturbed. As a result, the magnetic domain configuration rearranges in order to minimize the free energy under the new condition of applied magnetic field. In the behaviour of the magnetic domains under the action of a changing applied magnetic field two main mechanisms can be distinguished: *domain wall motion* and *magnetization rotation*. Figure 2.21 shows an initial magnetization curve with the regions designated in which each magnetization process is dominant.

Iron and steels have a high magnetocrystalline anisotropy, therefore the rotation of the magnetization out of an easy direction requires much applied field energy. Hence in weak to moderate magnetic fields the magnetization mainly changes by domain wall motion. Domain wall motion reduces the overall applied field energy of the ferromagnetic body: the magnetic domains with magnetization orientation closest to the applied magnetic field direction are energetically favoured and their volume will increase under the application of a magnetic field, at the expense of neighbouring magnetic domains which are not favourably oriented to the applied magnetic field direction. In the next paragraphs 2.4.2 and 2.4.3 we focus further on the (reversible and irreversible) domain wall motion process, more specifically in connection to the presence of microstructural defects and their influence on the domain wall motion.

At sufficiently large applied magnetic field levels most of the domain walls have disappeared, in other words most of the material volume is occupied by large mag-

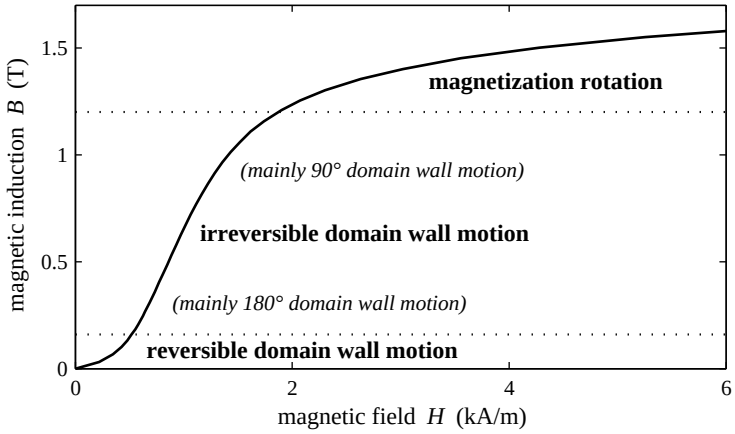

Figure 2.21. Indication of dominant magnetization processes along the initial - or virgin - magnetization curve of an low-alloyed ferritic steel.

netic domains with magnetization direction closest to the applied field direction. The principal magnetization process at large applied fields is the rotation of the magnetization vector into the direction of the applied magnetic field.

2.4.2 Pinning of domain walls by internal stresses

The microstructure of bulk polycrystalline ferromagnetic materials shows a high degree of structural disorder due to randomly distributed lattice imperfections such as dislocations, point defects, but also grain boundaries, second phases and so on, as been introduced in section 1.1.2. These stochastically distributed microstructural defects give rise to short range fluctuations in the local Gibbs free energy density w as a function of position $\mathbf{r}$. More specifically, the microstress field associated with defects such as dislocations can alter locally the magnetoelastic energy, whereas microstructural inhomogeneities such as second phases and grain boundaries can give rise to discontinuous magnetization variations, and hence to fluctuations in the magnetostatic energy.

For soft ferromagnetic materials such as iron and steels, it turns out that one of the main magnetization mechanisms is magnetic domain wall motion. In the particular case of planar domain wall motion, the multidimensional energy landscape $w(\mathbf{r})$ can be envisaged as a one-dimensional potential energy function $w(x)$, with the state x representing the position of a single magnetic domain wall. As an illustration, a conceptual example of such potential energy profile is shown in figure 2.22.

In the following we concentrate on the local fluctuations in magnetoelastic en-

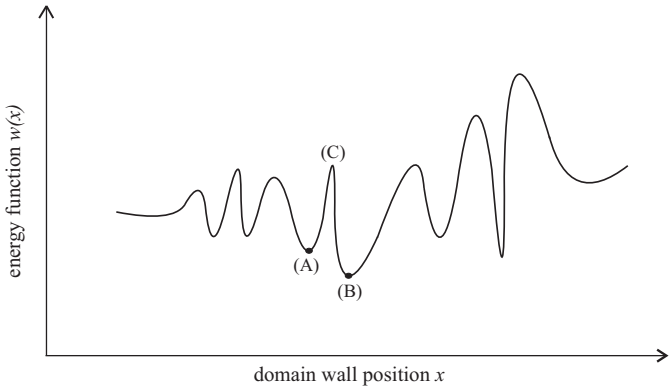

Figure 2.22. Illustrative micromagnetic energy profile characterized by short range fluctuations due to structural disorder. The local energy minima represent the stable magnetization configurations. These energy minima act as pinning sites for the magnetic domain wall during its motion.

ergy, arising from the stress tensor $\overline{\sigma}_{def}$ associated with microstructural defects such as dislocations and point defects (section 1.1.2). Through the magnetoelastic coupling as described in section 2.3.4 these highly inhomogeneous microstresses give rise to stochastic fluctuations in the magnetoelastic energy, as illustrated in figure 2.22. In this conceptual framework the equilibrium position of a domain wall is at a local energy minimum, whereas the local maxima in the energy profile act as energy barriers which obstruct the domain walls in their movement.

Under the application of an external magnetic field a force is exerted on the magnetic domain wall, but as long as the magnetic field is lower than some critical value, the domain wall remains in the same potential well, say (A) at figure 2.22. In such case, the domain wall returns to the original local minimum, when the applied field is switched off. This is called *reversible domain wall motion.*

On the other hand, in order to enable the domain wall to reach a new local energy minimum (B in figure 2.22) sufficient applied field energy is necessary to pass the domain wall over the energy barrier (C) between two energy minima. This process is called *irreversible domain wall motion*: when the applied field is switched off the domain wall remains in the new energy minimum (B). Moreover, the externally applied field needs to be large enough to overcome the pinning of the domain wall within a certain energy minimum. The unpinning causes a sudden movement of the domain wall to the next energy minimum, accompanied with a sudden change of the volume of neighbouring domains. This jerky motion of

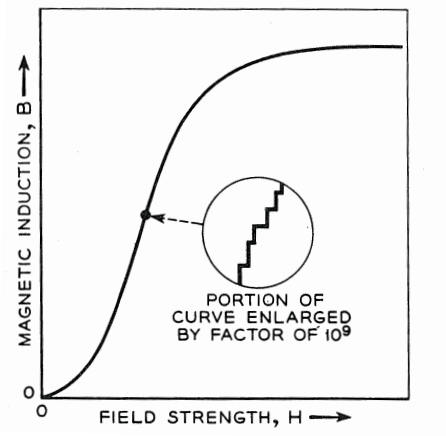

Figure 2.23. Illustration of the Barkhausen effect [Bozorth1951]. Due to the microstructural defects the displacement of the domain wall occurs by irreversible jumps from one local energy minimum to the next. As a function of a continuous change in applied field this gives rise to a discontinuous course of the magnetization curve. As a result the induced voltage (the derivative of the flux) contains several large peaks, which is known as Barkhausen noise.

the domain wall through the randomly fluctuating energy profile from one local minimum to the next leads to discontinuous changes in the macroscopic magnetization, also known as *Barkhausen jumps* [Barkhausen1919], as is illustrated in figure 2.23.

2.4.3 Simplified model to estimate the effect of internal stress on coercive field and initial permeability

A quantitative description of the influence of microstructural inhomogeneities on the magnetization processes in bulk ferromagnetic materials making use of all the micromagnetic energy concepts treated in section 2.3 is a very complex task and is out of our scope here [VandeWiele2008a]. Nevertheless, making use of the so-called strain theory [Kersten1938, Becker1938], we can give a simplified qualitative impression of the dominant features in the relation between the domain wall motion and the internal stress fields around microstructural defects. Such simplified model makes it then possible to estimate the effect of internal stress on coercive field and initial permeability.

Let us consider the planar movement of a single domain wall under the action of an applied magnetic field. Figure 2.24 shows parts of two magnetic domains separated by a 180° domain wall with domain wall surface area S_{dw}. The applied field $\mathbf{H}_{appl}$ makes an angle θ_H with $\mathbf{M}_2$, the magnetization of domain 2, an angle which is smaller than the angle between $\mathbf{H}_{appl}$ and $\mathbf{M}_1$, the magnetization of domain 1.

Under the application of an external magnetic field oriented as such, the displacement of the 180° domain wall in the positive x-direction (making domain 2 larger at the expense of domain 1) causes a decrease in applied field energy: making use of (2.41) the applied field energy density in the volume $S_{dw}\Delta x$ (the gray region in figure 2.24), is for situation (a): $w_{appl,(a)} = -\mu_0 H_{appl} M_s \cos(\pi - \theta_H)$ (considered region is part of domain 1), whereas for situation (b): $w_{appl,(b)} = -\mu_0 H_{appl} M_s \cos\theta_H$ (considered region is now part of domain 2). Hence the change in applied field energy is:

$$\begin{aligned} \Delta W_{appl} &= \left(w_{appl,(b)} - w_{appl,(a)}\right) S_{dw}\Delta x \\ &= -2\mu_0 H_{appl} M_s \cos\theta_H S_{dw}\Delta x. \end{aligned} \tag{2.61}$$

Concerning the other micromagnetic energy terms, the exchange and anisotropy energies can be regarded as being concentrated in the domain wall and since the domain wall area doesn't change here these two energy contributions can be considered to stay invariant during the domain wall movement. On the other hand the change in magnetostatic energy is neglected here for this two domain configuration under study (figure 2.24). Hence the two dominant micromagnetic energy

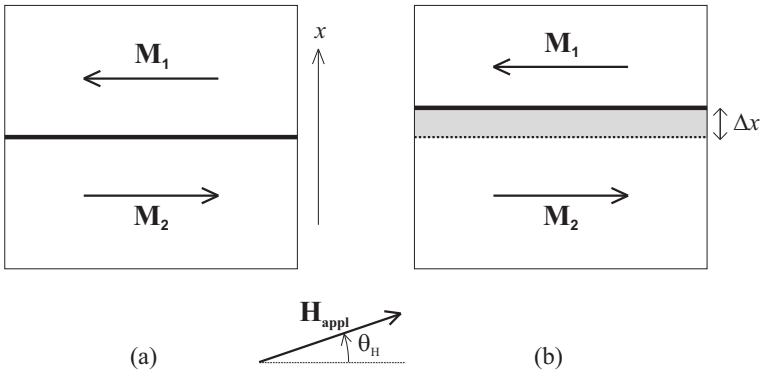

Figure 2.24. Sketch of two magnetic domains separated a 180° magnetic domain wall. The domain wall is represented by a bold line. Subfigure (a) depicts the situation before domain wall motion, whereas (b) shows the configuration after the domain wall motion as an effect of the applied magnetic field oriented as shown.

terms that change during domain wall motion are the applied field energy and the magnetoelastic energy.

As been said in section 2.4.2, the randomly distributed microstructural inhomogeneities in ferromagnetic solids (such as dislocations, point defects, impurities and so on) give rise to a magnetoelastic energy contribution which fluctuates irregularly as a function of domain wall position x, see figure 2.22. According to the strain theory, these short range fluctuations in magnetoelastic energy experienced by the domain wall can be considered to arise from variations in the localized internal stress field associated with the microstructural inhomogeneities.

In order to estimate the effect of the internal residual stress on the domain wall motion, here the irregularly fluctuating magnetoelastic energy distribution is simplified and modelled by a unidirectional internal stress of which the magnitude varies sinusoidally with position x:

$$\sigma_i(x) = \widehat{\sigma_i} \cos\left(\frac{2\pi x}{L_i}\right), \tag{2.62}$$

with amplitude $\widehat{\sigma_i}$ and periodicity L_i. Notice that the average of $\sigma_i(x)$ is zero, as it should be for internal residual stresses. Further, assuming isotropic magnetostriction (with λ_s the isotropic saturation magnetostriction) and following the relaxed approach (see section 2.3.4), the magnetoelastic energy can be written similar to (2.40) as follows:

$$w_{me}(x) \;=\; -\frac{3}{2}\,\lambda_s\,\sigma_i(x)\cos^2\theta_\sigma = -\frac{3}{2}\,\lambda_s\,\widehat{\sigma_i}\cos\left(\frac{2\pi x}{L_i}\right)\cos^2\theta_\sigma, \tag{2.63}$$

with θ_σ equal to the angle between the local magnetization and the internal stress

vector $\sigma_i \mathbf{e}_\sigma$. Notice that for positive λ_s, position $x = 0$ corresponds with a minimum for the magnetoelastic energy.

Now that the two dominant micromagnetic energy terms that change with domain wall motion - i.e. the energy of the applied field and the magnetoelastic energy - are treated, the equilibrium condition can be expressed as follows:

$$\frac{\mathrm{d}w_{appl}}{\mathrm{d}x} + \frac{\mathrm{d}w_{me}}{\mathrm{d}x} = 0, \tag{2.64}$$

or by making use of (2.61) and (2.63):

$$-2\mu_0 H_{appl} M_s s_{dw} \cos\theta_H + \frac{3\pi\lambda_s \widehat{\sigma_i}}{L_i} \sin\left(\frac{2\pi x}{L_i}\right) \cos^2\theta_\sigma = 0, \tag{2.65}$$

with s_{dw} the domain wall area per unit volume: $s_{dw} = S_{dw}/V_{md}$, with V_{md} the considered volume of the magnetic domains. For small displacement x the following approximation is valid: $\sin\left(\frac{2\pi x}{L_i}\right) \approx \frac{2\pi x}{L_i}$, and (2.65) can be solved:

$$x = \frac{\mu_0 H_{appl} M_s s_{dw} L_i^2 \cos\theta_H}{3\pi^2 \lambda_s \widehat{\sigma_i} \cos^2\theta_\sigma}. \tag{2.66}$$

As a result of this simple model, the initial susceptibility and coercive field can be derived as a function of the internal stress parameters $\widehat{\sigma_i}$ and L_i.

Initial susceptibility

The magnetization along the applied field direction, $M = \mathbf{M} \cdot \mathbf{e_H}$, changes as follows with the small displacement Δx of a 180° domain wall (see figure 2.24):

$$\begin{aligned} \Delta M &= M_s(\cos\theta_H - \cos(\pi - \theta_H)) s_{dw} \Delta x \\ &= 2M_s \cos\theta_H s_{dw} \Delta x. \end{aligned} \tag{2.67}$$

The initial differential susceptibility $\chi_{d,i}$ is a measure for the ease with which a domain wall can be moved. $\chi_{d,i}$ can be defined as follows:

$$\chi_{d,i} = \frac{\mathrm{d}M}{\mathrm{d}H_{appl}} = \frac{\mathrm{d}M}{\mathrm{d}x} \frac{\mathrm{d}x}{\mathrm{d}H_{appl}}. \tag{2.68}$$

Making use of (2.67) for $\frac{\mathrm{d}M}{\mathrm{d}x}$ and of (2.66) for $\frac{\mathrm{d}x}{\mathrm{d}H_{appl}}$ this gives:

$$\chi_{d,i} = \frac{2\mu_0 s_{dw}^2 M_s^2 L_i^2 \cos^2\theta_H}{3\pi^2 \lambda_s \widehat{\sigma_i} \cos^2\theta_\sigma} \tag{2.69}$$

We may conclude that:

$$\chi_{d,i} \sim \frac{L_i^2}{\widehat{\sigma_i}}, \tag{2.70}$$

so the initial susceptibility is high for small pinning energy (small internal stress amplitude $\widehat{\sigma_i}$), and for a small pinning site density (large periodic distance L_i between internal stress centers).

Coercive field

The coercive field H_c is a measure for the typical applied field strength at which domain walls unpin from microstructural defects, a process by which a substantial part of the magnetization is reversed. Alternatively formulated in the framework of the randomly fluctuating potential energy profile (figure 2.22) the coercive field can be envisaged as the critical field needed to carry a wall from one local energy minimum to another local energy minimum, in other words to overcome a certain energy barrier.

The applied field delivers the *driving force* for the domain wall motion: the effect of the applied field can be considered as exerting a force on the magnetic domain wall, whereas the opposing force originates from the local residual internal stress field of the distributed microstructural defects. Let us elaborate this concept of driving force somewhat further: the force exerted on a domain wall by the applied field H_{appl}, capable of moving the domain wall in the x direction perpendicular to the magnetic domain wall surface can be written conceptually as follows:

$$F = -\frac{\mathrm{d}W_{appl}}{\mathrm{d}x}. \tag{2.71}$$

So, in our specific case of a 180° domain wall (figure 2.24) this driving force can be derived starting from (2.61):

$$F = (2\mu_0 M_s S_{dw} \cos\theta_H) H_{appl}, \tag{2.72}$$

and the equilibrium condition (2.64) can be alternatively expressed as:

$$F = \frac{\mathrm{d}W_{me}}{\mathrm{d}x}. \tag{2.73}$$

The critical applied magnetic field needed to overcome the energy barrier corresponds with the maximum driving force exerted on the domain wall. On the one hand, deriving the maximum driving force F_{max} starting from (2.63) and (2.73):

$$F_{max} = \max\left(\frac{\mathrm{d}W_{me}}{\mathrm{d}x}\right) = \frac{3\pi V_{md}\lambda_s \widehat{\sigma_i} \cos^2\theta_\sigma}{L_i}. \tag{2.74}$$

On the other hand, according to (2.72) the relation between F_{max} and the critical applied magnetic field $H_{appl,crit}$ is:

$$F_{max} = (2\mu_0 M_s S_{dw} \cos\theta_H)\, H_{appl,crit}. \tag{2.75}$$

Hence the critical applied field, which is a measure for the coercive field is:

$$H_{appl,crit} = \frac{3\pi\lambda_s \widehat{\sigma_i}}{2\mu_0 M_s s_{dw} L_i \cos\theta_H} \tag{2.76}$$

We may conclude that:

$$H_c \sim \frac{\widehat{\sigma_i}}{L_i}, \tag{2.77}$$

so the coercive field is low for small pinning energy (small internal stress amplitude $\widehat{\sigma_i}$), and for a small number density of pinning sites (large periodic distance L_i between internal stress centers).

Some remarks

The simple model for domain wall motion described in this section section 2.4.3 contains some simplifications:

- the model takes into account only the interaction of a single domain wall with the defect stress field;
- the high degree of disorder in the distribution of microstructural defects which is inherent to real solids, is neglected here, since the magnetoelastic energy is implicitly described by a periodical function;
- the tensor of internal residual stress is replaced by a unidirectional stress vector;
- the domain wall motion is assumed to be planar (also called rigid wall approximation), so movement of domain walls by domain wall bowing is neglected in this model; also the magnetization rotation processes are not considered here;
- the change in magnetostatic energy resulting from magnetization variations around defects is neglected.

Therefore the modelling results have to be interpreted with caution. Nevertheless the trends of the coercive field and initial permeability dependence on the defect density and on the pinning energy correspond qualitatively with the experimental

results, see for instance the data presented in chapter 5 about the influence on the magnetic properties of point defects and precipitates due to neutron irradiation, and about the influence of dislocations introduced by plastic deformation (see also figure 2.20).

2.5 Conclusion

In this chapter the general theoretical framework is given for the ferromagnetic behaviour with special attention to the influence of lattice imperfections that are inherent to real magnetic materials such as iron and ferritic steels. First the basic concepts of ferromagnetism are introduced, both on the macroscopic and the microscopic level.

The main part of this chapter is devoted to the micromagnetic theory of competing energy contributions which are the origin for the equilibrium magnetic domain structure. Based on the micromagnetic energy concepts a domain wall model is derived that gives some qualitative results about the influence of defect density and pinning strength on macroscopic magnetic parameters such as coercive field and permeability.

In the following chapters the emphasis is on experimental work related to material degradation. The qualitative trends derived from the domain wall model can be instructive to interpret the experimental results.

Chapter 3

Magnetic measurement methods

In this chapter, the magnetic measurement methods used in the present study and the constructed measurement setups based on these methods are discussed. In almost all cases the experimental approach taken during the performed research is based upon the ***field-metric method*** under the condition of unidirectional quasi-static excitation, with the specific aim to determine the macroscopic scalar relation between the magnetic field $H(t)$ and the magnetization $M(t)$ of the sample.

The general principles of this method are discussed in section 3.1, whereas in section 3.2 more details are given about some of the specific measurement setups based on the field-metric method that are designed and constructed at EELAB in the frame of my PhD and that are used throughout the experimental research outlined in the following chapters. Of primary interest is the typical hysteretic behaviour present in the constitutive relation $M(H)$ of ferromagnetic materials. The magnetic measurement methods and setups under consideration are deployed to experimentally explore all features of this hysteretic magnetic behaviour.

In section 3.3, the magnetomechanical experimental setup is introduced. In principle, this setup is the incorporation of one of the magnetic measurement setups described in section 3.2, inside a mechanical testing apparatus. This magnetomechanical setup has the additional possibility, apart from applying a time-dependent magnetic field to the sample and simultaneously measuring $M(t)$ and $H(t)$, to also apply a time-dependent mechanical stress to the sample (mechanical loading is possible both in tension and in compression), and at the same time to measure both stress $\sigma(t)$ and strain $\varepsilon(t)$. With this setup it becomes possible to investigate the effects of the magnetoelastic coupling on a macroscopic scale (chapter 6).

On the other hand, during the course of my PhD research, some small excursion is also made towards a second type of experimental method, called the ***magnetic drag force method***, which starts from a completely different approach but

is however still strongly related to the magnetic hysteretic behaviour. This second method is introduced in section 3.4.

3.1 Field-metric method: general principles

3.1.1 Introduction

In the framework of this research, the *field-metric* method is used to determine the macroscopic *scalar* constitutive relation $M(H)$ of a ferromagnetic sample under *unidirectional* and *quasi-static* excitation conditions. For isotropic and nearly isotropic materials, such as the iron-based materials used in this study, the assumption of a scalar dependence of the macroscopic magnetization M on the macroscopic magnetic field H is reasonably valid. The term *field-metric* means that the performed magnetic characterization of the material starts with the combined simultaneous determination of two time-dependent quantities, the magnetic field $H(t)$ and the magnetization $M(t)$ of the sample. The experiments are performed under the specific condition of *unidirectional* excitation, which means that a time-dependent magnetic field is applied in one specific direction to the ferromagnetic sample under test (typically parallel to the longest sample dimension), i.e. $\mathbf{H}(t) = H(t)\mathbf{e}_H$, and the resulting magnetization of the sample is measured parallel to the direction of the applied magnetic field, i.e. $M(t) = \mathbf{M}(t) \cdot \mathbf{e}_H$. Also the sample's magnetic field H is determined parallel to $\mathbf{e}_H$.

The core elements of the considered measurement setup based on the unidirectional field-metric method are typically: (1) a closed magnetic circuit comprising the ferromagnetic material under test; (2) two windings, placed around the material under test: an outer excitation winding is used to apply the time-dependent magnetic field $H(t)$, and secondly an inner measurement winding, wound as close as possible around the ferromagnetic material is used to determine the resulting magnetization $M(t)$ or alternatively the magnetic induction $B(t)$; and (3) in some particular cases local H-sensors. The hardware combination of the closed magnetic circuit, excitation coil and B-measurement coil (and if applicable local H-sensors) is also called a *permeameter*.

These core hardware elements, treated in more detail in the following sections, are only a part of the complete experimental setup. In figure 3.1 the general concept of the complete magnetic measurement setup that is built around the permeameter or magnetic circuit is shown schematically. A power amplifier supplies the current to generate a magnetic field in the excitation coil, and the magnetic circuit magnetizes the sample as uniform as possible. The resulting magnetic properties are measured with appropriate sensors and if necessary analog signal conditioning is performed on the measured signals. By using a data-acquisition card (DAQ)

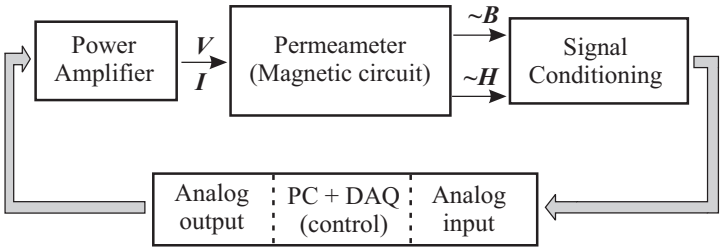

Figure 3.1. Schematic overview of the different hardware components in a typical magnetic measurement setup.

plugged in a PC, an analog-to-digital conversion is performed on the measured signals making it possible to perform additional processing within a software program written in *LabVIEW*. This software program also takes into consideration the user defined measurement parameters and conditions, and visualizes the measurement results. The data acquisition card, driven by the software program, controls the measurement process and generates the analog signals that serve as input for the linear power amplifier.

With the field-metric method and the experimental setups based on the field-metric method that are described later in this chapter, the constitutive relation $M(H)$ can be determined for excitation frequencies in the range of $f \approx 0$ (quasi-static) to typically 1 kHz. However, one should be cautious when interpreting the measured M- and H-values, since this interpretation is inherently connected to the underlying experimental principles of the field-metric method. As we will see later, the inductive method used to measure the magnetization (section 3.1.3) inherently results in an average magnetization value, $M_{meas} = M_{avg}$, averaged out over the cross section of the sample, whereas both direct and indirect methods to determine the magnetic field (section 3.1.4) inherently result in the magnetic field value at the surface of the sample, $H_{meas} = H_{surf}$.

On the other hand, for reasons explained in more detail in chapter 4, of primary interest in this research dealing with magnetic NDE is the investigation of the relation between the microstructural features and the hysteretic behaviour at *quasi-static* excitation conditions, in other words at excitation frequencies for which the occurrence of eddy currents can be neglected. Therefore, in the following paragraphs the field-metric method is described with particular interest for the application of the method at quasi-static excitation frequencies. Quasi-static excitation conditions imply that in absence of eddy currents the macroscopic quantities M and H are uniform over the cross section of the sample, and in other words the experimentally determined quantities $M_{meas}(= M_{avg})$ and $H_{meas}(= H_{surf})$ are representative for the macroscopically uniform M and H of the whole material sample. Notice however that at excitation frequencies for which the effect of eddy currents cannot be neglected, the measured M and H values always have to be

regarded as M_{avg} and H_{surf}, because the eddy currents lead to the attenuation of the magnetic field and magnetization with increasing depth.

3.1.2 Closed magnetic circuit

The field lines of the magnetic induction $\mathbf{B}$ always form closed loops ($\nabla \cdot \mathbf{B} = 0$, in other words $\mathbf{B}$ is solenoidal). The region occupied by these closed $\mathbf{B}$-field lines is called a *magnetic circuit*. Magnetic circuits are typically categorized as 'closed' or 'open', respectively indicating if the flux follows a well-defined path or not: a magnetic circuit is defined as 'closed' if a flux path lies entirely within a magnetic material with high permeability, $\mu_r \gg 1$, whereas the magnetic circuit is categorized as 'open' if the flux, in order to close its path, has to pass partially through a non-magnetic material, such as air.

A general problem when dealing with measurements on magnetic materials is the occurrence of *demagnetizing fields*, which unavoidably arise wherever the magnetization vector is discontinuous ($\nabla \cdot \mathbf{M} \neq 0$). In analogy with electrostatics ($\nabla \cdot \mathbf{D} = \rho$), this discontinuity of $\mathbf{M}$ can be understood as if fictitious magnetic charges are formed, which generate a magnetic field: $\nabla \cdot \mathbf{M} = \rho_m = -\nabla \cdot \mathbf{H}$.

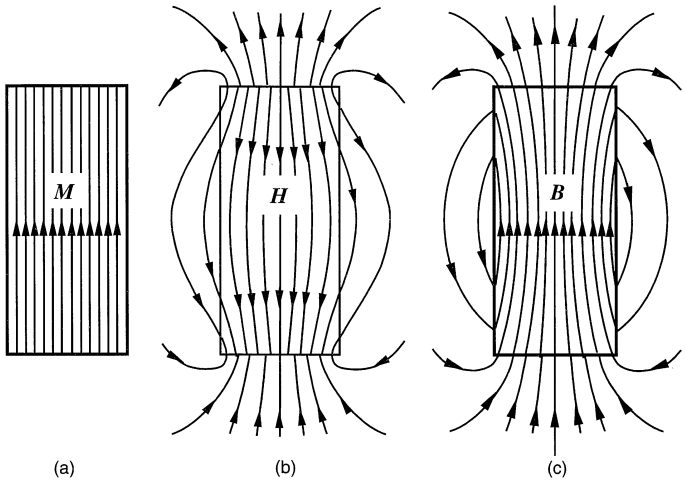

Figure 3.2. Illustration of the demagnetizing field concept in absence of any externally applied field (from [Fiorillo2004]): for reasons of clarity, a cylindrical magnetic sample is considered remanently magnetized along its longitudinal axis, and the remanent magnetization is assumed to be uniform, see (a). In (b) the resulting demagnetizing field is sketched, whereas in (c) the magnetic induction $\mathbf{B} = \mu_0(\mathbf{H} + \mathbf{M})$ is given. Notice that in free space $\mathbf{B} = \mu_0\mathbf{H}$, as indicated by the field lines of $\mathbf{H}$ and $\mathbf{B}$ in free space, see (b) and (c). The $\mathbf{B}$-lines close outside the depicted area of (c).

The concept of demagnetizing fields can be illustrated best in case of open magnetic samples. Let's consider in figure 3.2 a cylindrical sample of ferromagnetic material, that is remanently magnetized along its longitudinal axis, i.e. in absence of any externally applied magnetic field. At the sample ends the magnetization $\mathbf{M}$ is discontinuous, and as a consequence a magnetic field is generated both inside and outside the material. Inside the material this magnetic field counteracts the magnetization, therefore it is called a 'demagnetizing field', $\mathbf{H}_d$. Approximately, the demagnetizing field can be considered to be linearly dependent on magnetization: $H_d = -N_d M$, with N_d the demagnetizing factor, which depends primarily on sample geometry and magnetic permeability [Fiorillo2004].

In general, both the externally applied magnetic field $\mathbf{H}_a$ and the demagnetizing field $\mathbf{H}_d$ contribute to the total or *effective* magnetic field inside the sample, $\mathbf{H}_e = \mathbf{H}_a + \mathbf{H}_d$, and to the magnetic field distribution around the sample. As been said, the demagnetizing factor N_d and by extension the demagnetizing field is strongly dependent on the geometry of the magnetic circuit. Therefore, when conceiving a magnetic measurement circuit, it's important to minimize the role of demagnetizing fields, since they generate macroscopic magnetization inhomogeneities in the investigated samples and give rise to inaccuracies in the determination of the effective magnetic field, see section 3.1.4.

Within this context, it's therefore preferred to perform the field-metric measurements on a sample that is on itself a *magnetically closed circuit*, such as for instance a circumferentially magnetized ring core made from the material under test. This has the advantage that the material can be magnetized without the generation of demagnetizing fields, which simplifies the determination of the effective

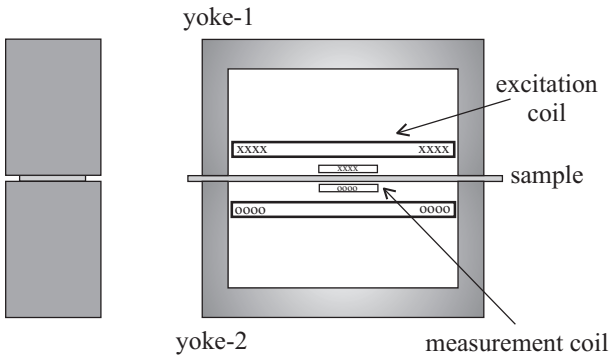

Figure 3.3. Typical configuration of the magnetic measurement circuit in case of straight open samples such as strips or bars: to artificially close the magnetic circuit two U-shaped high-permeability yokes are used. Also the typical configuration of both excitation and measurement coils are shown. The experimental configuration is designed in such a way that both magnetization and magnetic field are as uniform as possible along the longitudinal axis of the sample (over the considered measurement volumes).

magnetic field H of the sample, as we will see later.

It's necessary to underline however that the ferromagnetic samples investigated here always have a straight shape, such as strips, bars and rods. In other words these samples are on itself magnetically 'open' circuits. Moreover, in practice these shapes and their dimensions are unchangeable due to additional practical considerations, such as for instance the incorporation of the ferromagnetic sample and the surrounding magnetic circuit in a mechanical testing apparatus (see section 3.3). Therefore, since it's not possible to construct closed circuits from the material under test itself, the best practice is to close the magnetic flux path 'artificially' by adding two symmetrical closing yokes made of high-permeability material, placed above and under the sample under test. In figure 3.3, this typical configuration of the magnetic circuit for straight samples is drawn schematically.

To illustrate the closed magnetic circuit configuration for straight samples of figure 3.3, magnetostatic finite element (FE) computations are carried out for the following four configurations:

(1) excitation coil only (no sample, no yokes),
(2) excitation coil and sample (no yokes): *'open magnetic circuit'*,
(3) excitation coil and closing yokes (no sample),
(4) excitation coil, closing yokes and sample: *'closed magnetic circuit'*.

In other words, the first three situations consider only parts of the complete configuration, (4). In the FE computations, for all four configurations the same dimensions of the considered parts are used, as shown in figure 3.4. The sample length is 100 mm, whereas the interior length between the yoke pole pieces, l_m, is 40 mm. Sample diameter is 2 mm. The relative permeabilities of sample and yoke are respectively 1000 and 5000. In figure 3.4 the magnetic field patterns are shown for configurations (3) and (4).

Figure 3.5 gives insight in the spatial dependence of the magnetic field component H_x, parallel to the sample's longitudinal axis $\mathbf{e}_x$, for all four investigated configurations. When comparing situations (1) and (3), one can see in figure 3.5(a) that the addition of closing yokes results in a high degree of uniformity of H_x as a function of x, something which is even more apparent in case of the complete configuration (4), where the longitudinal magnetic field is quasi uniform for the central 90% of the sample in between the yoke pole pieces (-20 mm $< x <$ 20 mm).

For situation (2), representing an 'open' magnetic circuit configuration (coil + sample), the effective magnetic field in the sample is much lower compared to the other configurations, due to the strong demagnetizing field that occurs in case of an open magnetic circuit. The effective magnetic field in the sample can be

estimated as follows: $H_e = H_a + H_d = H_a - N_d M$ and with $M = \chi H_e$, giving:

$$H_e = \frac{H_a}{1 + N_d \chi} \tag{3.1}$$

In our example the magnetic susceptibility is $\chi = \mu_r - 1 = 999$. The demagnetizing factor N_d can be estimated based on the sample geometry and magnetic susceptibility: in our example of a cylindrical sample with a length to diameter ratio of 50, N_d is in between 1.7 10^{-3} (limit for $\chi \to \infty$) and 8 10^{-3} (limit for $\chi \to 0$) [Fiorillo2004]. The applied field in our example can be estimated as the value at ($x = 0$, $z = 0$) for configuration (1), see figure 3.5: $H_a = 943$ A/m. For configuration (2), following (3.1) this results in an estimated effective field H_e between 349 A/m (for $N_d(\chi \to \infty)$) and 105 A/m (for $N_d(\chi \to 0)$). On

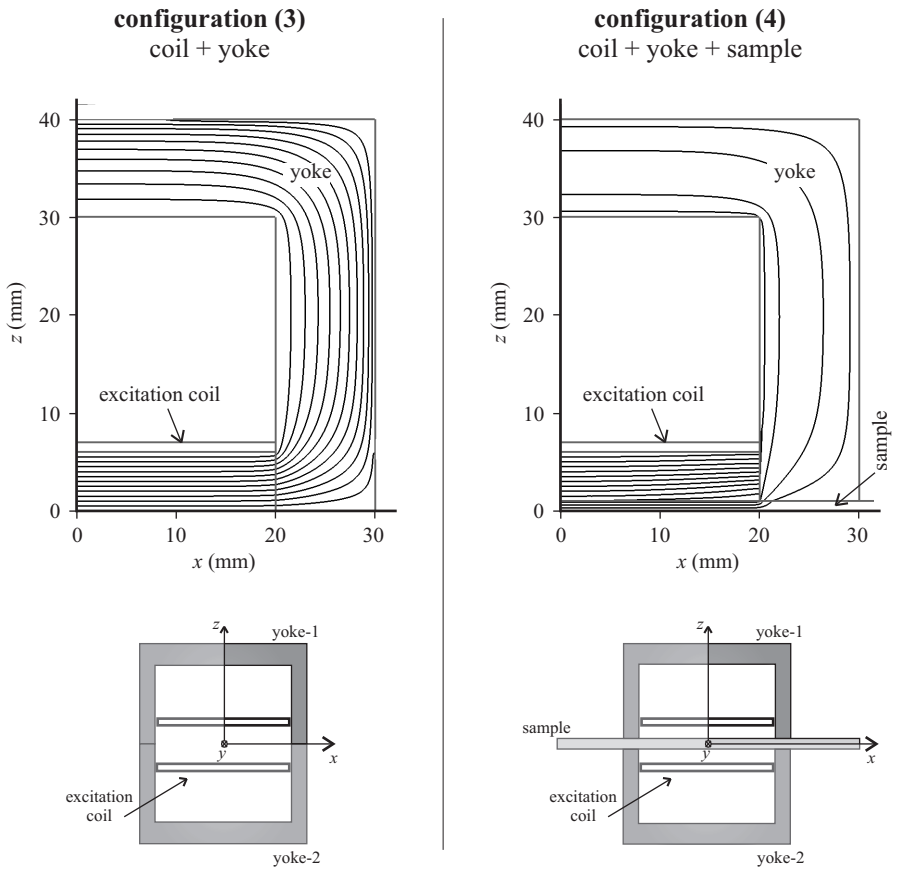

Figure 3.4. Magnetic field patterns numerically calculated for configuration (3): closing yokes and excitation coil; and for configuration (4): closing yokes, excitation coil and sample. Only 1/4 of the geometry is shown, as indicated schematically (not on scale) underneath the field pattern plots.

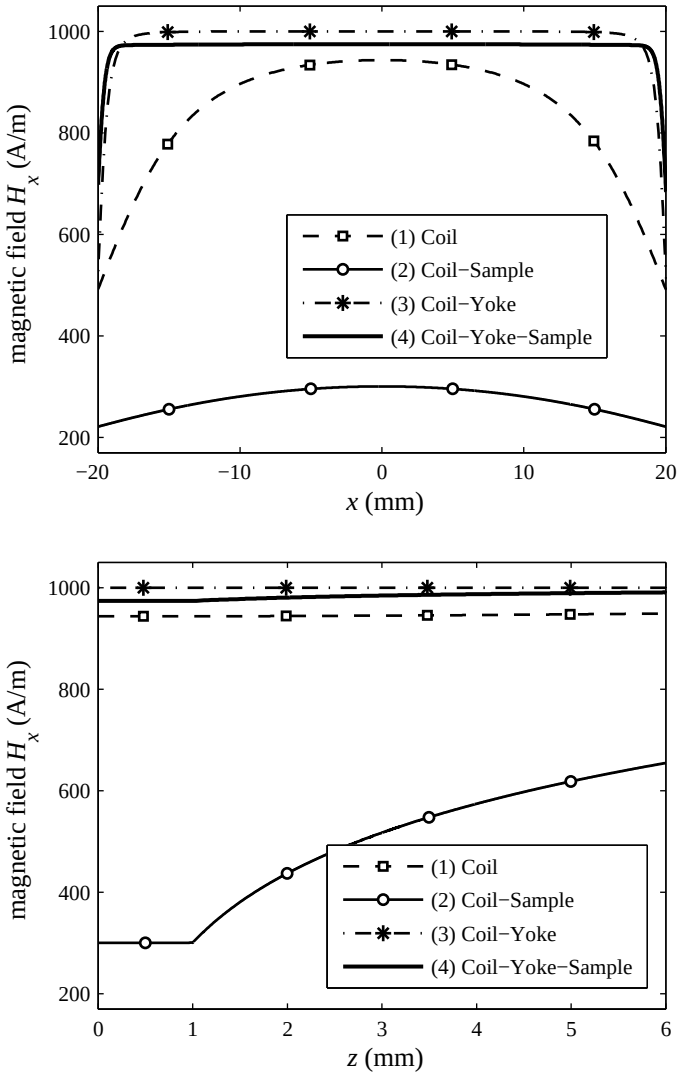

Figure 3.5. Spatial distribution of the magnetic field component H_x, parallel to the sample's longitudinal axis, for all four considered configurations indicated in the legend: (a) $H_x(x)$ at $(z = 0)$, i.e. the sample center line if a sample is present; and (b) $H_x(z)$ at $(x = 0)$. The utilized (x, y, z) coordinate system corresponds to figure 3.4. Remark: for all four computations, the value for $n_e I$ (with n_e the number of turns of the excitation winding and I the applied excitation current) is chosen to be 40 Ampère-turns. With the magnetic path length l_m chosen to be equal to the interior length between the yoke pole pieces, the applied magnetic field can be estimated as $H_a = n_e I / l_m$ = 1000 A/m (see section 3.1.4 for more details related to this remark).

the other hand, as shown in figure 3.5, the FE computation of the open magnetic circuit configuration (2) results in an effective magnetic field value of 300 A/m at the center of the sample ($x = 0$, $z = 0$). Calculating back this corresponds to a demagnetizing factor $N_d = (H_a - H_e)/(\chi H_e)$ = 2.1 10^{-3} (for $\chi = 999$), which is close to the $(\chi \to \infty)$-value.

Concerning $H_x(z)$ in figure 3.5(b), with $z < 1$ representing the sample and $z > 1$ the surrounding air: for the closed magnetic circuit configuration (4), the magnetic field in the surrounding air increases only slightly with distance away from the sample surface, a feature which will be employed further in the direct method for the determination of H, see section 3.1.4.

The double yoke closed magnetic circuit configuration is also the configuration adopted in the existing international standards of the International Electrotechnical Commission (IEC), that apply to the magnetic field-metric measurement on one single straight shaped sample, i.e. by using the single sheet tester for strips and sheets [IEC60404-3], see section 3.2.1, or by using the permeameters for bars and rods [IEC60404-4], see sections 3.2.2–3.2.3. We shall see later that the restricted sample shapes and also their dimensions, that brought us to this type of closed magnetic circuit, also play an important role in the choice for the optimal magnetic field determination method (section 3.1.4).

3.1.3 Determination of the magnetic induction $B(t)$

The determination of the magnetic induction $B(t)$ is based on Lenz-Faraday's law of electromagnetic induction. When a time-dependent magnetic flux $\phi(t)$ is linked with a measuring coil of n_m turns, a voltage $V_{in}(t)$ is induced over this coil, and this voltage is equal to the time-derivative of the coupled magnetic flux:

$$V_{in}(t) = -\frac{\mathrm{d}\psi}{\mathrm{d}t} = -n_m \frac{\mathrm{d}\phi}{\mathrm{d}t}. \tag{3.2}$$

The physical magnetic flux can then be determined by integration of the induced voltage $V_{in}(t)$:

$$\phi(t) = -\frac{1}{n_m} \int_0^t V_{in}(\tau)\mathrm{d}\tau. \tag{3.3}$$

For quasi-static variations of the magnetic flux, as is predominantly the case in the experimental work, the best practice is to perform this integration by an analog electronic integrator. The basic part of this device is an operational amplifier used in the inverting-integrating mode, as shown in figure 3.6. The relation between the input and output signal is as follows:

$$V_{out}(t) = -\frac{1}{RC} \int_0^t V_{in}(\tau)\mathrm{d}\tau. \tag{3.4}$$

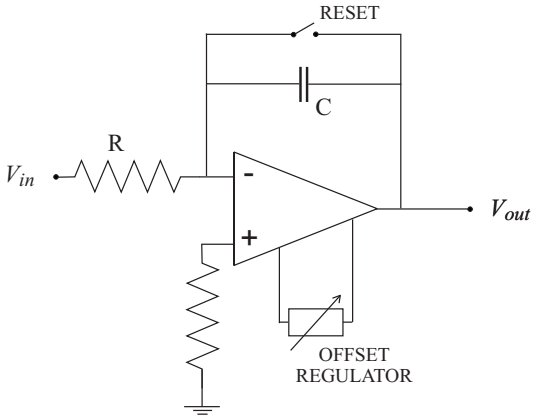

Figure 3.6. Analog electronic integrator (schematic).

In such devices the inevitable DC offset voltage at the input of real-life operational amplifiers should be minimized as much as possible, since this offset input voltage causes the output signal of the integrator to drift. Therefore, to minimize this output drift, a JFET-opamp is used with low input bias current specification and also an offset regulator (potentiometer) is added to the opamp circuit to manually fine tune the input offset voltage as close to zero as possible, whenever this is necessary before starting the actual measurements [DeWulf2002].

When combining the previous formula's (3.3) and (3.4), the output voltage of the analog integrator can also be interpreted as the amplification of the physical magnetic flux with a gain of n_m/RC:

$$V_{out}(t) = \left(\frac{n_m}{RC}\right)\phi(t) \tag{3.5}$$

Typical values for RC are in the range of 1 to 10 ms, and with a typical n_m of about 100 this results in a gain of 10^4 to 10^5.

This inductive method is typically used to measure the magnetic induction $B(t)$ of a ferromagnetic sample, by placing the coil, over which the induced voltage is measured, as close as possible around the sample. The total measured magnetic flux $\phi_{meas}(t)$ inside this measuring coil of cross sectional area S_{coil} consists of two contributions, i.e. ϕ_{mat}, which is the flux inside the ferromagnetic material with cross sectional area S_{mat}, and ϕ_{air}, the flux in the air surrounding the sample but which is still linked with the measurement coil:

$$\begin{aligned}\phi_{meas}(t) &= \phi_{mat}(t) + \phi_{air}(t) \\ &= \oint_{S_{mat}} \mathbf{B}(\mathbf{t}) \cdot \mathrm{d}\mathbf{S} + \oint_{(S_{coil}-S_{mat})} \mu_0 \mathbf{H}(\mathbf{t}) \cdot \mathrm{d}\mathbf{S}.\end{aligned} \tag{3.6}$$

In most practical cases the second term of formula (3.6) can be ignored (in other words $\phi_{meas} \approx \phi_{mat}$), especially when dealing with high-permeability materials and when S_{coil}/S_{mat} is close to 1, which can be practically approached for samples with large cross sections. The magnetic induction of the material, B_{mat}, can in this case be determined with good approximation as:

$$B_{mat}(t) = \frac{1}{S_{mat}} \oint_{S_{mat}} \mathbf{B}(\mathbf{t}) \cdot \mathrm{d}\mathbf{S} \approx \frac{\phi_{meas}(t)}{S_{mat}}. \tag{3.7}$$

In some practical cases, however, the cross section of the ferromagnetic sample, S_{mat}, is too small compared to S_{coil} and especially when measuring at high magnetic field levels, it can be appropriate to compensate for the air flux by performing the following correction with magnetic field :

$$B_{mat}(t) = \frac{\phi_{meas}(t)}{S_{mat}} - \frac{(S_{coil} - S_{mat})}{S_{mat}} \mu_0 H(t), \tag{3.8}$$

assuming that the magnetic field is uniform inside the excitation coil, both in the material and in the surrounding air, an assumption which is reasonably valid for the closed magnetic circuit, see figure 3.5(b), configuration (4). Notice that by using this method, the resulting B_{mat} in formula's (3.7) and (3.8) is actually the average value of the magnetic induction, averaged out over the cross section of the sample. The coil to measure B_{mat} also has a finite length, which implies that the resulting B is actually a volumetric average or in other words a macroscopic bulk property of the material.

Notice that with the same approach also the following correction can be performed in order to obtain the magnetic polarization:

$$J(t) = \mu_0 M(t) = \frac{\phi_{meas}(t)}{S_{mat}} - \frac{S_{coil}}{S_{mat}} \mu_0 H(t). \tag{3.9}$$

The air flux compensation described by formula's (3.8) and (3.9) can be performed afterwards in software, once $\phi_{meas}(t)$ and $H(t)$ are measured simultaneously. Good precision of this air flux compensation in software is reached when the input resolution being used to measure both $\phi_{meas}(t)$ and $H(t)$ is high, which is the case in our setup since these measurements are typically performed by using an acquisition card with 16-bit analog-to-digital conversion of the input signals.

Another way to determine the magnetic polarisation $J = \mu_0 M$, is by adding an *air flux compensator* in hardware [IEC60404-2, IEC60404-3]. In principle, this device is a mutual inductor consisting of two coupled windings in air, that is connected to its corresponding magnetic measurement circuit as shown in figure 3.7 by placing both primary excitation windings in series, and both secondary windings in series opposition. An essential feature of this device is that the compensator windings have to be fine-tuned in such a way that, in absence of the

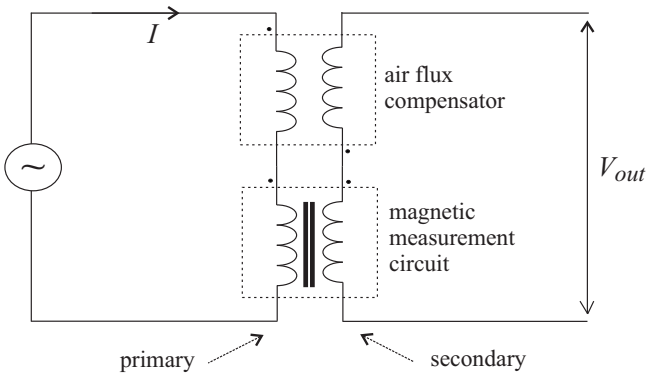

Figure 3.7. Air flux compensation carried out in hardware (schematic).

ferromagnetic sample under test, the induced voltages in both secondary windings (of the compensator and of the magnetic measurement circuit) cancel each other out, resulting in $V_{out} \approx 0$ (in practice the compensator is fine-tuned in such a way that V_{out} is less than 0.5% of the voltage induced in the secondary coil of the magnetic circuit alone [IEC60404-2]). If this condition is fulfilled, then V_{out} measured with the ferromagnetic sample inserted in the magnetic measurement circuit is proportional to the time derivative of the magnetic polarisation J. The magnetic polarisation $J(t)$ is then simply found by integrating $V_{out}(t)$.

Before fine-tuning the number of turns of the compensator's windings (typically of the secondary coil), the following equation can be helpful to approximately design the compensator:

$$\left[\frac{n_1 n_2 S}{l}\right]_{\text{measurement circuit}} = \left[\frac{n_1 n_2 S}{l}\right]_{\text{air flux compensator}} \tag{3.10}$$

In this equation n_1 and n_2 are the number of turns of respectively the primary and secondary coils, and S and l are respectively the cross section and the solenoid length of the primary coil.

The most obvious solution seems to be using a second identical but empty magnetic measurement circuit as air flux compensator, but even then it's still necessary to fine-tune the compensator's windings in order to obtain the condition $V_{out} \approx 0$ in absence of the sample in the actual magnetic measurement circuit. Moreover, a good practice is designing the air flux compensator with a smaller cross section than the measurement circuit, in order to allow more (primary and) secondary windings, which in turn increases the accuracy of the fine-tuning.

3.1.4 Determination of the effective magnetic field $H(t)$

When aiming at magnetically characterizing a ferromagnetic sample by determining its constitutive relation, apart from the magnetization also the effective magnetic field of the sample should be determined. However, it's important to realize that it is impossible to actually measure the magnetic field *inside* a solid specimen. Nevertheless, the effective magnetic field can be approximately determined by using one of the following approaches:

1. **indirect method:** under certain specific conditions it can be justified to postulate a constant magnetic path length, and the effective magnetic field is then determined based on Ampère's law, with as experimental input the measured excitation current;
2. **direct method:** alternatively, and especially when the conditions under (1) are not fulfilled, local measurements of the magnetic field in air in the close vicinity of the sample, can give an indication of the effective magnetic field, by linear extrapolation of this data towards the sample surface.

Both approaches will be treated in more detail in the following paragraphs. As been said before, both methods intrinsically result in the magnetic field at the surface of the sample. Since during this research we mainly deal with quasi-static excitation conditions, resulting in uniform magnetic fields over the cross section of the sample, the determined value for H is indicative for the uniform effective magnetic field in the material.

General description

The magnetic field $\mathbf{H}$ is generated by the current I in an excitation coil with n_e turns. The general expression for the magnetic field $\mathbf{H}$ in a closed magnetic circuit of length l is given by Ampère's law:

$$\oint_l \mathbf{H} \cdot \mathrm{d}\mathbf{l} = n_e I. \tag{3.11}$$

Dealing with the determination of the effective magnetic field existing in a straight ferromagnetic sample under test, it is important however to carefully consider the possible influences of all additional parts of the closed magnetic circuit, apart from the ferromagnetic sample itself. As been said before, the magnetic circuit is typically closed by placing two additional closing yokes above and underneath the sample. Moreover, let's consider in figure 3.8 the most general (and also worst case) scenario where the contacts between sample and yokes are not mechanically perfect, in other words there exist some tiny (parasitic) and non-controllable air

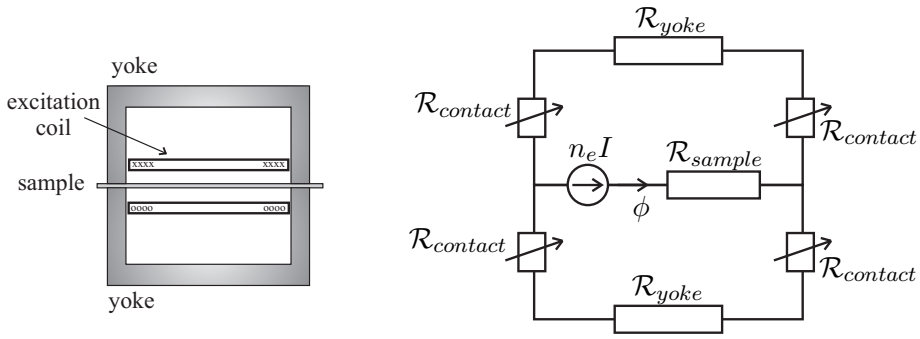

(a) (b)

Figure 3.8. Magnetic network model of the experimental configuration consisting of the sample under test, flux-closing yokes and parasitic air gaps, representing the imperfect contacts between sample and yokes. The sample-yoke contacts are represented by variable reluctances to illustrate the non-controllable character of the parasitic air gap length.

gaps between the sample and the two closing yokes. The magnetic circuit is not perfectly closed in that case, resulting in the generation of demagnetizing fields.

To consider the influence of the closing yokes and also the parasitic air gaps, a useful alternative approach is to describe the magnetic network in terms of reluctances: the reluctance of a part of the magnetic circuit is defined as $\mathcal{R} = l/\mu S$, with μ, l and S respectively the permeability, the length and the cross section of the flux-carrying part. The resulting expression corresponding to the magnetic circuit of figure 3.8 is:

$$(\mathcal{R}_{sample} + \mathcal{R}_{yoke}/2 + \mathcal{R}_{contact})\phi = \mathcal{R}_{total}\phi = n_eI. \tag{3.12}$$

Let's consider two illustrative examples to estimate the relative contribution of each of the three components to the total reluctance. In both examples the relative permeabilities of sample and yoke are $\mu_{r,sample} = 1000$ and $\mu_{r,yoke} = 5000$; the flux-path lengths of the sample and one yoke are l_{sample} = 40 mm and l_{yoke} = 100 mm.

- Example 1: Assume perfect sample-yoke contacts, and $S_{yoke}/S_{sample} = 10$. This situation results in $\mathcal{R}_{sample}$ equal to 97.6% of $\mathcal{R}_{total}$ whereas $\mathcal{R}_{yoke}/2$ is the remainder 2.4% of $\mathcal{R}_{total}$.

- Example 2: Assume imperfect contacts resulting in four parasitic air gaps of 10 μm each, and $S_{yoke} = S_{sample}$. In this case the reluctances $\mathcal{R}_{contact}$ and $\mathcal{R}_{yoke}/2$ are equal to each other and contribute each for 1/6 to $\mathcal{R}_{total}$, so $\mathcal{R}_{sample}$ is in this situation only 4/6 of $\mathcal{R}_{total}$.

Roughly speaking, with the conditions of the first example the indirect H-method can be applied, whereas for the conditions of the second example the direct H-method should be used.

Indirect method: based on measured excitation current

In some cases, especially for samples in the shape of strips or sheets with small thickness compared to their width and length, and with very smooth surfaces, it can be justified to neglect the influence of both the closing yokes and the imperfect contacts between sample and yokes. In more detail, these conditions are the following:

1. the cross section of the sample S_{sample} is much smaller than the active flux-carrying cross section of a closing yoke S_{yoke} (as a rule-of-thumb: $S_{yoke}/S_{sample} \geq 10$);
2. the permeability of closing yoke is as high as possible, and preferably μ_{yoke} is higher than the permeability of the sample; these first two conditions minimize the reluctance $\mathcal{R}_{yoke}$;
3. both the samples and the pole faces of the closing yokes are carefully grinded and polished in order to achieve optimal contacts between sample and yokes; this minimizes the reluctance $\mathcal{R}_{contact}$.

Under these conditions, the reluctances $\mathcal{R}_{yoke}/2$ and $\mathcal{R}_{contact}$ can be neglected compared to the reluctance of the sample:

$$H\ l_m = \mathcal{R}_{sample}\ \phi \approx n_e\ I. \tag{3.13}$$

In other words, under these conditions it's justified to determine the effective magnetic field H as follows:

$$H = \frac{n_e}{l_m} I. \tag{3.14}$$

Once the magnetic path length l_m of the sample is postulated, the magnetic field is determined as directly proportional to the measured excitation current I. The postulated magnetic path length l_m is typically chosen to be equal to the inner width between the closing yoke legs, as is also the adopted solution 'by convention' in the international standard dealing with the single sheet tester [IEC60404-3]. The single sheet tester is treated in more detail in section 3.2.1. In fact, the postulation of a constant magnetic path length is a simplification, since the magnetic path length depends on the magnetic induction and the excitation frequency [DeWulf2002].

Nevertheless, this indirect method has the advantage to result in good reproducibility, which is important when standardizing measurements for industrial comparison between different laboratories. However, notice that if this method of postulating a magnetic path length is erroneously used in case of imperfect contacts resulting in non-negligible air gaps between sample and yokes, this has strong and detrimental impact on the repeatability of the measurement.

Direct method: based on local magnetic field measurements

This method is based on the fact that across an interface between two different materials (such as between air and a ferromagnetic material) the tangential component of the magnetic field, H_t, is continuous: $H_{t,air} = H_{t,mat}$. On the other hand, the (unknown) macroscopic effective magnetic field at the sample surface of (nearly) isotropic ferromagnetic material is known to be parallel to the excitation coil axis. Therefore, if one is able to measure the magnetic field in air, exactly at the sample surface and parallel to the excitation coil axis, then the effective magnetic field at the surface of the sample can be determined. Moreover, for quasi-static excitation frequencies (which is predominantly the case in this study), the effective magnetic field inside the sample is quasi-uniform over the cross section of the sample (in other words no significant skin effect occurs), and therefore the determined effective magnetic field at the surface of the sample, $H_{t,mat}$, is actually a measure for the uniform effective magnetic field H inside the sample.

For the local measurement of the magnetic field in air, there exist several alternatives, e.g. transverse Hall sensors, giant magneto-resistance (GMR) sensors, H-coils. These local H-sensors can be calibrated in a known and spatially independent magnetic field, for instance generated by Helmholtz coils [Fiorillo2004]. H-coils are probes based on exactly the same inductive principles as the method to measure B (see section 3.1.3), but now the coils are placed in free space, resulting in induced voltages proportional to the time-derivative of $\mu_0 H$.

However, due to the finite dimensions of the H-sensors, the magnetic field in air cannot be measured exactly at the surface. To overcome this, several local H-measurements in the surrounding air can be performed at different distances close to the surface, and $H_{t,air}$ is then estimated by linear extrapolation towards the sample surface [Nakata1987, Perevertov2005, Stupakov2006]. This approach is justified by the observation that in a small region close to the sample surface, the magnetic field increases weakly and more or less in a linear fashion with distance away from the sample surface, as is illustrated by the following numerical results.

Magnetostatic finite element computations are carried out for two configurations: the first configuration (a) is a closed magnetic circuit with perfect contacts between sample and yokes, whereas configuration (b) is the same magnetic circuit

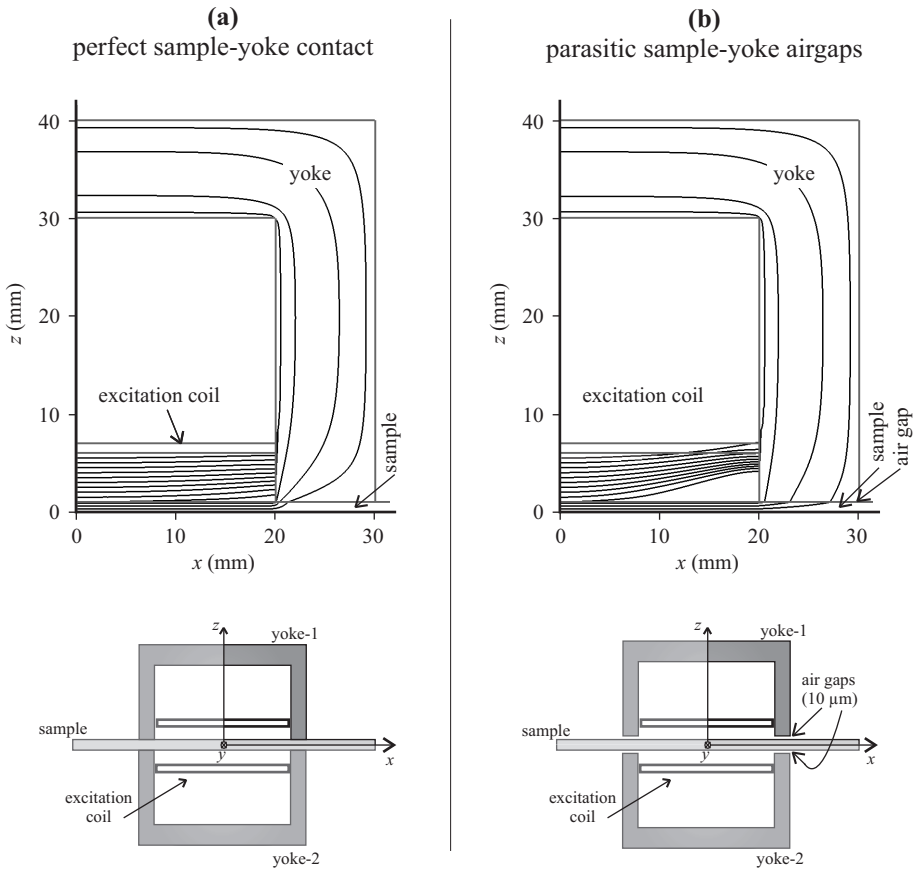

Figure 3.9. Magnetic field patterns, numerically calculated for two configurations: (a) closed magnetic circuit, with perfect contact between sample and yokes; (b) closed magnetic circuit, with parasitic air gaps of 10^{-5} m between sample and yokes. Only 1/4 of the geometry is shown, as indicated schematically (not on scale) underneath the field pattern plots. The interior length between the yoke pole pieces, l_m, is 40 mm. The relative permeabilities of sample and yoke are respectively 1000 and 5000.

but now with parasitic air gaps of 10 μm between sample and yokes[1]. In figure 3.9 the magnetic field patterns are shown for both configurations, indicating the considerable demagnetizing effect of the air gaps. Since the direct method to determine H will be applied to samples with rectangular or circular cross sections, respectively two-dimensional and axisymmetric numerical simulations are performed (for the latter the axisymmetry axis is along the x-direction).

Figure 3.10 and figure 3.11 show the spatial dependence of the magnetic field

[1]Actually, configuration (a) is identical to situation (4) of the numerical study of the closed magnetic circuit (see pp. 94–97).

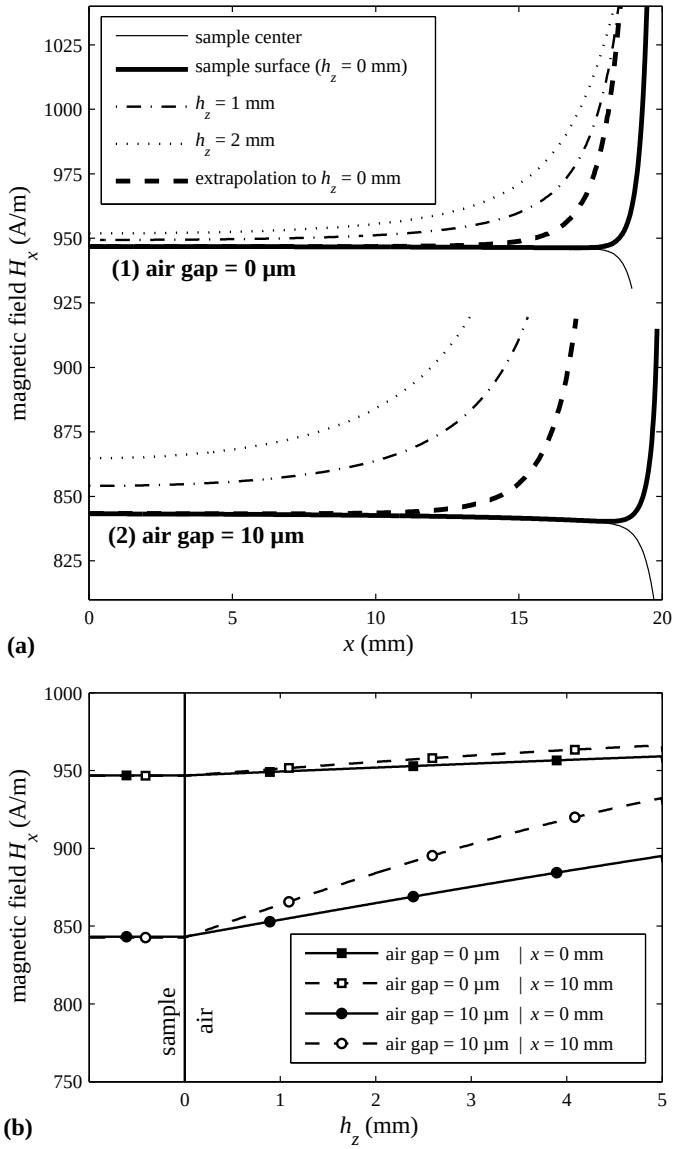

Figure 3.10. Numerical results of the two-dimensional FE computations. Spatial distribution of the magnetic field component H_x, parallel to the sample's longitudinal axis, for two configurations of the closed magnetic circuit: (1) perfect sample-yoke contact (air gap = 0 μm); and (2) imperfect sample-yoke contact (air gap = 10 μm). (a) $H_x(x)$ as a function of x, at the sample center, at distances h_z above the sample surface, and as a result of the linear extrapolation towards h_z = 0, for both air gap conditions. (b) H_x as a function of z at $(x = 0)$ mm and 10 mm, for both air gap conditions.

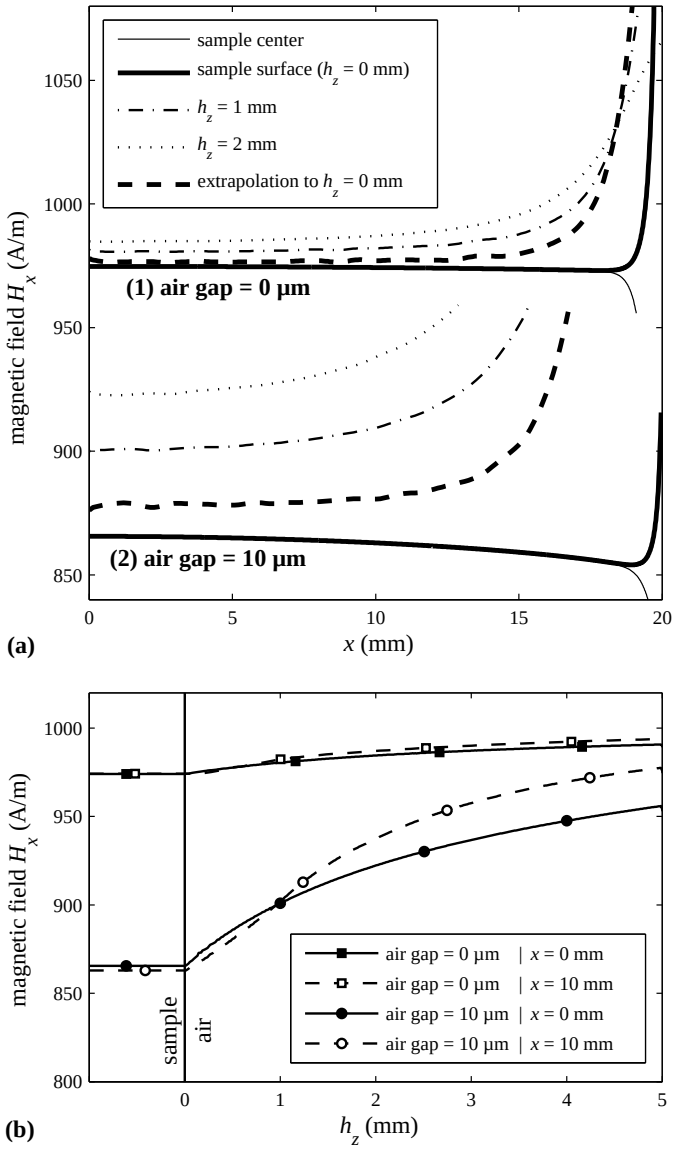

Figure 3.11. Numerical results of the axisymmetric FE simulation. Spatial distribution of the magnetic field component H_x, parallel to the sample's longitudinal axis, for two configurations of the closed magnetic circuit: (1) perfect sample-yoke contact (air gap = 0 μm); and (2) imperfect sample-yoke contact (air gap = 10 μm). (a) $H_x(x)$ as a function of x, at the sample center, at distances h_z above the sample surface, and as a result of the linear extrapolation towards h_z = 0, for both air gap conditions. (b) H_x as a function of z at $(x = 0)$ mm and 10 mm, for both air gap conditions.

component H_x, respectively for the two-dimensional and the axisymmetric case. For all computations the value for $n_e I_e$ (with n_e number of excitation windings and I_e excitation current) is chosen to be 40 Ampère-turns. Hence, the indirect method to determine H_x always results in $H_x = n_e I_e / l_m$ = 1000 A/m, for both air gap configurations and for both axisymmetric and two-dimensional cases. When compared to the magnetic field at the sample surface in both figures 3.10 and 3.11, it is seen that the indirect method results for all investigated cases in an overestimation due to the not considered influence of the reluctance if the yoke reluctance and - if applicable - of the imperfect contacts.

Concerning the direct method: the two-dimensional computation results in an almost linear increase of the magnetic field H_x with distance h_z above the sample surface (see figure 3.10), hence the linear extrapolation provides an accurate determination of the magnetic field at the sample surface, in case of situation 1 (without air gap) for -15 mm $< x <$ 15 mm (central 75% of l_m), and in case of situation 2 (with air gap) for -12 mm $< x <$ 12 mm (central 60% of l_m). In the axisymmetric case however, the assumption of linear dependence of $H_x(z)$ is less accurate, but still reasonably valid. The linear extrapolation at the central 50% of l_m, based on the H_x-values at h_z = 1 mm and 2 mm, leads to a slight overestimation, for situation 1 (no air gap) with 0.4%, and for situation 2 (air gap = 10 μm) with 2%, which is however a large improvement compared the overestimation when using the indirect method, respectively with 2.5% and 15%.

It is clear that this direct method to determine the effective magnetic field (by local H measurements and extrapolation towards the surface) is in fact a more general method which can be deployed in all circumstances, but typically this method is only used when the necessary conditions to utilize the indirect method (determining the magnetic field as proportional to the excitation current by postulating a magnetic path length) are not fulfilled. This is when the influences of the closing yokes and/or the imperfect contacts are too large to be neglected. The underlying reason is that the measurement of the excitation current (indirect method) is in practice a much more simple task than the variety of operations that has to be performed when using the direct (Hall sensor array) method. These operations can lead to additional measurement errors, such as for instance during the positioning of the H-sensors and the amplification of the output signals. Moreover, this direct method is based on the assumption of a linear behaviour of magnetic field with distance above the sample surface, an assumption which can introduce an additional systematic error to the magnetic field determination. Therefore all extra efforts of this direct method are only valuable in situations where the indirect method introduces too large systematic errors.

In sections 3.2.2 and 3.2.3 two examples are given of measurement setups based on the direct determination of the magnetic field, respectively for samples with square (or rectangular) cross section, and for samples with circular cross section.

3.2 Specific measurement setups based on the field-metric method

In this section several measurement setups based on the field-metric principles are discussed. As been said before, one of the practical constraints of the performed experimental research is the fact that the samples being investigated in the different research topics have different and unchangeable sample shapes and dimensions, such as strips and bars with rectangular or circular cross section. Moreover, the constrained dimensions of the samples under investigation are in general much smaller[2] than the dimensions specified in standardized magnetic measurement equipment for electrical steels, such as Epstein frame [IEC60404-2] or single sheet tester [IEC60404-3]. It is important to realize that no universal field-metric magnetic measurement setup exists, able to characterize all kinds of sample shapes and dimensions, and also that the modification and miniaturization of the magnetic measurement methods and setups to suit the small-sized samples under investigation, have to be performed carefully and in a well-considered manner.

So, in order to experimentally determine the constitutive relation $B(H)$ or equivalently $M(H)$, we have to cope with these different sample shapes and dimensions. In other words, the sample is the starting point around which the whole measurement setup is designed. The most obvious modifications concern of course the core elements of the measurement setup, i.e. excitation coil, measurement coil and the construction of the closed magnetic circuit, which dimensions have to be modified in such a way to suit the samples. Moreover, the appropriate method to determine the effective magnetic field has to be chosen carefully based on the considerations discussed above in section 3.1.4, which predominantly depend on the considered sample shapes and dimensions. For instance, for samples with large thickness compared to the thickness of the closing yokes, it can be necessary to determine the effective magnetic field based on local measurements of the magnetic field in the surrounding air (direct method).

In general when conceiving and developing a certain measurement setup, three considerations are important: accuracy, repeatability and reproducibility.

- The term *accuracy* is defined as the degree of conformity of a measured quantity to its actual 'true' value. Here, the determination of the 'true' or intrinsic constitutive relation $M(H)$ of the material itself is practically impossible, in the first place due to the approximative nature of the determination of the effective magnetic field H: both methods outlined in section 3.1.4

[2] The smallest samples that are successfully characterized in this research work (see sections 5.1.1 and 5.1.2) are 1.3 mm by 1.3 mm by 27 mm, whereas the standardized sample width is 30 mm or 300–500 mm (respectively for Epstein frame and single sheet tester), the standardized sample length is 300–500 mm, and the thickness is typically 0.3 mm to 1 mm.

introduce systematic deviations. Moreover, since the determination of the effective magnetic field and the homogeneity of the magnetization also depend on the geometrical features of the samples and the properties of the surrounding magnetic circuit, the developed setups have to be regarded as technical solutions to the magnetic measurement problem. These setups result, rather than in the intrinsic magnetic characterization of the material itself, in the magnetic characterization of the whole 'component', consisting not only of the sample, but also of the closed magnetic circuit.

- The term *repeatability* is defined as the degree of agreement between independent results obtained with the same method, on an identical sample, and under the same conditions (same operator, laboratory and apparatus). For all the constructed measurement setups the repeatability is checked, and a high level of repeatability is reached. This is important for the investigations in the following chapters because, regardless the accuracy problems, a good repeatability justifies the use of each setup to relatively compare the magnetic measurement results on samples of a certain sample set (with the same sample shape and same dimensions) in order to evaluate the variations of a certain (mechanical or microstructural) parameter.
- The term *reproducibility* is defined as the degree of agreement between independent results obtained with the same method on identical test material, but now under different conditions (different operator, laboratory and apparatus). In order to obtain good reproducibility, our approach is always to construct experimental setups as close as possible within the framework of the international standards that exist in the field of the magnetic characterization of a single sheet or strip by means of a single sheet tester [IEC60404-3], or the characterization of bars or rods by using an appropriate permeameter [IEC60404-4]. In the frame a Round Robin test organized by the Universal Network for Magnetic Non-destructive Evaluation [UNMNDE], see pg. 180, our laboratory EELAB have had the opportunity to compare our developed miniaturized magnetic setups with the setups designed by other laboratories around the world, especially the setup for Charpy-shaped samples, which will be described further in section 3.2.2. A fair reproducibility is observed with laboratories which also decided to utilize a direct method to determine the magnetic field.

3.2.1 (Miniature) Single Sheet Tester (SST)

The single sheet tester (SST) is a standardized experimental setup intended to magnetically characterize electrical steel sheets, i.e. samples with small thickness, but considerable width and length (500 mm). In principle, the specific configuration of the SST core elements (excitation coil, measurement coils and closing yokes) don't differ much from the general configuration shown in figure 3.3, see also section 3.1.2. Figure 3.12 shows schematically how the SST is incorporated

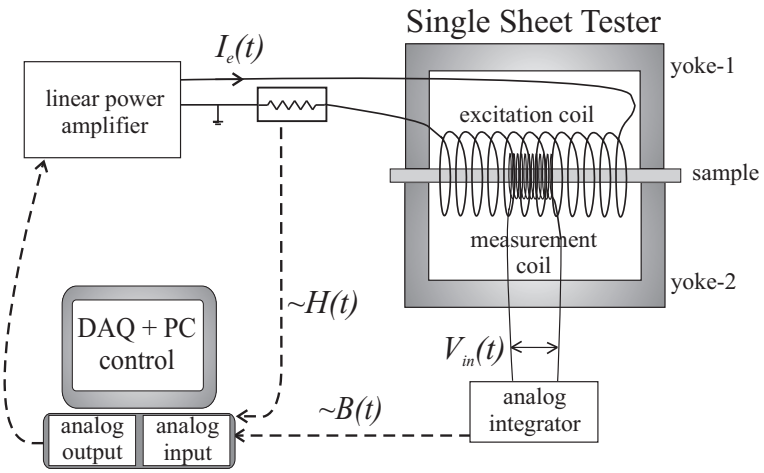

Figure 3.12. Schematic overview of the complete experimental setup in case of a single sheet tester as permeameter.

in the complete experimental setup. For reasons of reproducibility, one of the main features in the international measurement standard [IEC60404-3] is that the magnetic field H is determined as proportional to the measured excitation current I_e : $H = (n_e/l_m)I_e$, with n_e the number of turns of the excitation winding (indirect method, see section 3.1.4). In the international measurement standard the magnetic path length l_m is postulated by convention as the interior length between the yoke legs. However, from the discussion in section 3.1.4 it is clear that this method to determine H introduces a systematic error, and in order to minimize this systematic error a number of conditions should be fulfilled (as outlined in section 3.1.4, indirect method). In the measurement standard [IEC60404-3], a number of precautions are therefore taken into account in order to both minimize the systematic error and maximize the repeatability of the magnetic characterization by SST measurements. These precautions deal with dimensions of samples, closing yokes and coils, choice of the closing yoke material, careful consideration of the yoke-sample contacts,...

However, in our experimental investigations on mechanically degraded materials, the sample dimensions were usually constrained to much smaller dimensions than the standardized sheet dimensions (300 to 500 mm wide and 500 mm long). These limited sample dimensions compared to the standardized ones will force us to modification and miniaturization of the standardized concepts: in the case of small strip shaped samples (e.g. samples with a thickness of 1 mm, a length of circa 30 mm, and a width of 10 mm, to give an idea about the order of magnitude), the dimensions of the closing yokes and the coils can be modified to enclose the small strip samples. Moreover, this design can be performed in such a way to still

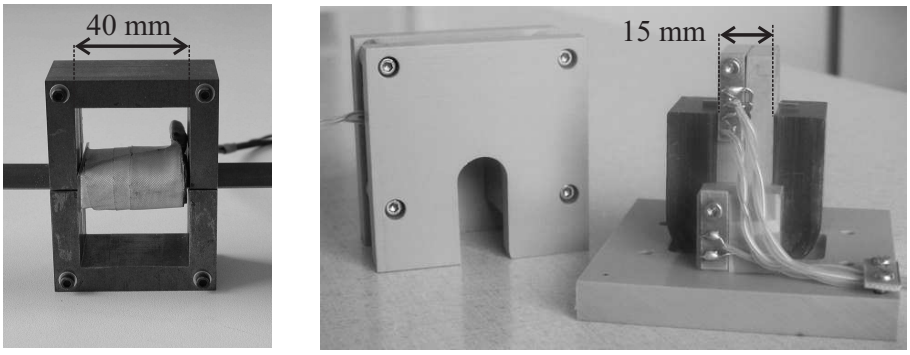

Figure 3.13. (a) Miniature SST for strip samples with as dimensions $l \geq 60$ mm; $b \leq 25$ mm; $d \leq 2$ mm. The closing yokes are made from U-shaped FeSi laminations of 0.5 mm thickness; the laminations are stacked parallel to the sample width. (b) Miniature SST for strip samples with as dimensions $l \geq 27$ mm; $b \leq 10$ mm; $d \leq 1.5$ mm. The closing yokes are made from nanocrystalline soft magnetic material (Finemet); the laminations are stacked parallel to the sample length. This setup is designed to perform magnetic measurements on samples manufactured from broken (irradiated) Charpy specimen, see section 5.1.

meet the conditions that are necessary to justify the indirect determination of the magnetic field as proportional to the excitation current. Basically this means that it is necessary to minimize the reluctance of the closing yokes, by maximizing its cross section and by choosing a high-permeability material for manufacturing the yokes, e.g. high-quality Fe-Si electrical steel ($\mu_r \approx 5 \cdot 10^3$) or nanocrystalline magnetic material ($\mu_r \approx 50 \cdot 10^3$), and to also minimize the reluctance of the contacts between sample and yokes, by carefully grinding the pole faces of the yokes and if necessary polishing the surface of the sample.

In other words, even for small strip samples it is possible to design a 'miniature' SST configuration, inspired by and as close as possible to the standardized SST, resulting in *reasonable accuracy* (i.e. reasonable systematic errors) and *good repeatability* for the magnetic characterization of small strip samples [DeWulf2003]. Similar to the standard SST, the arbitrary magnetic path length of the miniature SSTs is chosen as the interior length between the closing yoke legs, as can be seen in figure 3.13 which depicts two typical miniature SSTs that are constructed in the framework of this research.

3.2.2 Setup for samples with square cross section (Charpy type)

This particular experimental setup is designed in order to perform magnetic measurements on the typical (not broken) samples being used in Charpy impact tests.

The Charpy impact test is a standardized mechanical destructive test to experimentally determine fracture toughness, by measuring the energy that is required to break a material under high strain rate (impact) loading: prior to fracture, ductile materials absorb a high amount of energy, compared to brittle materials which tend to absorb only a very small amount of energy. When carrying out Charpy tests on a set of similar samples but at different temperatures, the transition of brittle behaviour at low temperatures, to the ductile behaviour at high temperatures, typical for b.c.c. metals like iron-based alloys and steels, can be studied. More details and experimental results of Charpy impact tests can be found in section 5.1 and section 5.2.

The dimensions and the shape of Charpy samples are standardized: the specimens are 55 mm long bars with a square cross section of 10 mm by 10 mm, and with a V-shaped notch of 2 mm deep introduced in the middle of one of the long sample sides, see figure 3.14. For samples with such dimensions its magnetic characterization is not straight-forward. Because the Charpy samples are short, miniature closing yokes have to be used. Here closing yokes are chosen with an inner width of 40 mm between the yoke legs. Moreover, since the cross section of the specimens is large, and of comparable size to the cross section of suitable closing yokes, the reluctance of the closing yokes cannot be neglected and therefore the appropriate method to determine the effective magnetic field is based on the *local measurement* of the tangential field followed by extrapolation towards the sample surface (direct method, as introduced in section 3.1.4).

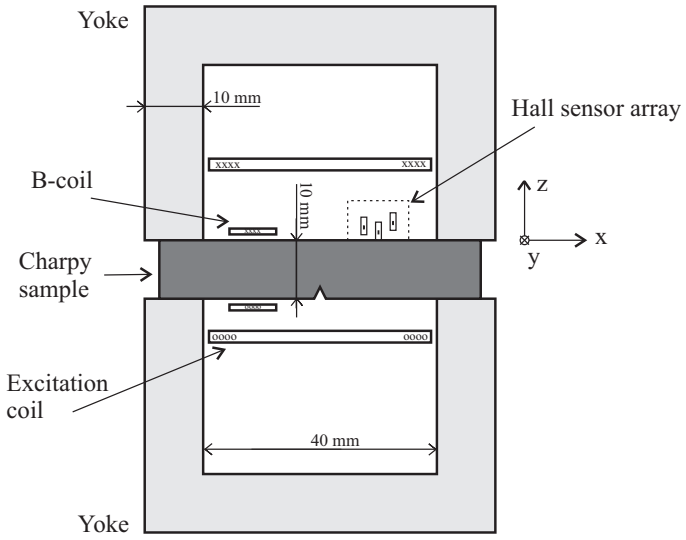

Figure 3.14. Design of the permeameter to magnetically characterize Charpy-type samples.

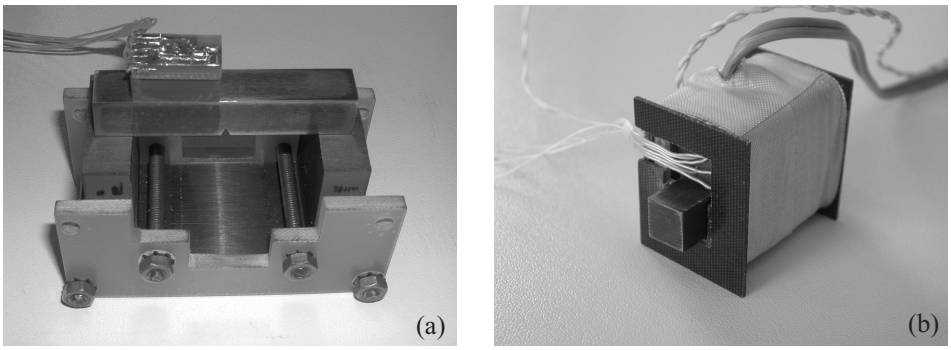

Figure 3.15. Pictures of some parts of the Charpy-sample permeameter: (a) the Hall sensor array is positioned on top of a Charpy sample, with the three Hall sensors mounted in a small PVC block (here only one of the two closing yokes is shown), (b) both sample and Hall sensor array are put into the coil pair holder, which comprises the excitation and measurement coil.

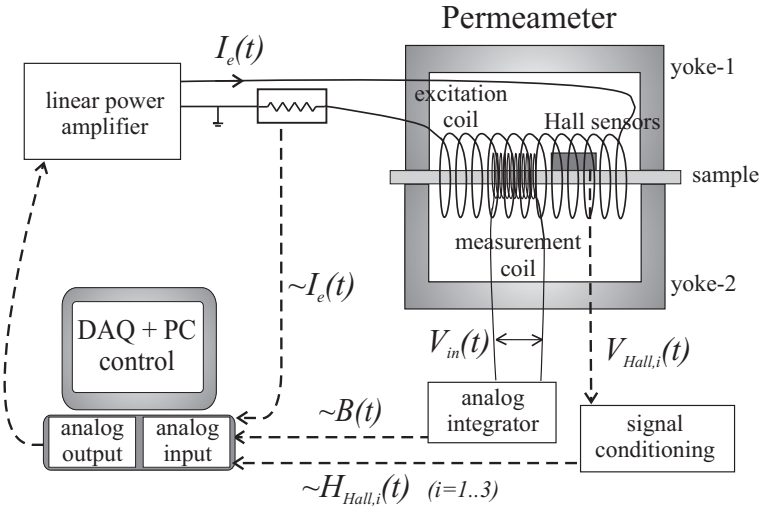

Figure 3.16. Schematic overview of the complete experimental setup in case of the permeameter with Hall sensor array.

In figure 3.14 the modified permeameter to perform magnetic measurements on Charpy-type samples is shown schematically. The sample is positioned between two flux-closing yokes, and around the sample both the excitation coil and the B-measurement coil are placed. Both coils are designed in such a way to have the necessary space available to also integrate the Hall sensor array consisting of three transverse Hall sensors. The pictures in figure 3.15 show in more detail how these different parts of the permeameter are constructed, such as the Hall sensor array and the modified coils. A general overview is given of all necessary

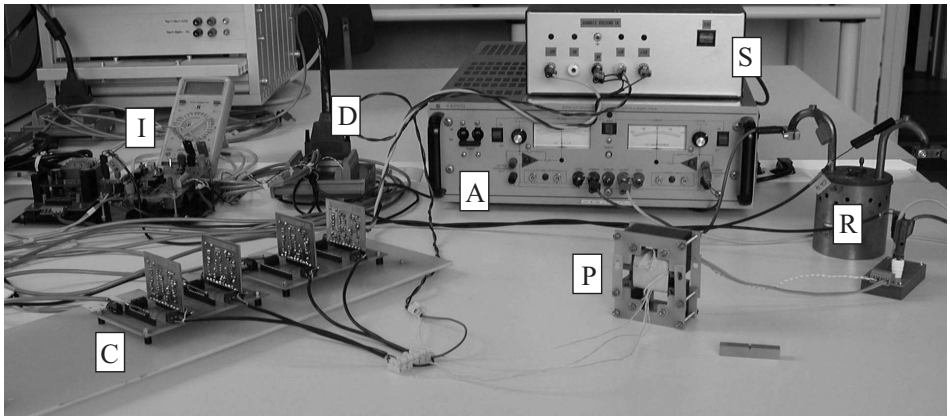

Figure 3.17. General overview of all hardware components in case of the measurement setup for Charpy-type samples. Core element is the permeameter (P), already shown schematically in more detail in figure 3.14. The Kepco linear power amplifier (A) supplies the excitation current, which is measured by the 4-point method using a high precision current sense resistor (R) . The analog integrator (I) is connected to the B-measurement coil and integrates the induced voltage. The Hall sensors are powered by a dc-voltage supply (S). The output signals of the Hall sensors are pre-amplified by a signal conditioning module (C), consisting of two stages (instrumentation amplifier + inverting amplifier). The DAQ-connector (D) provides the input signal for the linear power amplifier and also transmits all measured signals to the data-acquisition system incorporated in a PC, on which the measurement software is running.

hardware components for this particular method, schematically in figure 3.16 and by a picture in figure 3.17.

The Hall sensors have a sensitivity of $40\mathrm{mV}/(\mathrm{kA}/\mathrm{m})$, and the overall dimensions of one Hall sensor component in x, y and z directions as indicated in figure 3.14 are respectively d_x = 1.6 mm, d_y = 4 mm and d_z = 3 mm (the active Hall element is only a small fraction of that). The three Hall sensors are placed in such a way to measure the magnetic field component in the x-direction above the sample surface, H_x, when the notched sample side is facing down. With these three Hall sensors, the magnetic field component H_x in the vicinity of the sample is measured, for three discrete vertical positions z above the sample surface. Therefore the active Hall elements are carefully positioned at a distance z, as close as possible above the sample surface, respectively at $z = 1.25$ mm; 2.10 mm and 2.85 mm (+/- 0.05 mm); at the center of the sample in the y-direction; and at a distance x away from the sample center ($x = 0$), respectively at $x = 10$ mm; 7 mm and 13 mm.

Concerning the positioning in the z-direction: $z = 1.25$ mm is the closest possible location, due to the finite dimensions of the Hall sensor housing. Concerning the positioning in the x-direction: during preliminary experiments it was seen that the

influence of the notch at the lower sample side is also sensed on the upper sample side if the Hall sensor is too close to the sample center, and moreover, close to the closing yoke legs the magnetic field distribution also becomes inhomogeneous, see for instance figure 3.10. Taking together both considerations, only the region 5 mm $\leq x \leq$ 15 mm is appropriate for the local magnetic field measurement.

In order to determine the effective magnetic field at the sample surface, an approximately linear behaviour of the tangential magnetic field dependence on the vertical distance z away from the sample is a necessary condition to enable linear extrapolation of the signals of the three Hall sensors towards the sample surface. With the particular configuration of the excitation coil comprising both the sample and the Hall-sensors that is used here, see figure 3.14, the assumption that H_x is increasing in a linear fashion as a function of distance z above the sample surface was preliminary checked experimentally by placing one Hall sensor at different z locations. At least in the close vicinity of the sample where the Hall sensors are actually placed, this linear behaviour is reasonably valid. Figure 3.18 gives an idea of the individual Hall sensor measurements and the resulting effective magnetic field values obtained by extrapolation, whereas in figure 3.19 the quasi-linear increase of H_x with position z is illustrated.

In this context of the Charpy-type samples it is interesting to compare both methods for the determination of the effective magnetic field H, as introduced earlier in section 3.1.4. Therefore, in figure 3.20 the magnetic field determined by both methods is evaluated as a function of the excitation current I_e. At the beginning of this section we concluded that, since the conditions to determine the magnetic field as proportional to the excitation current (indirect method) are not fulfilled (because of the particular dimensions of the standardized Charpy specimen), it is highly preferable to determine the magnetic field by extrapolation of the locally measured H (direct method). As expected, a considerable discrepancy is therefore detected when comparing the more accurately determined effective magnetic field $H_{extrapol}$ (direct method) with the calculated H_{excit} (indirect method). In figure 3.20 the two following features are apparent: (a) $H_{extrapol}$ is considerably lower than H_{excit} due to the non-negligible reluctance of the closing yokes causing a considerable magnetomotive force drop in the closing yokes (this is especially noticeable at high absolute excitation currents); and (b) the relation between $H_{extrapol}$ and I_e shows hysteretic behaviour (this is especially noticeable at excitation currents close to zero). The effective magnetic field $H_{extrapol}$ actually lags behind the excitation current: $H_{extrapol}$ changes sign after I_e does.

Remember that the method of extrapolating local magnetic field measurements was introduced to more accurately determine the effective magnetic field in cases where not only the influence of the closing yokes is non-negligible, but also in cases where imperfect contacts exist between sample and yokes. This was checked experimentally by introducing extra air gaps of 0.05 mm on each of the four contacts between sample and yoke legs. As can be seen in figure 3.21, in the

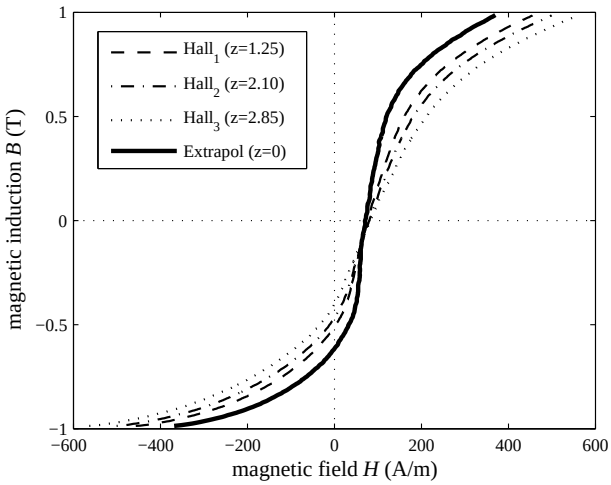

Figure 3.18. The effective magnetic field obtained by extrapolation towards the surface $(z = 0)$ is depicted here with a full line, as a function of magnetic induction $B(t)$ corresponding to one particular magnetization loop. For reasons of clarity, only the ascending branch is depicted. Also plotted here, again as a function of $B(t)$, are the three tangential magnetic field signals, $H_{Hall,i}(t)$ $(i = 1 \ldots 3)$, simultaneously measured with Hall sensors at three different positions z (mm) above the sample surface.

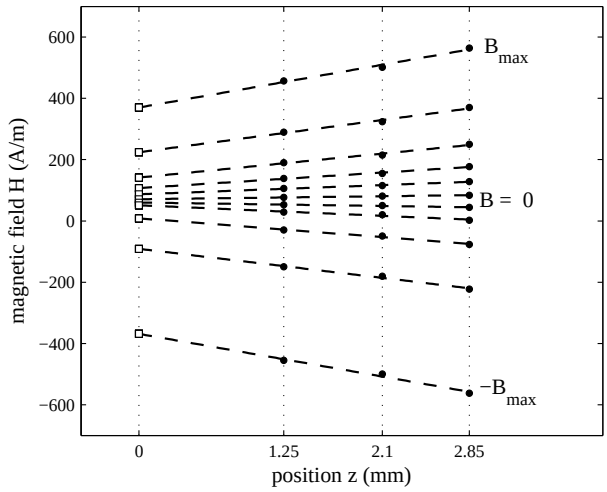

Figure 3.19. Alternative view of the same data as in figure 3.18. Here, the measured magnetic field signals $H_{Hall,i}(t)$ $(i = 1 \ldots 3)$ are given as function of position z above the sample surface, at equal values of the magnetic induction B (black dots). For reasons of clarity, only the data for a reduced number of B values is depicted. The linear extrapolation of this data towards $z = 0$ is also shown graphically, resulting in the effective magnetic field values (white squares) corresponding to the considered B values.

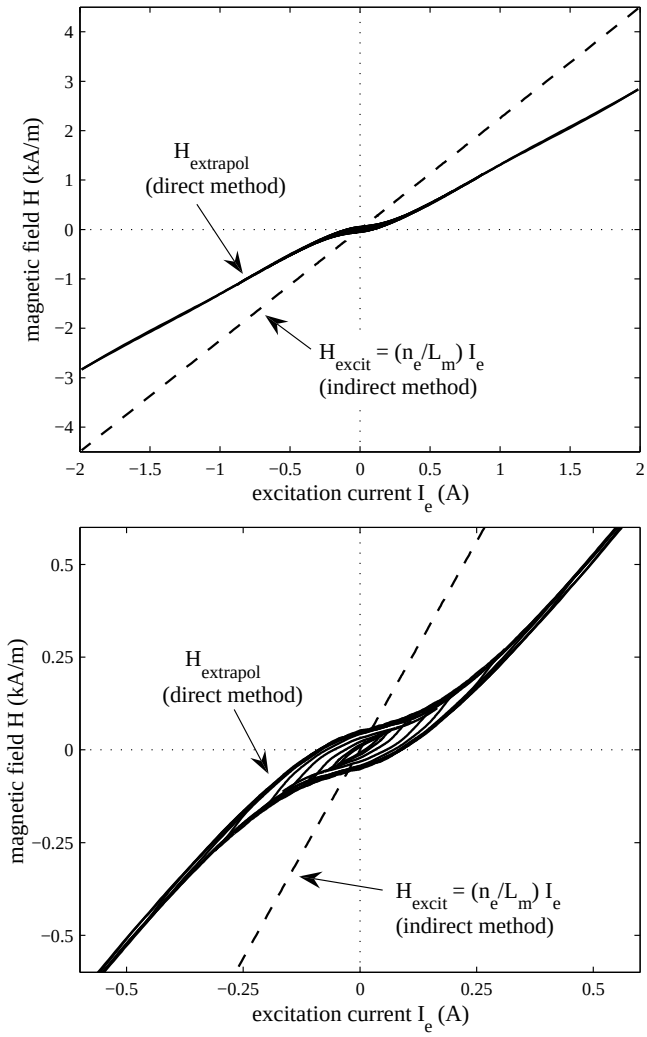

Figure 3.20. (a) Magnetic field determined by both direct and indirect methods, as a function of the excitation current, during the measurement of a number of magnetization loops on a Charpy-type sample. (b) Same data as (a), but zoomed in at the origin, to show in more detail the hysteretic relation between $H_{extrapol}$ and I_e. The different minor loops $(I_e, H_{extrapol})$ seen here correspond to different measured minor magnetization loops $(H_{extrapol}, B)$.

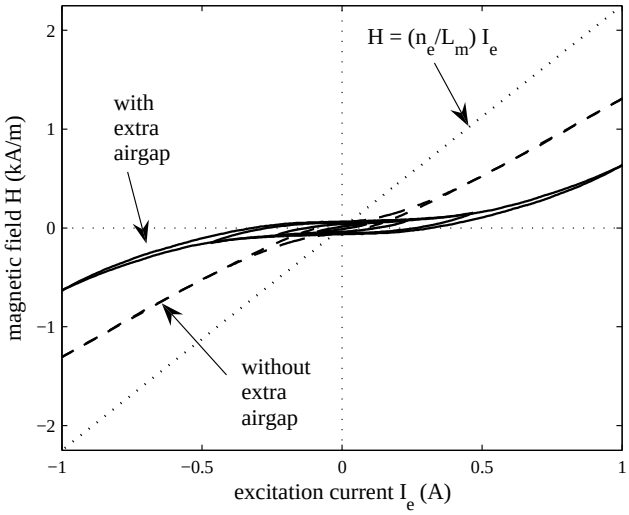

Figure 3.21. Relation between excitation current and effective magnetic field determined by extrapolation of local H measurements, for two situations: with and without the addition of four extra air gaps of 0.05 mm between the sample and the four yoke legs. The curve that is depicting the situation without the extra air gaps is actually identical to the one shown in figure 3.20.

case of extra air gaps much more excitation current is needed to obtain the same effective field as without these extra air gaps. Nevertheless for both situations (with/without air gaps) the magnetic characterization of the Charpy-sample resulted in comparable results, for instance the difference on maximum differential permeability was less than 5%.

3.2.3 Setup for samples with circular cross section

This particular experimental setup is designed in order to perform magnetic measurements on rods with circular cross section. These sample shapes are predominantly used in relation with the magnetomechanical setup (see section 3.3). When aiming at the evaluation of the magnetic and magnetoelastic behaviour at high compressive stresses (both static and cyclic mechanical loading), samples with circular cross section are better suited than strip samples, because the latter have the disadvantage to buckle already at moderate compressive stress levels, which is not the case for samples with circular cross sections at the stress levels considered here. More precisely, the samples utilized in the magnetomechanical setup are hourglass-shaped, machined out of cylindrical rods. The central sample region with smaller cross section which is subjected to the highest stress levels is further investigated and characterized both mechanically and magnetically.

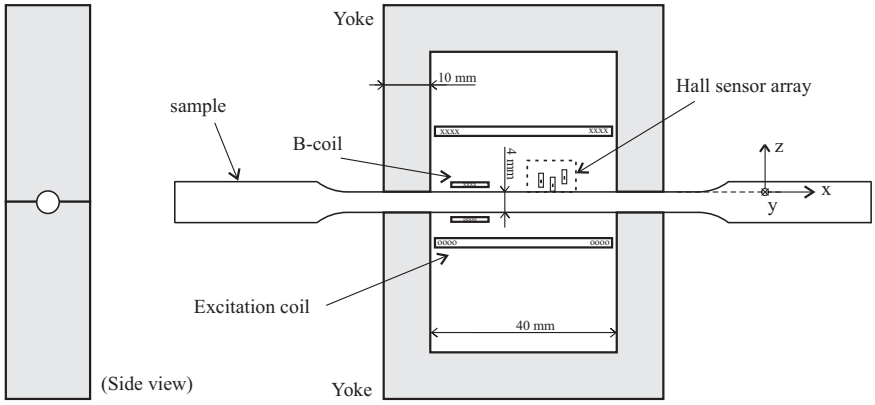

Figure 3.22. Schematic design of the permeameter to magnetically characterize cylindrical samples.

The modified permeameter to perform magnetic measurements on cylindrical samples is shown schematically in figure 3.22. The sample is positioned between two flux-closing yokes, of which the pole pieces are machined in such a way to accommodate the cylindrical specimen and to provide an as close as possible sample-yoke contact. This is realized by machining in each yoke half-circular notches, with the same radius as the samples under investigation, which is also the solution adopted in the magnetic measurement standard [IEC60404-4]. However, it is clear that a good contact with curved surfaces is more difficult to achieve than with flat surfaces in case of strip samples.

Moreover, for the particular permeameter of figure 3.22 the ratio between the cross section of the yoke and the cross section of the sample is about 4, which provides us with an additional reason, besides the contact problem, to prefer the direct method for the magnetic field determination. Its practical realization shows much similarities with the permeameter for samples with square cross sections, introduced in section 3.2.2. In general terms the schematic overview of figure 3.16 is also applicable here: again, a Hall sensor array consisting of transverse Hall sensors is used, and the magnetic field at the surface of the sample is obtained by linear extrapolation. Remember however that the FE computations in section 3.1.4 (direct method, (pp. 104–107) show that in case of cylindrical samples, a linear extrapolation leads to a slight overestimation of the actual magnetic field at the sample surface.

In figure 3.23 the magnetic field determined by direct and indirect methods is evaluated as a function of the excitation current I_e. Compared to the case discussed in section 3.2.2, the difference between both methods is less pronounced here. When comparing the cross-sectional dimensions of sample and yoke for both situations, and noticing that the permeability of the Charpy-samples is much higher

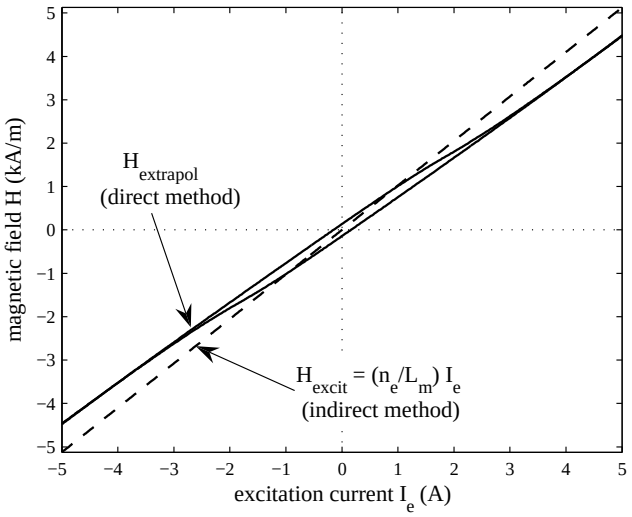

Figure 3.23. Magnetic field determined by both direct and indirect methods, as a function of the excitation current, during the measurement of a major magnetization loop on a cylindrical sample.

than the cylindrical samples under investigation, the effect of the closing yoke reluctances should be qualitatively lower in case of the cylindrical sample permeameter compared to the Charpy-type sample permeameter treated in section 3.2.2. The experimental result of figure 3.23 also indicates that the sample-yoke contacts for the cylindrical samples are of good quality.

3.3 Magnetomechanical setup

Basically, the magnetomechanical setup is the incorporation of one of the magnetic measurement setups described in section 3.2, inside a mechanical testing apparatus. This magnetomechanical setup has the possibility, apart from applying a time-dependent magnetic field to the sample and simultaneously measuring $M(t)$ and $H(t)$, to also apply a time-dependent mechanical stress to the sample, and to measure at the same time both stress $\sigma(t)$ and strain $\varepsilon(t)$.

Such a combined mechanical and magnetic experimental setup allows us to investigate the effects of magnetoelastic coupling, in other words the magnetomechanical behaviour of the material, see section 6.1. In the most general configuration of this magnetomechanical setup, as shown schematically in figure 3.24, both inputs H and σ can be time-dependent.

In this study, this setup is predominantly used to investigate the cases where only

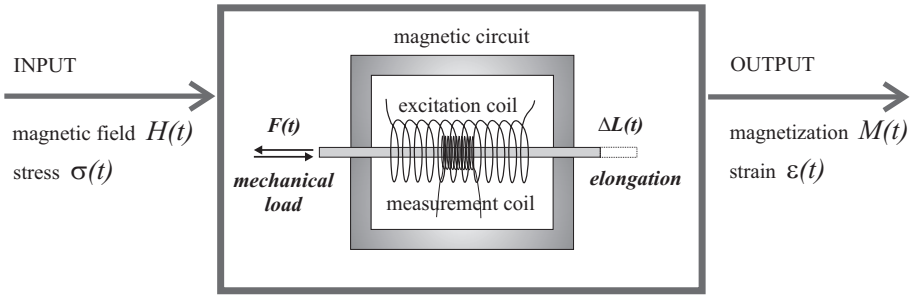

Figure 3.24. Diagram of the magnetomechanical setup as an input-output system, with the applied magnetic field and the applied mechanical stress as inputs, and the resulting magnetization and strain as outputs.

one of these inputs (H or σ) is periodically changing with time, whereas the other input is kept constant.

On the one hand, the magnetic characterization can be performed under static mechanical conditions: $M(H)$ hysteresis loops can be measured under (elastic) static stress σ (tension or compression).

On the other hand, the magnetization variation caused by a time-varying (elastic) stress applied on a sample under constant applied magnetic field can be studied, in other words the measurement of $M(\sigma)$ hysteresis loops can be performed under constant applied magnetic field, during one mechanical loading cycle. As an application, during mechanical fatigue tests the variations in the magnetomechanical behaviour are monitored, see section 6.2.

The mechanical part of this setup is designed at EELAB [Derese2003] in such a way to have the necessary space available to build the magnetic circuit around the sample, see figure 3.25. The mechanical testing apparatus consists of two parts. The first part is the electrical drive and transmission part, including a brushless DC-motor driven by an inverter, a $(92.8 : 1)$ speed reduction, and a screw-like transmission that converts the motor torque into an uniaxial force. The motor is actually a permanent magnet synchronous machine with field orientation, having the advantages of a DC-machine such as a high torque at low speeds (important feature during cyclic mechanical loading tests), but without the disadvantages of abrasive brushes, resulting in longer life expectancy without maintenance (also a very important feature, especially when applying this setup for fatigue testing of ferromagnetic samples).

The second part of the mechanical setup is the part located around the sample. The force applied to the sample and the sample elongation are measured, respectively by a load cell and by a linear quadrature incremental encoder. The resolution of

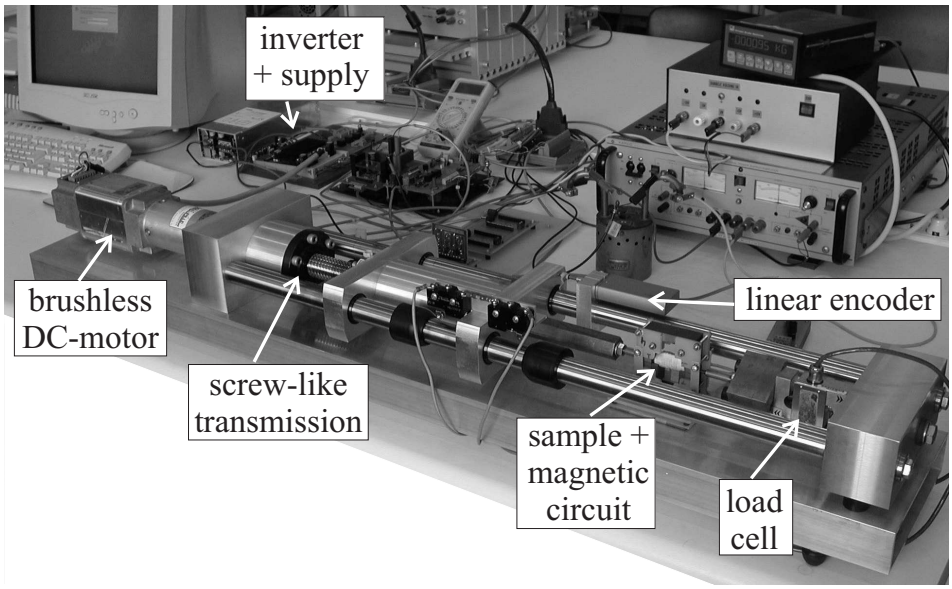

Figure 3.25. Overview of the complete magnetomechanical setup, with special attention to the mechanical part.

the linear encoder is 25 nm and the repeatability is 100 nm. The linear encoder is actually a quadrature encoder which means that it has two output channels making it possible to sense not only position, but also the movement direction.

All components of the apparatus, especially the transmission parts, are designed to allow a maximum uniaxial force of 17 kN. During the mechanical loading, the peak values of the uniaxial force in both movement directions can be controlled to their set points by adjusting the maximum torque setting of the brushless DC-motor, also in both movement directions.

The samples investigated with this setup are typically rectangular strips or cylindrical rods. The magnetic circuits that are used are the miniature SST for the strip samples (section 3.2.1), or the permeameter described in section 3.2.3 for the cylindrical rod samples. Both types of samples are hour-glass shaped: only the central narrower part (length $\approx$ 70 mm) of the sample is characterized both magnetically and mechanically. Due to the maximum uniaxial force of the mechanical apparatus ($F_{max} = 17$ kN), the cross-sectional dimensions of the samples are restricted when aiming at tensile straining the samples up to fracture. For instance, for materials with an ultimate tensile strength of approximately 500 MPa (such as for instance low carbon steels), the dimensions of the sample's central part are typically limited to a cross section of 24 mm^2. Then, the ultimate tensile strength corresponds to 70$\%$ of F_{max} (safety margin).

To assemble the strip or rod samples in the mechanical testing apparatus, different joints or clamps are constructed, as shown in figure 3.26.

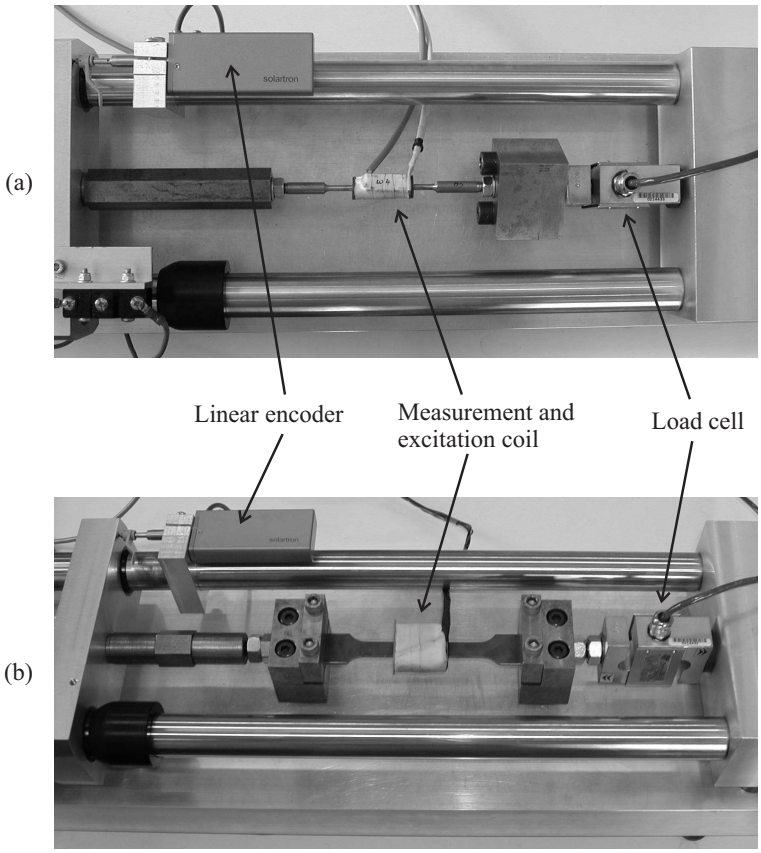

Figure 3.26. Sample-dependent part of the magnetomechanical setup for (a) cylindrical rod samples, and (b) rectangular strip samples. For reasons of clarity, the also sample-dependent flux-closing yokes placed underneath and above the sample are not present in this picture.

3.4 Magnetic drag force method

Consider a ferromagnetic strip being moved longitudinally through the magnetic field existing in the vicinity of one or more permanent magnets, see figure 3.27 to focus on one particular strip-magnet configuration. In this context, the magnetic drag force method is based on measuring the force that resists the longitudinal motion of the strip. This longitudinal force originates from the magnetic hysteretic material behaviour of the ferromagnetic strip: the forward and backward

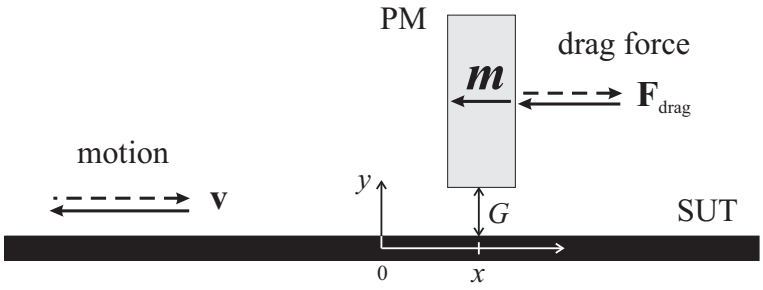

Figure 3.27. Schematic arrangement of the drag force setup: a ferromagnetic sample strip under test (SUT) is being moved along its longitudinal axis underneath a stationary permanent magnet (PM), with the magnetic moment of the PM parallel to the strip's longitudinal axis and also parallel to the movement direction.

movement through the magnetic field generated by the permanent magnet causes the local magnetization to traverse closed[3] magnetization loops, hence the mechanical work done to move the strip forward and backward equals the hysteresis losses of the strip.

In the next paragraphs the magnetic drag force method is treated in more detail. The initial research and development of the magnetic drag force method is carried out in close collaboration with the R&D companies Magnova (Pittsfield, MA, USA) and MagCanica (San Diego, CA, USA) and resulted in a number of joint papers [Garshelis2006, Vandenbossche2007a, Sergeant2008, Garshelis2008].

3.4.1 Drag force principle and experimental setup

A basic configuration for the magnetic drag force method [Garshelis2006] is shown schematically in figure 3.27, whereas the practical realization of the drag force apparatus can be seen in figure 3.28. The ferromagnetic strip under test (SUT) is maintained at a small but fixed distance G (typically in the order of 1 mm) away from a permanent magnet (PM). Both the SUT and the PM are constrained to disallow the mutual attractive force $\mathbf{F}_{attract}$. The Teflon guiding blocks (guides) only allow movement of the strip in its longitudinal direction $\mathbf{e}_x$. On the other hand the permanent magnet is mounted at the bottom end of a pendulum. This pendulum, made of aluminium and hung from instrument bearings, makes contact with a load cell. Therefore the only degree of freedom for the magnet-

[3]The actual closure of the magnetization loops is achieved only if the magnetic state before and after the sample movement is identical. In practice, this is realized by first bringing the sample to an initial magnetic state by moving the sample forward and backward, and then performing the actual drag force measurement during a second forward and backward movement, with identical start and end positions.

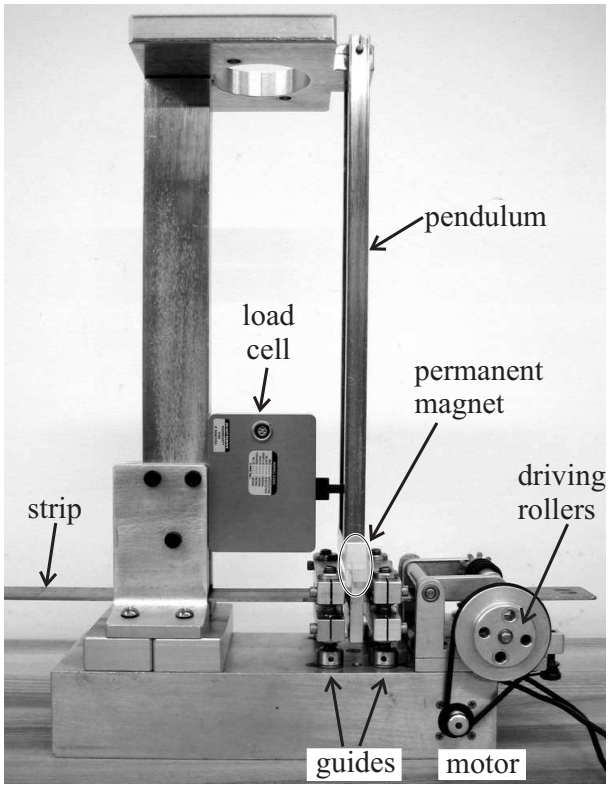

Figure 3.28. Picture of the practical realization of the drag force apparatus, with indication of the typical components. The location of the single permanent magnet inside the magnet holder at the bottom end of the pendulum, is also indicated. Not shown in the picture is the linear encoder to measure the longitudinal position x.

pendulum ensemble is an incremental movement along $\mathbf{e}_x$, necessary to allow the measurement of the force in the $\mathbf{e}_x$ direction.

The combination of the motor and the driving rollers make it possible to move the SUT back and forth along its longitudinal direction $\mathbf{e}_x$, at a constant velocity $\mathbf{v} = v\mathbf{e}_x$ slow enough to avoid the influence of eddy currents (v is typically 4 mm/s). The motion of the SUT, through the magnetic field existing in the vicinity of the permanent magnet,is resisted by a force $\mathbf{F}_{drag}$ originating from the magnetic hysteretic behaviour of the specimen. Since the SUT is typically a long strip with small thickness which is in motion, the measurement of $\mathbf{F}_{drag}$ is more conveniently made by its reaction on the PM, which is therefore supported in such manner as to both rigidly resist $\mathbf{F}_{attract}$ and provide for the measurement of $\mathbf{F}_{drag}$ by making contact with a load cell. The load cell can only detect force in one direction. Therefore the pendulum is biased to bear slightly against the load cell in the absence of any drag force, in such a way to ensure that the magnet-pendulum

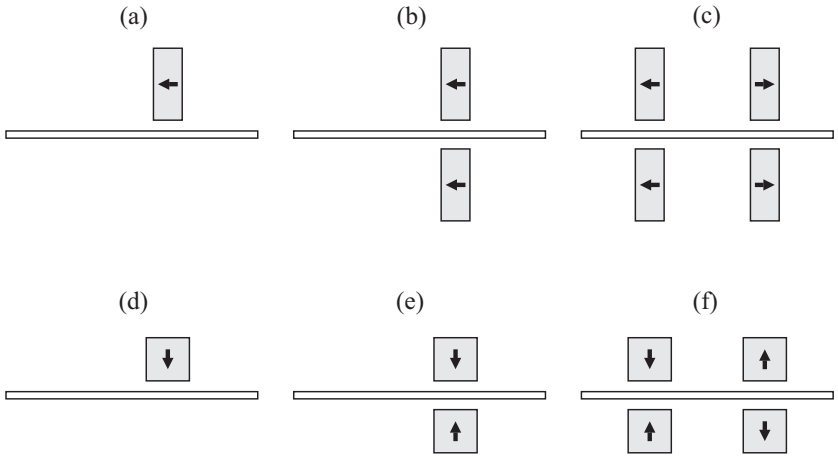

Figure 3.29. Schematical overview (not on scale) of some possible sample-magnet configurations, with one, two or four permanent magnets having magnetic moment orientations parallel (a-c) or normal (d-f) to the longitudinal axis of the strip.

ensemble always exerts a force in one direction on the load cell, this is: for all drag force values in either movement direction. The force on the SUT is a repulsive force acting to resist the motion of the sample, whereas the reaction on the PM is in the opposite direction, tending to drag the PM along in the direction of the motion, hence its appropriate appellation 'drag force'.

In the particular case of figure 3.27 only one PM is used and its magnetic moment $\mathbf{m}$ is directed parallel to the longitudinal axis of the strip ($\mathbf{m} = m\mathbf{e}_x$). Also other configurations are possible, for instance with multiple magnets (over and under the strip) and with magnets having moment orientations both parallel to and normal to the direction of motion, see figure 3.29 for some examples of possible configurations. Here in this work we will focus further on the particular configuration shown in figure 3.27 (situation (a) of figure 3.29). The permanent magnet being used is a 38 MGO NdFeB magnet, with a magnetic moment $m = 1.92\mathrm{Am}^2$. Other typical specifications of the magnet are the energy product $(BH)_{max} = 38$ MGO (MegaGaussOersted) $\approx$ 300 kJ/m^3, the remanent induction $B_r \approx 1.2$ T, and the coercive field $H_c \approx 800$ kA/m. The dimensions of the permanent magnet are 3.17 mm in the longitudinal direction of the strip [x], 12.7 mm in the vertical direction [y] and 50.8 mm in the direction of the strip width [z]. The investigated ferromagnetic strip samples are at least 280 mm long [x], between 0.13 mm and 1.6 mm thick [y], and always 25 mm wide [z]. Since the magnet width is twice the sample width, the magnetic field can be considered uniform across the sample width [z].

In the following, x denotes the magnet position with respect to the strip center, see figure 3.27. Before the actual drag force measurement, the sample is first moved

forward and then backward underneath the magnet in order to bring the sample to an initial magnetic state at $x = x_1$. The ferromagnetic strip sample is driven by a motor to move with a constant but slow speed $\mathbf{v}$. During the actual drag force measurement, the sample is moved forward from $x(t_1) = x_1$ to $x(t_2) = x_2$ (trajectory A), and then backward from x_2 to $x(t_3) = x_1$ (trajectory B). At t_3 the magnetic state is equal to the initial one at t_1, in other words, the traversed magnetization loops are closed. Therefore the mechanical work done to move the strip from x_1 to x_2 and back to x_1 equals the hysteresis losses of the strip. On the one hand the mechanical work can be written as:

$$W_{mech} = \int_{t_1}^{t_3} \mathbf{F}_{drag}(t) \cdot \mathbf{v}(t)\, \mathrm{d}t = \int_{x_1}^{x_2} [\mathbf{F}_{drag,A}(x) - \mathbf{F}_{drag,B}(x)] \cdot \mathbf{e}_x\, \mathrm{d}x. \tag{3.15}$$

On the other hand the hysteresis losses in this particular situation are given by:

$$W_{hyst} = \int_V \left(\oint_{loop} \mathbf{H} \cdot \mathrm{d}\mathbf{B} \right) \mathrm{d}V \quad = \int_V \left(\int_{t1}^{t3} \mathbf{H} \cdot \frac{\mathrm{d}\mathbf{B}}{\mathrm{d}t} \mathrm{d}t \right) \mathrm{d}V, \tag{3.16}$$

with V the volume of the strip. Finally, after defining the *drag force difference* as:

$$\Delta F_{drag}(x) = [\mathbf{F}_{drag,A}(x) - \mathbf{F}_{drag,B}(x)] \cdot \mathbf{e}_x, \tag{3.17}$$

the energy balance corresponding to the above-mentioned drag force experiment is as follows:

$$\begin{aligned} W_{mech} &= W_{hyst} \\ \int_{x_1}^{x_2} \Delta F_{drag}(x)\, \mathrm{d}x &= \int_V \left(\int_{t1}^{t3} \mathbf{H} \cdot \frac{\mathrm{d}\mathbf{B}}{\mathrm{d}t} \mathrm{d}t \right) \mathrm{d}V. \end{aligned} \tag{3.18}$$

The permanent magnet hangs on the bottom end of a pendulum in such a way that, in absence of movement and associated drag force, the magnet bears slightly against the load cell, giving rise to a force offset, $\mathbf{F}_{offset}$. During the forward and backward movement of the sample, the measured force obtained by the load cell is $\mathbf{F}_{meas}(t) = \mathbf{F}_{offset} + \mathbf{F}_{drag}(t)$. Hence, the drag force difference $\Delta F_{drag}(x)$, a main variable of the drag force method, can be experimentally determined as the difference between the measured forces at identical x positions, $\Delta F_{meas}(x)$, without the necessity to know $\mathbf{F}_{offset}$.

Additionally a linear encoder is used to measure the longitudinal position x of the sample relative to the permanent magnet (the linear encoder is however not shown in the picture of figure 3.28). The linear encoder makes it possible to evaluate the measured force F_{meas} and the drag force difference ΔF_{drag} as a function of position x.

3.4.2 Typical experimental results

A typical drag force measurement result obtained on a low-carbon steel sample is depicted in figure 3.30(a). The measured force F_{meas} is plotted against longitudinal position x during the sample movement in both directions. When comparing, at equal positions x, the measured force corresponding to both movement directions, some typical qualitative features become apparent, common features that are manifested as fine-scale variations exhibiting local minima and maxima in the

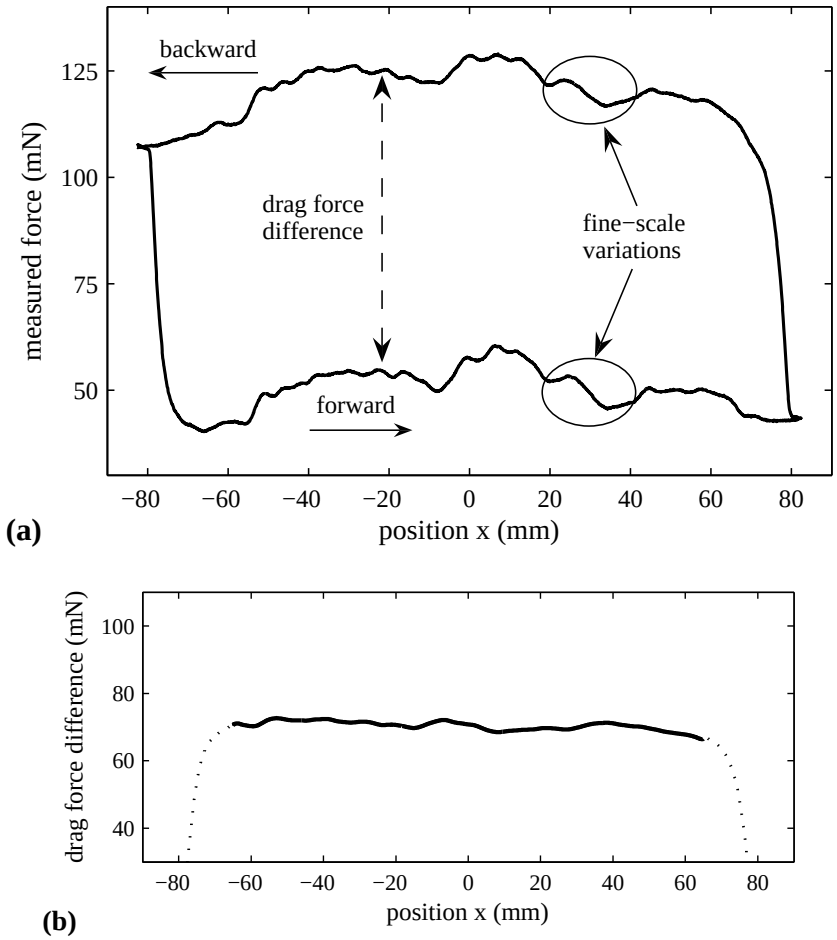

Figure 3.30. Experimental results of the drag force measurement obtained on a low-carbon steel sample (grade AISI C1018) of 1.6 mm thickness: (a) measured force for both movement directions, as a function of magnet position x relative to the sample center, (b) drag force difference ΔF_{drag} as a function of position x (solid line), after making abstraction of the end effects related to the change in direction (dotted lines).

measured force data. Remarkably, these fine-scale variations are closely identical for both movement directions, and moreover their measurement is also repeatable, providing an effective 'signature' unique to each investigated strip. The origin of these fine-scale features present in the force signature is a topic for further investigation; one hypothesis is that the fine-scale variations are assumed to be related to local microstructural imperfections.

Another feature visible in figure 3.30(a) is the vertical displacement between the measured force plots for both movement directions. This vertical displacement is in fact the graphical representation of the drag force difference $\Delta F_{drag}(x)$, as defined by (3.17). Notice that this variable is an intermediate quantity in the energy balance as shown in formula (3.18). In spite of the typical fine-scale features in the drag force 'signature' (figure 3.30(a)), the drag force difference shown in figure 3.30(b) is more or less constant, illustrating the homogeneous properties of the sample.

3.4.3 Which hysteresis loops?

The drag force originates from the magnetic hysteresis behaviour of the ferromagnetic sample under test: when a sample with magnetic hysteretic properties is involved, the magnetization M as a function of magnet position x is asymmetric relative to the magnet center, which arises from the hysteretic $M(H)$ relation of the sample material, resulting in a longitudinal force acting on the sample. In the theoretical case when the sample exhibits no magnetic hysteresis, the magnetization distribution is symmetric, resulting in no net drag force difference. In this context, the question remains which particular hysteresis loops are actually traversed during the forward and backward movement.

The treatment of this question by numerical modelling of the phenomena provides more in-depth understanding about the drag force method. It's evident that the numerical calculation depends on the particular magnet configuration. The geometry used in the following numerical drag force calculation is again the typical single magnet configuration of figure 3.27, with the magnetic moment of the permanent magnet parallel to the longitudinal axis of the sample. The drag force profile is calculated by a numerical time-stepping model [Sergeant2008]: at every time step in the calculation, the magnet is slightly moved over a fixed sample[4]. This numerical model is based on two-dimensional (x, y) magnetostatic finite element computations, including the magnetic hysteretic material behaviour using the Preisach model (this hysteresis model is treated in more detail in section 4.2).

The classical finite element (FE) problem [Silvester1990] is formulated in terms of the vector potential $\mathbf{A}$, defined as follows: $\mathbf{B} = \nabla \times \mathbf{A}$. As there are no current

[4]Remember that in the actual experiment the sample is moved relative to a fixed magnet.

sources in the problem ($\mathbf{j}_c = 0$), the equations to be solved are:

$$\nabla \times \left((\overline{\mu})^{-1} \nabla \times \mathbf{A} \right) = \mathbf{0}, \quad \text{or:} \quad \nabla \times (\nabla \times \mathbf{A}) = \mu_0 \, (\nabla \times \mathbf{M}). \tag{3.19}$$

However, in a problem with hysteresis it is not possible to solve the vector potential FE problem using the permeability tensor defined as $\overline{\mu} = \mathbf{B}/\mathbf{H}$, because this permeability may become negative, zero or infinite, which can lead to numerical instabilities. To overcome this, the equations are reformulated in such a way that the magnetic hysteretic material behaviour is described through differential permeabilities. Consequently the basic unknown for the FE problem becomes the time derivative of the vector potential $\mathbf{A}$. Following such approach, the equation to be solved in case of the magnet is, with $\mathbf{M}_m$ the magnetization of the magnet:

$$\nabla \times \left(\nabla \times \frac{\partial \mathbf{A}}{\partial t} \right) = \mu_0 \left(\nabla \times \frac{\partial \mathbf{M}_m}{\partial t} \right). \tag{3.20}$$

For the sample, we introduce the differential permeability tensor $\overline{\mu}_d$ which relates the time derivatives of the magnetic induction and the magnetic field vectors $\mathbf{B}$ and $\mathbf{H}$:

$$\frac{\partial \mathbf{B}}{\partial t} = \overline{\mu}_d \frac{\partial \mathbf{H}}{\partial t}. \tag{3.21}$$

In the ferromagnetic sample, the equation is then as follows:

$$\nabla \times \left((\overline{\mu}_d)^{-1} \nabla \times \frac{\partial \mathbf{A}}{\partial t} \right) = \mathbf{0}. \tag{3.22}$$

The differential permeability is function of the position x in the sample, therefore the sample is space-discretized into a number of grid points in which the differential permeability is determined by the classical scalar Preisach hysteresis model, based on the magnetic field history. To handle the 2D-behaviour of $\mathbf{H} = H_x \mathbf{e}_x + H_y \mathbf{e}_y$, the following approximation is considered: because for the configuration of figure 3.27 the field is mainly along the x-axis, the scalar hysteresis model is applied only to H_x, whereas for H_y a single-valued non-linear characteristic (so without hysteresis) is used. The non-diagonal elements of the permeability tensor $\overline{\mu}_d$ are zero.

Once the magnetic induction and magnetic field vectors are calculated at each particular time instant, the force is obtained by using the principle of the Maxwell stresses $\mathbf{T}$:

$$\mathbf{F} = \oint_{S'} \mathbf{T} \mathrm{d}S = \oint_{S'} \left[\mu_0 (\mathbf{n} \cdot \mathbf{H}) \mathbf{H} - \frac{\mu_0}{2} (\mathbf{H} \cdot \mathbf{H}) \mathbf{n} \right] \mathrm{d}S, \tag{3.23}$$

with S' a surface which is closely surrounding the considered ferromagnetic member (here the sample) and which is lying completely in free space just outside the

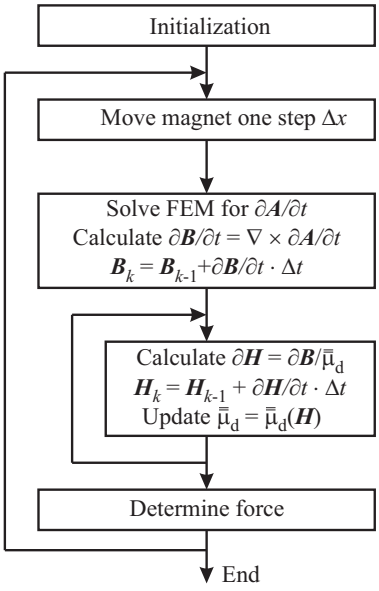

Figure 3.31. Schematic overview of the different numerical steps in order to calculate the force profiles as a function of magnet position x relative to the strip center, corresponding to a certain trajectory of the sample, typically consisting of a forward and backward movement.

ferromagnetic sample, and with **n** the outward unit vector normal to the surface S'. The complete numerical scheme comprising time-stepping, FEM calculations and permeability evaluations, is summarized in figure 3.31.

With this numerical drag force model, simulations are carried out on a ferromagnetic sample of 1.6 mm thick and 150 mm long, and for the typical geometry of the experimental setup as shown in figure 3.27 (single magnet with magnetic moment $\mathbf{m}$ parallel to $\mathbf{e}_x$). The results of one particular simulation are combined in figure 3.32.

Initially, the magnet is at the right of the sample in position (0), and the sample is in a remanent state (H = 0 A/m, B = -0.3 T). During the initialization course (0)→(1), plotted with dotted lines in figure 3.32, the longitudinal force F_x in N per meter length in the z-direction becomes high (264 N/m) as the magnet moves to the left, comes closer to the sample end, and attracts it. After that, the force profile becomes more or less flat up to position (1). Between (0) and (1) the sample center passes the permanent magnet and is magnetized towards positive saturation at position (0'), and back to a negative H at position (1), the actual starting position for the drag force determination.

At starting position (1) the movement direction is changed and we follow the solid

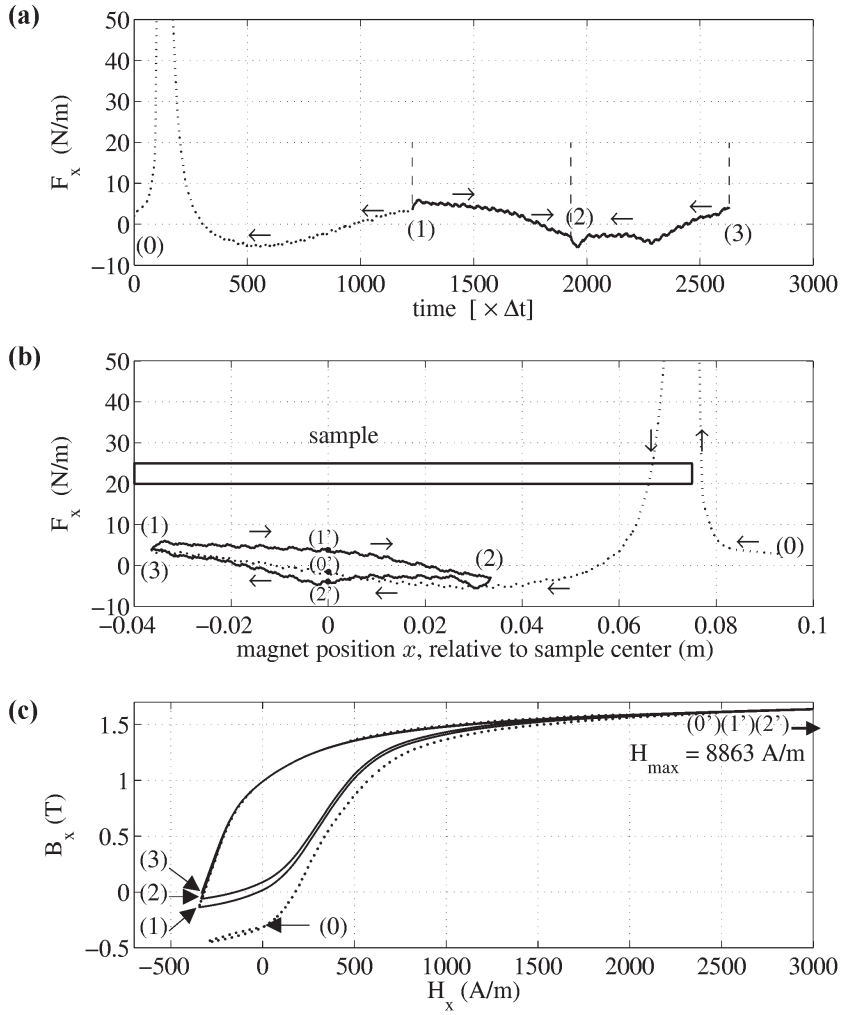

Figure 3.32. Numerical results of a simulated drag force experiment, comprising an initialization course (0)→(1) (dotted lines), and the actual forward (1)→(2) and backward (2)→(3) movement (solid lines). The arrows in sub-plots (a) and (b) indicate the movement direction of the magnet. In (a) the simulated force profile is shown as a function of time, whereas (b) depicts the same data as a function of the magnet position relative to the sample. The corresponding calculated $B(H)$ trajectory and traversed closed hysteresis loops at the center of the sample is shown in sub-plot (c).

line from position (1) to (2). The force is higher due to magnetic hysteresis. Finally, at position (2) the movement direction is changed again. The sample is brought back to the starting position (3) = (1), see figure 3.32(b). During the trajectory (1)→(2), the sample is magnetized towards positive saturation at position (1') and back to negative H, and even so for the trajectory (2)→(2')→(3). At po-

sition (3), the magnetic state of the sample is the same as at the starting position (1), and the magnetization loops are closed.

The drag force difference $\Delta F_{drag}(x)$ is obtained by subtraction: at equal x the force profile while the magnet moves to the right (upper solid line) minus the force profile while the magnet moves to the left (lower solid line). The area enclosed by the solid line in figure 3.32(b) is actually the visualization of the left hand side of formula (3.18), the formula which describes the energy balance between mechanical work and hysteresis loss. It is checked that the hysteresis loss $\int_V \left(\oint H \mathrm{d}B\right) \mathrm{d}V$, calculated on the basis of the two closed hysteresis loops, i.e. loops (1)→(1')→(2) and (2)→(2')→(1) in figure 3.32, equals the mechanical work $\int_{x_1}^{x_2} \Delta F_{drag}(x)\ \mathrm{d}x$, provided that the numerical step Δx is sufficiently small.

It was also checked that in case of a single valued $B(H)$ characteristic (without hysteresis involved), the force profiles for both forward and backward movement directions actually coincide, in other words the force profile $F_x(x)$ for trajectory (1)→(2) is identical to $F_x(x)$ for trajectory (2)→(3). This obviously results in no net drag force difference, reflecting the fact that the hysteresis loss is also zero in this case.

3.4.4 Possible applications

Inherent to the drag force approach and its typical magnet configuration (figure 3.29 shows some possible configurations), the magnetic field in the sample is not uniform. Consequently, the drag force method is not intended to be an alternative for accurate conventional hysteresis loss measurements.

Considering the underlying mechanism giving rise to the drag force during the sample movement, i.e. the traversal of magnetization loops in the ferromagnetic sample or in other words the reorganisation of the magnetic domain configurations, it is expected that the microstructural changes that affect this magnetic domain reorganisation and consequently the macroscopic magnetic hysteretic behaviour, are also reflected in the experimentally obtained drag force profiles. Therefore, the drag force method shows potential in the field of non-destructive evaluation of ferromagnetic materials. In this context the measured force and the drag force difference can be explored as a function of longitudinal position of the sample relative to the permanent magnet(s), without bothering too much about the particular traversed magnetic hysteresis loops during the movement of the ferromagnetic strip under investigation.

Since the drag force method is fast and robust, and since it provides repeatable information which is qualitatively related to magnetization processes and the underlying microstructure of the material, possible applications can be found in the

field of quality control during the manufacture of ferromagnetic materials. Based on the measured force profiles or the drag force difference, the material quality can be monitored on a continuous basis during the production, after intermediate thermal and mechanical fabrication processes, and also afterwards to ensure the consistent quality of the finished products.

In this work we will focus further on the possible application of the drag force difference ΔF_{drag} as a function of longitudinal sample position. As an example, in section 5.3 the drag force method is utilized to evaluate non-destructively the micro residual stress distribution introduced on both sides of a ferromagnetic strip by cyclic mechanical bending, based on the evaluation of the variations in the drag force difference.

Chapter 4

Magnetic hysteretic characterization

4.1 Introduction about magnetic NDE

Magnetic hysteretic NDE techniques are generally based on the knowledge that the development of microstructural defects and the variations of the internal micro stress distributions around those defects influence the magnetic domain wall motion, which consequently leads to altered macroscopic magnetic hysteretic properties. In principle, we may identify microstructural changes, and the deterioration of mechanical properties of ferromagnetic materials in a non-destructive manner by the characterization of the magnetic hysteretic behaviour.

The magnetic measurement setups treated in chapter 3 are capable to operate in a frequency range from quasi-static (can be as low as typically 0.05 Hz) to typically 1 kHz. However, in the context of magnetic hysteretic NDE our focus is predominantly on the rate-independent or quasi-static magnetic hysteretic behaviour. Following the principle of loss separation [Bertotti1988], the magnetic behaviour can be divided into three major contributions: (1) the rate-independent or quasi-static hysteretic part, (2) the classical dynamic part, and (3) the excess dynamic part. All three contributions are dependent to some extent on microstructural features, but in our context of magnetic NDE on low-carbon construction steels, only the quasi-static contribution is of practical importance in relation with microstructural changes. The excess dynamical part depends on grain size: for low-carbon steels having small grain size, the excess dynamical part is small and can be neglected. Concerning the classical dynamical part, the material parameter that is dependent on microstructure is the conductivity, but to determine conductivity, more accurate methods can be put forward, such as a four-point resistivity measurement.

The core issue in relation to magnetic hysteretic NDE techniques is to define magnetic parameters that are sensitive enough to identify the changes of microstructural properties under investigation. As a first step, the classical magnetic hysteresis parameters characterizing the saturation magnetization loop such as coercive field, remanent induction, permeability, and electromagnetic losses can be used for NDE purposes [Bose1986, Lo2000]. Such conventional magnetic hysteresis parameters are introduced already in section 2.1.

Indeed, one of the most popular visualizations of the rate-independent magnetic hysteretic behaviour is the saturation loop, but the magnetic hysteretic behaviour is much more than the saturation loop. In this research work, the magnetic hysteretic non-destructive evaluation method is extended, by increasing the input of experimental data for the magnetic evaluation technique. This is done by considering a whole set of *minor* magnetization loops from low to high magnetic induction levels, instead of taking into account only the *major* saturation magnetization loop.

In order to take such experimentally obtained overall magnetic hysteretic behaviour into account, the use of a hysteresis model such as the Preisach model is proven to be very useful, especially in order to elegantly describe and further analyze the set of experimentally obtained minor hysteresis loops. The classical scalar Preisach hysteresis model is treated in the next section 4.2. The Preisach distribution function is shown to be dependent on microstructure [Basso1995, Dupré1999, Melikhov2001].

For the magnetic hysteretic characterization aiming at magnetic hysteretic non-destructive evaluation, also other alternative approaches, which also start from a set of experimentally obtained minor hysteresis loops, are proposed by other research groups [Tomáš2004, Takahashi2006a].

4.2 Classical Preisach hysteresis model

The classical Preisach hysteresis model elegantly describes the quasi-static (or rate-independent) hysteretic magnetization process [Preisach1935, Bertotti1998, Mayergoyz2003]. Such description is performed using an infinite collection of elementary magnetic dipoles with asymmetric rectangular hysteresis loops, see figure 4.1, which are defined by two statistically distributed parameters, namely the elementary loop coercive field h_c and the elementary loop mean field h_m, or alternatively by two related parameters, namely the switching fields α and β, with:

$$\begin{cases} \alpha = h_m + h_c \\ \beta = h_m - h_c \end{cases} \tag{4.1}$$

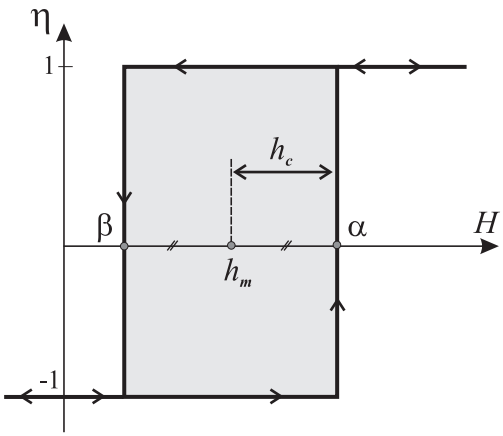

Figure 4.1. Elementary Preisach dipole, with annotation of the elementary switching fields α and β ($\alpha \geq \beta$), and of h_c, the elementary or local coercive field of the Preisach dipole ($h_c \geq 0$), and h_m, the elementary or local interaction (or mean) field of the Preisach dipole.

Remark that the existence of elementary Preisach dipoles with asymmetric characteristic hysteresis loop (this is the case for $h_m \neq 0$) can be justified physically by considering the mutual interaction between the different elementary dipoles [Dupre1995] – the magnetic dipole senses not only the externally applied magnetic field, but also the interaction magnetic field originating from other magnetic dipoles – therefore the local mean field h_m is also called the local interaction field.

For a given elementary dipole (h_c, h_m) (or alternatively (α, β)), the polarity η can be $+1$ or -1, depending on the actual value of the magnetic field $H(t)$ and/or on the history of the magnetic field, H_{his}. The polarity $\eta(h_c, h_m, H(t), H_{his})$ is $+1$ when the magnetic field $H(t) > (h_m + h_c)$ and -1 when $H < (h_m - h_c)$, as can be seen in figure 4.1. Between those two cases the polarity depends on H_{his}, which denotes the last extremal value of H lying outside the interval $[h_m - h_c, h_m + h_c]$: the polarity η equals $+1$ when $H_{his} > (h_m + h_c)$, or -1 when $H_{his} < (h_m - h_c)$. In terms of switching fields α and β the polarity η can be written alternatively as follows:

$$\eta(\alpha, \beta, H, H_{his}) = \begin{cases} +1\text{: if } H(t) > \alpha \text{ or } (\beta < H(t) < \alpha \text{ and } H_{his} > \alpha) \\ -1\text{: if } H(t) < \beta \text{ or } (\beta < H(t) < \alpha \text{ and } H_{his} < \beta) \end{cases}$$

The hysteretic magnetic behaviour can be described by the Preisach distribution function (PDF) $P(h_c, h_m)$ or alternatively $P(\alpha, \beta)$, which represents the statistical density of the elementary dipoles (α, β). The magnetization in the Preisach

model is expressed as an integral over the entire elementary dipole collection:

$$M(H, H_{his}) = M_{rev}(H) + M_{irr}(H, H_{his}), \quad (4.2)$$

$$M_{irr}(H, H_{his}) = \frac{1}{2\mu_0}\int_{-\infty}^{+\infty} \mathrm{d}\alpha \int_{-\infty}^{\alpha} \eta(\alpha, \beta, H, H_{his}) P(\alpha, \beta) \mathrm{d}\beta. \quad (4.3)$$

More details about the Preisach hysteresis model can be found in [Dupre1995, Makaveev2003].

The Preisach distribution function can be extracted directly[1] out of a number of experimentally obtained magnetization loops. Here, typically a whole set of measured quasi-static first-order symmetric magnetization loops, from low to high magnetic induction levels, serves as experimental input for the determination of the Preisach distribution function. In figure 4.2(a) an example of such a set of so-called symmetric minor hysteresis loops is shown.

This direct mathematical method encompasses the following steps:

1. The inherent experimental noise on the measured set of magnetic hysteresis loops is filtered away by the construction of splines which correspond as close as possible to the ascending branches of the hysteresis loops (the descending branch is symmetric to the ascending one), and which also fulfil the criterion $\frac{\mathrm{d}B}{\mathrm{d}H}(H) > 0$. This is primordial since in the following steps differentiation will be carried out.

2. The Preisach distribution function actually corresponds to the irreversible magnetic behaviour, see (4.3). Hence a subdivision into the reversible and the irreversible part of the magnetization has to be carried out. This is performed by considering the permeability at the reversal point (for instance at the start of the descending branch, as shown in figure 4.2). At the reversal point only reversible magnetization processes occur (such as reversible domain wall motion or domain wall bowing, see section 2.4), hence the permeability at the reversal point can be considered as the reversible permeability μ_{rev}.

   For each measured hysteresis loop the reversible permeability can be deduced at the reversal point, which then results in an expression $\mu_{rev}(H_i)$,

[1] It is important to recognize that the method that is used here to determine the Preisach distribution function is a direct mathematical transformation of the experimentally obtained set of magnetic hysteresis loops (by utilizing the Everett approach, see text). In other words, the PDF is not the result of some fitting procedure, where a predefined analytical expression for the PDF is assumed and some parameters are fitted. Although an analytical distribution function, such as a Lorentzian, can be appropriate in case of electrical steels, this is certainly not the case when dealing with hysteresis loops obtained on fatigued or plastically deformed construction steels [Vandenbossche2005]. Hence such analytical approach is not suited for magnetic NDE and microstructural characterization.

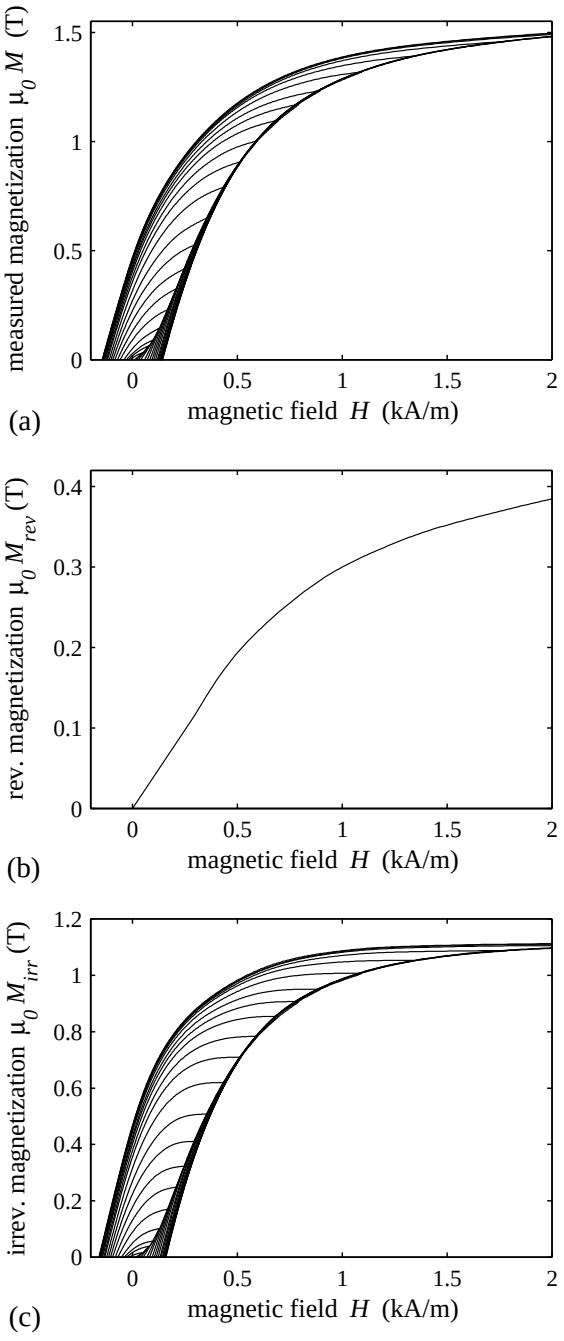

Figure 4.2. (a) Measured magnetization loops, (b) Reversible magnetization curve, (c) Irreversible magnetization loops, all three corresponding with the same experiment on an Fe-Cu model alloy sample.

with H_i the set of values of the magnetic field at each reversal point. Starting from the set of measured hysteresis loops $M(H)$, the single valued reversible magnetization M_{rev} as a function of H, and the set of irreversible hysteresis loops can then be obtained as follows:

$$M_{rev}(H) = \frac{1}{\mu_0}\int_0^H \mu_{rev}(H_i)\mathrm{d}H_i \tag{4.4}$$

$$M_{irr}(H) = M(H) - M_{rev}(H) \tag{4.5}$$

Figure 4.2(b) and (c) shows the reversible magnetization and the irreversible magnetization loops, obtained starting from the measured set magnetization loops, shown in part (a) of the same figure.

3. The set of irreversible hysteresis loops is then arranged into so-called two-dimensional Everett maps [Everett1955, Mayergoyz2003].

   The Everett function $E_{irr}(\alpha,\beta)$ can be defined as follows: when the magnetic field H varies, starting from an extremal field value α to a field value β, in such a way that no past extremal values of H are evaded from the material memory, then $E_{irr}(\alpha,\beta)$ is the absolute value of the irreversible magnetization variation that corresponds with the magnetic field trajectory from α to β. This can be alternatively written as a formula:

   $$E_{irr}(\alpha,\beta) = \mu_0 \left| M_{irr}(H=\beta) - M_{irr}(H=\alpha) \right|, \tag{4.6}$$

   with α an extremal value for the magnetic field H.

4. As a last step the PDF is obtained by differentiating the Everett function:

   $$P(\alpha,\beta) = -\frac{\partial E_{irr}(\alpha,\beta)}{\partial\alpha\partial\beta}. \tag{4.7}$$

The PDF does not change during the magnetization process and characterizes the microstructure and the material under investigation. In this context, the features of the Preisach model can be used as a tool for magnetic NDE: the PDF acts as a "snapshot" for the microstructural state of the material.

In the framework of the Preisach model the following properties can be defined: the local interaction field distribution $Q_m(h_m)$ and the local coercive field distribution $Q_c(h_c)$:

$$Q_m(h_m) = \int_0^{+\infty} P(h_c,h_m)\mathrm{d}h_c, \tag{4.8}$$

$$Q_c(h_c) = \int_{-\infty}^{+\infty} P(h_c,h_m)\mathrm{d}h_m. \tag{4.9}$$

Starting from these distributions, the following parameters can be defined:

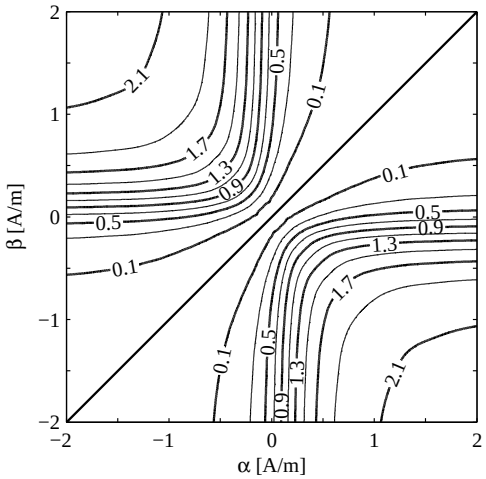

Figure 4.3. Everett map, corresponding to the set of irreversible magnetization loops, shown in figure 4.2(c). Labels on the contours are E_{irr} (T).

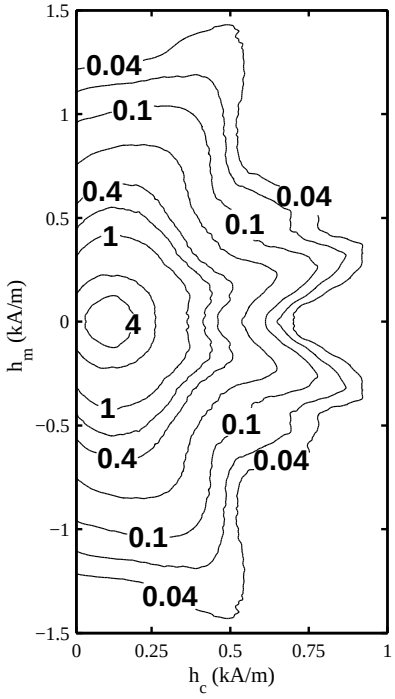

Figure 4.4. Preisach distribution function, obtained starting from the Everett map shown in figure 4.3. Labels on the contours are P (10^{-6} H/A).

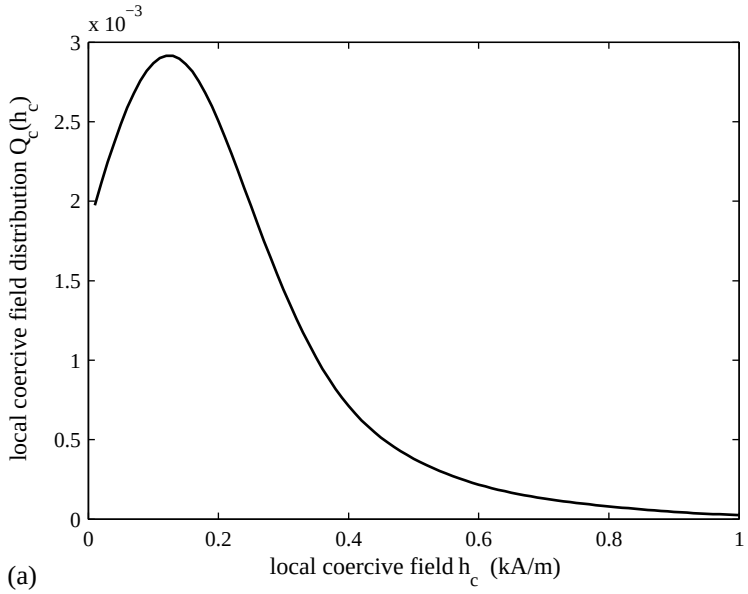

(a)

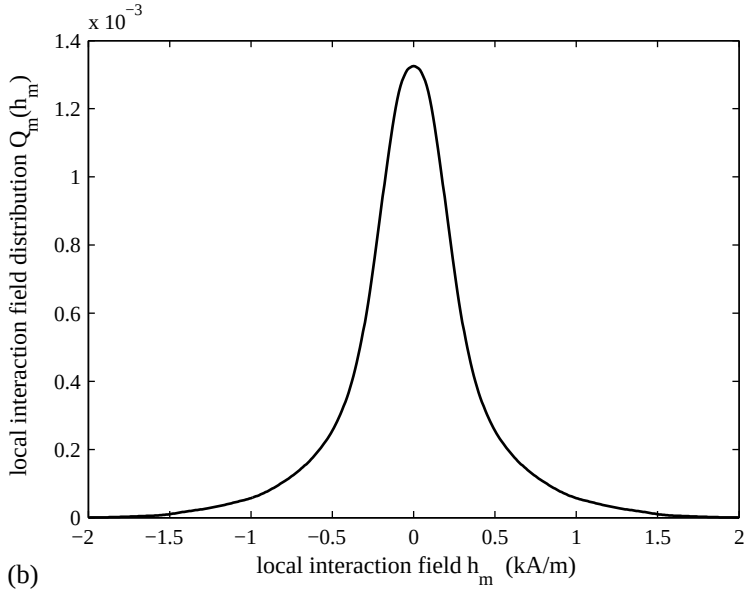

(b)

Figure 4.5. (a)Local coercive field distribution and (b) local interaction field distribution, corresponding to the Preisach distribution function shown in figure 4.4.

- $Q_{c,max}$: peak intensity of the local coercive field distribution $Q_c(h_c)$
- $Q_{m,max}$: peak intensity of the local interaction field distribution $Q_m(h_m)$
- $h_{m,fwhm}$: full width at half maximum of the distribution $Q_m(h_m)$
- $S = A_s/A_0$: the shape parameter of the distribution $Q_m(h_m)$
- $W = A_w/A_0$: the wing parameter of the distribution $Q_m(h_m)$

with A_0, A_s and A_w defined as follows:

$$A_0 = \int_{-\infty}^{+\infty} Q_m(h_m)\mathrm{d}h_m, \tag{4.10}$$

$$A_s = \int_{-\mathrm{FWHM}/2}^{\mathrm{FWHM}/2} Q_m(h_m)\mathrm{d}h_m, \tag{4.11}$$

$$A_w = \int_{\mathrm{FWHM}}^{+\infty} Q_m(h_m)\mathrm{d}h_m, \tag{4.12}$$

In the following chapter, the Preisach-based parameters $Q_{c,max}$, $Q_{m,max}$, $h_{m,fwhm}$, S and W are utilized for magnetic NDE purposes.

Chapter 5

Effect of microstructural degradation on magnetic behaviour

In this chapter the effect of microstructural changes on the magnetic hysteretic behaviour is investigated, for three distinct cases of material degradation processes: irradiation-induced Cu-precipitation and matrix damage, leading to embrittlement and hardening (section 5.1), changes in dislocation density and distribution, due to plastic deformation (section 5.2), and variations in the localized macro residual stress distribution, due to cyclic bending (section 5.3).

For the first two cases, magnetic hysteretic characterization methods are applied, utilizing both the conventional magnetic hysteresis loop parameters (such as permeability, remanence, coercivity, and so on) and also the advanced parameters which are defined in the frame of the Preisach hysteresis model, as introduced in section 4.2. For the third and last case – the macro residual stress variations due to cyclic bending – the so-called magnetic drag force experimental method is being used, an experimental method which is introduced in section 3.4.

5.1 Embrittlement and hardening, due to neutron irradiation or thermal aging

Neutron irradiation of b.c.c. (body-centered cubic) iron-based materials is known to cause undesired changes of the mechanical behaviour such as hardening and embrittlement. This effect can be detrimental for reactor pressure vessel steels during long-term service in the nuclear industry. Therefore this material degra-

dation process of hardening and embrittlement of nuclear reactor pressure vessels (RPV) is a main concern for the nuclear industry in order to cope with extended life times of nuclear power plants. Indeed, the reactor pressure vessel is a crucial structural component of a nuclear power plant (see section 1.1.4, example 2, for more details), and the plant life management is to a large extent governed by the integrity of the reactor pressure vessel [Davies2002].

The process of hardening and embrittlement is the macroscopic outcome of underlying microstructural changes: the neutron irradiation is known to enhance the diffusion processes, the clustering of solute atoms (such as copper[1]) and the creation of nano-sized defects, and is therefore responsible for the formation and growth of copper-rich precipitates (CRPs) and the increase of matrix damage (e.g. vacancy-interstitial clusters). Both the nano-sized Cu-rich precipitates and the matrix damage impede the dislocation motion, resulting in undesired changes of the mechanical material properties, such as a decrease of toughness and ductility, and an increase of hardness, yield stress and ductile-to-brittle transition temperature [Fisher1985].

Conventionally, the material status concerning embrittlement, hardening and fracture toughness is evaluated by destructive tests (e.g. Charpy impact and tensile tests) on surveillance specimens, made of exactly the same material as the pressure vessel. Therefore a number of so-called surveillance capsules, each containing a number of such surveillance samples, are originally inserted inside the nuclear reactor pressure vessel, before taking the nuclear reactor into operation.

At fixed time intervals (say, every five years) a certain surveillance capsule is taken out of the reactor pressure vessel, during a major power plant revision, in order to perform destructive tests such as Charpy impact tests and tensile tests to assess the embrittlement, the hardening and the fracture toughness properties [Chaouadi2007]. Normally, the remains of those destructive tests, i.e. the broken sample pieces, are not inserted back into the reactor, but they are stored in a controlled environment outside the reactor for further investigation[2].

Typical observations of such destructive tests can be found in section 1.1.4 (example 2), and also further in this section 5.1: with increasing neutron irradiation fluence or neutron dose, the yield stress and the ductile-to-brittle transition temperature increase, whereas the ductility and the upper shelf energy[3] decrease.

[1] Cu-alloyed steels are commonly used as materials for reactor pressure vessels in nuclear power plants, mainly because these steels exhibit an improved strength at the elevated reactor operating temperatures ($\approx 300^\circ$C).

[2] Actually, the RPV steel samples of a certain Belgian surveillance program, on which the magnetic hysteresis measurements are performed (sample set 'BSP', see further in section 5.1.3) are cut from these broken Charpy or tensile test sample pieces, which, in a way, act as snap shots of the material state history of the RPV steel.

[3] The upper shelf energy is the energy required for a ductile fracture during the Charpy impact test, see also section 1.1.4.

However, in order to cope with extended life times of nuclear power plants and considering the limited number of specimens originally inserted into the reactor in order to perform such destructive mechanical tests, there is a tendency to develop non-destructive evaluation (NDE) techniques. Such NDE techniques can be considered as additional and/or possible replacement techniques to assess the material condition. Their advantage is that the surveillance specimens can be reused, so without losing precious surveillance material.

In such context, also magnetic non-destructive evaluation techniques can be considered to assess the embrittlement [Takahashi2006a, Altpeter2001, Chi1999], because the development of irradiation-induced microstructural defects – more precisely the variation of the micro-stress distribution around those defects – influences the magnetic domain wall motion, and hence leads to altered macroscopic magnetic properties, such as the magnetic hysteretic behaviour.

The subjects treated further in this section 5.1 can be situated in the general framework of the irradiation-induced embrittlement and hardening of reactor pressure vessels used in the nuclear industry. The following research work is carried out in collaboration with SCK·CEN, the Belgian nuclear research center, which has achieved a high level of expertise in this field, especially about mechanical and microstructural testing of irradiated materials. We at EELAB had the opportunity to perform magnetic hysteretic experiments on irradiated samples provided by SCK·CEN, and inside the hot-cells of the Institute for Nuclear Materials at SCK·CEN.

In the following three paragraphs, the magnetic hysteretic characterization is applied to (1) thermally aged Fe-Cu model alloys, to investigate the effect of Cu-precipitation separately from the matrix damage; (2) irradiated pure iron, to study the effect of matrix damage separately from the Cu-precipitation; (3) irradiated Fe-Cu model alloys and (4) actual reactor pressure vessel steels, to investigate the combined effects of Cu-precipitation and matrix damage.

5.1.1 Hardening and softening due to thermal aging of Fe-Cu model alloys

In order to study in detail the hardening and embrittlement processes due to Cu-precipitation, separately from the effects of the irradiation-induced matrix damage, the investigation of the thermal aging of Fe-Cu model alloys at approximately 500°C is a common and adequate practice since many years [Othen1991, Charleux1996, Chaouadi2005]. Indeed, during thermal aging experiments of Fe-Cu model alloys, one observes hardening processes due to Cu-precipitation, quite similar to the irradiation-enhanced Cu-precipitation hardening [Deschamps2001, Chaouadi2005].

For the Fe-1wt%Cu model alloy under investigation, a major part of the alloyed Cu is still in solid solution in the initial material state before thermal aging: the solubility limit at 500°C is 0.17 wt% Cu for an Fe-Cu binary model alloy [Perez2005] (solubility limit: maximum concentration of solute, Cu, dissolvable in solvent, Fe). Hence, during the thermal aging process at 500°C, the solute Cu is able to precipitate gradually. By deliberately choosing the annealing temperature sufficiently low (as been said, typically 500°C) compared to the solubility limit (i.e. 750°C for 1 wt%Cu [Perez2005]), the predominant microstructural variation during the thermal aging process is the formation and growth of Cu-precipitates, which is well documented in literature [Othen1991, Charleux1996, Deschamps2001, Chaouadi2005].

Apart from the Cu-precipitation, no other significant microstructural changes are observed during the thermal aging at 500°C of Fe-1wt%Cu binary model alloys, which makes the thermal aging process a suitable tool to investigate the effect of Cu-precipitation on the macroscopic properties, separately from other microstructural changes. Therefore the origin of the variation in the macroscopic material properties being further investigated (both mechanical and magnetic properties) is related to the size and morphology of the developing Cu-precipitates.

In Fe-1wt%Cu model alloys, the formation and growth of Cu-precipitates at the beginning of the thermal aging process results in mechanical hardening (the high density of small Cu-precipitates results in strong obstruction to the dislocation motion), whereas for aging times higher than a certain critical value – the so-called over-aging regime – mechanical softening occurs (the decreased density of somewhat larger Cu-precipitates impedes the dislocation motion less and less).

In the following, we explore the possibility of the advanced evaluation of magnetic hysteretic properties, for the assessment of the hardening and softening of a Fe-1wt%Cu model alloy, due to the copper precipitation induced by thermal aging. We found that the specific microstructural variations due to thermal aging, which are related to the size and morphology of the copper-rich precipitates (CRPs), cause substantial variations of the macroscopic magnetic hysteretic properties.

Table 5.1. Impurity composition (in ppm) of the investigated Fe-1wt%Cu model alloy.

Cu	Mn	Ni	W	Cr	P	N	C	S
9500	270	255	180	145	110	58	35	20

Sample preparation and characterization

The Fe-1wt%Cu model alloy is prepared by melting an ultra low carbon steel in air, followed by adding the appropriate amount of pure copper. Details about the preparation are presented in [Konstantinović2007]. The chemical composition of

the alloy can be found in table 5.1. After being cooled down, the material is heated up to 1050°C, followed by hot rolling. In order to obtain a full solid solution of the copper, a normalization heat treatment for 1h at 850°C is carried out, followed by water quench.

Different samples are cut from the same sheet and then subjected to a thermal aging process: heat treatment is performed at a constant temperature of 500°C in an argon atmosphere, for six different aging times t_a: 0.17h, 1h, 3h, 15h, 80h and 120h. The heat treatment is followed by fast quenching into iced water. An

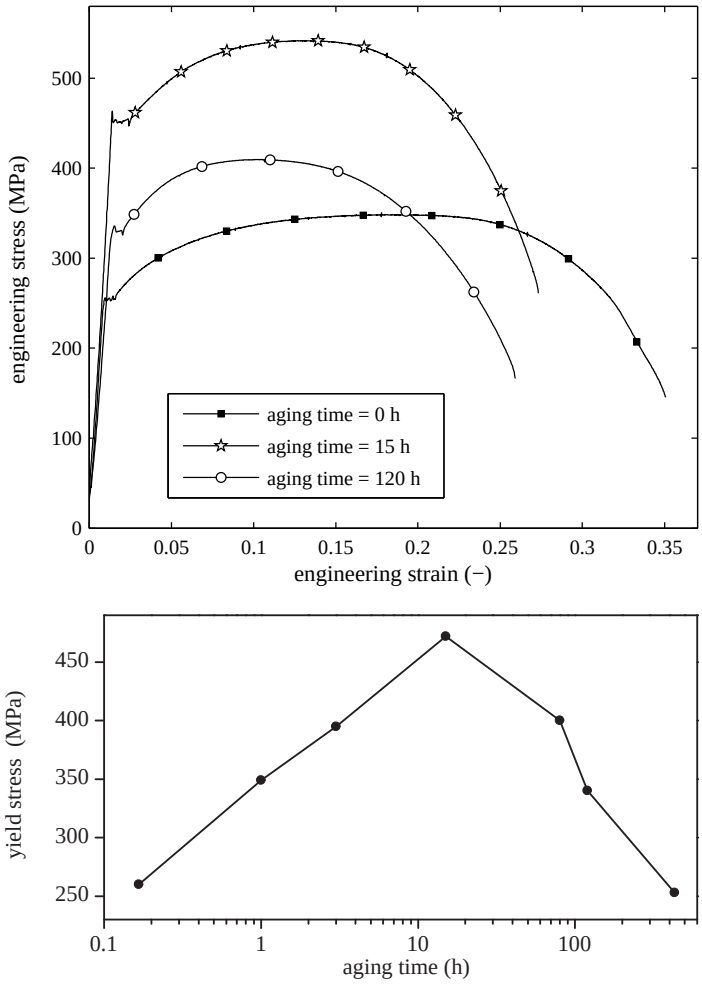

Figure 5.1. (a) Subset of the tensile test results, viz. engineering stress versus engineering strain curves for the samples aged for 0h, 15h and 120h. (b) Yield stress σ_y as a function of aging time. The initial value of the yield stress is $\sigma_y(0)$ = 252 MPa.

additional seventh sample is also cut from the same sheet, as a reference sample, denoted as 0h aging time.

Thermally aged samples from the same batch are characterized both macroscopically and microscopically, macroscopically by mechanical tensile tests and microscopically by small angle neutron scattering (SANS) experiments.

Tensile tests are performed with an Instron machine at a constant strain rate of $1.4 \cdot 10^{-4} s^{-1}$, on specimens that are 24 mm long, with a cylindrical gauge section of 2.4 mm in diameter and 12 mm in length. More details (and also more results) concerning the tensile tests can be found in [Konstantinović2007]. Figure 5.1(a) visualizes a subset of the experimentally determined engineering stress-strain curves. As shown in figure 5.1(b), the sample aged for t_a = 15h has the highest yield stress σ_y and therefore it represents the peak hardening regime. For samples with lower aging times, σ_y increases as a function of t_a, whereas for the samples that are aged for more than 15h, σ_y decreases with t_a. This is fully in agreement with previously published results [Fujii1968]. Further, the flow curve (i.e. true stress σ as a function of true plastic strain ε_p) can be expressed by

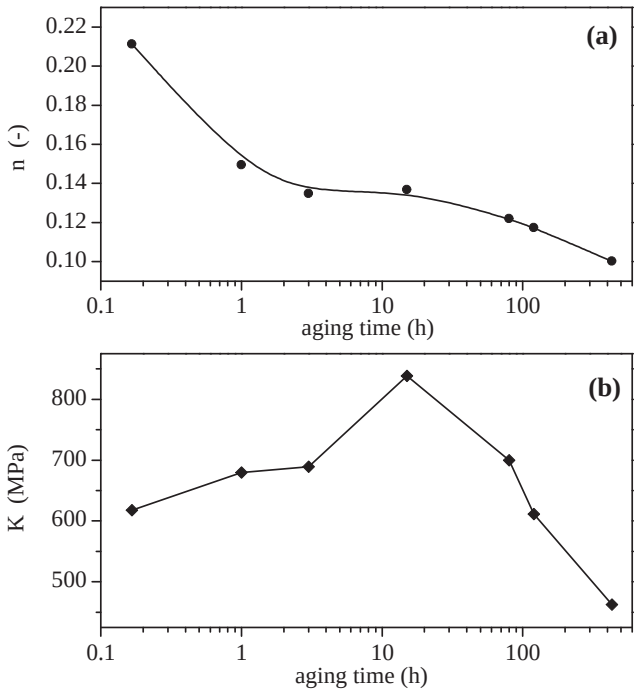

Figure 5.2. Strain hardening index n and strength coefficient K as a function of aging time. These parameters n and K are defined by $\sigma = K(\varepsilon_p)^n$, with σ the true stress and ε_p the true plastic strain.

Hollomon's power law $\sigma = K(\varepsilon_p)^n$, in the case of uniform plastic deformation, in other words until the onset of necking. The strain hardening index n and the strength coefficient K are shown in figure 5.2 as a function of aging time. The strength coefficient K mimics the behaviour of the yield stress, whereas the strain hardening index n continuously decreases with aging time indicating the loss of strain hardening capability with aging time.

Small angle neutron scattering (SANS) experiments are performed by SCK at the Paul Scherrer Institute in Switzerland, for details see [Vandenbossche2007b]. The SANS experimental technique is based on the principle that an initially parallel neutron beam is scattered by nano-size defects. With SANS, small nano-size heterogeneities of the investigated sample, such as precipitates and fluctuations in chemical composition, can be detected and their size distribution can be quantified. Here, the SANS experimental results are used to quantify the size distribution of the Cu-rich precipitates. As can be seen in figure 5.3 and table 5.2, the SANS data confirm the expected increase of the precipitate size and the decrease of the precipitate density as a function of thermal aging time.

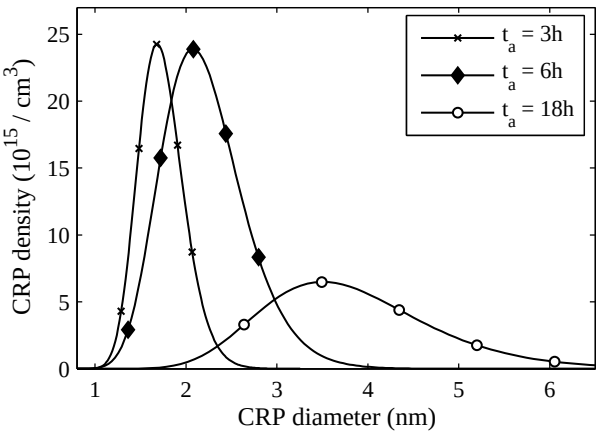

Figure 5.3. Size distribution of the Cu-rich precipitates (CRPs) as obtained by SANS experiments. Notice the asymmetry in the size distribution, which results in a mean diameter that is higher than the peak diameter, see also table 5.2.

Table 5.2. Size and density of the Cu-rich precipitates (CRPs) as a function of aging time, as obtained by SANS experiments.

aging time (h)	total CRP density (10^{15}/cm^3)	peak CRP diameter (nm)	mean CRP diameter (nm)
3	915	1.69	1.74
6	727	2.08	2.21
18	185	3.49	3.83

Experimental results of the magnetic hysteretic characterization

Magnetic measurements are performed on rectangular samples (dimensions 1.3 x 1.3 x 26 mm) with a specially designed miniature single sheet tester, having a magnetic path length of 20 mm. The principles and the specific experimental details concerning magnetic measurements with a single sheet tester are treated in chapter 3. To avoid substantial dynamic effects, all magnetic measurements are performed at an excitation frequency of 0.2 Hz.

To fully characterize the magnetic hysteretic behaviour, for each specimen a set of 40 quasi-static first order symmetric magnetization loops is measured, for a range of peak magnetization values, with steps of $\Delta(\mu_0 M) \approx 0.04$ T. The experimentally obtained magnetization loops are then analysed as a function of aging time: (1) based on the conventional hysteresis loop parameters, and (2) based on Preisach hysteresis model features.

(1) A selection of the experimentally obtained magnetization loops is shown in figure 5.4: for three samples, i.e. the initial one and the samples aged for 15h and for 120h, the magnetization loop at a peak magnetization level of 1.2 T is visualized. Even though these are not saturation loops they give already an indication of the specific variation of the conventional hysteresis parameters such as remanence, coercivity and permeability as a function of the thermal aging process. In figure 5.5 we plot as a function of aging time the relative variation of the conventional hysteresis parameters such as remanence, coercivity and maximum differential permeability relative to their initial values prior to the thermal aging process. Figure 5.6 shows for each of the investigated samples, as a function of yield stress σ_y, the variation of the most sensitive parameter, i.e. $\mu_{r,d,max}$, which is the maximum of relative differential permeability $\mu_{r,d}$:

$$\mu_{r,d} = \frac{1}{\mu_0}\frac{\mathrm{d}B}{\mathrm{d}H}. \tag{5.1}$$

(2) Next, we analyse the variations of the magnetic hysteresis behaviour as a function of aging time by using the Preisach hysteresis formalism as introduced in chapter 4. In the framework of the Preisach model the the local interaction field distribution $Q_m(h_m)$ and the local coercive field distribution $Q_c(h_c)$ can be defined, by integrating the Preisach distribution function $P(h_c, h_m)$ in function of the parameters h_m, the local interaction (or mean) field, and h_c the local coercive field, see also chapter 4:

$$Q_m(h_m) = \int_0^{+\infty} P(h_c, h_m)\mathrm{d}h_c, \tag{5.2}$$

$$Q_c(h_c) = \int_{-\infty}^{+\infty} P(h_c, h_m)\mathrm{d}h_m. \tag{5.3}$$

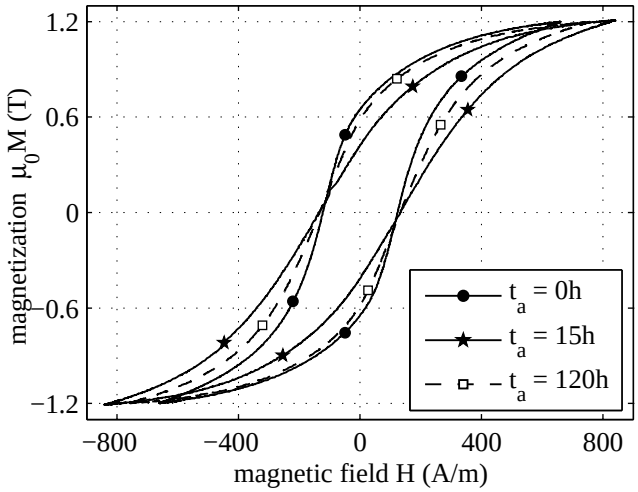

Figure 5.4. Magnetization loops ($\mu_0 M_{peak}$ = 1.2 T) for three samples, i.e. the initial sample (0h), the sample with the highest yield stress (which occurs at t_a = 15h), and the sample with the highest aging time (t_a = 120h).

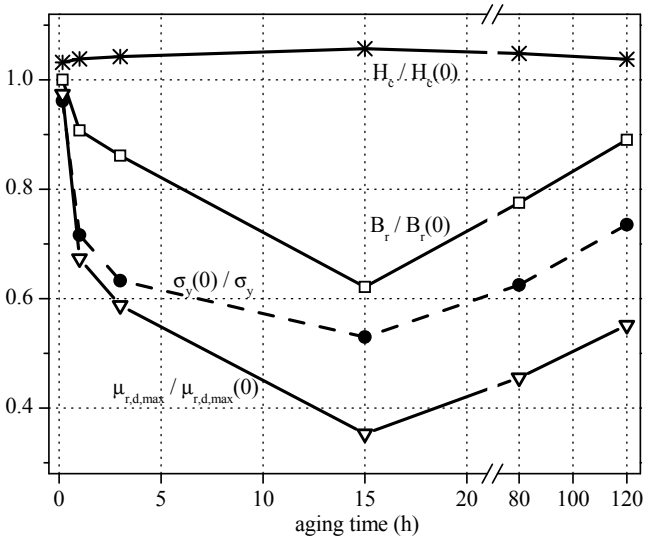

Figure 5.5. Relative variation of the coercive field H_c, remanence B_r, and maximum of relative differential permeability $\mu_{r,d,max}$ as a function of aging time, relatively compared to their initial values $H_c(t_a = 0)$ = 141 A/m; $B_r(t_a = 0)$ = 0.73 T; $\mu_{r,d,max}(t_a = 0)$ = 7862. The variation of the reciprocal value of the yield stress σ_y is also indicated, the initial yield stress is $\sigma_y(t_a = 0)$ = 252 MPa. Both B_r and $\mu_{r,d,max}$ vary substantially and show a minimum for the sample aged for 15h, for instance $\mu_{r,d,max}$ is decreased with approximately 65%. H_c varies only slightly (between 141 and 150 A/m), but shows a maximum at t_a = 15h.

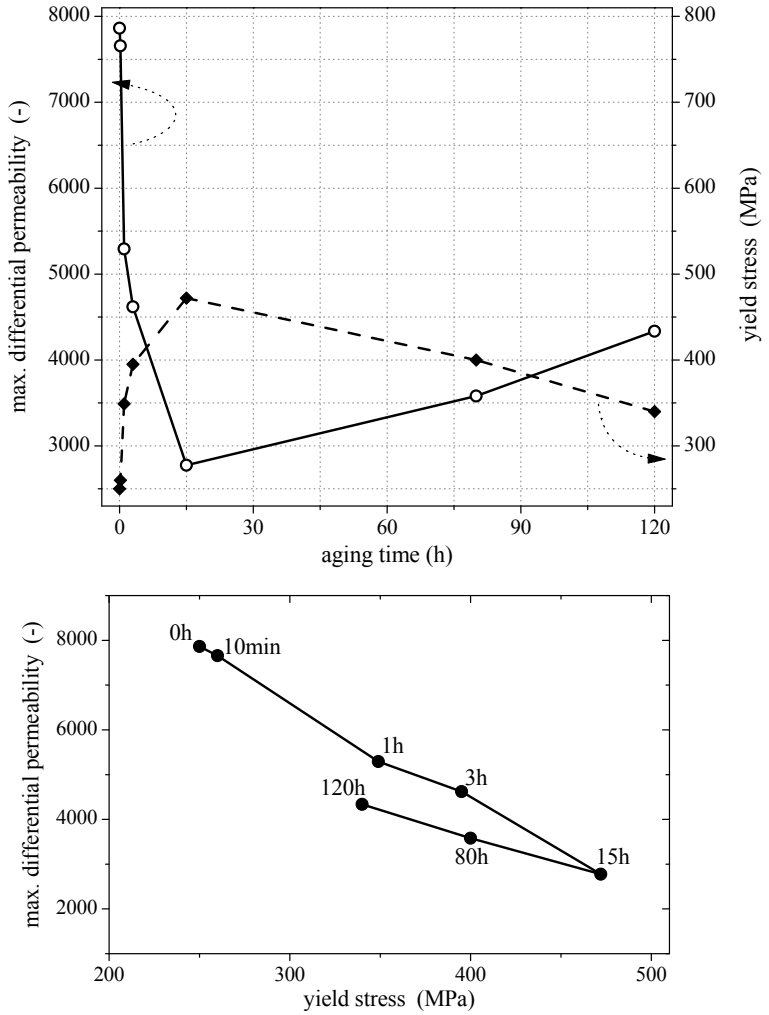

Figure 5.6. (a) Maximum of relative differential permeability $\mu_{r,d,max}$ and yield stress σ_y as a function of aging time, for each of the investigated samples. (b) Alternative view on the same data, with aging times as indicated on the graph.

Figure 5.7 shows the local field distributions as a function of aging time. The peak value of both $Q_m(h_m)$, denoted by $Q_{m,max}$, and $Q_c(h_c)$, denoted by $Q_{c,max}$ first decreases, then increases, showing a minimum for the sample thermally aged for 15 hours. Figure 5.8 visualizes the variation of the peak values of the local coercive field and local interaction field distributions, relative to their peak values prior to the thermal aging process, together with the variation of $h_{m,fwhm}$, which is the "full width at half maximum" of the local interaction field distribution $Q_m(h_m)$. Alternatively, figure 5.9 shows in absolute values the variation of the peak value

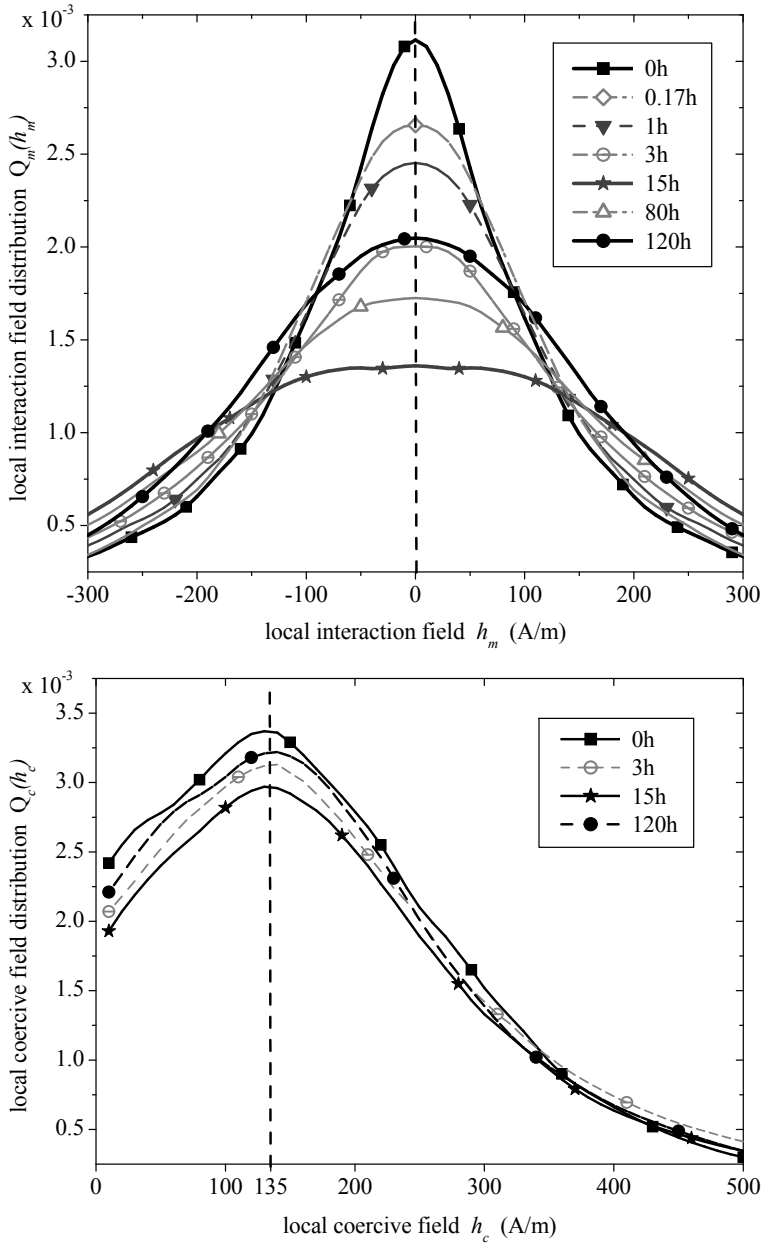

Figure 5.7. (a) Local interaction field distribution $Q_m(h_m)$ for several thermal aging times. The peak position remains the same for all aging times (h_m = 0 A/m), whereas the peak value of Q_m shows a minimum for the peak hardening sample (t_a = 15h). (b) Local coercive field distribution $Q_c(h_c)$ for several thermal aging times. The peak position of this distribution remains the same for all aging times, i.e. $h_c \approx 135$ A/m, in agreement with the results of the macroscopic coercive field H_c.

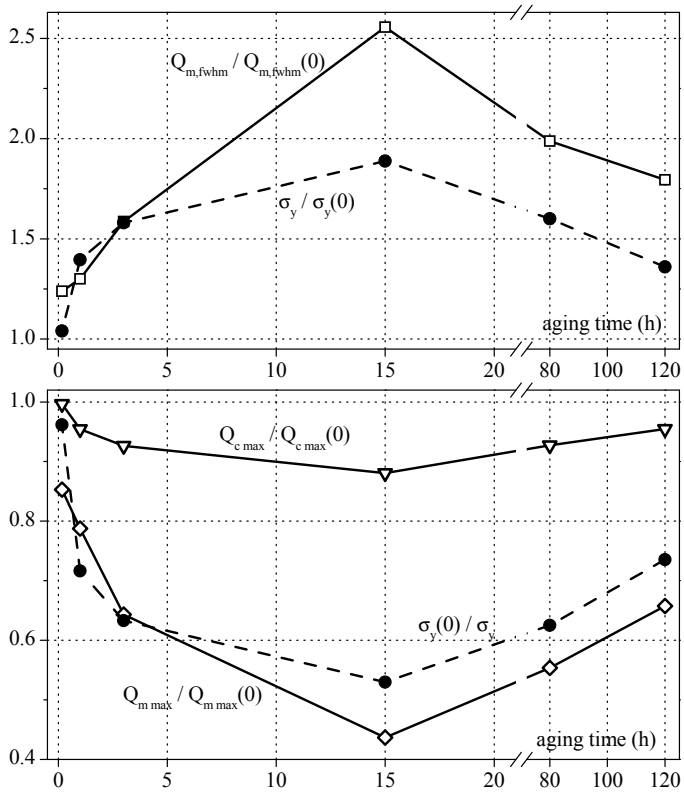

Figure 5.8. Relative variation of the peaks of local field distributions, $Q_{m,max}$ and $Q_{c,max}$, and of the full with at half maximum of the local interaction field distribution, $h_{m,fwhm}$, as a function of aging time, relatively compared to their initial values $Q_{m,max}$(0) = 3.11e-3; $Q_{c,max}$(0)= 3.37e-3; $h_{m,fwhm}$(0) = 209 A/m. Yield stress data is also incorporated, the initial yield stress σ_y(0) is 252 MPa. Notice that $Q_{m,max}$ an $h_{m,fwhm}$ vary substantially, whereas $Q_{c,max}$ only varies slightly.

of the local interaction field, $Q_{m,max}$, and of the yield stress, σ_y, for each of the seven investigated thermally aged samples.

Discussion

From the behaviour of the investigated mechanical and magnetic parameters as a function of the thermal aging at 500°C we identify three main regimes: aging times lower than 15h (regime *I*), aging times around 15h (regime *II*) and aging times larger than 15h (regime *III*). When analyzing the conventional magnetic hysteretic parameters and the Preisach parameters shown in figure 5.5 and figure 5.8 respectively, we see that these magnetic parameters as a function of aging

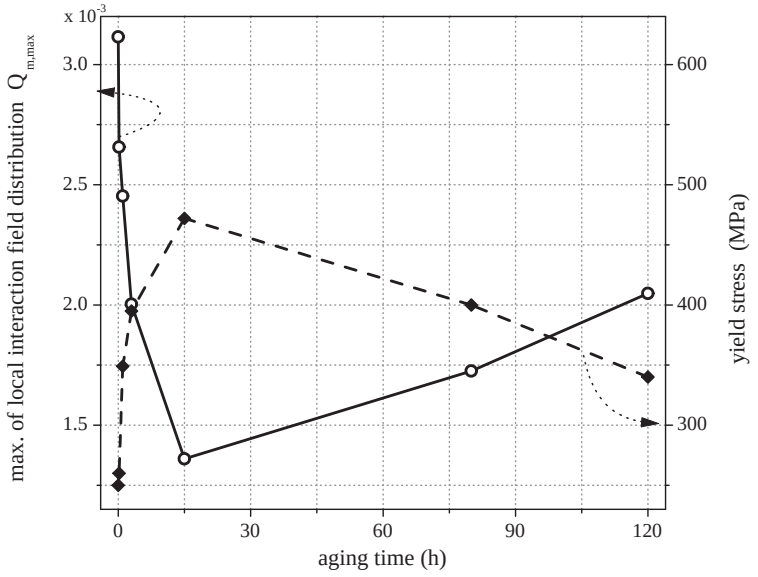

Figure 5.9. Peak value of the local interaction field distribution, $Q_{m,max}$, and yield stress, σ_y, as a function of aging time, for all seven investigated thermally aged samples.

time fully mimic the behaviour of the yield stress, or its reciprocal value, depending on whether the magnetic parameter increases or decreases with aging time in regime *I* ($t_a < 15$h). Accordingly, regime *I* has been found to correspond to the solid solution hardening regime, regime *II* to the peak hardening, and regime *III* to the over-aging (softening) regime. This behaviour of mechanical hardening followed by softening can be related to the morphology of the Cu-rich precipitates (CRPs). The formation and growth of CRPs is well documented in literature, for instance microstructural analysis (based on high resolution transmission electron microscopy, and X-ray absorption techniques) has shown [Deschamps2001] that with increasing aging time the mean CRP size increases (up to approximately 3 nm at peak hardening, and further increasing in the over-aged regime), and that also the distance between the CRPs increases. Our SANS experiments (see figure 5.3 and table 5.2) confirm the increase of the CRP size and the decrease of the CRP density for the thermally aged Fe-1wt$\%$Cu samples investigated here.

Current understanding of the hardening and softening behaviour is based on the idea that the hardening occurs due to the resistance created by the precipitates to the dislocation movement. The Cu-precipitates form obstacles to the dislocation motion. If, in addition, dislocations are assumed to be flexible, different sections of the dislocation line will be able to move partially independent from each other. So, above a certain critical precipitation size (which can be also regarded as critical distance between precipitate clusters, see above), the created stress in

the matrix will no longer induce resistance to dislocation motion, and the material should re-establish a lower elasticity limit [Russell1972].

Furthermore, advanced experimental studies, for instance with high resolution TEM and X-ray absorption techniques [Othen1991, Othen1994, Deschamps2001, Perez2005], and also simulations, based on the so-called molecular dynamics calculations [Hu1999, Blackstock2001], indicate that the Cu-precipitation sequence characteristic for Fe-Cu alloys is as follows:

$$\text{BCC} \rightarrow \text{9R} \rightarrow \text{FCC}.$$

Starting from Cu in solid solution, BCC Cu-precipitates are formed, which are fully coherent with the Fe-matrix, but are metastable (the lattice parameter of BCC Cu (0.296nm) is slightly higher than in case of BCC Fe (0.287nm)). These Cu-rich precipitates increase in size with increasing aging time.

When the CRPs reach a critical size ($\approx$ 3 nm to 4 nm, regardless of the total Cu-concentration [Othen1994]), the coherency strain energy becomes too large, and a strain-induced martensitic transformation to the 9R lattice structure occurs, which is FCC-like with a high density of twins (twins which help to minimize the misfit with the iron matrix). In other words, the Cu-precipitates evolve towards incoherent phases in the Fe-matrix. Figure 5.10 shows in qualitative way the differences between coherent and incoherent precipitates.

At larger sizes ($\approx$ 17 nm [Othen1994]), the CRPs further evolve to the equilibrium

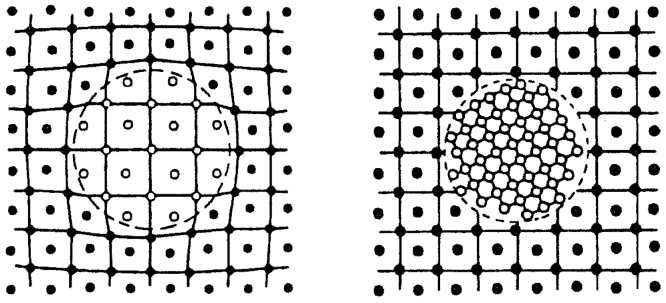

Figure 5.10. Schematic drawing of a coherent and an incoherent precipitate, giving an impression about the local residual stresses around such crystal defects. (a) *Coherent precipitate*: the precipitate adapts to the same lattice structure as the Fe-matrix (b.c.c.), and moreover all lattice planes of the matrix continue through the precipitate. However, differences in lattice parameter in matrix and precipitate result in elastic distortions, hence local residual stresses are present in both Fe-matrix and precipitate. (b) *Incoherent precipitate*: both phases have different crystal structure and a phase boundary is present between matrix and precipitate, with large interfacial energy. Drawings taken from [Gottstein2004].

FCC phase. In any of these cases, the Cu-precipitates induce a certain distortion of the Fe-crystal lattice, resulting in a internal micro stress field distribution, which is localized not only inside the precipitates, but also in the Fe-matrix close to the precipitates.

On the other hand, concerning the magnetic behaviour, it is known that the magnetic domain wall movement is influenced by internal micro stress fields, as treated in chapter 2, due to the magneto-elastic interaction of domain walls with micro stress fields. Applied here to the case of thermal aging of Fe-Cu model alloys, the observed variations of the investigated macroscopic magnetic parameters due to the thermal aging process can be related to the interplay of the magnetic domain walls and the localized micro stress fields around the Cu-rich precipitates (CRPs). These stress fields originate from the distortion of the Fe-crystal lattice induced by the CRPs.

Furthermore, atomistic simulations [Hu1999] utilizing the molecular dynamics method, indicate that the growth of precipitates and the phase transformation of the CRPs (from coherent BCC to incoherent 9R) induce changes of the micro stress fields: as a function of CRP size, the magnitude of the internal compressive stress fields in the vicinity of the CRPs first increases and then decreases. The largest (compressive) internal stresses are found for a CRP size of approximately 2.5 nm, according to the calculations of [Hu1999], which matches more or less with the peak hardening regime, see figure 5.3.

The variation of the magnetic properties as a function of aging time is in agreement with this evolution of the micro stress fields during the Cu-precipitation process. For instance, the maximum differential permeability $\mu_{r,d,max}$ is a measure of the mean free path length of the magnetic domain wall movement once the magnetic domain wall is depinned, which is indicated also by the simplified qualitative model of the effect of internal defect stresses on the permeability and the coercivity, see section 2.4.3. Due to the micro stress field distribution the mean free path length is assumed to decrease during the hardening stage and to increase during mechanical softening, which is in agreement with the experimentally observed variation of $\mu_{r,d,max}$ during the thermal aging process. Also, the variations of peak value $Q_{m,max}$ and the width $h_{m,fwhm}$ (full width at half maximum) of the local interaction field distribution, as a function of the aging time, indicate that the largest interaction between the domain walls occurs at peak strength, where the internal micro stress level is the highest.

Conclusion about thermal aging of Fe-Cu

The formation and growth of Cu-precipitates during the thermal aging process at 500°C leads to variations of the investigated magnetic hysteretic properties, such as remanence, maximum permeability, width and peak value of the local inter-

action field distribution $Q_m(h_m)$ (which is defined in the frame of the Preisach hysteresis model). Moreover, the regimes that can be indicated in their relation to the aging time correspond with the mechanical hardening and softening regimes, in other words the magnetic parameters fully mimic the yield stress variation.

The hardening regime corresponds to small coherent Cu-precipitates, which obstruct the dislocation motion and the magnetic domain wall movement, whereas the softening regime corresponds to larger and well separated incoherent Cu-precipitates, which are softer obstacles to both dislocations and magnetic domain walls. Furthermore, the extremum values of all investigated magnetic parameters correspond with the mechanical peak hardening, at an aging time of 15h.

Moreover, when compared to the initial case, the peak hardening values of the magnetic parameters, such as remanence, maximum permeability, width and peak value of the local interaction field distribution, change with approximately 50% or more. This pronounced sensitivity indicates the potential of magnetic NDE for the evaluation of hardening and softening phenomena induced by Cu-precipitation.

5.1.2 Irradiation-induced embrittlement of nominally pure iron and Fe-Cu model alloys

As introduced earlier, neutron irradiation gives rise to hardening and embrittlement of iron, iron alloys and ferritic steels, due to irradiation-induced microstructural processes such as (1) Cu-precipitation and (2) Fe-matrix damage (point-defect clusters).

In the previous section 5.1.1 on thermally aged Fe-Cu model alloys, we explored the possibility of the magnetic hysteretic characterization for the assessment of the mechanical hardening due to Cu-precipitation, separately from irradiation-induced matrix damage. We found that the specific microstructural variations due to thermal aging related to the formation and growth of copper precipitates, cause substantial variations of the macroscopic magnetic hysteretic properties.

In this section 5.1.2 we extend this approach towards the magnetic evaluation of irradiated pure iron. The experiments on the pure iron samples make it possible to study in detail the hardening and embrittlement processes due to the irradiation-induced matrix damage, separately from the effects associated to Cu-precipitation.

The obvious next step is then of course to investigate the combined effects of irradiation-induced Cu-precipitation and matrix damage. This is performed first on irradiated Fe-Cu model alloys, which have a lower dislocation density and lower impurity content than the actual RPV ferritic steels. This topic is also treated in this section 5.1.2. Finally, in the following section 5.1.3, the same magnetic hysteretic characterization techniques are applied to the irradiation-induced

hardening and embrittlement processes of the actual RPV ferritic steels.

Summarizing, in this section 5.1.2 the magnetic hysteretic characterization is applied to on the one hand a set of irradiated pure iron samples and on the other hand sets of irradiated Fe-0.1wt%Cu and Fe-0.3wt%Cu model alloy samples. These three sample sets were part of one particular irradiation campaign at SCK·CEN, which is designated as 'REVE'.

Sample preparation and characterization

The pure iron and the Fe-Cu model alloys are prepared by melting an ultra low carbon steel in air. For the Fe-0.1wt%Cu and Fe-0.3wt%Cu model alloys, the appropriate amount of pure copper is added. A final heat treatment at 1075 K for 1 h, followed by a water quench, results in dislocation densities of about 10^{10}/cm^2 for all three materials [Verheyen2006]. The average grain size and some details about the composition are listed in table 5.3.

Table 5.3. Nominal composition and average grain size, of the pure Fe and the Fe-x%Cu model alloys.

Material	Nominal composition	Average grain size
pure Fe	$<$ 200 ppm impurities	250 μm
Fe0.1%Cu	0.1wt%Cu; and $<$ 30 ppm C	125 μm
Fe0.3%Cu	0.3wt%Cu; and $<$ 30 ppm C	177 μm

For each of the three materials, different samples are cut from the same sheet and then irradiated in the Belgian test reactor BR2 at 573 K and 150 bar, using a fast neutron flux of about $9 \cdot 10^{13}$ neutrons/cm^2/s, a value which is more than 100 times higher than the typical neutron flux of a commercial nuclear reactor. More details about the sample preparation and the neutron irradiation are presented in [Verheyen2006].

In the following, for each of these three materials, five sample sets are investigated: one as-received and four irradiated sample sets with neutron fluences of $18, 36, 70$ and $130 \cdot 10^{18}$ neutrons/cm^2.

Tensile tests are performed on all sample sets, as reported in [Verheyen2006]. The irradiation-induced hardening is indicated by a consistent increase of the yield stress with neutron fluence or neutron dose, see figure 5.11. This increase in yield stress saturates more or less at fluences higher than $20 \cdot 10^{18}$ neutrons/cm^2. which is in agreement with previously published results [Chaouadi2005]. Furthermore, one can see that the yield stress variation depends on the initial Cu-content in solid solution: the addition of more Cu induces more hardening.

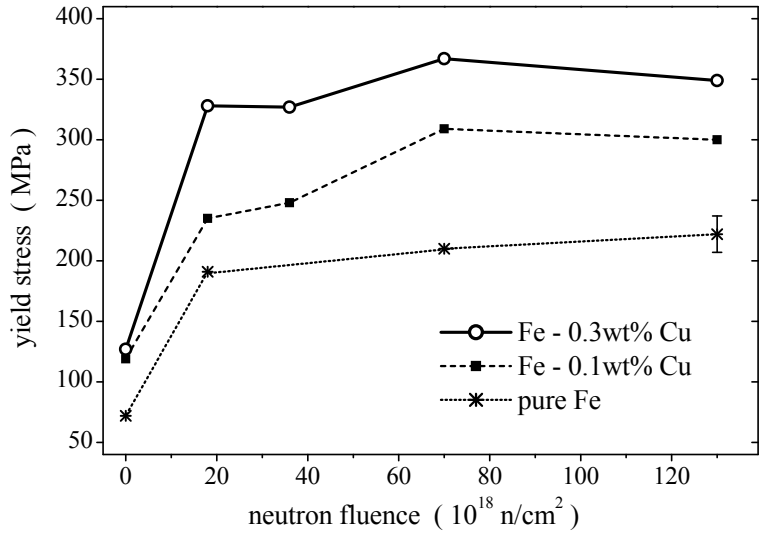

Figure 5.11. Variation of yield stress (measured at room temperature) as a function of neutron fluence, for the investigated pure Fe and Fe-Cu model alloy samples. The error bar plotted on the graph for pure Fe is also indicative for the results on the other materials.

Magnetic hysteretic characterization

All pure Fe and Fe-Cu model alloy samples being used for the magnetic characterization have a length of 26 mm and a square cross section of 1.3 mm by 1.3 mm. These samples are cut to these dimensions, before the neutron irradiation process. As a matter of fact, the actual objective of such a typical sample shape and size is to perform internal friction (IF) measurements at SCK·CEN [Konstantinovic2008]. However, as is discussed later, such IF sample shape is not an optimal choice for magnetic measurements, but nevertheless these irradiated IF sample sets are useful to investigate the sensitivity of the magnetic hysteresis evaluation of irradiation-induced hardening and embrittlement.

Magnetic hysteretic measurements are performed on all three sample sets (pure Fe, Fe-0.1Cu and Fe-0.3Cu), inside a hot-cell at SCK·CEN which allows remote and safe manipulation of active samples, making use of a specially designed miniature single sheet tester (SST), with closing yokes made of nanocrystalline soft magnetic material (Finemet). The principles and the specific experimental details concerning magnetic measurements in general, and more specifically about single sheet testers, are treated in chapter 3.

To fully characterize the magnetic hysteretic behaviour, for each specimen a set of 40 quasi-static first order symmetric magnetization loops is measured, for a range of peak magnetization values with steps of $\Delta(\mu_0 M) \approx 0.04$ T. To avoid substan-

tial dynamic effects, all magnetic measurements are performed at an excitation frequency of 0.2 Hz.

The experimentally obtained magnetization loops are then analyzed as a function of neutron fluence. In the previous section section 5.1.1, about the hardening of thermally aged Fe-Cu model alloys, it appears that valuable information concerning the progression of the mechanical hardening is present in the change of the magnetic hysteresis loop shape. The loop shape can be indicated by the relative differential permeability $\mu_{r,d}(H)$ (see equation 5.1), the Preisach distribution function, and the Preisach-related distribution of the local interaction field $Q_m(h_m)$ (see chapter 4, and equation 5.2). Therefore, we focus here on two main parameters, which are the maximum of $\mu_{r,d}(H)$ and the peak intensity of $Q_m(h_m)$, denoted respectively as $\mu_{r,d,max}$ and $Q_{m,max}$. Remember that for the thermally aged Fe-Cu (see section section 5.1.1, both these parameters decreased significantly with increasing aging time during the hardening stage.

Initial experiments are performed to estimate the repeatability of the magnetic measurements. Preliminary measurements outside the hot-cell indicated that the sample positioning is achievable in a repeatable way, in other words when performed outside the hot-cell, the sample positioning has a negligible effect on the repeatability of the magnetic measurements. However, inside the hot-cell the positioning of the closing yoke on top of the sample has to be performed with remote manipulators. This remote positioning of the closing yoke on top of the sample, combined with the quite small and square cross section (1.3 x 1.3 mm) of the IF-shaped samples, results in some repeatability problems: due to the existence of some non-controllable parasitic air gaps between yokes and sample there is some scatter on the magnetic measurement results. Estimates of the repeatability on the measurement of the maximum differential permeability are 7% deviation for the Fe and Fe-Cu samples, whereas the highest measured irradiation-induced permeability variation is about 35% for all materials.

Results and discussion

In figures 5.12 and 5.13, the magnetic characterization results in terms of $\mu_{r,d,max}$, the maximum value of the relative differential permeability, and $Q_{m,max}$, the peak intensity of the local interaction field distribution, are depicted as a function of neutron fluence for the irradiated pure Fe and Fe-Cu model alloys. Error bars are added to indicate the possible fluctuations due to the inaccuracy of the sample positioning, as discussed above.

For all three materials, both $\mu_{r,d,max}$ and $Q_{m,max}$ decrease with increasing neutron fluence. Such a trend of the magnetic properties as a function of increasing defect density is confirmed both by theoretical assumptions and by earlier investigations, see section 5.1.1: the mechanical hardening stage of thermally aged Fe-

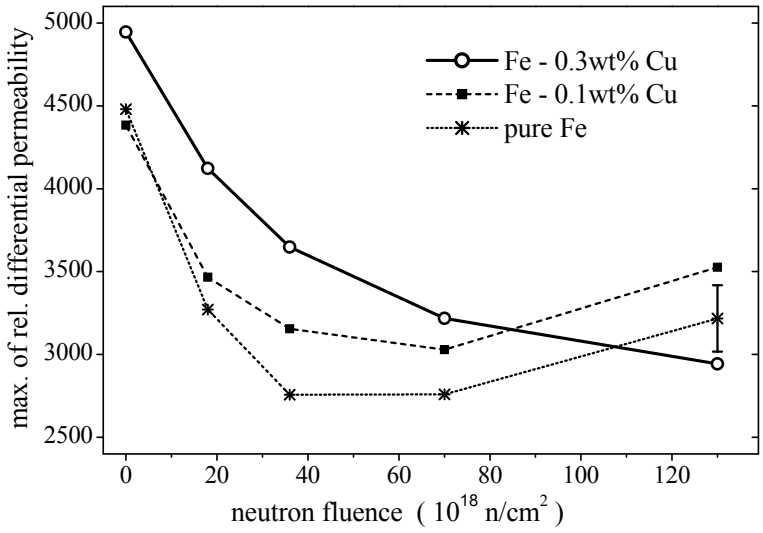

Figure 5.12. Variation of $\mu_{r,d,max}$, the maximum value of the relative differential permeability, as a function of neutron fluence, for the investigated pure iron and Fe-Cu model alloy samples. The plotted error bars for pure Fe, are indicative for all data points on the graph, also for the results on the Fe-Cu model alloys.

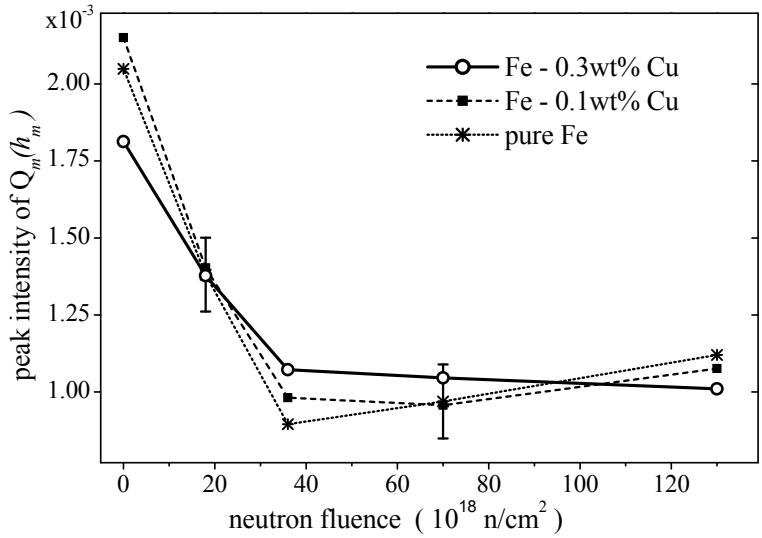

Figure 5.13. Variation of $Q_{m,max}$, the peak intensity of the local interaction field distribution, as a function of neutron fluence, for the investigated pure Fe and Fe-Cu model alloy samples. The plotted error bars for pure Fe, are indicative for all data points on the graph, also for the results on the Fe-Cu model alloys.

1wt%Cu model alloys corresponds also with a decrease of $\mu_{r,d,max}$ and $Q_{m,max}$. Concerning the magnetic behaviour, it is known that the magnetic domain wall movement is influenced by internal micro-stress fields located around microstructural defects, as introduced in chapter 2. The decrease of the investigated magnetic parameters with increasing fluence can be explained as a consequence of the increasing hindrance of the magnetic domain wall movement by the nano-sized defects induced by neutron irradiation, i.e. Cu-rich nano-precipitates and point defect clusters known as matrix damage.

Moreover, it can be seen that the magnetic behaviour is sensitive to both irradiation-induced hardening mechanisms (precipitation of Cu-rich nano-clusters, and formation of point-defect clusters known as 'matrix damage'): the same decreasing trend in magnetic parameters during the mechanical hardening becomes apparent, regardless the underlying origin of the hardening, which can be either Cu-precipitation during thermal aging of Fe-Cu (section 5.1.1), only matrix damage in case of irradiation of pure Fe, or both mechanisms in case of irradiated Fe-Cu model alloys.

Remark that for two out of three materials (i.e. pure Fe and Fe-0.1%Cu) and for the highest neutron fluence ($130 \cdot 10^{18}$ n/cm^2), the magnetic characterization results deviate from the monotonously decreasing trend of both magnetic parameters. Nevertheless still a clear distinction can be made between non-irradiated and irradiated samples. Further investigation is necessary to determine whether this deviating result can be attributed to (1) the inaccuracy of the sample positioning (as described earlier in this paragraph), or (2) to irregularities during the sample preparation (each data point corresponds to a different sample, and it is known for instance that the magnetic properties can be altered by the cutting procedure or by the orientation of the sample with respect to the rolling direction), or (3) whether there is some plausible explanation (such as irradiation-induced softening) linked with the specific microstructure of highly irradiated materials [Takahashi2006b].

5.1.3 Irradiation-induced embrittlement of nuclear reactor pressure vessel steels

In this section the magnetic characterization of the irradiation-induced hardening and embrittlement is performed on actual reactor pressure vessel steels that are utilized in the nuclear industry. Two different sample sets of irradiated RPV ferritic steels are investigated, which are designated further as 'JRQ' and 'BSP'.

The first sample set, denoted by **'JRQ'** (which stands for *Japanese Reference Quality*), consists of both Charpy impact test samples and tensile test samples. These samples are cut – before the neutron irradiation process – out of a certain plate of ferritic RPV steel (ASTM A533 grade B class 1). The JRQ steel plate has been introduced by the International Atomic Energy Agency (IAEA), as a ref-

erence material for the intercomparison of international scientific studies dealing with the irradiation-induced embrittlement of RPV steel [IAEA2001]. The JRQ steel plate was subjected to the following heat treatments: normalized at 900 °C, water quenched, tempered at 665 °C for 12 hours, and stress relieved at 620 °C for 40 hours [IAEA2001]. The chemical composition of the JRQ ferritic steel is given in table 5.4.

In the following, four JRQ sample sets are investigated, one as-received, and three sample sets irradiated each at a different nuclear reactor, hence the samples are irradiated with different neutron flux levels. The resulting neutron fluence values of the three irradiated samples are 5.7, 10 and $21 \cdot 10^{18}$ n/cm^2 [Sevini2004].

The second sample set, denoted by **'BSP'** (which stands for *Belgian Surveillance Program*), is a set of irradiated surveillance samples – Charpy impact test and tensile test specimens – which actually monitor the hardening and embrittlement status of the reactor pressure vessel of a certain operating Belgian nuclear reactor. More details about this sample set and about the nuclear reactor are not available for the general public.

We had the opportunity to magnetically characterize BSP samples out of five different surveillance capsules, which are taken out of the nuclear reactor pressure vessel after five different neutron fluence values. Unfortunately, an unirradiated sample of the BSP reactor pressure vessel steel was not available for the magnetic characterization.

Table 5.4. Nominal chemical composition of the JRQ A533-B steel, in wt%.

Cu	Ni	P	C	Si	Mn	Cr	Mo	Fe
0.14	0.82	0.017	0.18	0.24	1.37	0.13	0.5	bal.

Mechanical characterization

To mechanically characterize the irradiation-induced hardening and embrittlement, both tensile tests and Charpy-V impact tests are performed on all samples of both materials (1 unirradiated and 3 irradiated samples for JRQ, 1 unirradiated and 5 irradiated samples for BSP). The results of both mechanical tests are summarized in figure 5.14: the yield stress increases with increasing neutron fluence, and the Charpy impact tests indicate an increase of ductile-to-brittle transition temperature (DBTT, defined at an energy level of 41 J) and a decrease of upper shelf energy (USE) with increasing neutron fluence. For both materials BSP and JRQ, also the mechanical data is available for the unirradiated material state. Comparing both materials, one can see that the hardening rate (increase rate or decrease rate of the mechanical parameters, with respect to the neutron fluence) is much higher for the irradiated JRQ steel, as compared to the irradiated BSP steel.

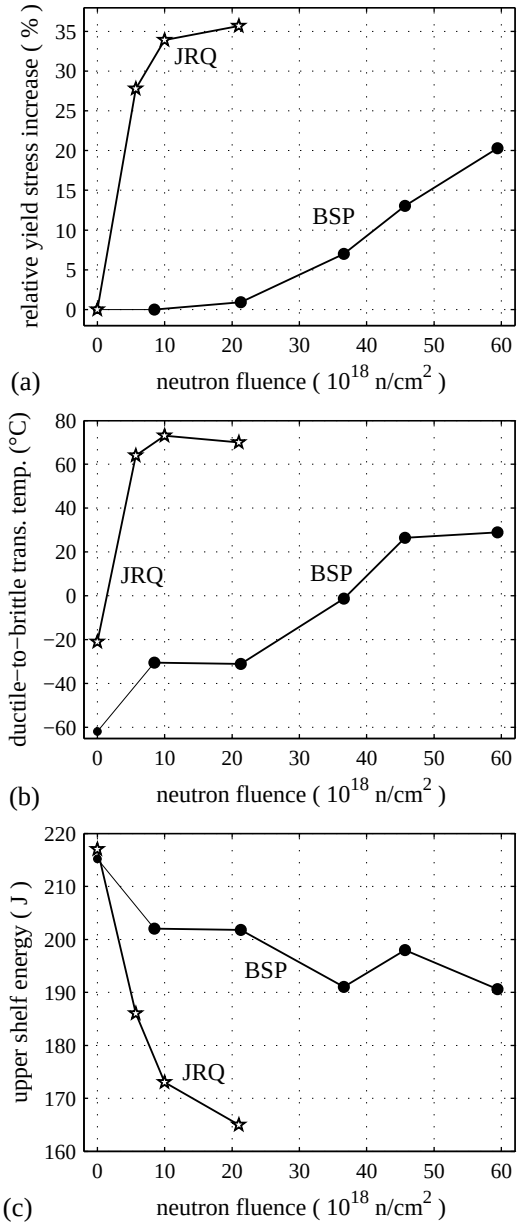

Figure 5.14. (a) relative yield stress increase compared to the unirradiated state, $\frac{\sigma_y(i)-\sigma_y(0)}{\sigma_y(0)}$, (b) ductile-to-brittle transition temperature, DBTT, and (c) upper shelf energy, USE, for both JRQ and BSP sample sets, as a function of neutron fluence. DBTT and USE are obtained with Charpy impact tests.

As is especially apparent for the JRQ sample set, irradiated Cu-rich RPV steels exhibit strong initial hardening at small neutron fluences, mainly due to the irradiation enhanced-Cu-precipitation, combined by matrix damage. Even for small contents of Cu in commercial RPV steels (typically 0.1 wt% Cu) in combination with neutron irradiation, the irradiation-enhanced precipitation of Cu occurs. The Cu-precipitates play an important role at the early stages of irradiation, but it saturates at a certain neutron fluence (when the majority of the Cu in solid solution is precipitated). At larger neutron fluences, the hardening due to matrix damage becomes more dominant than the Cu-precipitation hardening [Chaouadi2005]. In fact, since for the case of irradiated Cu-rich RPV steels the Cu-precipitation hardening is accompanied with matrix damage hardening, a softening effect equivalent to the overaging of thermally aged model alloys (which is only affected by Cu-precipitates and not by matrix damage) is never observed, and is not likely to occur in irradiated Cu-rich steels.

Remark that the amount of experimental scatter on the Charpy impact test results (DBTT and USE) is quite large (see figure 5.14(b) and (c)), but this is however inherent to the nature of the Charpy impact test itself[4]. The uncertainty of the yield stress is about 6%, whereas the uncertainty on the Charpy parameters is typically much larger. As can be seen in figure 5.14, for the JRQ steel the USE is monotonically decreasing. For the three irradiated JRQ samples the value for DBTT is more or less the same, but however much higher than the DBTT of the unirradiated JRQ sample. For the BSP steel it is more or less the opposite: the DBTT is monotonically increasing (with some scatter on the results), whereas the USE is not much decreased and moreover non-monotonic.

Magnetic hysteretic characterization

Magnetic hysteretic measurements are performed on both irradiated sample sets (JRQ and BSP) using a miniature single sheet tester (SST) which is put inside a hot-cell at SCK·CEN allowing remote and safe manipulation of active samples. This SST is now designed especially at EELAB for a sample cross section of 10 mm by 1 mm (instead of 1.3 mm by 1.3 mm, as in section 5.1.2), and again with closing yokes made of nanocrystalline soft magnetic material (Finemet). The principles and the specific experimental details concerning magnetic measurements in general, and more specifically about single sheet testers, are treated in chapter 3.

Dealing with the sample shape: remember that the specific sample shape and size

[4]Typically a minimum of 8 samples are used to reconstruct with reasonable accuracy the ductile-to-brittle transition curve, which is the relation of the impact energy E as a function of the testing temperature T. Then a $\tanh$ is fitted through these resulting data points, $E(T) = E_0/2[1+\tanh((T-T_0)/C)]$, with parameter E_0 the upper shelf energy (USE) and T_0 the ductile-to-brittle transition temperature.

of the irradiated pure iron and Fe-Cu model alloy samples, which were in fact designed for internal friction measurements [VanOuytsel2000, Konstantinovic2008] and not for magnetic hysteresis measurements, resulted in some repeatability problems for the magnetic measurements, caused by parasitic air gaps due to the inaccurate remote positioning inside the hot-cell of samples with such small square cross section (1.3 mm x 1.3 mm), a topic which is treated in section 5.1.2.

However, in this section 5.1.3 dealing with actual reactor pressure vessel steels, the samples being used for the magnetic hysteretic characterization now originate from irradiated Charpy impact or tensile test samples, that have been first tested up to destruction. In this case, we are now free to cut the broken surveillance samples into dimensions that are more suitable for magnetic hysteresis measurements and also for the associated remote positioning inside the hot-cell of the sample in between the two closing yokes of the miniature single sheet tester.

The JRQ and BSP steel sample sets that are characterized magnetically, originate from irradiated broken Charpy and tensile samples. Here, as chosen dimensions, all JRQ and BSP samples being used for the magnetic characterization have now a rectangular cross section of 1 mm by 10 mm, and a length of 26 mm.

For the magnetic measurements on JRQ and BSP steel samples reported in this section 5.1.3, the repeatability of the sample-yoke contact and the remote positioning of the sample (with dimensions 1 mm x 10 mm x 26 mm) in the closing yokes is now improved significantly, when compared to the repeatability of the magnetic results on IF-sized samples (1.3 mm x 1.3 mm x 26 mm) such as in section 5.1.2. Estimates of the repeatability on the measurement of maximum differential permeability are 2% deviation for the (10 mm x 1 mm) RPV steel samples, compared to 7% deviation for the (1.3 mm x 1.3 mm) Fe and Fe-Cu samples, whereas the highest measured irradiation-induced permeability variation is about 30% and 35% for RPV steels and model alloys, respectively.

Moreover, to minimize the effect of residual plastic deformation induced by the Charpy test itself, the sample is cut from an irradiated broken Charpy piece, tested to fracture at the lowest test temperature[5], hence the fracture is brittle and the plastic deformation is minimal. In more detail, the (1 mm x 10 mm x 26 mm) sample for the magnetic hysteretic measurements is cut from the (10 mm x 10 mm x 27.5 mm) broken Charpy piece, at the same sample side as the notch, and some material closest to the notch is removed. The purpose of those two last specifications related with the notch is again the minimization of residual plastic deformation in the (1 mm x 10 mm x 26 mm) sample.

[5] As an illustration of the importance of this specification to cut a sample from the broken Charpy piece tested at the lowest temperature: also a sample cut from a broken Charpy piece tested at 300 °C originating from the second BSP surveillance capsule is characterized magnetically, resulting in for instance $\mu_{r,d,max}$ = 1235, whereas the value corresponding to the sample with the lowest Charpy test temperature is 1623, see figure 5.15.

Results and discussion

Magnetic hysteretic measurements are performed on both sample sets (JRQ and BSP). In order to fully characterize the magnetic hysteretic behaviour, again for each specimen a set of 40 quasi-static first order symmetric magnetization loops is measured, for a range of peak magnetization values. To avoid dynamic effects, all magnetic measurements are performed at 0.2 Hz excitation frequency.

Again, as in sections 5.1.1 and 5.1.2, it appears that valuable information concerning the progression of the hardening and the embrittlement is present in the change of the magnetic hysteresis loop shape with increasing neutron fluence. The loop shape can be indicated by the relative differential permeability $\mu_{r,d}(H)$ (see equation 5.1), the Preisach distribution function, and the Preisach-related distribution of the local interaction field $Q_m(h_m)$ (5.2) and the distribution of the local coercive field $Q_c(h_c)$ (5.3), see also section 4.2.

In the case of the JRQ and BSP irradiated sample sets, the following parameters are investigated, parameters that are already defined in section 4.2:

- $\mu_{r,d,max}$: maximum of the differential permeability $\mu_{r,d}(H)$)
- $Q_{c,max}$: peak intensity of the local coercive field distribution $Q_c(h_c)$
- $Q_{m,max}$: peak intensity of the local interaction field distribution $Q_m(h_m)$
- $h_{m,fwhm}$: full width at half maximum of the distribution $Q_m(h_m)$
- S: the 'shape' parameter of the local interaction field distribution $Q_m(h_m)$
- W: the 'wing' parameter of the local interaction field distribution $Q_m(h_m)$

In figure 5.15 those six magnetic characterization parameters are shown as a function of neutron fluence, and this for both materials (BSP and JRQ). The uncertainty of the magnetic parameters is typically 2–3%. The decrease of the maximum differential permeability $\mu_{r,d,max}$, and the decrease of the peak intensities of both the local interaction field and local coercive field distributions, $Q_{m,max}$ and $Q_{c,max}$, with increasing neutron fluence, and the increase of the FWHM are fully in agreement with the results in section 5.1.2 dealing with the irradiation-induced hardening of the Fe-Cu model alloys, and with the mechanical hardening stage of the thermally aged Fe-Cu model alloys (section 5.1.1).

Again, as in sections 5.1.1 and 5.1.2, the variation of the coercive field H_c with increasing fluence, and also the related variation of the h_c value at the peak position of the Q_c distribution, is much smaller than the six parameters defined above and depicted in figure 5.15. For instance, for JRQ h_c at $Q_{c,max}$ is 630 A/m for the unirradiated sample, and about 710 A/m for the three irradiated samples.

In figure 5.16 two out of six characteristic parameters, i.e. $\mu_{r,d,max}$, the maximum value of the relative differential permeability, and $Q_{m,max}$, the peak intensity of

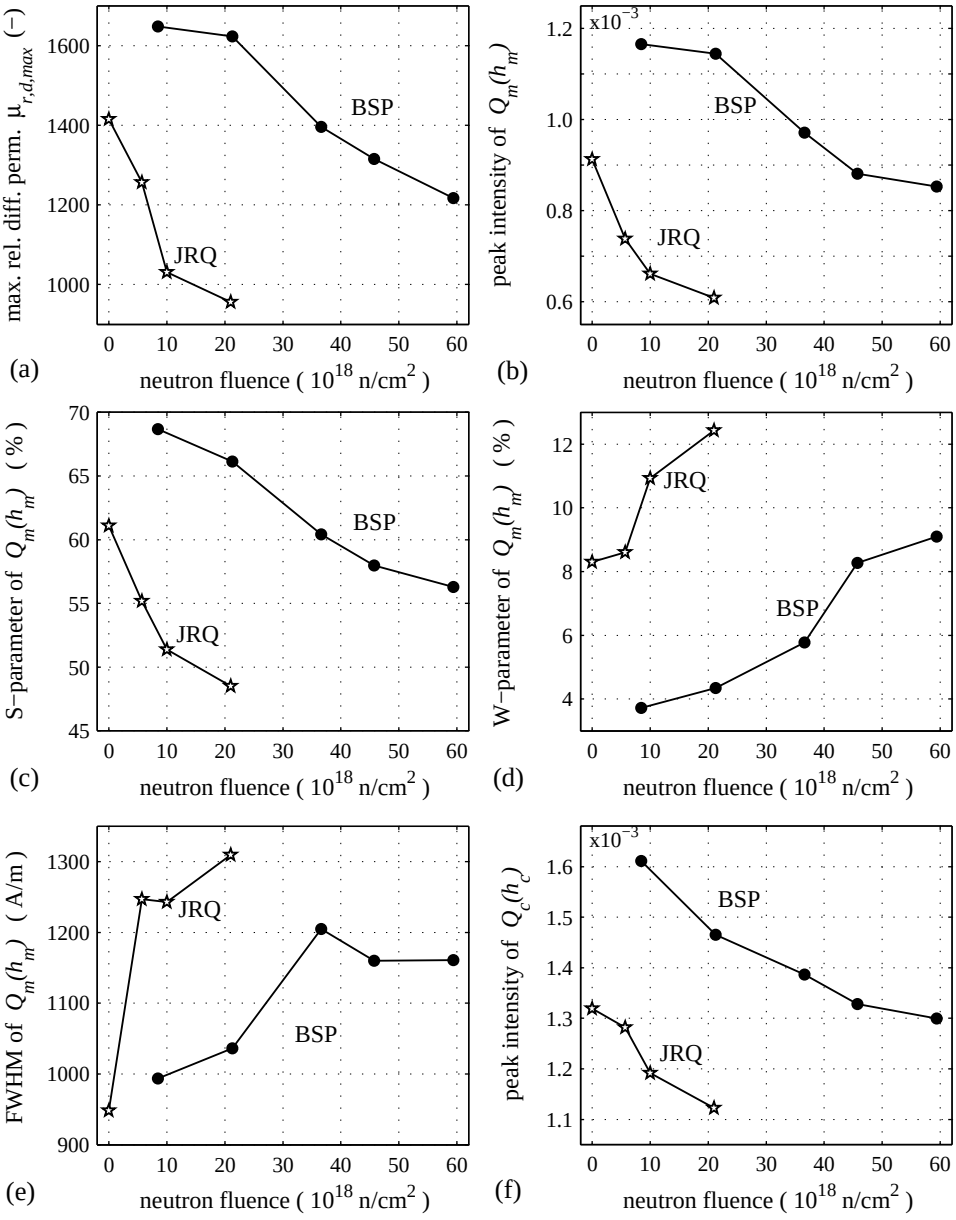

Figure 5.15. Six magnetic parameters, viz. (a) $\mu_{r,d,max}$ (maximum of relative differential permeability), (b) $Q_{m,max}$, (c) S, (d) W and (e) $h_{m,fwhm}$ (respectively peak intensity, S-parameter ('shape'), W-parameter ('wing'), and full width at half maximum (FWHM), of the local interaction field distribution $Q_m(h_m)$), and (f) $Q_{c,max}$ (peak intensity of $Q_c(h_c)$), all as a function of neutron fluence, for both JRQ and BSP sample sets.

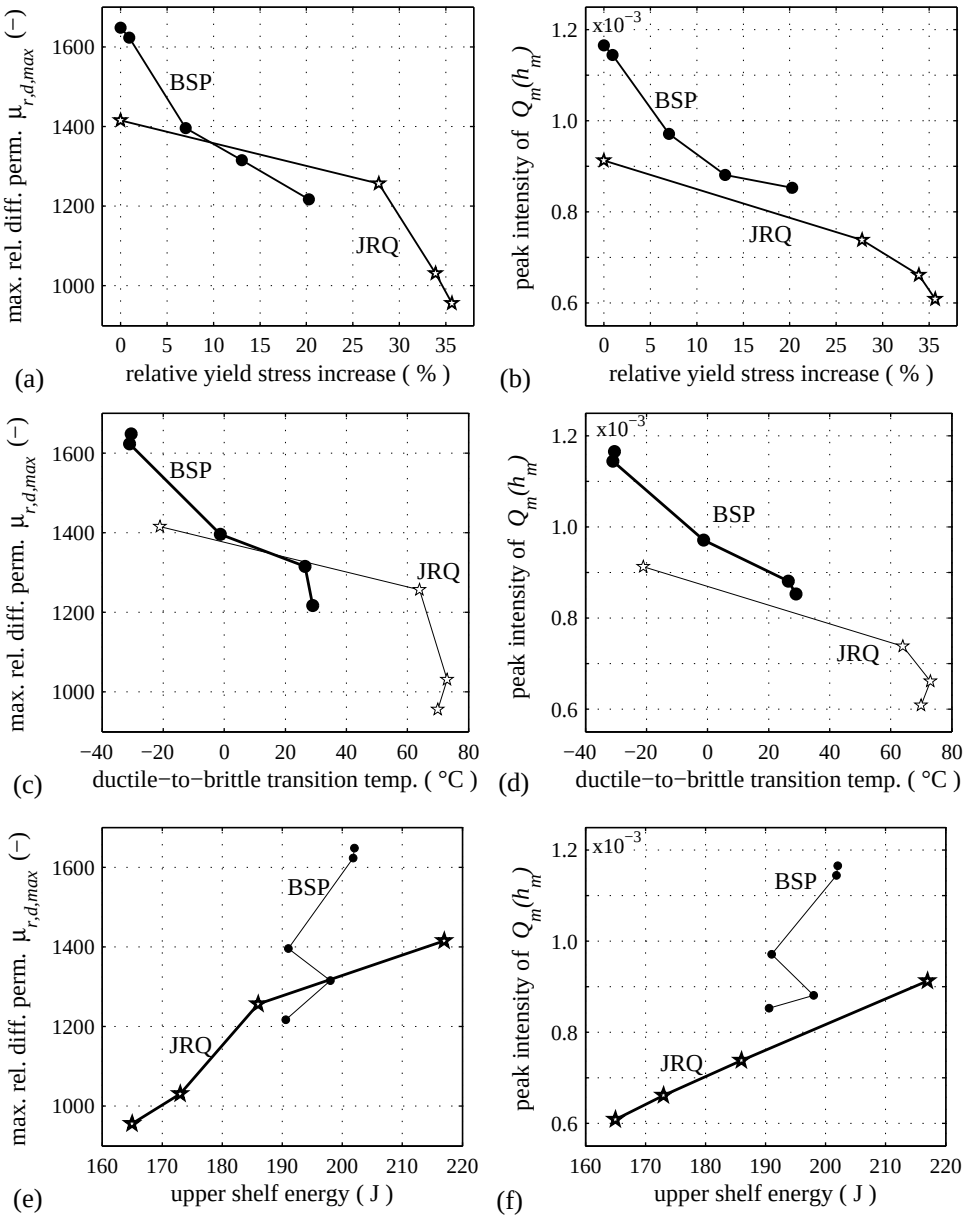

Figure 5.16. Two magnetic parameters, viz. $\mu_{r,d,max}$ (maximum of relative differential permeability) and $Q_{m,max}$ (peak intensity of the local interaction field distribution $Q_m(h_m)$), both as a function of three mechanical parameters, viz. relative yield stress increase compared to the unirradiated state, $\frac{\sigma_y(i)-\sigma_y(0)}{\sigma_y(0)}$, ductile-to-brittle transition temperature, DBTT, and upper shelf energy, USE, for both JRQ and BSP sample sets.

the local interaction field distribution, are depicted as a function of three mechanical parameters, i.e. the yield stress increase, the DBTT, and the USE. Monotonic curves are observed for both magnetic parameters and for both BSP and JRQ steels, as a function of the relative yield stress increase. Dealing with the Charpy test data, for the BSP samples a consistent trend in the magnetic parameters is apparent as a function of the DBTT, and for the JRQ samples a trend is visible as a function of USE. This is inherently connected with the typical DBTT-shift and USE behaviour of both sample sets, see figure 5.14.

5.1.4 General conclusion about iradiation-induced hardening and embrittlement

The formation of nano-size defects during neutron irradiation, i.e. the irradiation-assisted Cu-precipitation accompanied with matrix damage, leads to variations in the magnetic hysteretic behaviour for all investigated materials, i.e. nominally pure Fe, Fe-Cu model alloys, and RPV steel (both a reference quality RPV steel, 'JRQ', and the surveillance samples of the reactor pressure vessel of an actual nuclear reactor, 'BSP'.

Two parameters related to the magnetization loop shape (maximum relative differential permeability and peak intensity of the local interaction field distribution) are investigated: both parameters decrease with increasing neutron fluence for all investigated materials.

The magnetic behaviour is sensitive to both irradiation-induced hardening mechanisms: a decreasing trend in magnetic parameters during the mechanical hardening is noticeable, regardless the origin of hardening, which can be either Cu-precipitation (thermal aging of Fe-Cu), only matrix damage (irradiation of pure Fe), or both mechanisms (irradiation of Fe-Cu or steel). These results suggest that the magnetic domain wall movement is hindered by the nano-sized defects induced by irradiation.

The change of the magnetic parameters is found to be up to 40%, which indicates the sensitivity and the potential of magnetic characterization for the assessment of irradiation-induced material hardening and embrittlement.

5.2 Plastic deformation, due to tensile straining or cold rolling

5.2.1 Plastic deformation due to tensile straining

In this section, the results are shown of the magnetic characterization performed at different plastic deformation levels, which are obtained by unidirectional tensile straining, but after release of the applied stress. Figure 5.17 shows the flow stress $\Delta\sigma$ as a function of plastic strain ε_{pl}. The flow stress $\Delta\sigma$ is defined as $(\sigma - \sigma_y)$, with σ_y the yield stress, and with σ the maximum applied stress just before the stress release. The release to zero stress results in a certain permanent plastic strain, ε_{pl}.

For this experiment one particular sample is used, and this sample is first stressed up to $\sigma = \sigma_1$, which is slightly higher than σ_y. Then the stress is released to zero, and a certain plastic strain $\varepsilon_{pl,1}$ remains. This results in the second data point on figure 5.17 (the first point corresponds with the elastic state). At the unloaded plastically strained state, magnetic measurements are performed. Then the sample is reloaded again, now up to $\sigma_2 > \sigma_1$, resulting in $\varepsilon_{pl,2}$ after stress release. This loading-unloading procedure is repeated several times, resulting in 14 data points (13 plastic strain values and one data point for the as-received sample obtained before the plastic deformation).

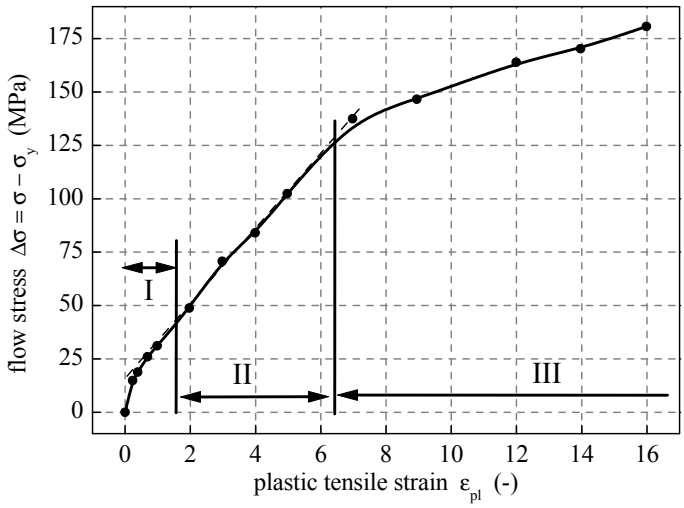

Figure 5.17. Flow stress $\Delta\sigma$ as a function of plastic strain ε_{pl}, with indication of the three strain hardening stages (stage I: $\varepsilon_{pl} \approx 0$ to 1.5%, stage II: $\varepsilon_{pl} \approx 1.5$ to 6.5%, stage III: $\varepsilon_{pl} \approx 6.5$ to 16%). Sample fractured at $\varepsilon_{pl} = 17.8\%$.

In the flow stress $\Delta\sigma$ versus plastic strain ε_{pl} behaviour corresponding with our particular experiment, three strain-hardening stages can be determined (as indicated in figure 5.17 with I, II and III), which nicely corresponds with results in literature [Astié1981, Iordache2003]. As is shown, the stage II corresponds with a linear strain hardening rate, whereas stage I and stage III correspond with a higher and a lower strain hardening rate, respectively.

These different stages in the mechanical behaviour correspond with differences in microstructure. As is shown in section 5.2.2, together with an increase in dislocation density, the dislocation arrangement also evolves from isolated dislocations (stage I) towards structures with dislocation tangles, walls and cells (stage III) [Astié1981]. This has an influence on the mechanical behaviour, but also on the magnetic behaviour.

Quasi-static magnetic measurements are performed on one particular steel sample, for all plastic strain settings as shown in figure 5.17. The material under test is an hour-glass shaped strip sample of a non-oriented electrical steel sheet, with a thickness of 0.35 mm and with a electromagnetic loss of 2.3 W/kg at 50 Hz sinusoidal induction and at a peak induction value of 1.5 T (grade V230-35A). Such electrical steel has a typical Si-content of 3 wt%, and a typical grain size of 0.15 mm. Length of the sample is 200 mm, sample width is 15 mm.

Figure 5.19 shows the dependence of the coercive field on the flow stress and on the square root of the plastic strain. The coercive field versus flow stress behaviour shows the same three strain-hardening stages as indicated in the flow stress versus

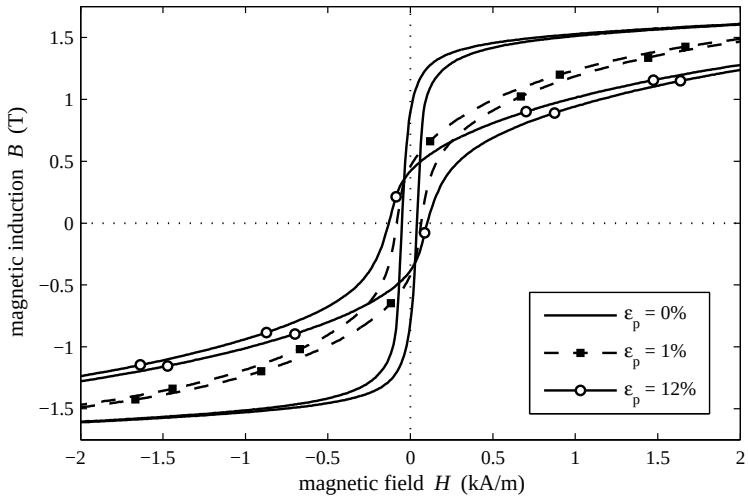

Figure 5.18. A subset of the measured quasi-static magnetization loops for several plastic strain values.

plastic strain behaviour, see figure 5.17. These step-wise linear trends correspond also with other results in the literature, on other types of steel [Küpferling2007, Iordache2003].

The use of the square root of the plastic strain can be attributed to the following line of reasoning. It is theoretically predicted that the increase of H_c depends on

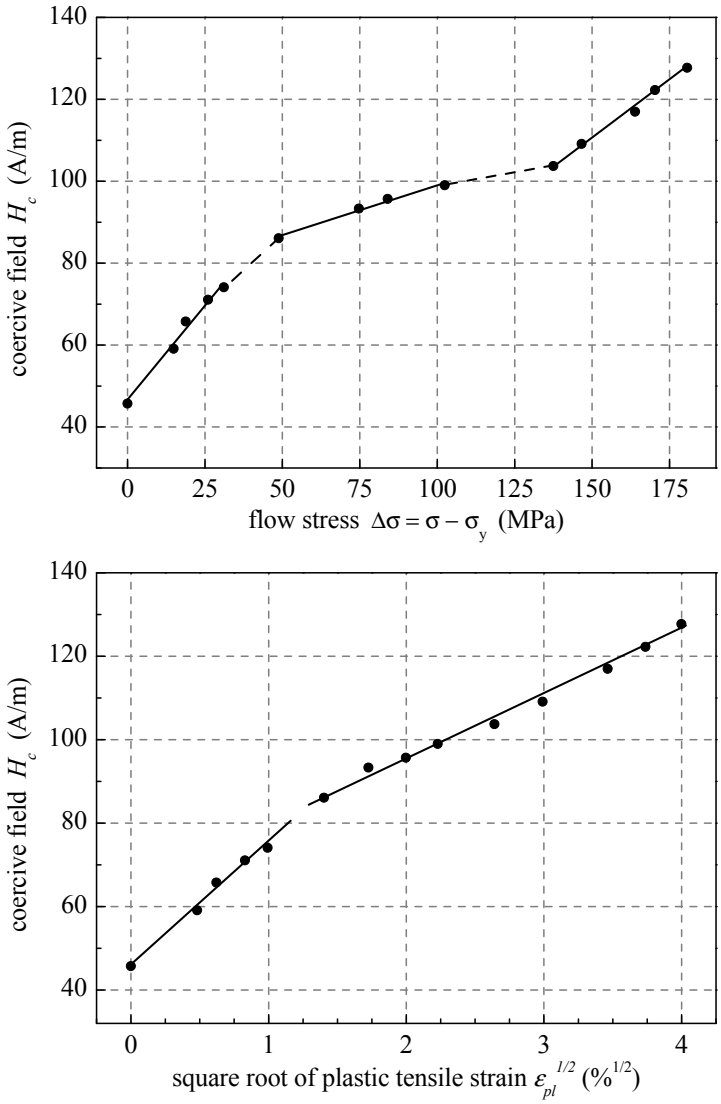

Figure 5.19. Dependence of the coercive field on the flow stress and on the square root of the plastic strain.

the dislocation density ρ_d, and this according to $\Delta H_c \sim \rho_d^{1/2}$ [Kronmüller1972], see section 1.1.3. Also, within a few percent deformation $\varepsilon_{pl} \sim \rho_d$ is reasonably valid. Hence, it can be predicted that $\Delta H_c = k\, \varepsilon_{pl}^{1/2}$, with parameter k somewhat dependent on the dislocation structure [Küpferling2007].

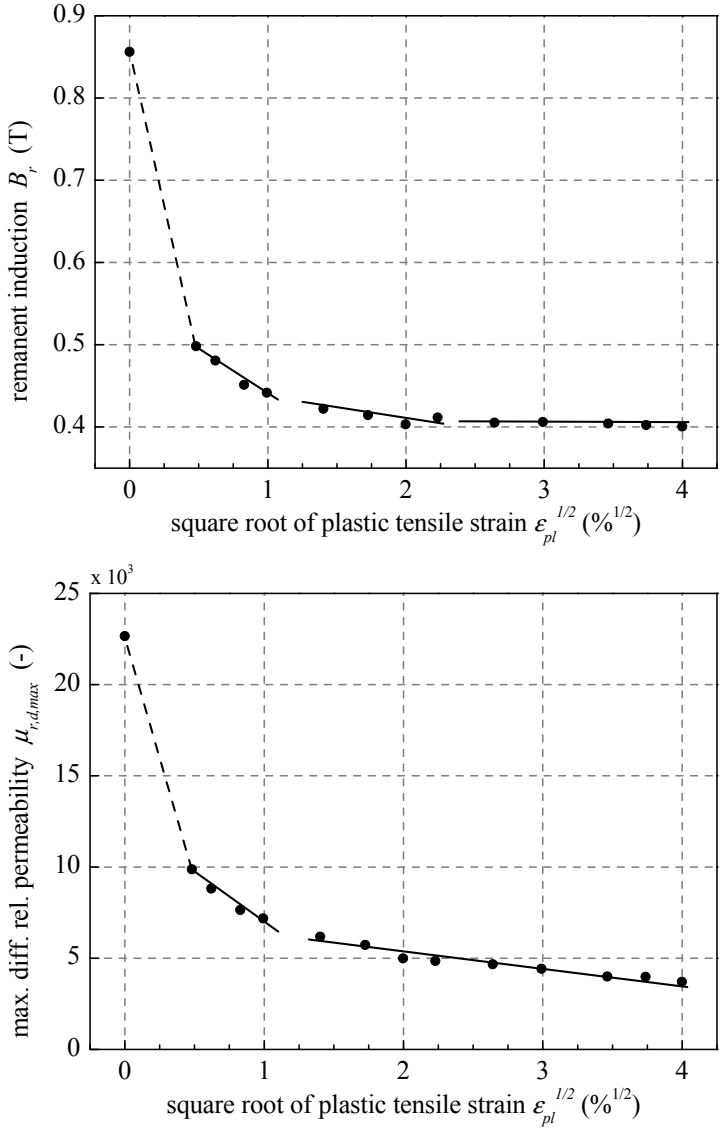

Figure 5.20. Dependence of the remanent induction and of the maximum relative differential permeability on the square root of the plastic strain.

Also shown in figure 5.20 is the dependence of the remanent induction and of the maximum relative differential permeability on the square root of the plastic strain. For these parameters the large difference between the as-received and the first plastically deformed state is a typical feature, see also in the next paragraph about the effect of cold rolling (figure 5.25).

5.2.2 Plastic deformation due to cold rolling

Concerning the effect of plastic deformation, also a second set of experiments is conducted. Instead of the tensile strained sample treated in section 5.2.1, now the magnetic hysteretic characterization is performed on a set of cold-rolled low carbon steel samples.

This set of samples is part of a Round Robin test between different laboratories that is executed in the frame of the "Universal Network for Magnetic Non-Destructive Evaluation" [UNMNDE], an international scientific consortium with academic partners from Japan, UK, USA, Italy, Czech Republic, South Korea, Germany, France, Greece, Hongary, Brazil,... For Belgium, our laboratory EE-LAB takes part in this consortium.

This set of cold-rolled samples originates from Iwate University, Japan, and some details about the samples are already published [Takahashi2006a, Vértesy2008]. The sample preparation is as follows: five low-carbon steel plates (0.16 wt% C, 0.20 wt% Si, 0.44 wt% Mn) were annealed at 900 °C for 1 h, followed by air-cooling. Then, four of them were cold-rolled to a thickness reduction of 5%, 10%, 20% and 40%. Specifically for the Round Robin test magnetic measurements, both Charpy impact test samples and "picture frame" shaped samples are machined out of each plate (also out of the original, not cold-rolled plate), with the longest sample axis along the rolling direction. Dimensions and shape of such samples are shown in figure 5.21.

The microstructure is examined by transmission electron microscopy (TEM). The

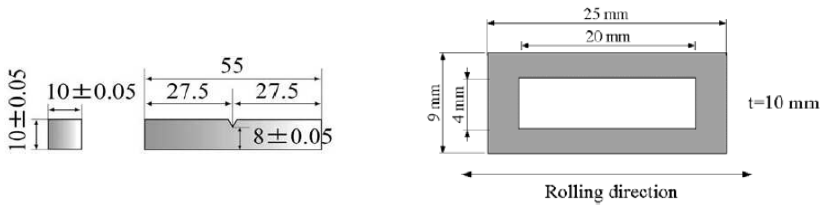

(a) Charpy sample (b) Picture frame

Figure 5.21. Shape and dimensions of the Charpy impact and the picture frame samples.

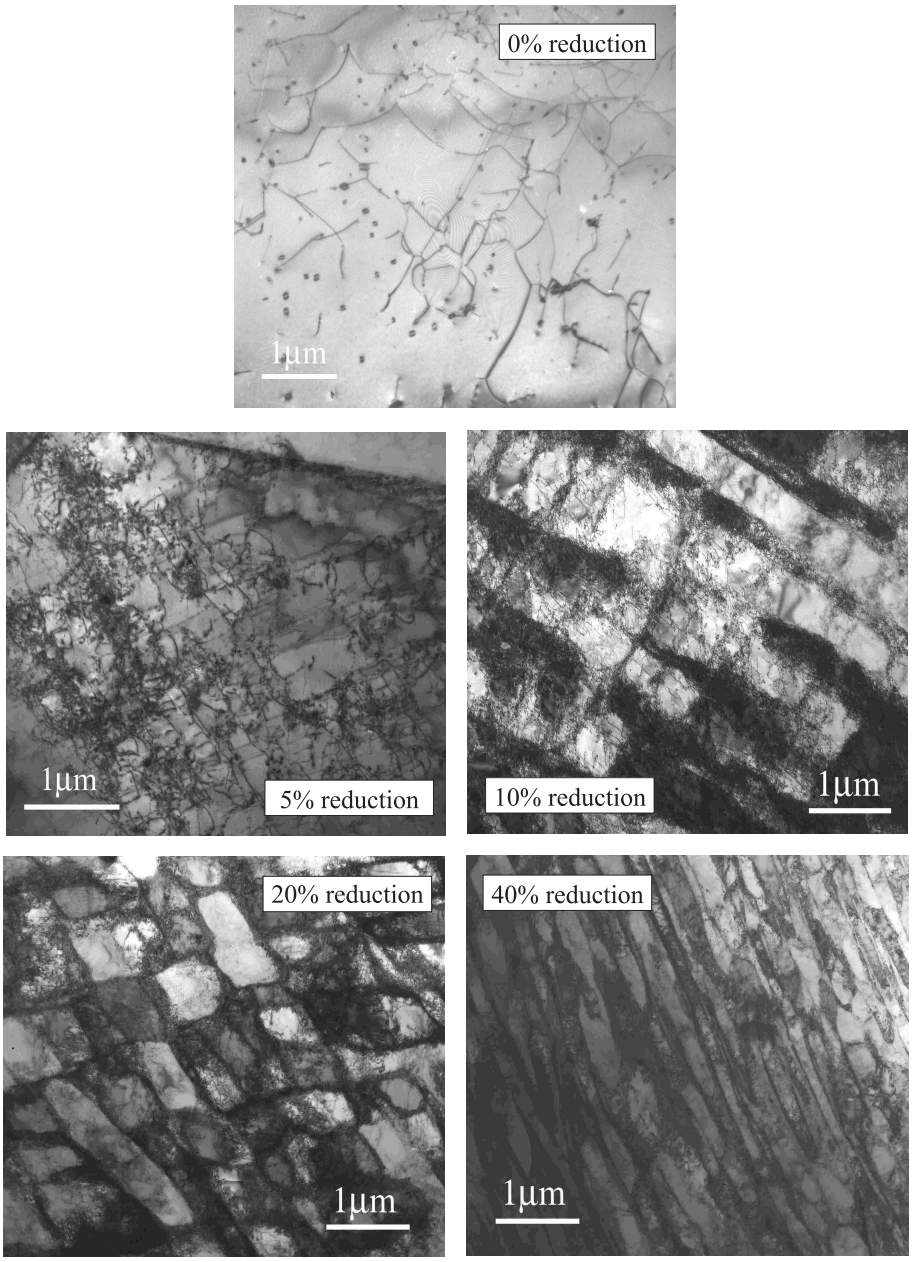

Figure 5.22. TEM images for the five cold rolled samples under investigation [Takahashi2006a].

results are shown in figure 5.22. For the as-received sample (0% rolling reduction) homogeneously distibuted dislocations are visible whereas for higher rolling reduction dense dislocation tangles and dislocation cells are formed. Also the dislocation density increases, from 10^9 cm^{-2} to 10^{11} cm^{-2} [Takahashi2006a].

As destructive mechanical tests, both Charpy impact tests and Vickers hardness measurements are carried out. For the Charpy tests, the absorption energy curves as function of the testing temperature are shown in figure 5.23. The ductile-to-brittle transition temperature (DBTT) and the Vickers hardness are given in figure 5.24 for the five cold-rolled samples. Both parameters increase more or less linearly with the square root of the rolling reduction. Details about both tests can again be found in [Takahashi2006a].

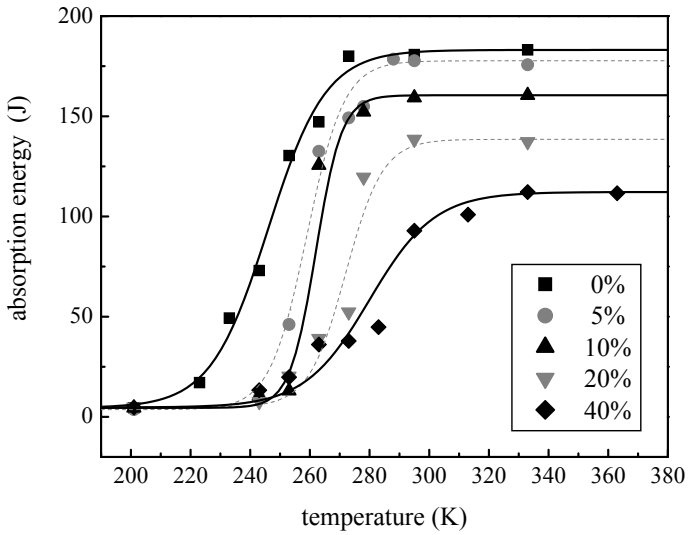

Figure 5.23. Charpy energy versus testing temperature, for the five cold rolled samples under investigation. Since Charpy impact tests give rise to considerable scatter, for each testing temperature five samples were tested and both the largest and smallest values of absorption energy were eliminated when averaging the data [Takahashi2006a].

Magnetic measurements are carried out at EELAB on both the Charpy shaped samples and on the 'picture frame' samples, see figure 5.21 for an illustration about the sample shapes. From the magnetic measurements point of view, the Charpy sample is an open magnetic circuit, whereas the 'picture frame' is a closed magnetic circuit, see chapter 3 for more details about this distinction and the associated differences. For the picture frame, magnetic measurements can easily be performed by adding two windings around the frame, an excitation winding and a measurement winding for the induced voltage.

For the Charpy samples however, magnetic measurements are less straight-forward.

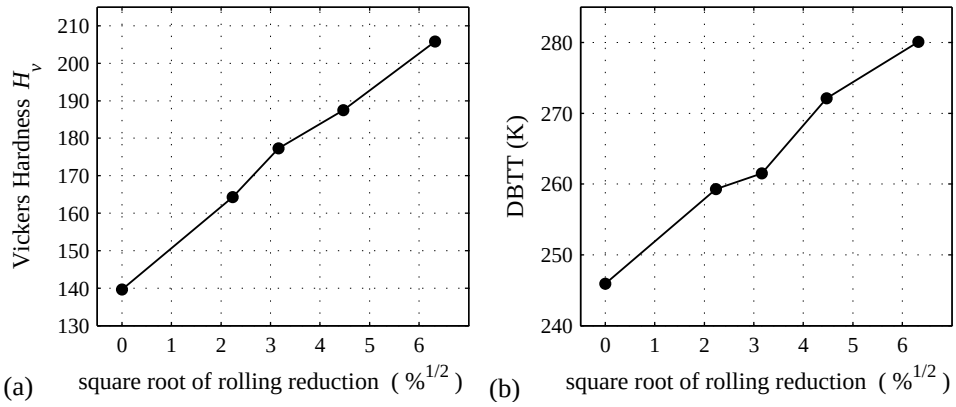

Figure 5.24. Variation of Vickers hardness and DBTT with square root of rolling reduction. The square root dependence is introduced in section 5.2.1. Details about the Charpy test can be found in figure 5.23. For the Vickers hardness, five samples were tested for each reduction and 10 indents were taken for each sample [Takahashi2006a].

The measurements are performed with a specially designed miniature single sheet tester at EELAB, with the incorporation of an array of 3 Hall sensors which are used to determine the magnetic field at the sample surface by extrapolation. This is certainly necessary, since the cross section of the Charpy sample is of the same order of magnitude as the cross section of the closing yoke. As a matter of fact, in section 3.2.2 the measurement setup that is designed especially to measure Charpy samples is treated in more detail.

For both sample types (open and closed), field-metric measurements are performed. Each time, a set of 40 first order symmetric quasistatic magnetization loops is measured (for a range of field amplitudes) at an excitation frequency of 0.05 Hz. The experimentally obtained magnetization loops are then analyzed based on the conventional saturation loop and virgin curve parameters, and based on Preisach hysteresis model features, see chapter 4 for more details about these parameters. The results are combined in figure 5.25. For both Charpy and picture frame measurements, the same trends in the magnetic hysteretic parameters as a function of Vickers hardness is apparent. Remark however that there is no reason to obtain exactly the same absolute values on both Charpy and picture frame samples, since both measurement setups introduce systematic deviations.

Conclusion about the topic of plastic deformation

For both plastic deformation mechanisms (cold-rolling and tensile straining) the degradation of the magnetic parameters with increasing plastic strain is a consequence of the strong pinning effect of the dislocation tangles, walls and clusters,

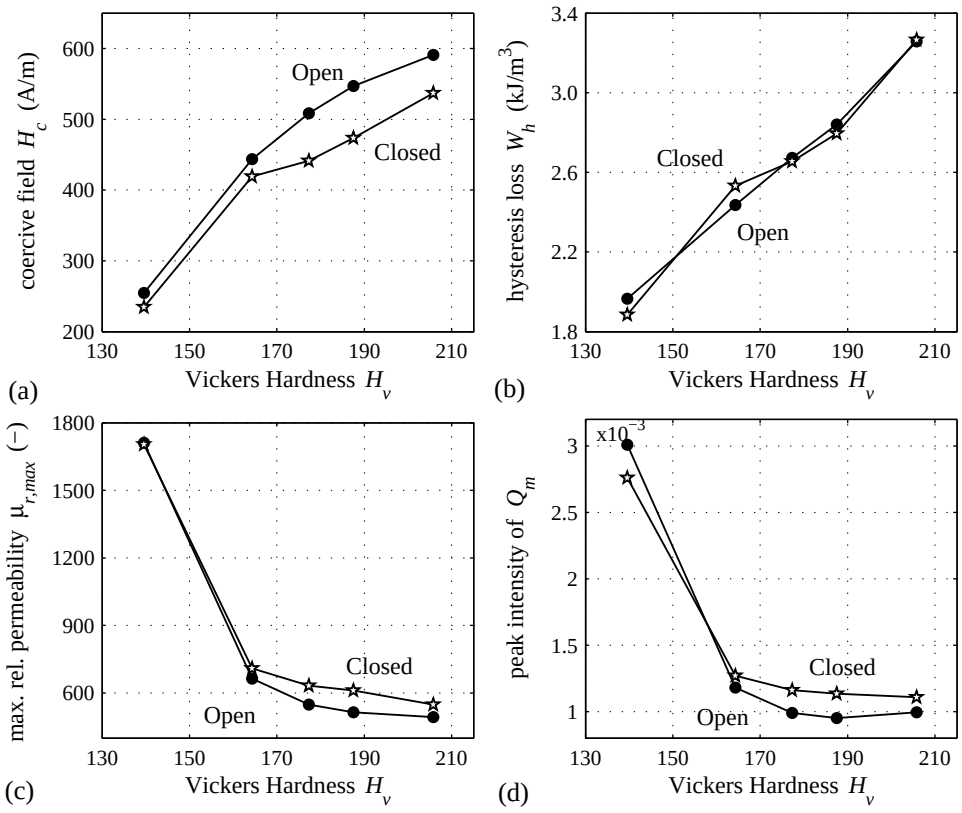

Figure 5.25. Results of the magnetic characterization on both the open (Charpy) and the closed (picture frame) samples.

which obstruct the domain wall motion. The plastic deformation also gives rise to additional stress anisotropy originating from the internal residual stresses that remain in the material after release of applied stresses in the plastic deformation regime. Both effects contribute to the changes in the magnetic behaviour with increasing plastic deformation.

5.3 Localized residual stress, due to cyclic bending

So far, in sections 5.1 to 5.2, we utilized the field-metric method to characterize the *magnetic hysteretic behaviour* in order to evaluate several material degradation processes. The research treated in this section is conceived in a different way, since the underlying motive here is to investigate the potential of another method, i.e. the magnetic drag force method, more specifically its potential for application in the field of magnetic evaluation of *localized* material degradation.

The magnetic drag force method is introduced and treated extensively in section 3.4. The method is based on measuring the force that resists the longitudinal motion of a ferromagnetic strip moving through the magnetic field in the vicinity of a permanent magnet. Considering the underlying mechanism giving rise to the drag force during the sample movement, i.e. the traversal of magnetization loops in the ferromagnetic sample or in other words the reorganisation of the magnetic domain configuration, it is expected that the microstructural changes that affect this magnetic domain reorganisation and consequently the macroscopic magnetic hysteretic behaviour, are also reflected in the experimentally obtained drag force profiles. Therefore, the drag force method shows potential in the field of non-destructive evaluation of ferromagnetic materials.

Moreover, there are two main indications in favour for the drag force method as a magnetic NDE tool for *localized* material degradation. Firstly, one of the inherent features of the drag force method is that the force is measured as a function of longitudinal sample position x and that the majority of the drag force is developed on a small region of the sample localized along its longitudinal axis. Experiments indicate that the measured drag force as a function of longitudinal position shows local minima and maxima (see for example figure 3.30), giving rise to a drag force signature that is repeatable and unique for each investigated strip. This opens perspectives to utilize the drag force method to investigate material properties that are inhomogeneous along the longitudinal axis of the sample.

Secondly, when using one single magnet in the drag force setup (as shown on figure 3.27 and also in this chapter on figure 5.32), the magnetic field inside the strip attenuates with increasing depth from the surface, and therefore the contribution to the resulting drag force decreases with increasing depth. In other words, the drag force measurement is more responsive to the magnetic characteristics of the material closest to the surface, which opens perspectives to exploit the drag force method for the determination of surface localized material properties. These two considerations that are typical for the drag force method, are in contrast with field-metric methods where intrinsically only the bulk magnetic properties, averaged out over a certain volume of the sample, can be determined.

In this context of analyzing the possibilities and the sensitivity of the magnetic

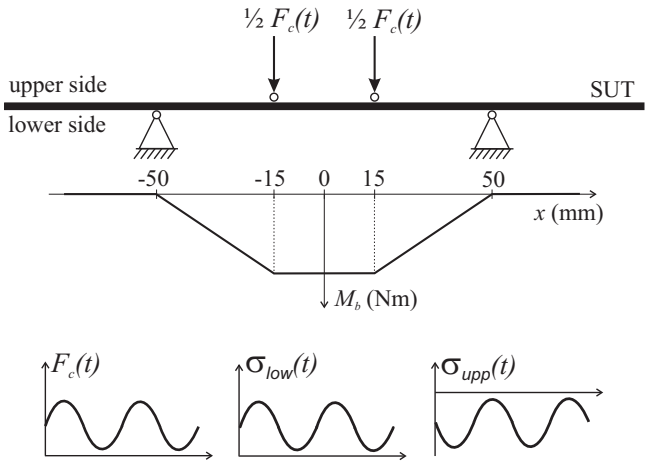

Figure 5.26. Schematical overview of the four-point cyclic bending principle, with indication of the main dimensions. The cyclic force F_c is always applied in the downwards direction, leading to cyclic compressive stresses on the upper sample side and cyclic tensile stresses on the lower sample side. The amplitude of these cyclic stresses is maximal and uniform between the two central upper contact points.

drag force method for the evaluation of localized inhomogeneities in material properties, the method is applied to the assessment of samples subjected to cyclic bending in one direction (see figure 5.26). As we will see in the next paragraph, in that particular case both sample sides are cyclically stressed differently (in compression or in tension). Hence, we assume to see differences in the drag force signature between both sample sides, due to changes in residual micro stress distributions.

Experimental details and procedure

For the cyclic bending of the ferromagnetic samples under investigation, a four-point bending test is used. The principle of four-point cyclic bending is given schematically in figure 5.26, whereas figure 5.27 shows the practical realization of the cyclic bending apparatus designed at EELAB [DierickWarlop2005]. The two upper contact points provide the application of the cyclic force $F_c(t)$ and face the sample side that will be denoted further as the upper sample side, whereas the sample is simply lying with the lower sample side on the two static contact points.

One of the main features of a cyclic bending test implemented with four contact points is that the flexure or the bending moment $M_b(t)$ for all t, is maximal and also uniform in the central part of the sample between the two upper contact points (i.e. sample section [-15 mm ; 15 mm] for our particular setup), leading to stress

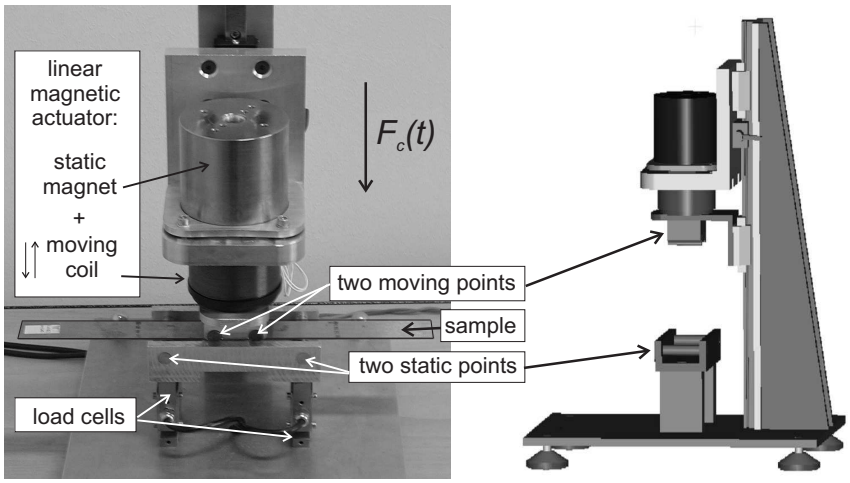

Figure 5.27. Four-point cyclic bending apparatus, designed and constructed at EELAB. A linear magnetic actuator consisting of a static permanent magnet and a moving coil is used for the application of the cyclic force. Attached to the moving coil are the two upper contact points. During operation, this ensemble is moving up and down in such a way that the contact with the investigated sample is always preserved. For this particular application, the typical advantages of a magnetic implementation for the linear actuator are (1) linear dependence of the force on the excitation current, leading to easy control of the force amplitudes; and (2) high acceleration, leading to high mechanical frequencies of the cyclic bending test. For the following experiments, the linear magnetic actuator is operating at a mechanical frequency of 8 Hz.

amplitudes which are maximal for the central sample region and decrease with position x in a linear fashion to reach zero amplitude at the location of the static contact points.

This particular configuration of figures 5.26 and 5.27 restricts the cyclic applied force to be always in downwards direction ($F_c(t) > 0$). Therefore, this apparatus provides the maximal and uniform flexure to the central 30 mm region of the strip in one direction only: during the test, the upper sample side is subjected to cyclic time varying compressive stress, whereas the lower sample side is subjected to cyclic time varying tensile stress.

With this four-point bending machine the following experiment is carried out: three strips, denoted by S1, S2 and S3, are cyclically bent with different set points of flexural stress amplitudes, respectively 165, 175 and 185 MPa, each time for 400 000 cycles. The samples under investigation are made of annealed low carbon AISI C1018 steel, with a yield strength of 320 MPa, and have the following dimensions: 300 mm long, 1.6 mm thick and 25 mm wide.

Both before and after the cyclic bending test, the samples are characterized: (1)

by measuring the drag force signature during forward and backward movement at both surface sides of the sample, and (2) by determining the bulk magnetic hysteretic properties using the field-metric method (with a miniature single sheet tester, see section 3.2.1). For part (1), the magnetic drag force setup is the same as the one that is treated throughout the introduction of the drag force method in section 3.4: one permanent magnet is present above the sample under test, with its magnetic moment parallel to the sample's longitudinal axis (see figure 3.27).

Results and discussion

The drag force experiment is treated extensively in section 3.4: during the forward and backward movement of the ferromagnetic sample underneath a permanent magnet, both the drag force and the position x is measured as a function of time. The measured force is further analyzed and interpreted as a function of strip position x, by relatively aligning the force signals of the two movement directions at equal sample positions x. In the following, the position x = 0 corresponds with both the center of the sample along its length, and with the center of the 30 mm region of maximum flexural stress during the cyclic bending test. Figure 5.28 shows the measured force as a function of position x, experimentally determined on sample S3 for three conditions: (a) before cyclic bending, (b) after cyclic bending, measured with the upper sample side closest to the permanent magnet, and (c) after cyclic bending, measured with the lower sample side closest to the magnet.

When compared to the measured force signature of the initial material condition, it can be seen that the measured force signatures, both for the upper and lower sample side, vary largely over the total sample movement. Moreover, after cyclic bending the force signatures of all the examined strips contain characteristic features which make it possible to distinguish between the upper or the lower sample side: e.g. for the central sample region, F_{meas} during forward movement increases at the upper side, and decreases at the lower side.

Additional and useful information is found when the obtained experimental results are analyzed in terms of the *difference* of both drag force signatures in the two movement directions, defined by $\Delta F_{drag}(x)$, the drag force difference. Notice that this is an intermediate quantity in the energy balance as derived at p. 128:

$$\begin{aligned} W_{mech} &= W_{hyst} \\ \int_{x_1}^{x_2} \Delta F_{drag}(x)\,\mathrm{d}x &= \int_V \left(\int_{t1}^{t3} \mathbf{H} \cdot \frac{\mathrm{d}\mathbf{B}}{\mathrm{d}t} \mathrm{d}t \right) \mathrm{d}V. \end{aligned} \tag{5.4}$$

During the drag force measurement, the sample is moved forward from $x(t_1) = x_1$ to $x(t_2) = x_2$, and then backward from x_2 to $x(t_3) = x_1$, and it is provided

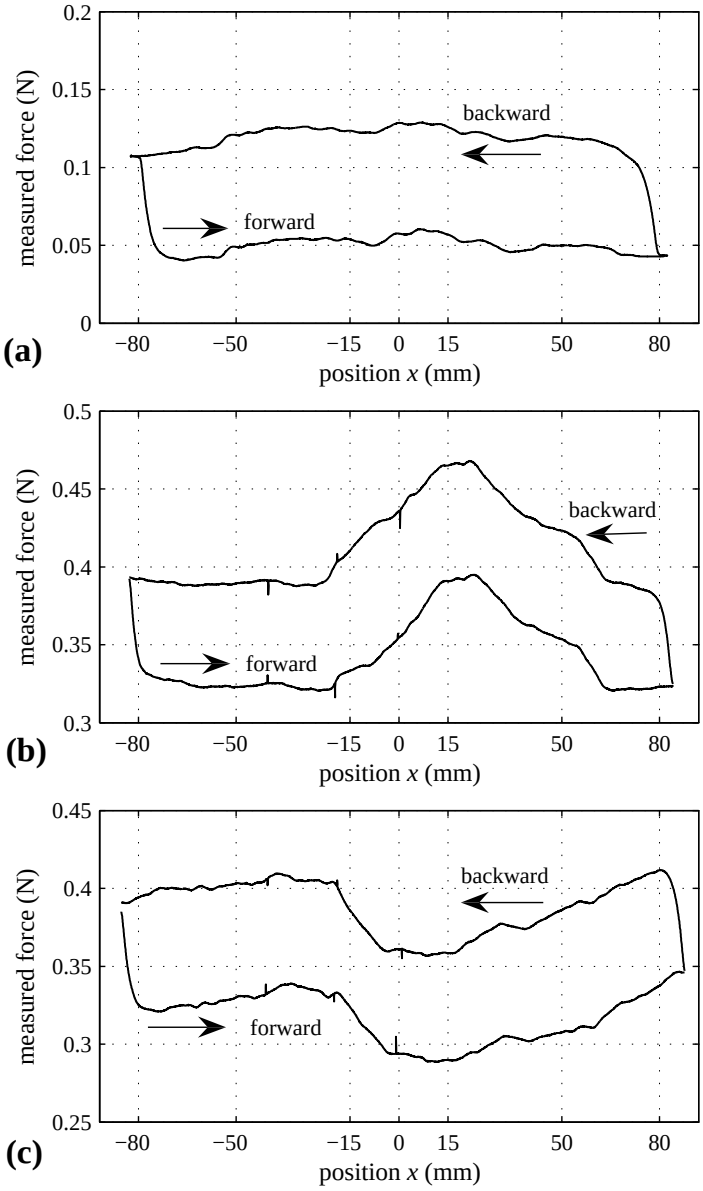

Figure 5.28. Measured force as a function of position x, for sample S3, during movement in forward and backward direction: (a) before the bending test, (b) after the test, with upper sample side closest to magnet, (c) after the test, with lower sample side closest to magnet. Due to the attractive forces between the magnet and the sample ends, the maximum possible travel during the experiment is $\approx$ 160 mm (for a sample length of 300 mm). In subplots (b) and (c) at x = 0, x = -20 mm and x = -40 mm, three position marker pulses of optical origin are noticeable, which were intentionally added to the load cell voltage, to check the position measurement by the linear encoder.

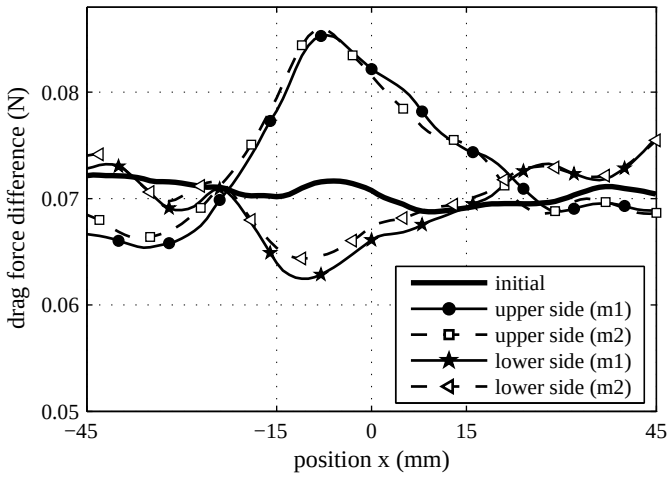

Figure 5.29. Drag force difference ΔF_{drag} as a function of position x, for sample S3, for the initial case and after the test, measured on the upper and lower sample side. To indicate the repeatability, the results are given for two consecutive runs under identical experimental conditions (marked in the figure by 'm1' and 'm2').

that the end magnetic state at t_3 is equal to the initial one at t_1, in other words, the traversed magnetization loops are closed. Therefore the mechanical work done to move the strip from x_1 to x_2 and back to x_1 equals the hysteresis losses of the strip.

Figure 5.29 shows the drag force difference ΔF_{drag} as a function of strip position x, in case of the experiments on sample S3, for the same three conditions as in figure 5.28. For the initial material condition $\Delta F_{drag}(x)$ is more or less constant, illustrating the homogeneous properties of the initial sample. For the lower sample side, $\Delta F_{drag}(x)$ is shown to be lower for positions in the central section of the sample where the maximal uniform flexural stress is applied (-15 mm $< x <$ 15 mm), whereas at the upper sample side, $\Delta F_{drag}(x)$ shows higher values for the central section of the sample. This indicates that by investigating the quantity $\Delta F_{drag}(x)$ it becomes again possible to distinguish between the lower side (decrease of ΔF_{drag}) and the upper side (increase of ΔF_{drag}) of the sample.

Define the parameter ΔF_{center} as the average of the drag force difference ΔF_{drag} for the central 20 mm of the sample: $\Delta F_{center} = \frac{1}{b-a} \int_a^b \Delta F_{drag}(x) \mathrm{d}x$, with a = -10 mm and b = 10 mm. In figure 5.30 the post-stressed values of this parameter ΔF_{center} are compared with its initial values (before the bending test) for each of the three investigated samples, i.e. as a function of the flexural stress amplitude. This is done by introducing the parameter R, defined as the ratio between ΔF_{center}(after test) and ΔF_{center}(initial). For the upper sample side, $R > 1$ (i.e.

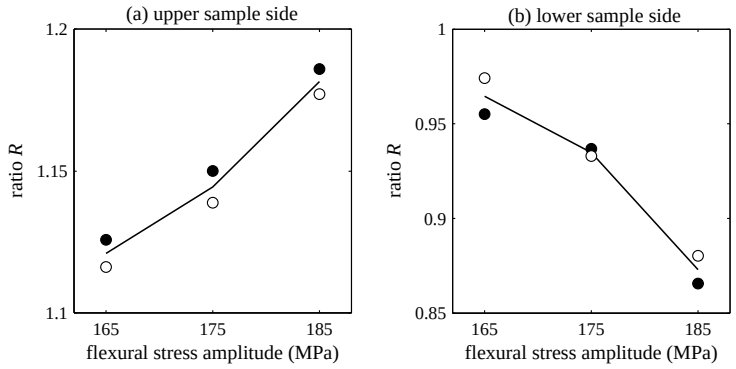

Figure 5.30. Ratio R between ΔF_{center}(after test) and ΔF_{center}(initial), as a function of flexural stress amplitude, for both the upper and the lower sample side. The markers indicate two experimental results under identical conditions to give an idea about the repeatability of the experiments.

ΔF_{center}(upper side, after test) $> \Delta F_{center}$(initial), see also figure 5.29), and this ratio R is found to increase with increasing flexural stress amplitude. For the lower sample side, $R < 1$, and this ratio decreases with increasing flexural stress amplitude.

In figure 5.31 the drag force results, obtained on both sample sides, are compared with field-metric results measured on the same samples. The comparison is car-

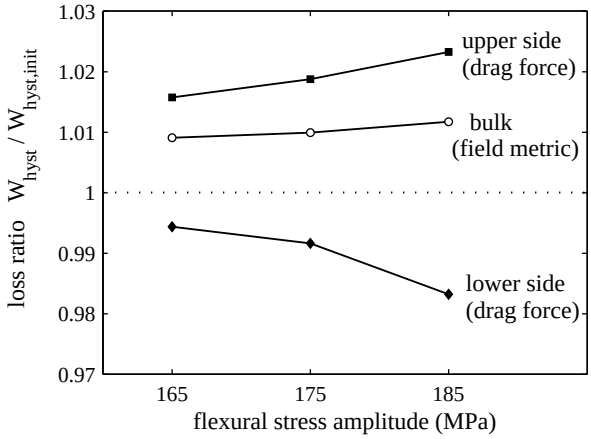

Figure 5.31. Comparison between drag force results, obtained on both sample sides, and field-metric results measured on the same samples, based on the ratio between the hysteresis losses W_{hyst} after bending and the initial values of the hysteresis losses $W_{hyst,init}$ before the tests.

ried out based on hysteresis loss values; remember that hysteresis losses W_{hyst} can be estimated based on the drag force difference $\Delta F_{drag}(x)$, see formula (5.4). The parameter that is used for this comparison is the loss ratio between the hysteresis losses W_{hyst} after bending (at a certain flexural stress amplitude) and the initial values of the hysteresis losses $W_{hyst,init}$ before the tests. It is seen that compared to the field-metric method the drag force measurement is more sensitive, and moreover based on the results one can distinguish between both sides of the cyclicly bent samples.

Drag force simulations

Furthermore, numerical simulations are performed on the geometry of figure 5.32 to qualitatively check some of the obtained experimental results. To calculate the drag force during the forward and backward movement of the strip under the magnet, a numerical time-stepping model is used, introduced in section 3.4 (pp. 130–134), which is based on 2D finite element computations, with incorporation of the magnetic hysteretic material behaviour using the Preisach model. Firstly, the drag force is simulated for a strip with homogeneous magnetic properties (see figure 5.33, 'initial'): the drag force difference ΔF_{drag} as a function of position x is constant, which is consistent with the experimentally obtained results. Secondly, simulations are performed for a strip with the same magnetic properties, except for the upper half of the central region (-10 mm $< x <$ 10 mm): this region, marked as 'B' in figure 5.32, is described by a modified Preisach distribution function corresponding with a decreased (case 1) or increased (case 2) differential relative permeability $\mu_{r,d}(H)$. The simulation results indicate that a locally decreased permeability results in a locally increased drag force difference, whereas a locally

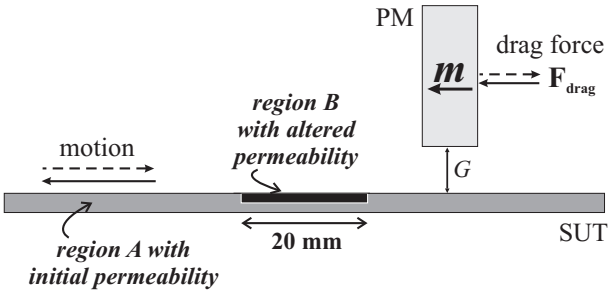

Figure 5.32. Geometry that is used for the numerical drag force simulations treated in this paragraph. Simulations are performed with different differential relative permeability $\mu_{r,d}(H)$ in subregion 'B' of the sample. Additional simulation details: the total travel of the sample is 120 mm, the sample length is 300 mm, the sample thickness is 1 mm and the air gap G is 3.5 mm. Due to numerical stability considerations it was necessary to work in the simulations with a larger G than the experimental one.

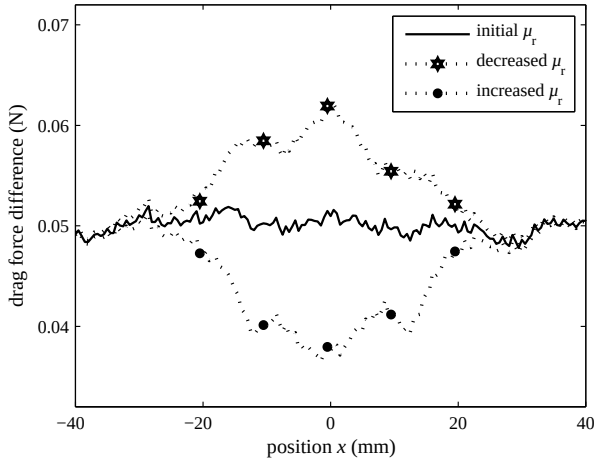

Figure 5.33. Calculated drag force difference ΔF_{drag} as a function of x, as a result of three simulations with different differential relative permeability $\mu_{r,d}(H)$ in subregion B of the sample. ('initial'): permeability of subregion B is same as for the rest of the sample. ('decreased'): permeability of subregion B is lower than for the rest of the sample. ('increased'): permeability of subregion B is lower than for the rest of the sample.

decreased drag force difference is seen for a locally increased permeability.

Conclusion about drag force results (section 5.3)

By analyzing the difference in drag force signature between both forward and backward movement directions, it is possible to deduce whether a part of material was, during a cyclic bending test, subjected to applied cyclic compression or tension. Moreover, the position of the localized stressed region can be indicated. Further quantitative analysis shows that the increase of flexural stress amplitude leads to an increased variation between the drag force difference corresponding to the localized stressed region, and the drag force difference of an unaffected part of the material.

The experimentally observed changes in drag force signature after the cyclic bending test indicate the occurrence of a certain degree of structural damage, which apparently has magnetic consequences. It is presumed that the difference in drag force signature is due to changes in micro residual stress distribution across the thickness of the sample, altering the magnetic anisotropy.

Based on the difference of the drag force profiles in both movement directions, it is possible to deduce whether some part of material was, during a bending test, subjected to applied compression or tension, and also the position of the localized

stressed region can be indicated. Hence the drag force method shows potential towards magnetic NDE of macro and micro residual stress inhomogeneities that are located on/near the surface.

Chapter 6

Effect of fatigue damage on the magnetomechanical behaviour

Mechanical stress is, together with magnetic field, one of the primary factors that can change the magnetization of a ferromagnetic substance. In section 6.1 we explore some features of the so-called magnetomechanical behaviour, i.e. the combined effects of elastic mechanical stress and magnetic field on the magnetization. Magnetomechanical experiments are conducted for three different material classes (different, concerning their magnetomechanical behaviour), and for different conditions of elastic stress and magnetic field (both as static or dynamic quantities).

Such an experimental study of the magnetomechanical behaviour is performed in order to better understand the physical mechanisms involved, with the aim to develop magnetic non-destructive evaluation methods for the continuous monitoring of the metal fatigue damage process, a subject which is treated in section 6.2.

6.1 Magnetomechanical behaviour

6.1.1 Magnetomechanical behaviour on the magnetic domain scale

As introduced in the framework of the micromagnetic theory (section 2.3), not only the application of an external magnetic field, but also the application of an external mechanical stress[1] can lead to the rotation of the local magnetic moments at the microscopic scale. In other words, an applied mechanical stress leads to

[1]The following convention is valid throughout this work: tensile stress is positive ($\sigma > 0$), compressive stress is negative ($\sigma < 0$).

the motion of magnetic domain walls and therefore can have an influence on the macroscopic magnetization of a ferromagnetic substance.

When mechanical stress is applied to a ferromagnetic material, the direction of the local magnetic moments is mainly controlled by the combined action of the magnetocrystalline anisotropy energy and the magnetoelastic interaction energy.

The *magnetocrystalline anisotropy energy* gives rise to the existence of preferred crystallographic directions for the local magnetic moments (so-called easy directions), such as for instance the $\langle 100 \rangle$ directions in case of iron crystals. A demagnetized ferromagnetic crystal for instance is composed of multiple magnetic domains with for each magnetic domain the domain magnetization vector along one of the possible easy directions.

The *magnetoelastic energy* arises from the micro-scale interactions between the magnetization and the mechanical strain in the crystal lattice. As a reminder, starting from formula (2.37) describing the magnetoelastic coupling energy according to the so-called relaxed approach (see section 2.3.4, page 64), and when only considering here the macroscopically applied stress $\overline{\sigma}_{appl}$ (so disregarding $\overline{\sigma}_{def}$, the stress field due to crystal defects):

$$w_{me} = -\overline{\sigma}_{appl} \cdot\cdot \overline{\varepsilon}_{\lambda,sp}. \tag{6.1}$$

A simplified but nevertheless instructive formula for the magnetoelastic energy contribution arising from an unidirectionally applied mechanical stress σ_{appl}, assuming unidirectional magnetostriction λ, and with θ equal to the angle between the spontaneous magnetization and the applied uniaxial stress σ_{appl} is [Sablik1988]:

$$w_{me} \;=\; -\frac{3}{2}\,\lambda\,\sigma_{appl}\cos^2\theta. \tag{6.2}$$

This formula reflects qualitatively that if the unidirectional magnetostriction λ and the applied stress σ_{appl} have the same sign, then the magnetoelastic energy is lowest for magnetic domains with $\theta = 0$ (spontaneous magnetization and applied stress direction are parallel). On the other hand, if λ and σ_{appl} have opposite sign, then the magnetoelastic energy is lowest for magnetic domains with $\theta = 90^\circ$ (spontaneous magnetization and applied stress direction are perpendicular).

Let us start the description of the magnetomechanical behaviour with the effect of a **constant uniaxial stress applied to a demagnetized specimen**, so without any applied magnetic field. Figure 6.1 visualizes the stress-induced magnetic domain processes in a simplified but qualitative way with the aid of a domain configuration consisting of four domains separated by 90° and 180° domain walls. Domain configuration (a) corresponds in this simplified scheme to the demagnetized state.

Further, consider a material that elongates if a magnetic field is applied, in other words a material with positive magnetostrictive behaviour ($\lambda > 0$). When applying a certain value of tensile stress ($\sigma_{appl} > 0$) along the $\mathbf{e}_y$-direction to a

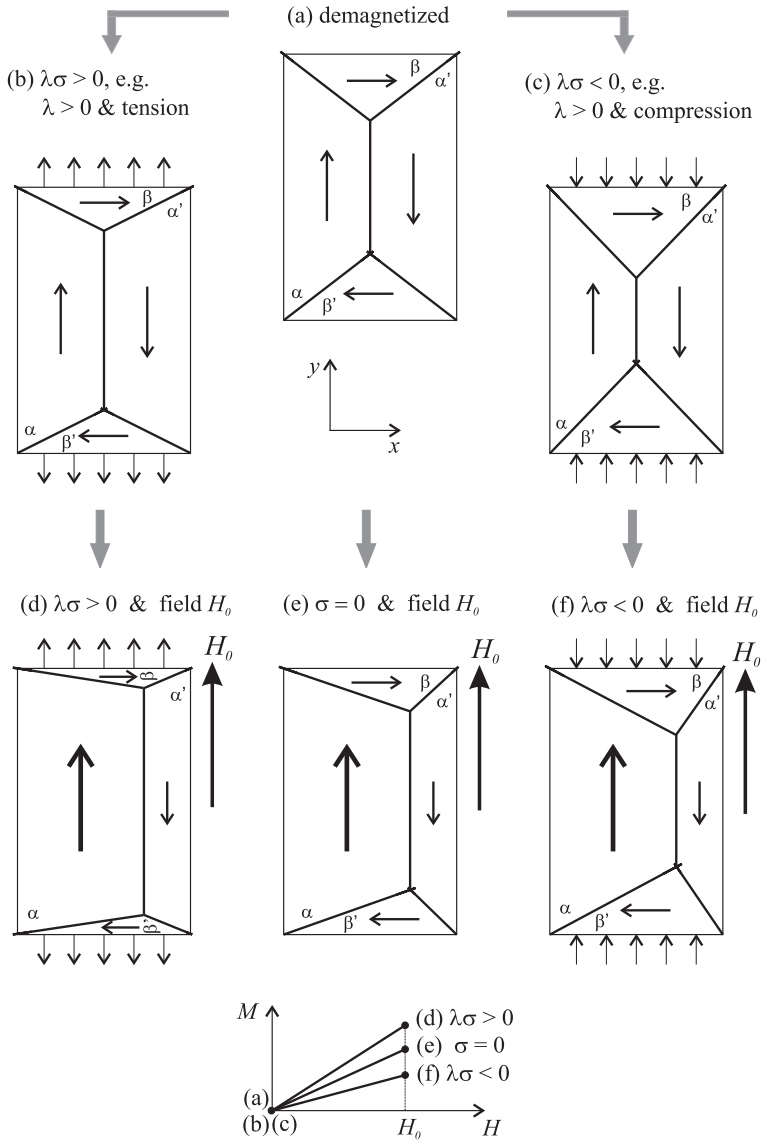

Figure 6.1. Effect of constant applied elastic tension ($\sigma > 0$) or elastic compression ($\sigma < 0$) on a simplified configuration with four domains α, α', β and β', starting from the demagnetized state (a). Here, to keep the notation short in this figure σ stands for the applied stress. Situation (b) corresponds with $\lambda\sigma > 0$, (c) corresponds with $\lambda\sigma < 0$. Here, a material with positive magnetostrictive behaviour ($\lambda > 0$) is considered. In part two of this figure, (d)(e)(f), the effect of applying a constant uniaxial magnetic field, after the application of a constant elastic stress, is illustrated on the four-domain configuration. More description in the accompanying text.

material having positive magnetostrictive behaviour, as shown in figure 6.1(b), then the magnetic domains α and α' along the $\mathbf{e}_y$-direction become energetically favoured: the magnetoelastic energy of domains α and α' in situation (b) is decreased compared to the demagnetized situation (a), according to (6.2), whereas the magnetoelastic energy of β and β' remains invariant when comparing situation (b) to (a), since $\cos^2\theta = 0$, for β and β'. Therefore domains α and α' grow at the expense of domains β and β', by the motion of the 90° domain walls, leading to the domain configuration of figure 6.1(b).

On the other hand, when applying a certain value of compressive stress ($\sigma_{appl} < 0$) along $\mathbf{e}_y$ to a demagnetized ferromagnetic sample with positive magnetostrictive behaviour, then the magnetoelastic energy of domains α and α' increases compared to the demagnetized state, according to (6.2). Therefore these magnetic domains shrink in size, again by the motion of 90° domain walls, compare figure 6.1(c) with (a).

For a material with negative magnetostrictive behaviour ($\lambda < 0$), the effect is just the opposite as the one described above, i.e. for materials with negative magnetostriction situation (b) corresponds with compression, whereas situation (c) corresponds with tension.

Also, the second part of figure 6.1 shows the effect of **applying a constant uniaxial magnetic field, after the application of a constant uniaxial stress**, see situation (d) for tensile stress and (f) for compressive stress (in case of a material with positive magnetostrictive behaviour). As a comparison, situation (e) shows schematically the domain configuration at zero stress due to applied magnetic field. Now, due to the applied field energy only domain α is energetically favoured and all other domains α', β and β' shrink in size by both 180° and 90° domain wall motion.

The change in magnetization M along the $\mathbf{e}_y$-direction is given at the bottom of figure 6.1 for all mentioned situations. As can be seen from the domain configurations (b) and (c), it is theoretically predicted that a mechanical stress applied to a demagnetized specimen does not produce any net magnetization, which is verified by experiments, see further in section 6.1.4: applying a cyclic elastic stress on a demagnetized sample does not alter the magnetization.

Although the configuration of figure 6.1 is a simplified one, since the stress direction and the field direction are taken parallel to an easy axis, generally speaking the conclusions remain the same for an applied uniaxial mechanical stress and an applied uniaxial magnetic field which both make a certain angle with an easy axis:

- Mechanical stress induces a preferential occupancy of one of the three easy directions, an effect which is called *stress anisotropy*. This stress anisotropy is determined by the sign of the product $\lambda\sigma_{appl}$. When dealing with positive magnetostrictive behaviour and tensile applied stress, then the domain mag-

netization vectors along the easy crystallographic direction that is oriented closest to the uniaxial applied stress axis are favoured. When dealing with positive magnetostrictive behaviour and compressive applied stress, then the domain magnetization vectors along the nearest easy crystallographic direction that is oriented perpendicular to the uniaxial applied stress axis are favoured. For a material with negative magnetostrictive behaviour the effect is just the opposite as the one described above.

- Mechanical applied stress leads to the motion of 90° domain walls but not to the motion of 180° walls, since the magnetoelastic energy of both domains separated by a 180° wall is equal: according to (6.2), and even if the applied mechanical stress makes a certain angle $\theta \neq 0$ with the domain magnetization vector, the expression $\cos^2\theta$ is equal for domains α and α'.
- Mechanical stress applied to a demagnetized specimen does not produce any net magnetization. This theoretical result is verified experimentally by applying a cyclic elastic stress on a demagnetized sample, see section 6.1.4.

6.1.2 Magnetomechanical behaviour on the macroscopic scale

The effect of applied mechanical stress on the macroscopic magnetization, in most cases in combination with the application of a certain magnetic field, is called the *magnetomechanical effect*. Such magnetomechanical behaviour is, together with the tightly connected phenomenon of magnetostriction, the macroscopic outcome of the magnetoelastic coupling. The general conceptual framework of the macroscopic magnetoelastic coupling, as introduced already in section 2.1, is shown schematically in figure 6.2. In our study, all four macroscopic properties magnetic field H, mechanical stress σ, magnetization M and strain ε are considered along the same direction and can be expressed as scalar properties.

In the most general case the ferromagnetic material under test is subjected to both a time-dependent applied magnetic field and a time-dependent applied mechanical

Figure 6.2. Concept of macroscopic magnetoelastic coupling, shown schematically as an input-output system with the applied magnetic field and the applied mechanical stress as inputs and the resulting bulk magnetization and longitudinal strain as outputs.

stress. Both the resulting magnetization and the elongation appear to be dependent on both inputs:

$$\begin{bmatrix} M \\ \varepsilon \end{bmatrix} = \begin{bmatrix} M(H,\sigma) \\ \varepsilon(H,\sigma) \end{bmatrix} = \begin{bmatrix} \chi(H,\sigma) & f_1(H,\sigma) \\ f_2(H,\sigma) & s(H,\sigma) \end{bmatrix} \begin{bmatrix} H \\ \sigma \end{bmatrix} \tag{6.3}$$

with $\chi(H,\sigma)$ the magnetic susceptibility, $s(H,\sigma)$ the mechanical compliance, and with the cross terms $f_1(H,\sigma)$ and $f_2(H,\sigma)$ representing the macroscopic magnetoelastic coupling.

In the following we focus on the magnetomechanical effect $M = M(\sigma, H)$. In order to investigate the magnetomechanical behaviour experimentally, a combined mechanical and magnetic setup is designed and built at EELAB, see section 3.3.

Both magnetic field and mechanical stress can be static or dynamic quantities. Therefore in the following paragraphs three distinct cases of magnetomechanical behaviour are examined:

1. magnetization variation under the application of a constant elastic stress σ_0 and a time-dependent magnetic field (section 6.1.3):

$$M(t) = M(\sigma_0, H(t)); \tag{6.4}$$

2. magnetization variation under the application of a time-dependent cyclic elastic stress and a constant magnetic field H_0 (section 6.1.4):

$$M(t) = M(\sigma(t), H_0); \tag{6.5}$$

3. magnetization variation under the application of a time-dependent cyclic elastic stress and a time-dependent cyclic magnetic field, with the magnetic excitation frequency significantly larger than the mechanical frequency (section 6.1.5):

$$M(t) = M(\sigma(t), H(t)). \tag{6.6}$$

The theoretical description at the beginning of this chapter (section 6.1.1) indicates that the magnetostrictive and magnetomechanical behaviour are tightly coupled. Therefore, concerning their magnetomechanical behaviour, ferromagnetic materials can be divided into three different classes:

- materials with negative magnetostriction (e.g. nickel and cobalt),
- materials with positive magnetostriction (e.g. Fe-Ni alloys with less than 80% Ni-content [Bozorth1951]), and last but not least:
- materials for which the sign of the magnetostriction (positive or negative) depends on the applied magnetic field and/or the applied mechanical stress (e.g. iron and low-alloyed ferritic steels).

Table 6.1. Some details about the three different materials on which the magnetomechanical behaviour is examined in section 6.1.

material	**nickel**	**18%-Ni maraging steel**	**low-carbon steel**
magneto-striction	always negative	always positive	positive or negative, depends on H and σ
composition (wt%)	100% Ni	77% Fe, 18.5% Ni, 3% Mo, 1.4% Ti, 0.1% Al, 0.03% C	99.1% Fe, 0.52 % Mn, 0.12% C
yield stress	70 MPa	350 MPa	390 MPa
sample dimensions	strip 0.254 mm thick 25 mm wide	strip 0.69 mm thick 25 mm wide	cylindrical rod hour-glass shape 4 mm diameter
remarks	as received nickel	"maraging" stands for: martensitic, obtained after thermal aging	hot-rolled ferritic steel (also called 'mat-B'

In the next paragraphs we shall discuss the experimentally observed magnetomechanical behaviour of three materials which are characteristic for the three material classes described above, see table 6.1.

In this research work our interest is mainly on ferritic low-carbon steels. Compared to the other two material classes, we shall see that the magnetomechanical behaviour of ferritic steels is less straight-forward: for instance the magnetization versus stress dependence shows non-monotonic features, reflecting the also more complex magnetostrictive features.

6.1.3 Case 1: static elastic stress and dynamic magnetic field

In this paragraph the results are combined of the experimentally observed magnetic hysteretic and magnetic anhysteretic behaviour, measured under the application of various values of static elastic stress, and this for the three materials that are introduced in table 6.1. The experimental procedure is as follows:

1. After demagnetizing the sample, a certain value of static elastic tensile or compressive uniaxial stress is applied.
2. For each set point of static elastic stress σ_0, the anhysteretic magnetization curve is measured on a point by point basis with the field-metric method. The anhysteretic magnetization value M_{anh} is determined experimentally for a certain value H_0 of the magnetic field by applying to the sample under constant stress σ_0 a particular magnetic field waveform $H(t)$, which is the superposition of that particular value H_0 and an alternating magnetic field

waveform with decaying field amplitude. During this process the magnetization evolves towards the final magnetization value at equilibrium (when $H(t)$ has become H_0) which is the anhysteretic magnetization value M_{anh} that corresponds with $H = H_0$. To obtain the complete magnetization curve $M_{anh}(H)$, this procedure is then repeated for a set of magnetic field values.

The results of such measurements are given in figures 6.3 to 6.5 for the three materials introduced in table 6.1. Part (a) of these figures shows M_{anh} as a function of H, for a selection of σ_0 values. Part (b) of these three figures gives an alternative presentation of the magnetic anhysteretic behaviour, i.e. M_{anh} as a function of σ_0, for a selection of H values, and can be envisaged as the anhysteretic or reversible magnetomechanical behaviour [Hubert2008, Langman1985].

3. For each set point of elastic stress also the hysteretic behaviour is measured. Results are in figures 6.6 to 6.8 for the three investigated materials.

In case of **nickel**, for a given value of magnetic field the *anhysteretic* magnetization decreases with increasing (tensile) stress, in other words $\frac{\mathrm{d}M_{anh}}{\mathrm{d}\sigma} < 0$ for all considered values of elastic σ and H, see figure 6.3.

For nickel the magnetostriction is negative, with a saturation magnetostriction value at zero stress equal to $\lambda_s = -35{\cdot}10^{-6}$, and $\frac{\mathrm{d}\lambda}{\mathrm{d}H} < 0$ for all considered elastic σ and positive H values [Cullity1972]. In other words, from the experiments on nickel it follows that the sign of $\frac{\mathrm{d}M_{anh}}{\mathrm{d}\sigma}$ corresponds with the sign of $\frac{\mathrm{d}\lambda}{\mathrm{d}H}$, both are negative for all considered static elastic σ and positive H.

Dealing with the *hysteretic* properties, the coercive field increases linearly, the remanent induction decreases linearly, and the permeability also decreases with increasing (tensile) elastic stress, see figure 6.6.

For **18%-Ni maraging steel**[2], a material with positive magnetostrictive behaviour ($\lambda_s \approx 32{\cdot}10^{-6}$ at zero stress, and $\frac{\mathrm{d}\lambda}{\mathrm{d}H} > 0$, for all considered elastic σ and positive H [Garshelis1990]), the effect of stress on the reversible anhysteretic magnetomechanical behaviour, and the effect of stress on the magnetic hysteretic properties are just the opposite as compared to negative magnetostrictive materials.

For a given value of magnetic field the *anhysteretic* magnetization increases with increasing (tensile) stress, in other words $\frac{\mathrm{d}M_{anh}}{\mathrm{d}\sigma} > 0$, for all considered values of elastic σ and H, see figure 6.4. So, again the sign of $\frac{\mathrm{d}M_{anh}}{\mathrm{d}\sigma}$ corresponds with the sign of $\frac{\mathrm{d}\lambda}{\mathrm{d}H}$, both are positive for all considered static elastic σ and positive H.

[2]The generic term "maraging" is derived from the martensitic phase of the matrix, and from the fact that the material is heat treated by a moderate temperature aging process to obtain high mechanical strength.

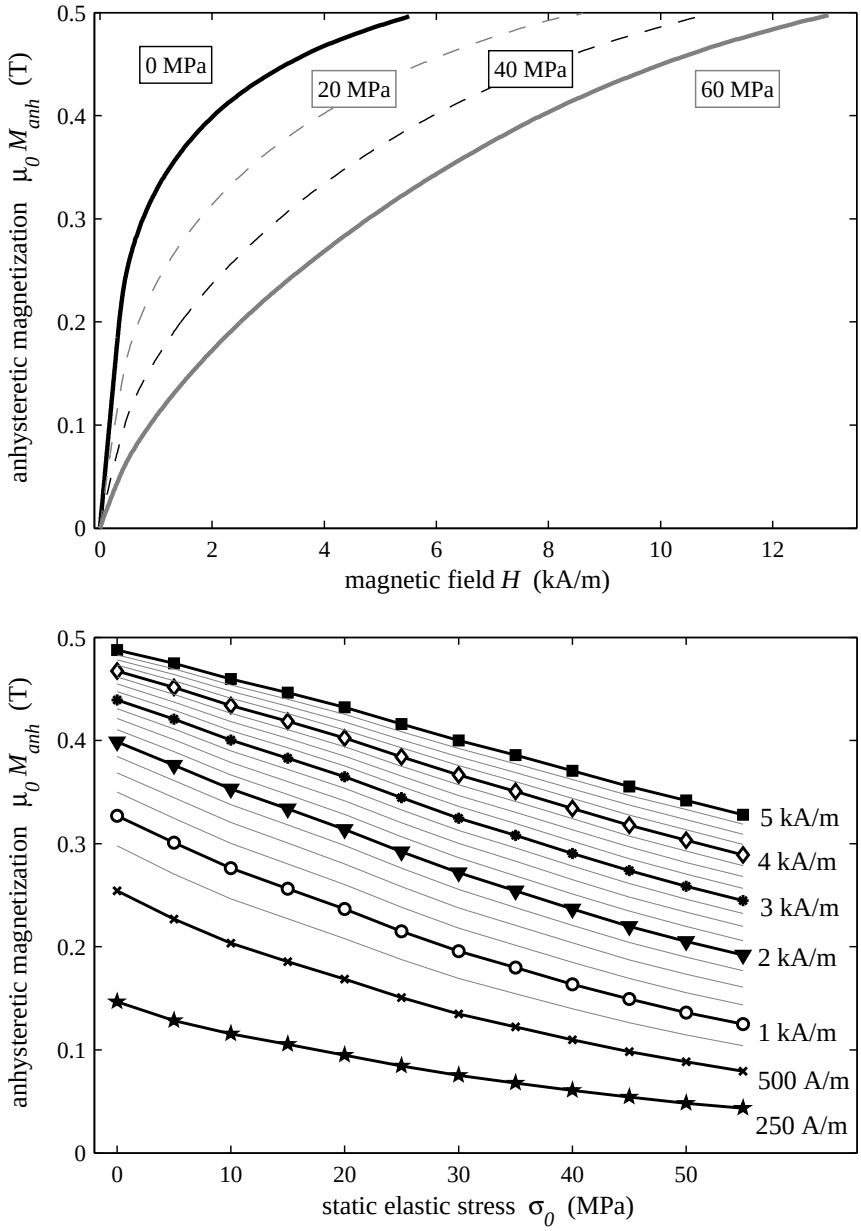

Figure 6.3. For **nickel**: (a) experimentally determined anhysteretic curves $M_{anh}(H)$, for a selection of applied static elastic tensile stress values σ_0 (yield stress = 70 MPa); (b) alternative presentation of the anhysteretic magnetomechanical behaviour, i.e. M_{anh} as a function of σ_0, for a selection of H values (step in H: 250 A/m). Due to the small thickness of the strip-shaped sample (0.254 mm) the sample is buckling under compressive stress, so it is not possible to perform experiments under compression.

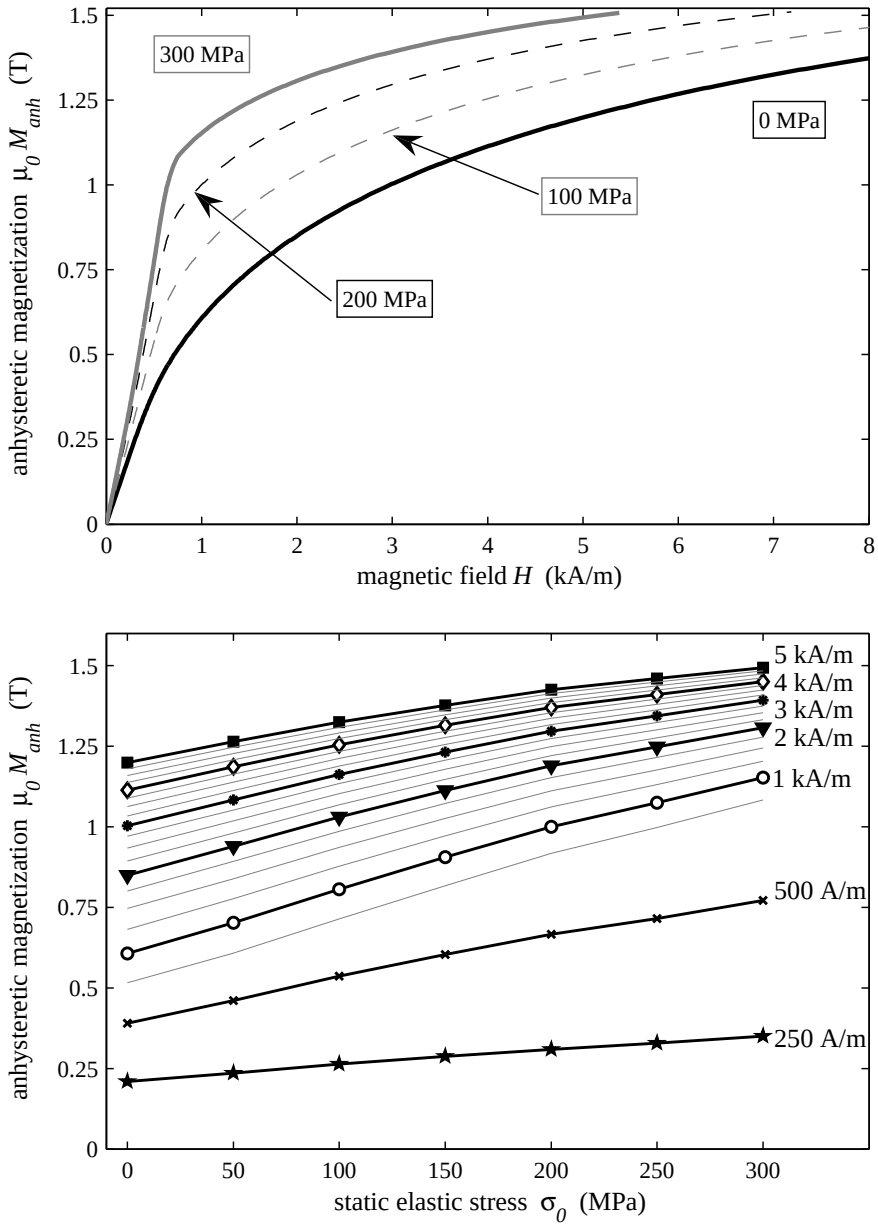

Figure 6.4. For **18%-Ni maraging steel**: (a) experimentally determined anhysteretic curves $M_{anh}(H)$, for a selection of applied static elastic tensile stress values σ_0 (yield stress = 350 MPa); (b) alternative presentation of the anhysteretic magnetomechanical behaviour, i.e. M_{anh} as a function of σ_0, for a selection of H values (step in H: 250 A/m). Due to the small thickness of the sample (0.69 mm) the sample is buckling under compressive stress, so it is not possible to perform experiments under compression.

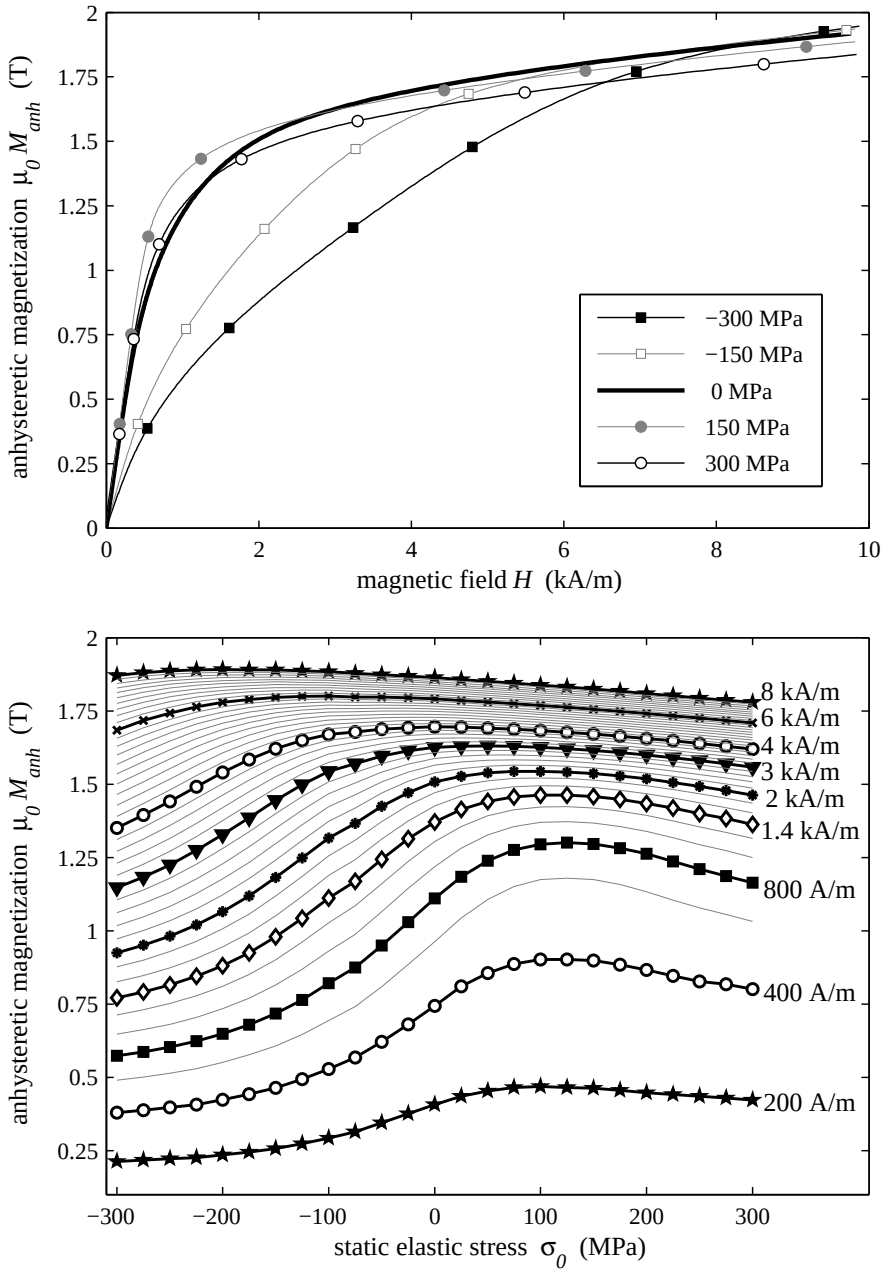

Figure 6.5. For **low-carbon steel**: (a) experimentally determined anhysteretic curves $M_{anh}(H)$, for a selection of applied static elastic tensile and compressive stress values σ_0 (yield stress = 390 MPa); (b) alternative presentation of the anhysteretic magnetomechanical behaviour, i.e. M_{anh} as a function of σ_0, for a selection of H values (step in H: 200 A/m). Material: steel mat-B.

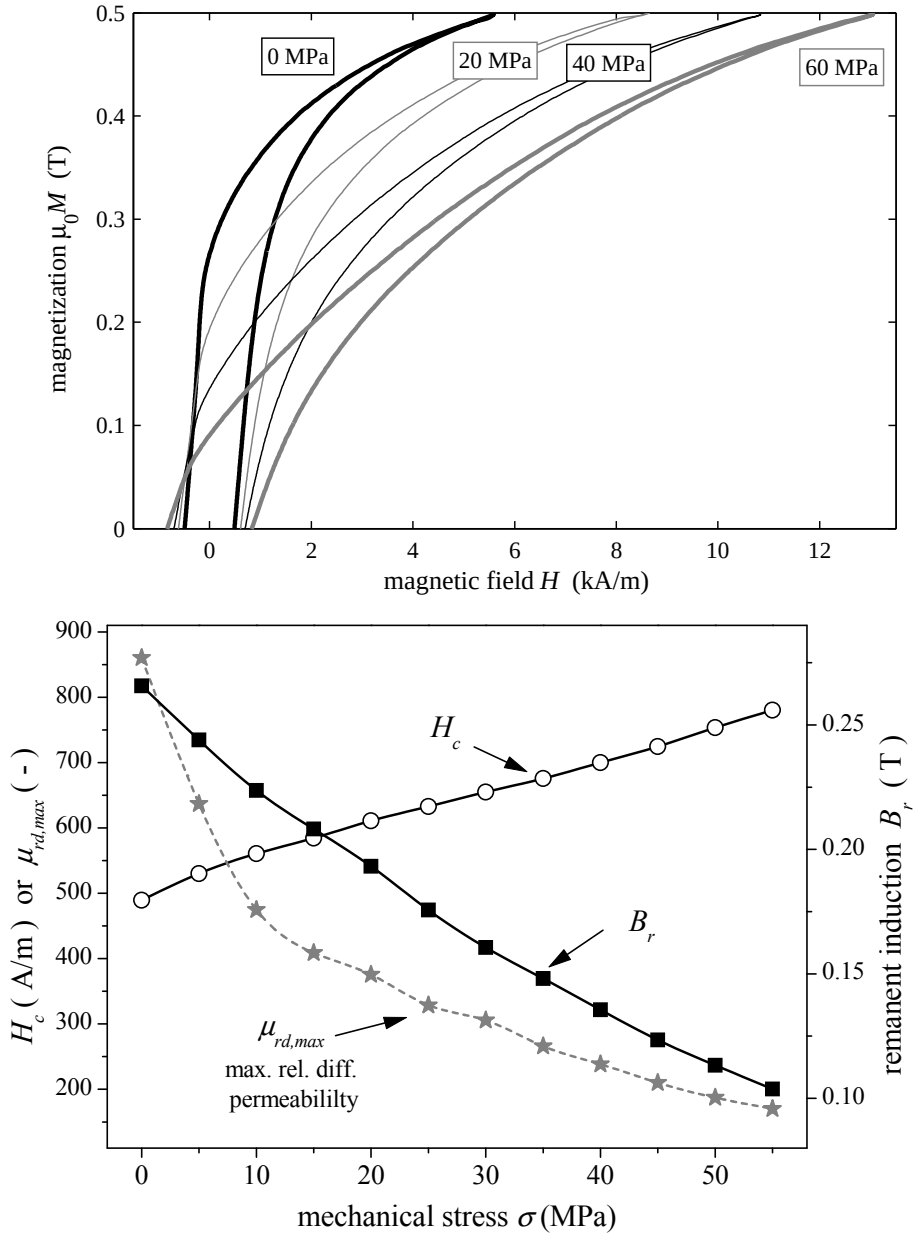

Figure 6.6. For **nickel**: (a) experimentally obtained hysteresis loops ($B_{max} = 0.5$ T) for a selection of applied static elastic tensile stress values σ_0 (yield stress = 70 MPa); (b) hysteresis loop parameters as a function of the applied static elastic stress σ_0. Due to the small thickness of the strip-shaped sample (see table 6.1) the sample is buckling under compressive stress, so it is not possible to perform experiments under compression.

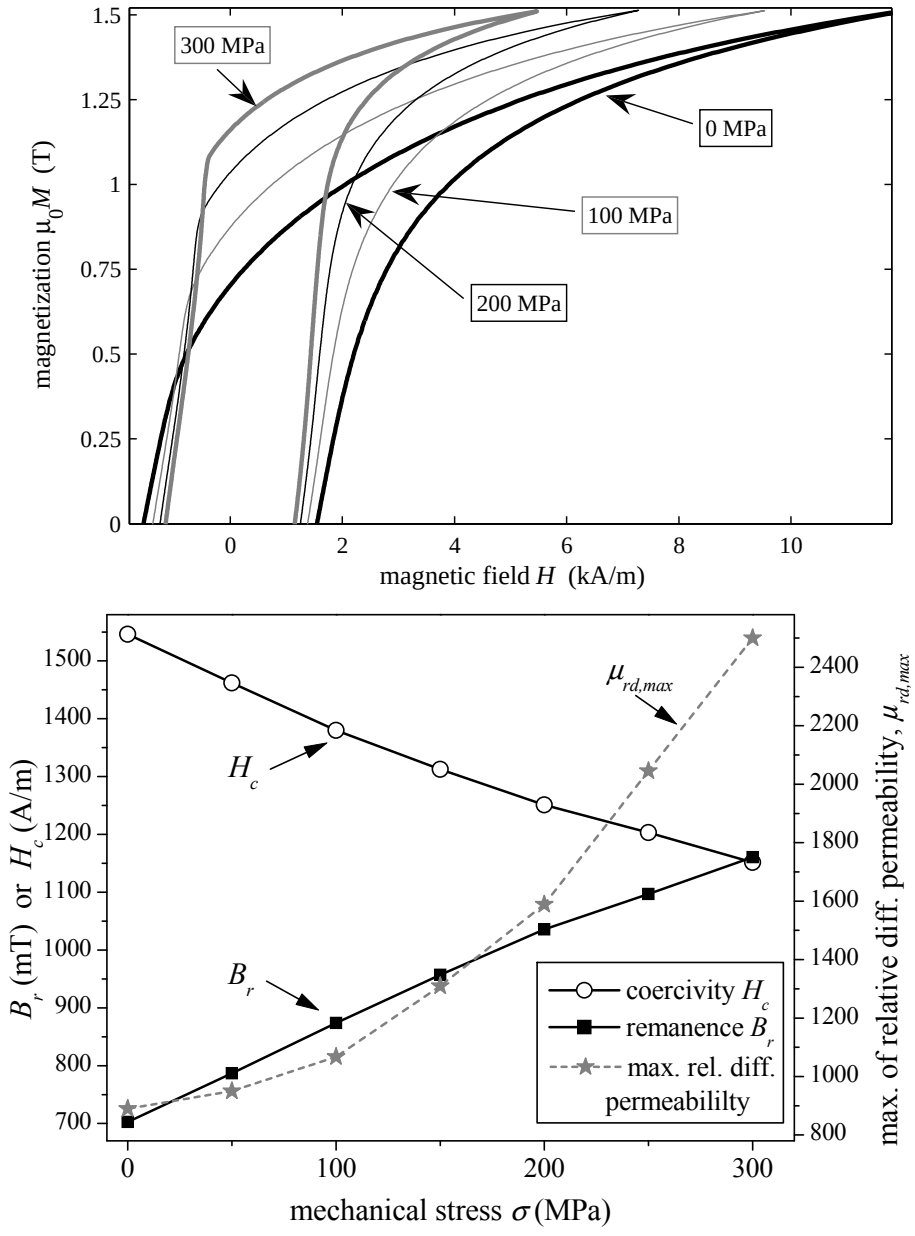

Figure 6.7. For **18%-Ni maraging steel**: (a) experimentally obtained hysteresis loops ($B_{max} = 1.5$ T) for a selection of applied static elastic tensile stress values σ_0 (yield stress = 350 MPa); (b) hysteresis loop parameters as a function of the applied static elastic stress σ_0. Due to the small thickness of the strip-shaped sample (see table 6.1) the sample is buckling under compressive stress, so it is not possible to perform experiments under compression.

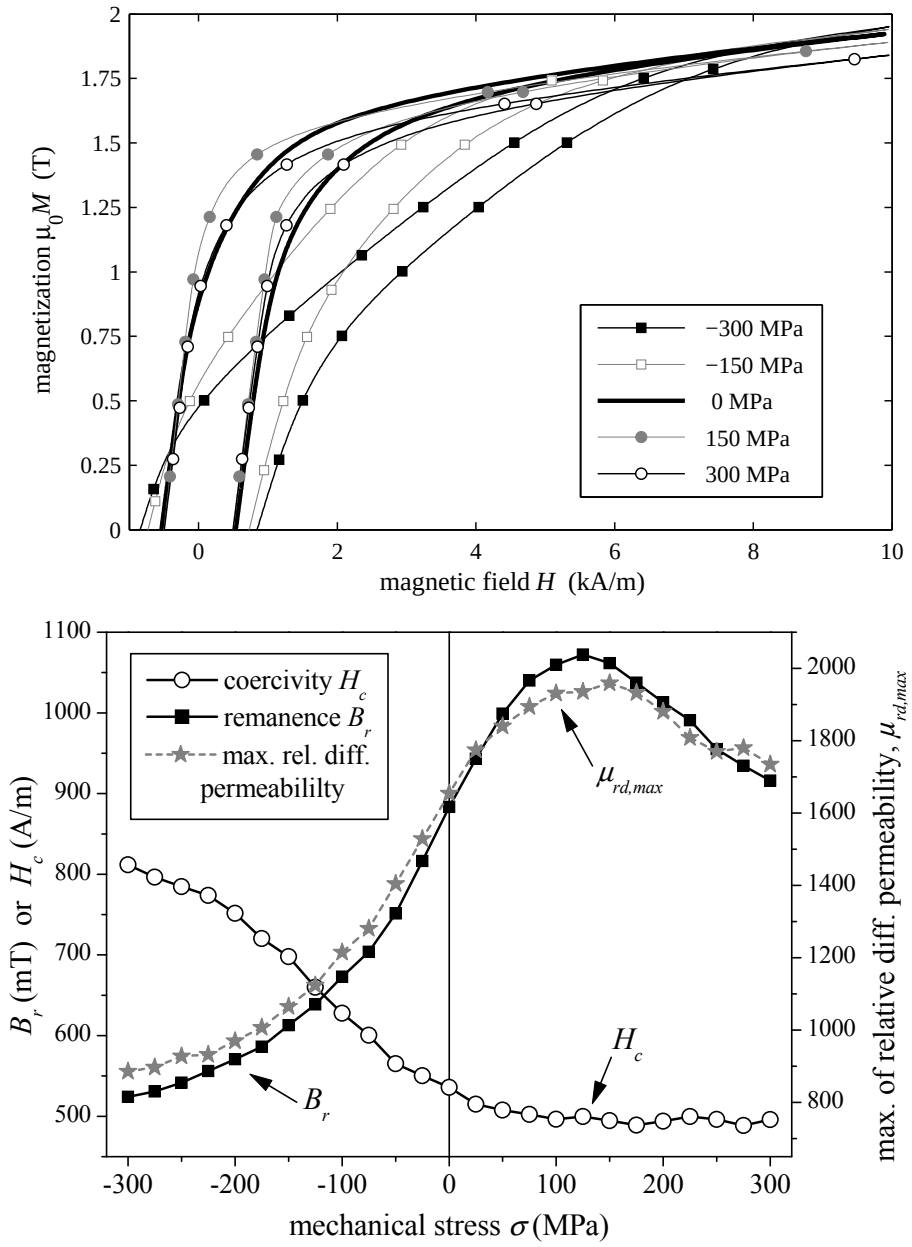

Figure 6.8. For **low-carbon steel**: (a) experimentally obtained hysteresis loops ($H_{max} = 10$ kA/m) for a selection of applied static elastic tensile and compressive stress values σ_0 (yield stress = 390 MPa); (b) hysteresis loop parameters as a function of the applied static elastic stress σ_0. Remark: $\sigma_0 \approx 150$ MPa corresponds with the Villari reversal (maximum permeability and remanence), see (a) and (b). Material: steel mat-B.

Dealing with the *hysteretic* properties of 18%-Ni maraging steel, again the effect of stress is just the opposite compared to nickel: the coercitive field decreases linearly, the remanent induction increases linearly and the permeability also increases with increasing (tensile) elastic stress, see figure 6.7.

For **iron and low carbon steel** the magnetostriction at zero stress is positive at low magnetic fields, but becomes zero and even negative at high magnetic fields, as depicted by the thick black line in figure 6.9. Moreover, the magnetostriction also depends on the applied stress: tensile stress results in lower magnetostriction values whereas compression gives higher magnetostriction values, see figure 6.9.

Therefore the magnetomechanical behaviour of iron and ferritic steels is more complicated than the magnetomechanical behaviour of materials with strictly positive or strictly negative magnetostriction: the most remarkable feature is the non-monotonic anhysteretic $M_{anh}(\sigma_0)$ behaviour for a given value of H, see figure 6.5(b) in case of low-carbon steel: M_{anh} first increases, reaches a maximum for a certain σ_0 and then decreases. Moreover the stress value that corresponds to the change of sign of $\frac{\mathrm{d}M_{anh}}{\mathrm{d}\sigma}$ depends on H. This can be clearly noticed in figure 6.10 where $\mu_0 \left(\frac{\mathrm{d}M_{anh}}{\mathrm{d}\sigma}\right)$ is shown as a function of magnetic field and applied elastic stress: the higher the magnetic field, the lower the elastic stress value that

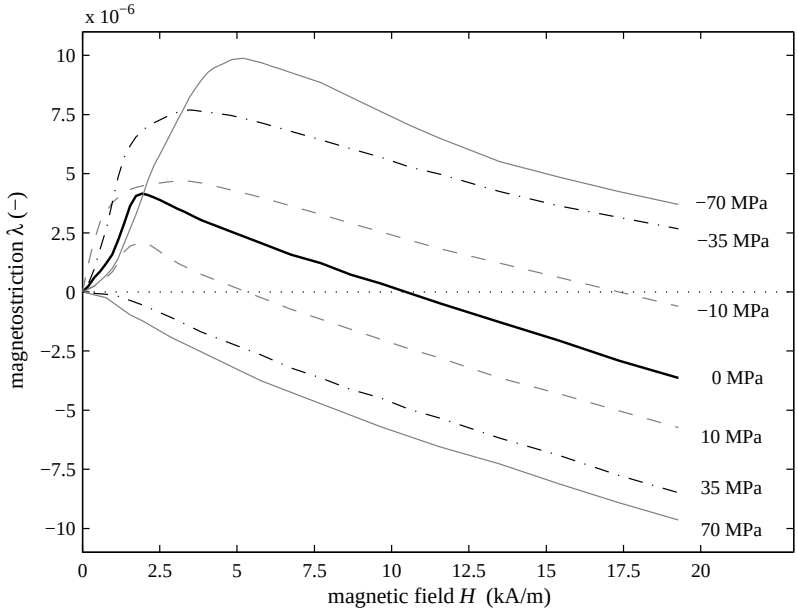

Figure 6.9. Anhysteretic magnetostriction of iron as a function of magnetic field, for a number of applied tensile and compressive stress values. Data taken from [Kuruzar1971].

corresponds with $\frac{\mathrm{d}M_{anh}}{\mathrm{d}\sigma} = 0$.

Those (H,σ) values at zero $\frac{\mathrm{d}M_{anh}}{\mathrm{d}\sigma}$ can be assigned to the so-called *Villari reversal*. The classical definition of the Villari reversal [Villari1865] starts from the anhysteretic magnetization curve $M_{anh}(H)$, experimentally obtained at different applied static elastic stress values, such as the set of curves shown in figure 6.5(a): when comparing the anhysteretic curve under applied tensile stress with the zero stress curve, M_{anh} increases for low H, whereas M_{anh} decreases for high H. Moreover, the H value that corresponds with the crossing of both tensile and zero stress curves decreases with increasing applied stress σ.

This non-monotonic property of the anhysteretic magnetomechanical behaviour, in other words the *Villari reversal*, is connected with the corresponding magnetostrictive behaviour as a function of H and σ. Dealing with the magnetostrictive behaviour of iron, see figure 6.9, also the lower the elastic stress, the higher the magnetic field value that corresponds with the extremum magnetostriction ($\frac{\mathrm{d}\lambda}{\mathrm{d}H}$ = 0). Although figure 6.9 and figure 6.10 are the result from experiments on different ferritic materials, nevertheless the (H,σ) region for which $\frac{\mathrm{d}M_{anh}}{\mathrm{d}\sigma}$ is positive, respectively negative (see figure 6.10) roughly corresponds with the region of positive, respectively negative $\frac{\mathrm{d}\lambda}{\mathrm{d}H}$, see figure 6.9.

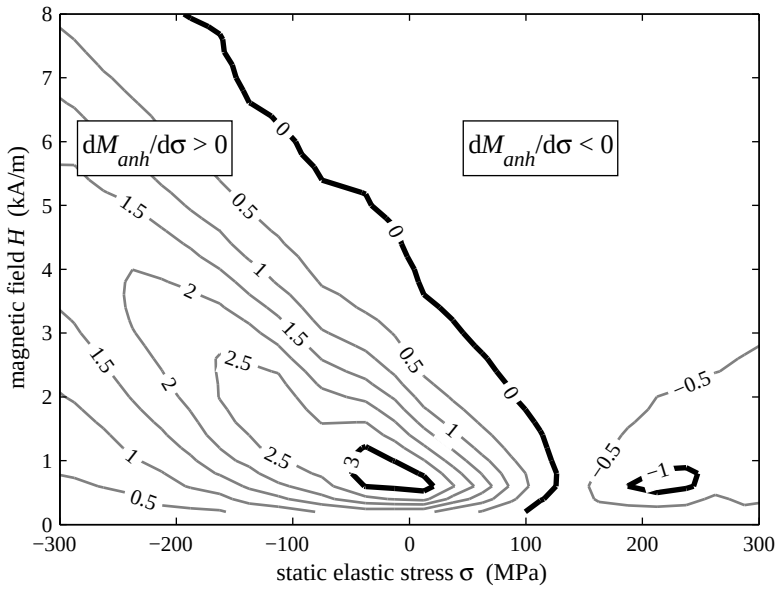

Figure 6.10. Contourplot of $\mu_0 \left(\frac{\mathrm{d}M_{anh}}{\mathrm{d}\sigma}\right)$ as a function magnetic field H and applied elastic stress σ, for the low-carbon steel (corresponding with the data in figure 6.5). The labels on the contours are expressed in mT/MPa. The maximum equals 3.2 mT/MPa and occurs at (σ, H) $\approx$ (0 MPa, 700 A/m). Material: steel mat-B.

As a **conclusion**, the experimental results in this paragraph indicate that for all three investigated materials (nickel, 18%-Ni maraging steel and low-carbon steel), there is a correspondence in the anhysteretic magnetomechanical behaviour described by $\frac{\mathrm{d}M_{anh}}{\mathrm{d}\sigma}(\sigma, H)$ and the anhysteretic magnetostrictive behaviour described by $\frac{\mathrm{d}\lambda}{\mathrm{d}H}(\sigma, H)$. This macroscopic magnetoelastic coupling can be described conceptually as follows, for reversible (incremental) changes in stress and magnetic field, with σ_0 and H_0 respectively the stress and field value at the considered working point [Bozorth1951]:

$$\left.\frac{\mathrm{d}M_{anh}}{\mathrm{d}\sigma}(\sigma, H_0)\right|_{\sigma=\sigma_0} \sim \left.\frac{\mathrm{d}\lambda}{\mathrm{d}H}(\sigma_0, H)\right|_{H=H_0} \tag{6.7}$$

6.1.4 Case 2: dynamic elastic stress and static magnetic field

In this paragraph the magnetization variation resulting from a time-dependent applied stress $\sigma(t)$ under a constant applied magnetic field H_0 is investigated:

$$M(t) = M(\sigma(t), H_0). \tag{6.8}$$

Actually, in the literature the general term *"magnetomechanical effect"* is predominantly used for such processes. In this context, some authors [Craik1971, Jiles1995, Makar1995] have investigated the magnetization variation of a single increase and decrease of stress (zero-tensile-zero or zero-compressive-zero) under the application of a constant magnetic field, starting from the demagnetized state. Others [Ruuskanen1991, Vandenbossche2006, Hubert2008] have studied the periodical variation of magnetization due to the periodical stress cycling under the application of a constant magnetic field.

In fact, the first category deals with a initial or transitional stress-induced change in magnetization (analogous to the initial or virgin magnetization curve $M(H)$), whereas following the second approach, one typically concentrates on the steady-state "regime" of closed and repeated $M(\sigma)$ hysteresis loops, occurring after the transitional stage during the very first stress cycle is completed.

In this work the focus is on the stress-magnetization loops, not on the transitional stress-magnetization behaviour. The experimental procedure to measure the stress-magnetization loops under static magnetic field is as follows:

- demagnetization of the sample at zero mechanical stress;
- application of the constant magnetic field H_0;
- application of the cyclic elastic stress $\sigma(t)$: (a) manually from $\sigma = 0$ to $\sigma_{min} < 0$ (compression); (b) the motor is switched on starting from σ_{min} in order to avoid overshoot during first stress cycle; the motor torque settings are modified if necessary by the labview program in order to control the maxima and minima of the stress cycles.

Table 6.2. Some details about the three different low-carbon steels that are examined further in this chapter 6.

	mat-A	**mat-B**	**mat-C**
material	free-cutting steel rod (11SMn30), stress-relief annealed after machining to hour-glass shape	hot-rolled low-carbon steel rod, as-received after machining to hour-glass shape	hot-rolled low-carbon steel strip (S235JR)
chemical composition (wt%)	98.3% Fe 0.14% C 1.1 % Mn 0.3 % S 0.05% Si 0.1 % P	99.1% Fe 0.12% C 0.52% Mn 0.01% S 0.22% Si 0.01% P	98.6% Fe 0.20% C 0.80% Mn 0.01% S 0.28% Si 0.06% P
yield stress	285 MPa	390 MPa	238 MPa
sample shape	cylindrical rod hour-glass shape	cylindrical rod hour-glass shape	rectangular strip hour-glass shape
sample size	4 mm diameter	4 mm diameter	2 mm thick 12 mm wide

During the cyclic stressing the magnetization M is obtained by analog integration of the measured induced voltage, see chapter 3. However, the integration constant is not known a priori. A similar approach as in [Hubert2008] is followed to determine this integration constant when measuring magnetomechanical hysteresis loops: define X as the average of the M values at the mean cyclic stress σ_m (one M value at the descending branch and the other one along the ascending branch of the $M(\sigma)$ loop), and then make X equal to the M_{anh} value corresponding to the mean cyclic stress σ_m and the static magnetic field H_0:

$$\frac{M_{hyst,desc}(\sigma_m, H_0) + M_{hyst,asc}(\sigma_m, H_0)}{2} = M_{anh}(\sigma_m, H_0) \tag{6.9}$$

As an illustration of the experimentally obtained magnetomechanical hysteresis loops, in figure 6.11 the magnetization $M(\sigma(t), H = H_0)$ is shown as a function of one cycle of completely reversed mechanical stress $\sigma(t)$ obtained under the application of a static magnetic field $H = H_0$ = 800 A/m, for two different low-carbon ferritic steels: mat-A in (a) and mat-B in (b). In table 6.2 the details can be found about the three low-carbon steels mat-A, mat-B[3] and mat-C, three materials which are examined further in this chapter 6.

[3]Mat-B is also the low-carbon steel that is used in section 6.1.3, see figures 6.5, 6.8 and 6.10.

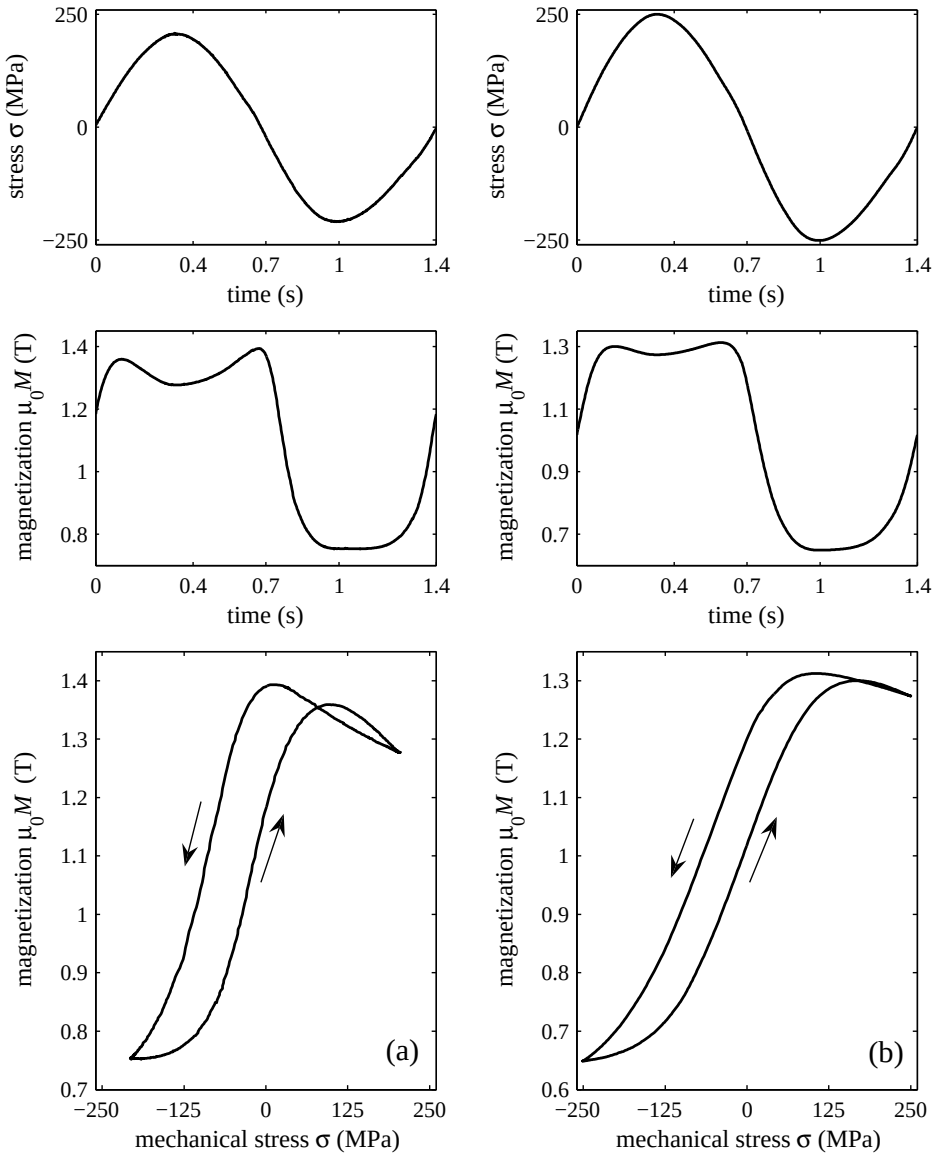

Figure 6.11. Magnetization $M(\sigma(t), H = H_0)$ as a function of one cycle of mechanical stress $\sigma(t)$, obtained experimentally under the application of a constant magnetic field H_0 = 800 A/m, for two different low-carbon ferritic steels: mat-A in (a) and mat-B in (b). In both examples the stress cycle is completely reversed: the average of the mechanical stress cycle equals zero.

For low-carbon ferritic steels the magnetization-stress behaviour has the following typical features:

1. *hysteretic* behaviour: in general, the magnetization during the increase and the decrease of stress does not coincide with each other;
2. *asymmetric non-linear* magnetization variation: different behaviour in tension compared to compression (even if the mean stress is zero), and moreover *non-monotonic* behaviour: the maximum magnetization corresponds with a certain tensile stress not equal to the maximum tensile stress (non-monotonic behaviour is also one of the main features of the anhysteretic stress-magnetization for low-carbon steels, see section 6.1.3);
3. for some materials and sufficiently high σ_{max}, the stress-magnetization curve shows a *crossing point* [Craik1971], see example (a) in figure 6.11.

The main mechanisms of the $M(\sigma(t), H_0)$ magnetomechanical effect can be listed as follows [Jiles1995]:

1. the stress-induced preferential occupancy of one of the three easy directions (*stress anisotropy*), determined by the sign of the product $\lambda\sigma_{appl}$, with λ the unidirectional magnetostriction and σ_{appl} the applied elastic stress. The associated magnetic domain mechanism is the stress-induced unpinning and motion of the 90° domain walls;
2. the time-dependent applied elastic stress $\sigma(t)$ causes not only domain wall motion but also motion of dislocations and changes in the internal stress fields around defects such as inclusions, vacancies, point defects, internal stresses which in turn alter the domain wall pinning energies.

Next, for the same three ferromagnetic materials as the ones used in the preceding section 6.1.3, namely nickel, 18%-Ni maraging steel and low-carbon ferritic steel (see table 6.1 for details), figures 6.12 and 6.13 show the hysteretic magnetomechanical behaviour $M(\sigma(t))$ during one particular stress cycle, for different settings of static magnetic field H_0. Also, such hysteretic magnetomechanical behaviour is compared to the reversible anhysteretic magnetomechanical behaviour as already shown and discussed in section 6.1.3. For all three materials there is a fair correspondence between the anhysteretic and the hysteretic magnetization versus stress behaviour: for nickel the hysteresis loops correspond with $\frac{\mathrm{d}M}{\mathrm{d}\sigma} < 0$, for the maraging steel the slope of the hysteresis loop is positive, whereas for the low-carbon steel again the typical non-monotonic behaviour is apparent.

Dealing with the effect of the static magnetic field magnitude H_0: the hysteresis loop width is higher at low static magnetic fields H_0, for all three materials.

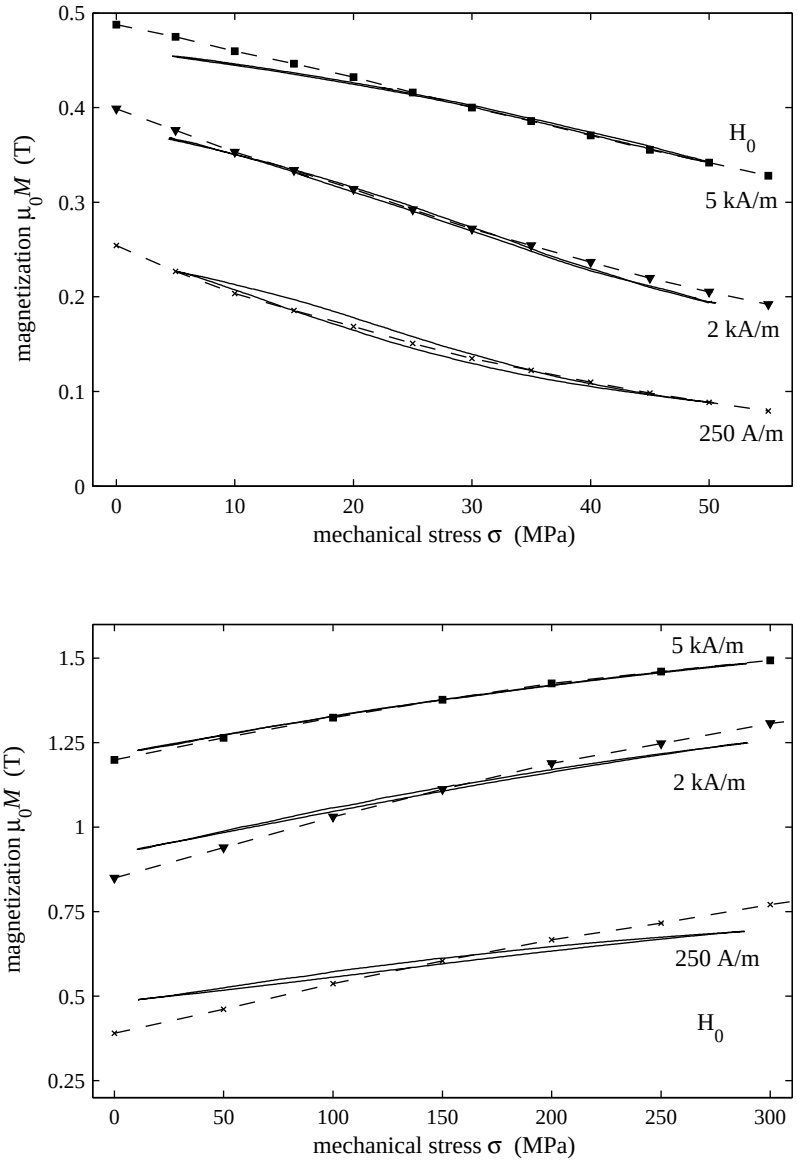

Figure 6.12. For **nickel** (top) and **18%-Ni maraging steel** (bottom): experimentally obtained magnetomechanical hysteresis loops $M(\sigma(t))$, for different settings of static magnetic field H_0 (full lines), and compared to the reversible anhysteretic magnetomechanical behaviour at corresponding settings of H_0 (dashed lines with symbols). Samples are strips with small thickness, therefore compression is not possible due to buckling of the sample.

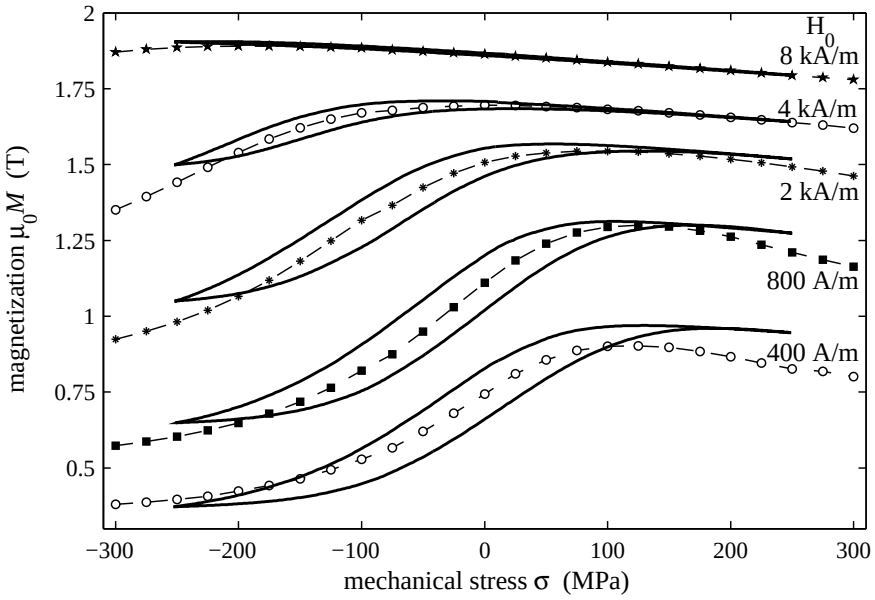

Figure 6.13. For **low carbon steel**: experimentally obtained magnetomechanical hysteresis loops $M(\sigma(t))$, for different settings of static magnetic field H_0 (full lines), and compared to the reversible anhysteretic magnetomechanical behaviour at corresponding settings of H_0 (dashed lines with symbols). In this case, the sample is an hour-glass shaped cylindrical rod, hence completely reversed cyclic stress is possible. Material: steel mat-B.

At low H_0 the domain configuration consists of a high number of domains and domain walls, which take part in the stress-induced domain wall unpinning and domain wall motion processes, leading to hysteretic behaviour. As H_0 increases, the number of moving domain walls decreases since the domain configuration evolves to almost one single domain with magnetization vector near or along the field direction, therefore there is less hysteretic behaviour and the loop width becomes smaller for high H_0.

In section 6.1.1 it was derived theoretically that starting from a demagnetized sample and applying a certain elastic stress to it (so without magnetic field, H_0 = 0), this results in the stress-induced motion of 90° domain walls, but it does not result in a change in magnetization. Some authors [Craik1971, Ruuskanen1991, Hubert2008] have verified this experimentally and have found that this is approximately true. We also performed magnetization measurements under cyclic elastic stress on demagnetized samples, and found a peak-to-peak magnetization variation of about 27 mT, or approximately 3% of the peak-to-peak magnetization variation when an static magnetic field $H_0 = 800$ A/m is applied before the start of the stress cycling under the same stress conditions on the same sample.

6.1.5 Case 3: dynamic elastic stress and dynamic magnetic field

In the two preceding sections the magnetomechanical behaviour $M(\sigma, H)$ is investigated with one of both inputs (σ or H) held constant. The obvious next step is to consider the effect on magnetization when applying both a time-dependent

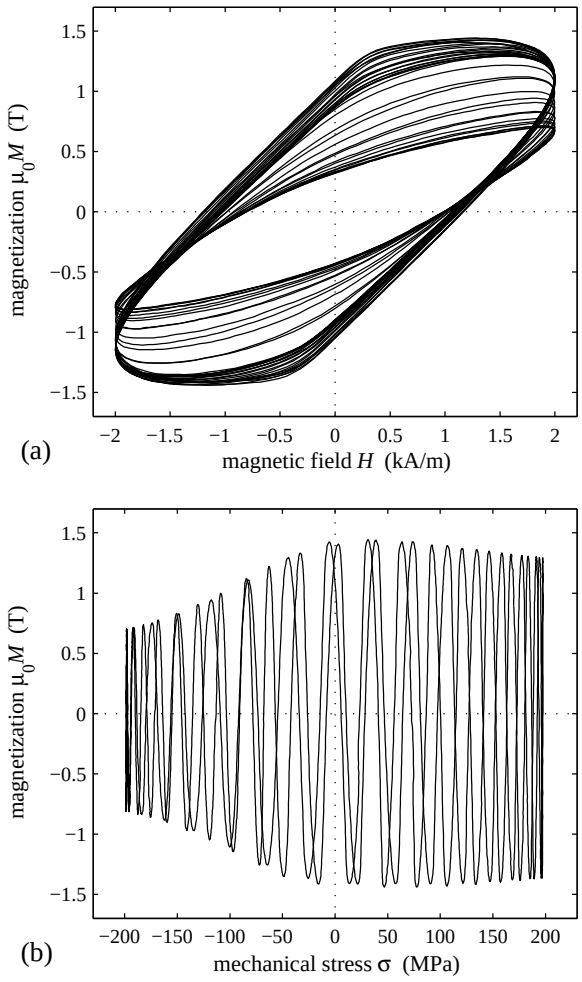

Figure 6.14. Magnetization $M(\sigma(t), H(t))$ for one cycle of mechanical stress $\sigma(t) = \sigma_a \sin(2\pi f_{mech} t)$, obtained experimentally under the application of a time-varying magnetic field $H(t) = H_a \sin(2\pi f_{mag} t)$. In (a) $M(t)$ is shown as a function of $H(t)$ and in (b) as a function of $\sigma(t)$, both for one mechanical cycle. Material: low-carbon steel mat-A. H_a = 2 kA/m, f_{mag} = 25 Hz, σ_a = 200 MPa, and $f_{mech} = f_{mag}/35$ = 0.714 Hz, i.e. exactly 35 magnetic periods in one mechanical period.

elastic stress and time-dependent magnetic field:

$$M(t) = M(\sigma(t), H(t)). \tag{6.10}$$

In more detail, a time-dependent magnetic field is continuously applied to the sample during the stress-controlled cyclic loading, and for each cycle the magnetization variation $M(\sigma, H)$ due to the magnetomechanical effect is measured. Here, the magnetic excitation frequency is significantly larger than the mechanical frequency, with f_{mag}/f_{mech} an integer. An example of such typical $M(\sigma(t), H(t))$ behaviour is depicted in figure 6.14 for the low-carbon ferritic steel mat-A as introduced in table 6.2.

6.2 Fatigue damage assessment by magnetomechanical monitoring

During the service life of constructions or machines the cyclic mechanical loading of steel parts can lead to an accumulation of fatigue damage. As introduced in section 1.1.4, the fatigue damage progression can be divided into different (partially overlapping) stages, based on studies of the basic structural changes [Dieter1988, Cui2002, Socha2003]:

- **Fatigue damage initiation**: microstructural changes associated with localized micro-plastic deformation in some individual grains, i.e. the generation of dislocations (increase of dislocation density), the rearrangement of dislocations into dislocation tangles and walls, and the development of persistent slip bands. Result is the nucleation of micro-sized cracks along the developed slip bands in a number of grains.
- **Slip-band (stage-I) crack growth**: inside unfavourably oriented grains, micro-cracks develop along slip planes of high shear stress. To develop further, such crack must propagate into the neighbouring grains, which have different lattice orientations and therefore different slip systems, so the crack needs to reorientate at the grain boundary towards a particular slip direction of the surrounding grain. Typically, the majority of the fatigue lifetime (i.e. the majority of the number of stress cycles) corresponds with micro-crack (nucleation and) growth, which is a regime of stable damage progression. Result is the formation of dominant crack(s).
- **Transgranular (stage-II) crack growth**: as the crack propagates, the plastic zone around the crack tip increases and the resistance to crack growth diminishes: the crack becomes insensitive to grain boundary obstacles and to the particular slip systems of individual grains: the crack now develops in the plane normal to the tensile stress direction, and at much faster rates per loading cycle compared to stage-I crack growth. Result is the growth of

a well-defined macro-crack with such critical macroscopic dimensions, that the remaining cross-sectional area of the material can no longer support the maximum applied load, and the material fails by ultimate fracture during the last stress cycle.

To avoid that the fatigue damage process ends in a sudden fracture, it is vital to assess the material degradation, preferably in a non-destructive fashion. Concerning ferromagnetic materials, the microstructural dependence of the magnetic behaviour (as introduced in chapters 1 and 2) makes magnetic techniques appropriate for non-destructive evaluation. In such context typically the change in magnetic hysteresis loop parameters can be determined **at several interruptions of the cyclic loading** [Bose1986, Lo2000, Melikhov2002, Vandenbossche2005]. However, due to the abrupt character of metal fatigue it can be difficult to make predictions about the onset of fatigue failure based on experimental data obtained at only a limited number of load interruptions.

Therefore we explore in this section 6.2 the possibility to examine the fatigue process **during the cyclic mechanical loading itself**, in order to experimentally obtain information for every single mechanical loading cycle. For this purpose the magnetomechanical effect can be exploited, as introduced in section 6.1: the magnetization depends on both magnetic field and mechanical stress, hence during the cyclic mechanical loading the application of a magnetic field can be considered, and the magnetization variation resulting from both the applied mechanical stress and the enforced magnetic field can be continuously monitored throughout the cyclic mechanical loading test. In the following section 6.2.1 two such magnetomechanical evaluation techniques are introduced, differing only in the magnetic field that is continuously applied during the cyclic loading, which can be either a time-independent (static) magnetic field, or a time-dependent (dynamic) field.

The setup to investigate experimentally the magnetomechanical effect is the incorporation of a magnetic measurement setup inside a mechanical testing apparatus. During the cyclic mechanical uniaxial loading, a magnetic field H is continuously enforced parallel to the stress direction and the following properties are monitored continuously along the stress direction: magnetization M(t), strain $\varepsilon(t)$, stress $\sigma(t)$, and magnetic field $H(t)$. In section 3.3 this magnetomechanical setup is described in more detail.

6.2.1 Introduction of two magnetomechanical methods

Method H_{stat}: monitoring magnetomechanical behaviour at constant field

As a first method, a constant magnetic field is continuously applied to the sample during a stress-controlled cyclic loading test, and for each stress cycle the

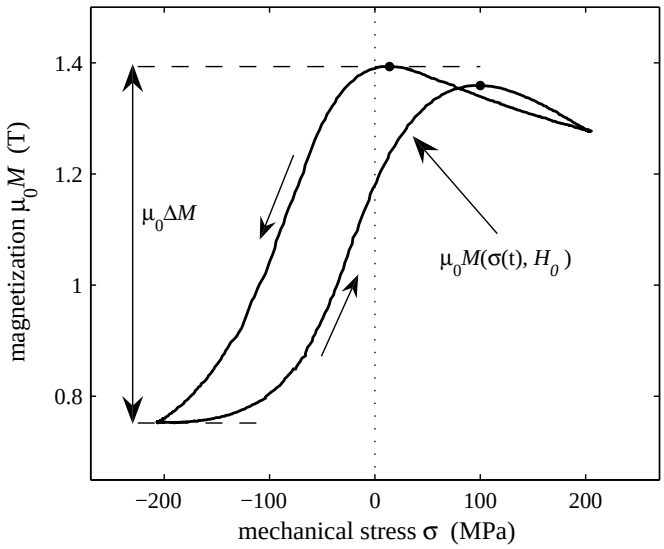

Figure 6.15. Method H_{stat}: the magnetization $M(\sigma(t), H = H_0)$ as a function of one stress cycle $\sigma(t) = \sigma_a \sin(2\pi f_{mech} t)$ is obtained experimentally under the application of a constant magnetic field $H = H_0$. The monitoring parameter ΔM is indicated graphically. The $M(\sigma)$ behaviour shown here corresponds with cycle number $n = 5000$ of a fatigue test on material mat-A. H_0 = 800 A/m, σ_a = 208 MPa, and f_{mech} = 0.714 Hz.

stress-induced change in magnetization $M(\sigma)$ due to the magnetomechanical effect is measured. This $M(\sigma)$ behaviour is showing hysteretic, asymmetric and non-monotonic features, see figure 6.15, which are typical for iron and ferritic steels [Ruuskanen1991, Hubert2008]. When following a particular $M(\sigma)$ loop one can see that, starting at maximum magnetization M_{max} situated at ca. 14 MPa and with σ decreasing, M decreases to M_{min}. When σ again increases, M increases to a local maximum at ca. 100 MPa and then decreases slightly. With σ again decreasing, M increases to M_{max}.

For method H_{stat}, the parameter which is continuously monitored throughout the fatigue test, is the peak-to-peak magnetization ΔM for each particular mechanical stress cycle, defined as follows:

$$\Delta M = \max(M(\sigma)) - \min(M(\sigma)). \tag{6.11}$$

Method H_{dyn}: monitoring magnetomechanical behaviour at cyclic field

As a second method, a time-dependent periodic magnetic field is continuously applied to the sample during a stress-controlled cyclic loading test, and for each

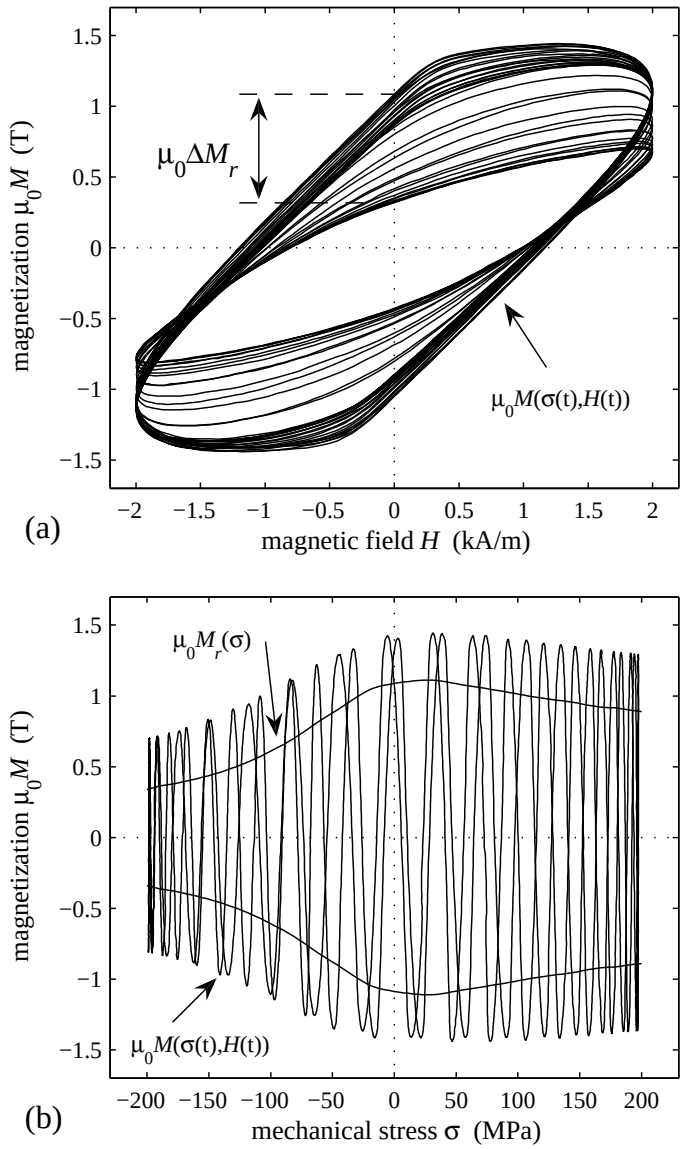

Figure 6.16. Method H_{dyn}: the magnetization $M(\sigma(t), H(t))$ for one cycle of mechanical stress $\sigma(t) = \sigma_a \sin(2\pi f_{mech} t)$ is obtained experimentally under the application of a time-varying magnetic field $H(t) = H_a \sin(2\pi f_{mag} t)$. In (a) $M(t)$ is shown as a function of $H(t)$ and in (b) as a function of $\sigma(t)$, both for one mechanical cycle. The monitoring parameter ΔM_r is indicated graphically. The $M(\sigma, H)$ behaviour shown here corresponds with cycle number $n = 5000$ of a fatigue test on material mat-A. H_a = 2000 A/m, f_{mag} = 25 Hz, σ_a = 200 MPa, and $f_{mech} = f_{mag}/35$ = 0.714 Hz, i.e. exactly 35 magnetic periods in one mechanical period. Also shown in (b) is the remanent magnetization M_r as a function of σ.

stress cycle the magnetization $M(\sigma, H)$ due to the magnetomechanical effect is measured. Here, the magnetic excitation frequency is significantly larger than the mechanical frequency, with f_{mag}/f_{mech} an integer (here typically of the order of 35). This second method can be considered as the most general case of the magnetomechanical effect where the ferromagnetic material under test is subjected to both a time-dependent magnetic field and a time-dependent mechanical stress. The typical $M(\sigma, H)$ behaviour is depicted in fig. 6.16.

For method H_{dyn}, the parameter which is continuously monitored throughout the fatigue test, is the peak-to-peak remanent magnetization ΔM_r for each particular mechanical stress cycle, defined as follows:

$$\Delta M_r = \max(M_r(\sigma)) - \min(M_r(\sigma)). \tag{6.12}$$

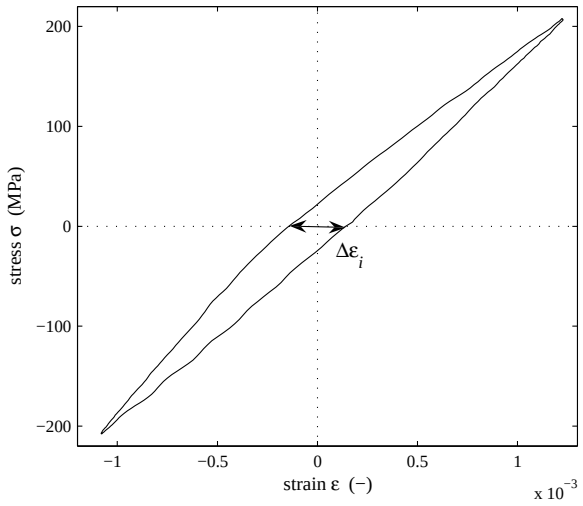

Figure 6.17. Definition of the inelastic strain range $\Delta\varepsilon_i$, as the stress-strain hysteresis loop width.

Validation by monitoring the mechanical stress-strain behaviour

Furthermore, to validate both magnetomechanical methods, also the stress-strain hysteresis loops[4] $\sigma(\varepsilon)$ are measured simultaneously throughout the same fatigue test. In figure 6.17 a typical stress-strain hysteresis loop is depicted. Such mechanical behaviour during each single stress cycle is due to both reversible (elastic) and

[4]The applied stress σ and the longitudinal strain ε are derived from the applied force to the sample and the elongation of the sample, which are measured with a load cell and a linear encoder, respectively, see section 3.3 for more details.

irreversible (inelastic) deformation. The elastic deformation by reversible dislocation motion is the largest contribution to the overall deformation, whereas the inelastic deformation due to irreversible slip takes only a small part in the overall deformation. In such context, the assessment of the different stages in the fatigue life is carried out on the basis of the inelastic strain $\varepsilon_i = \varepsilon - \sigma/E$, with E the elastic modulus. During the fatigue test the local inelastic deformation associated with the stress field around a crack tip can be observed on a macroscopic scale as an increase of the stress versus elastic strain hysteresis loop width, also called the inelastic strain range [Socha2003]:

$$\Delta\varepsilon_i = \max(\varepsilon_i) - \min(\varepsilon_i), \tag{6.13}$$

a parameter which is then monitored throughout the fatigue test for each mechanical stress cycle n.

6.2.2 Results for uniaxial fatigue tests with non-zero mean stress

In this paragraph the results are shown that are obtained on mat-C steel samples (see table 6.2 for details about this material). Such samples are hour-glass shaped

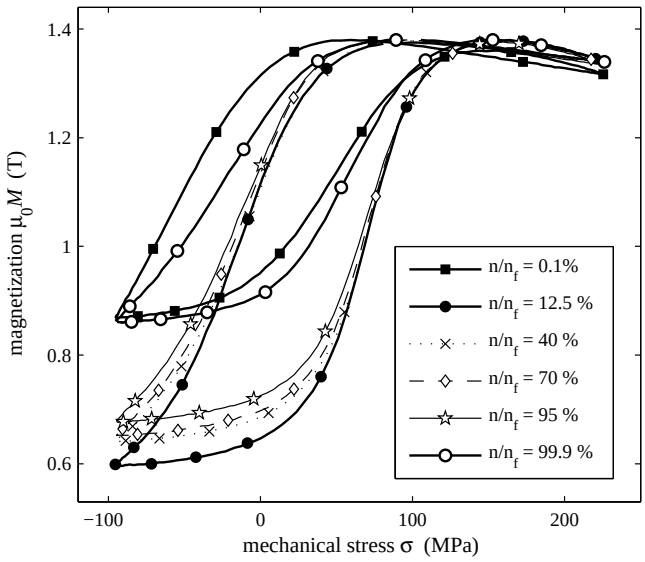

Figure 6.18. Selection of $M(\sigma)$ hysteresis loops throughout the fatigue lifetime n/n_f (as indicated in the legend), obtained by method H_{stat} on material mat-C. Fatigue test details: stress amplitude $\sigma_a = 160$ MPa, mean stress $\sigma_m = 65$ MPa (in other words: $\sigma_{min} = -95$ MPa, $\sigma_{max} = 225$ MPa). Number of cycles to failure n_f = 35502. Continuously applied static magnetic field $H_0 = 370$ A/m.

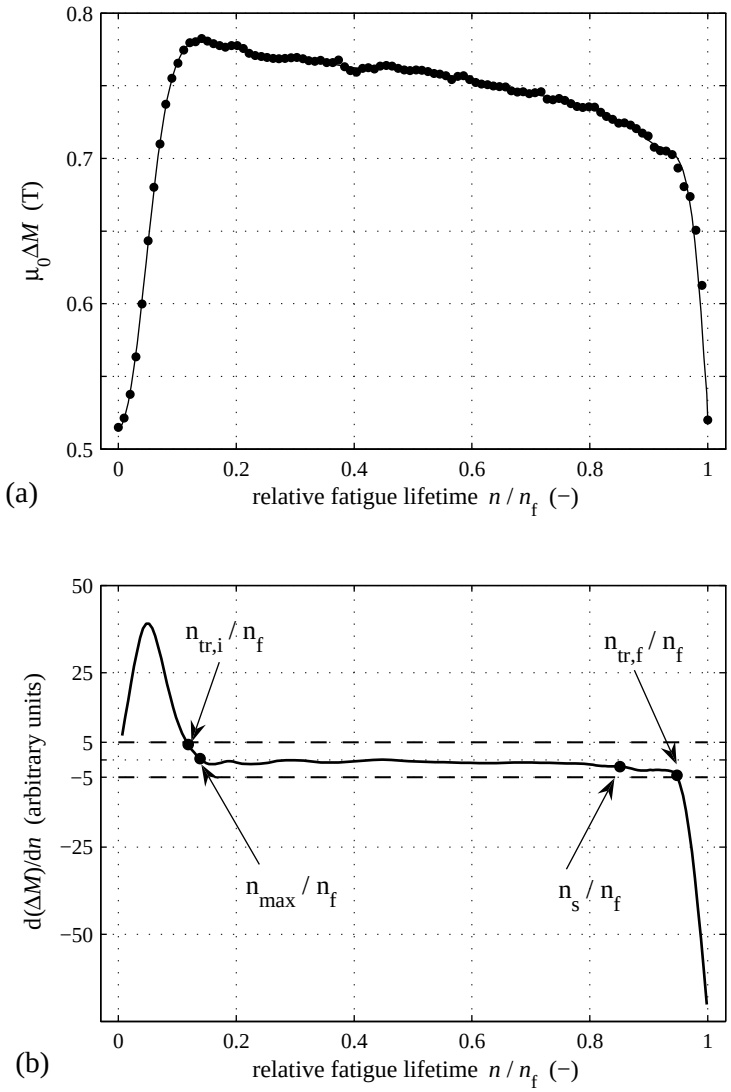

Figure 6.19. (a) Peak-to-peak magnetization ΔM as a function of the fatigue lifetime n/n_f, corresponding with the fatigue test of figure 6.18. For clarity, only one data point is shown every 1% of the relative fatigue lifetime. (b) Slope of $\Delta M(n)$, corresponding with the result shown in part (a) of the same figure. The annotations $n_{tr,i}$ (n at the end of the initial transition stage), n_{max} (n at the maximum of the magnetomechanical monitoring parameter ΔM), n_s (n at the change in slope of ΔM), and $n_{tr,f}$ (n at the begin of the final transition stage) are explained further in the text, see pages 229–233.

strip samples with a thickness of 2 mm, which start to buckle at compressive stresses of about -110 MPa. Therefore the uniaxial fatigue tests on these samples are executed with a minimum stress value of about -95 MPa, and with a non-zero positive mean value of the cyclic stress, σ_m (typically σ_m = 65 MPa), in other words the fatigue tests are not fully reversed.

For such fatigue tests, during the cyclic mechanical loading, a constant magnetic field is applied to the sample, and the magnetization variation during each stress cycle due to the magnetomechanical effect is measured continuously. Such magnetomechanical monitoring method is introduced in section 6.2.1 as method H_{stat}.

In figures 6.18 and 6.19 the results are shown for a particular fatigue test executed on a mat-C steel sample, with the following specifications: stress amplitude σ_a = 160 MPa, and mean stress σ_m = 65 MPa. The characteristic trends are similar for tests with other specifications.

Figure 6.18 shows the magnetization variation as a function of cyclic mechanical stress, for several stress cycles during the fatigue lifetime, under continuously applied static magnetic field H_0 = 370 A/m .

The variation of the peak-to-peak value of the magnetization ΔM under constant applied magnetic field H_0 and during a certain stress cycle n, is shown in figure 6.19, as a function of the fatigue lifetime n/n_f. Three stages can be distinguished in this parameter with respect to the fatigue lifetime: ΔM first increases, then stabilizes (a slow decrease is visible), and finally starts to decrease fastly.

In order to determine the start of the final transition stage, the following approach is taken: at each cycle number n the long-term linearized trend of $\Delta M(n)$ is calculated from the last (typically 50) cycles. Figure 6.19(b) shows the slope, corresponding with the result in part (a) of the same figure. The number of cycles $n_{tr,f}$ at the start of the final transition stage corresponds with the instant when the slope of $\Delta M(n)$ becomes lower than a certain threshold value, as indicated in figure 6.19(b). For the particular fatigue test corresponding with figures 6.18 and 6.19, a significant decrease - compared with the long-term linearized trend - is visible starting from $n_{tr,f}/n_f = 95\%$.

6.2.3 Results for uniaxial fully reversed fatigue tests

Fully reversed uniaxial fatigue tests are cyclic mechanical loading tests with constant stress amplitude σ_a and zero mean stress σ_m. In order to prevent buckling of the samples during the compressive part of the fully reversed stress cycle, the investigated samples are hour-glass shaped samples with circular cross section, machined out of cylindrical rods (diameter 8 mm). Only the central sample region with smaller cross section (diameter 4 mm; length 60 mm), which is subjected to

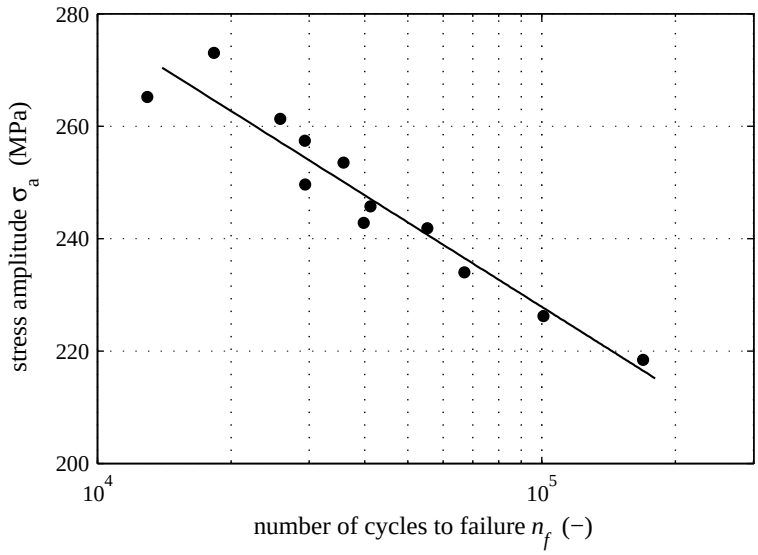

Figure 6.20. S-N curve obtained from fatigue tests on steel mat-B. Markers are the actual test results, whereas the line represents a logarithmic fit.

the highest stress levels, is further examined.

Samples of two different ferritic structural steels are considered, mat-A and mat-B, see table 6.2 for more details about these materials. For both steels mat-A and mat-B, a number of fully reversed fatigue tests are performed, with typically the number of cycles to failure n_f in between 10^4 and $2 \cdot 10^5$, see for instance on figure 6.20 the S-N curve corresponding with the performed fatigue tests on mat-B.

The two considered magnetomechanical examination techniques, as introduced in section 6.2.1 (H_{stat} and H_{dyn}), are carried out for both materials mat-A and mat-B, hence resulting in four characteristic fatigue assessment results, as depicted in the four figures 6.21 to 6.24. The fatigue test details corresponding with those figures are given in table 6.3. The trends are similar for fatigue tests on the same material with other test specifications concerning σ_a.

Some remarks related with these fatigue tests and the magnetomechanical monitoring methods:

- For method H_{stat}, H_0 is set to 800 A/m, and for method H_{dyn}, H_a is set to 2 kA/m. This choice of settings is motivated by the fact that, at the first stress cycle, these magnetic field values result in the highest absolute values of the considered parameters, respectively ΔM and ΔM_r.

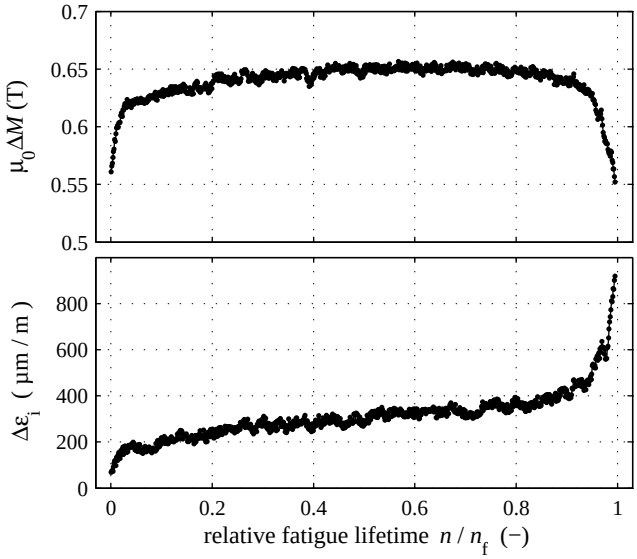

Figure 6.21. Peak-to-peak magnetization ΔM and inelastic strain range $\Delta\varepsilon_i$ versus relative fatigue lifetime, n/n_f, obtained on mat-A with method H_{stat} (H_0 = 800 A/m).

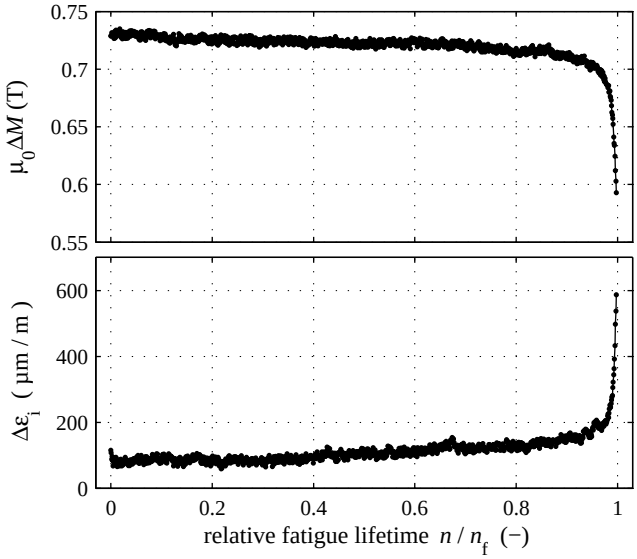

Figure 6.22. Peak-to-peak magnetization ΔM and inelastic strain range $\Delta\varepsilon_i$ versus relative fatigue lifetime, n/n_f, obtained on mat-B with method H_{stat} (H_0 = 800 A/m).

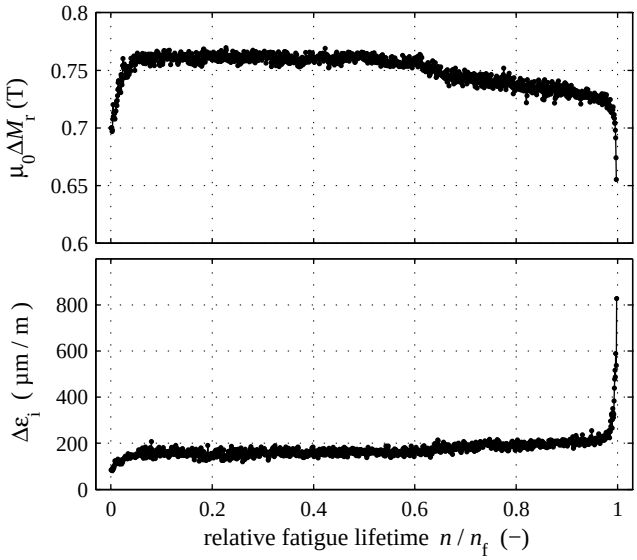

Figure 6.23. Peak-to-peak remanent magnetization ΔM_r and inelastic strain range $\Delta\varepsilon_i$ versus relative fatigue lifetime, n/n_f, obtained on mat-A with method H_{dyn} (H_a = 2 kA/m, f_{mag} = 25 Hz).

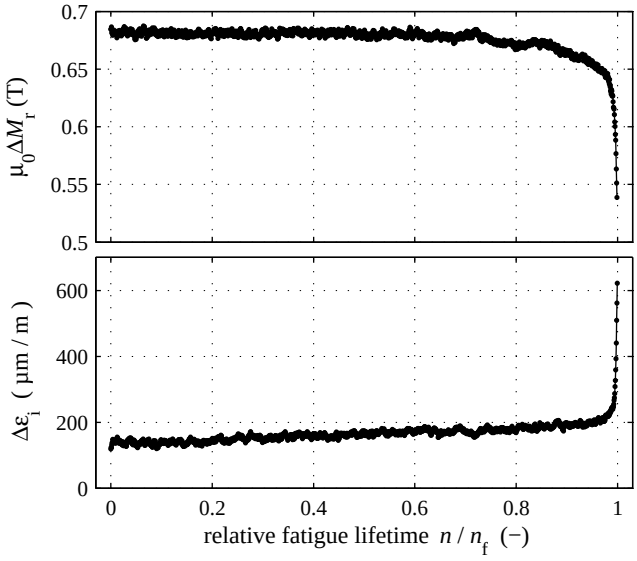

Figure 6.24. Peak-to-peak remanent magnetization ΔM_r and inelastic strain range $\Delta\varepsilon_i$ versus relative fatigue lifetime, n/n_f, obtained on mat-B with method H_{dyn} (H_a = 2 kA/m, f_{mag} = 25 Hz).

- In figures 6.21 to 6.24, the monitoring parameters ΔM (or ΔM_r) and $\Delta\varepsilon_i$ are depicted with data points rather than with trend curves. Such a way of presentation gives a good impression about the experimental scatter on the considered parameters. For clarity, only one data point is shown for every 25 load cycles.

- The magnetization is determined from the measured magnetic flux and the cross section of the sample. Here a constant cross section is assumed throughout the fatigue test, which is justified by the fact that the plastic deformation during the performed fatigue tests is very small: the plastic strain is always smaller than 10^{-4}, hence also the cross section of the sample changes with less than 10^{-4} during the fatigue tests.

When comparing both magnetomechanical methods performed on one particular material (i.e. comparing figure 6.21 with 6.23, and comparing figure 6.22 with 6.24), the same trends become apparent: for the annealed material mat-A three stages in the fatigue lifetime can be distinguished: both ΔM and ΔM_r first increase, then stabilize, and finally start to decrease significantly at about 96% of the fatigue lifetime. For the as-received material mat-B only two stages in the fatigue lifetime can be distinguished: both ΔM and ΔM_r are quasi-constant during the majority of the fatigue lifetime and finally start to decrease at about 98% of the fatigue lifetime. Here, for both methods H_{stat} and H_{dyn} the same approach as in figure 6.19 is followed to determine the start of the final transition stage: at each cycle number n the long-term linearized trend of $\Delta M(n)$ (or $\Delta\varepsilon_i(n)$) is calculated from the last (typically 50) cycles. The number of cycles $n_{tr,f}$ at the start of the final transition stage corresponds with the instant when the absolute value of the slope of $\Delta M(n)$ (or $\Delta\varepsilon_i(n)$) becomes higher than a certain threshold value, defined as 5 times the absolute value of the average slope during the second fatigue stage.

Table 6.3. Material details (yield strength σ_y) and fatigue test details (stress amplitude σ_a and number of cycles to failure n_f), combined with results of the magnetomechanical techniques, corresponding to figures 6.21 to 6.24. Based on both $\Delta M_{(r)}$ and $\Delta\varepsilon_i$, estimates are made about the fatigue lifetime $n_{tr,f}/n_f$ at the transition to the final fatigue stage.

material	method	fig.	σ_y (MPa)	σ_a (MPa)	n_f (-)	$n_{tr,f}/n_f$, transition of $\Delta M_{(r)}$	$n_{tr,f}/n_f$, transition of $\Delta\varepsilon_i$
mat-A	H_{stat}	(6.21)	285	208	21 244	95.5 %	96 %
mat-A	H_{dyn}	(6.23)	285	200	36 947	97 %	98.5 %
mat-B	H_{stat}	(6.22)	390	250	29 352	98.4 %	98.6 %
mat-B	H_{dyn}	(6.24)	390	246	41 215	98 %	98.8 %

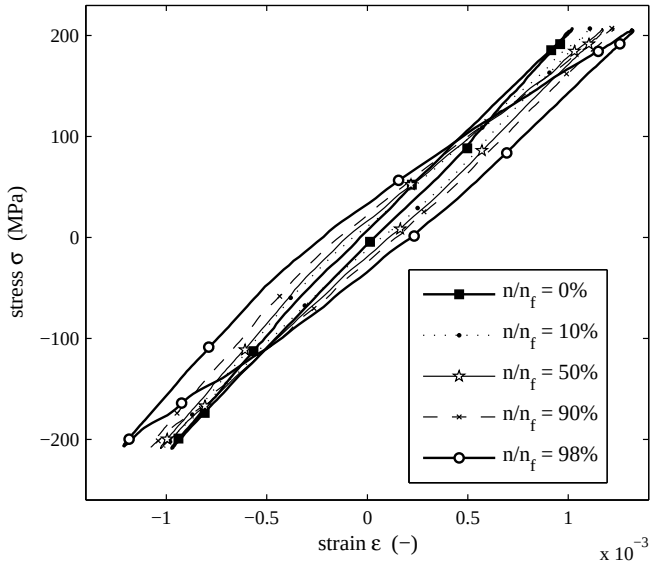

Figure 6.25. Selection of stress-strain hysteresis loops throughout the fatigue lifetime n/n_f (as indicated in the legend) for material mat-A.

In the last two columns of table 6.3, the resulting values of $n_{tr,f}/n_f$ are given for both tests, for both materials, and for both monitoring parameters $\Delta M_{(r)}$ and $\Delta\varepsilon_i$. Also, the start of the final transition stage, described by the number of cycles at the transition, $n_{tr,f}$, is determined for all performed fatigue tests. For all fatigue tests performed on material mat-B for instance (see the S-N curve in figure 6.20), the number of cycles of the final fatigue stage, $(n_f - n_{tr,f})$, is found to be in the range of 400 to 600 cycles.

The obtained mechanical validation results making use of the inelastic strain range $\Delta\varepsilon_i$, are in agreement with the results of [Socha2003]. Also three stages can be distinguished: first a high increase, then a slow increase, and finally a high increase of $\Delta\varepsilon_i$. Figure 6.25 shows the variation of the stress-strain hysteresis loops for a fatigue test on material mat-A. Also in agreement with [Socha2003] is the decrease of the elasticity modulus with increasing fatigue damage progression (in other words the stress-strain loops become less and less steep), especially during the final fatigue stage.

Moreover, the fatigue-induced variation of the inelastic strain-stress hysteresis loop width $\Delta\varepsilon_i$ fully mimics the observed trends in the magnetomechanical parameters (i.e. also three stages for mat-A and two stages for mat-B), showing clearly the correlation between the changes of the magnetomechanical and the mechanical properties. For both ΔM and ΔM_r, and also for $\Delta\varepsilon_i$, an initial transition stage at the beginning of the fatigue test is not present for mat-B, probably due to

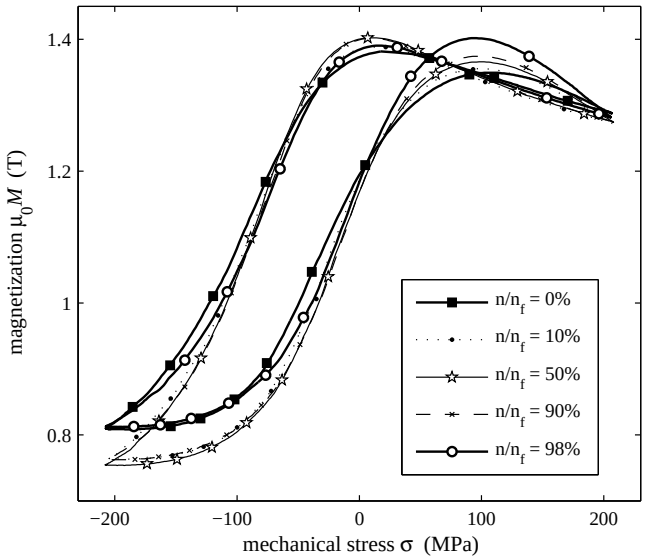

Figure 6.26. Selection of $M(\sigma)$ loops throughout the fatigue lifetime n/n_f (as indicated in the legend) obtained by method H_{stat} on material mat-A.

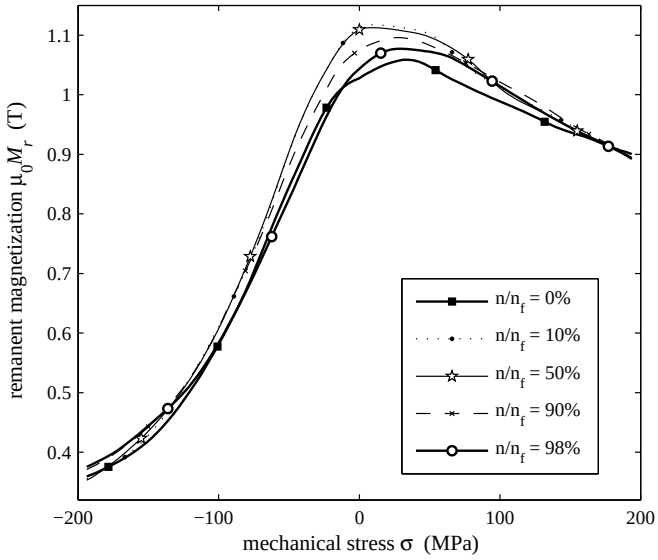

Figure 6.27. Selection of $M_r(\sigma)$ curves throughout the fatigue lifetime n/n_f (as indicated in the legend) obtained by method H_{dyn} on material mat-A.

the higher initial dislocation density of the as-received steel mat-B compared to the stress-relief annealed steel mat-A.

In addition, figures 6.26 to 6.27 show in more detail the particular variation of the $M(\sigma)$ hysteresis loops and of the $M_r(\sigma)$ curves, for method H_{stat} and method H_{dyn} respectively. These figures indicate that starting from this particular magnetomechanical behaviour, also other parameters than $\Delta M_{(r)}$ can be determined. For example, for method H_{stat}, the $M(\sigma)$ loop area, the maximum value of the slope $\mathrm{d}M/\mathrm{d}\sigma$, or the local maximum of the magnetization along the descending branch (at the so-called Villari reversal, see section 6.1) are possible alternative monitoring parameters. For method H_{dyn}, the $M(H)$ loop area (losses) at a certain mechanical stress value shows potential as monitoring parameter. Nevertheless, when analyzing the results it appeared that the originally defined monitoring parameters ΔM and ΔM_r are more robust to experimental noise, and slightly more sensitive to the fatigue damage progression.

Concerning the fatigue assessment and the estimation of $n_{tr,f}$, both methods (H_{stat} and H_{dyn}) give rise to comparable results. In practice however, method H_{stat} is much more convenient than H_{dyn}, which becomes apparent when comparing the number of measuring points to obtain the magnetization experimentally during each mechanical period: typically 600 instead of 21000 (35 magnetic periods per mechanical period, multiplied by 600 points per magnetic period) respectively for H_{stat} and H_{dyn}.

As a conclusion, both magnetomechanical methods provide information about the different fatigue stages and also of the final fatigue stage. This is the case for the three investigated materials (mat-A, mat-B and mat-C). As been said before, three stages can be clearly identified for mat-A and mat-C, whereas for mat-B the first initial transition stage is not present, and only the equivalent of stages 2 and 3 are observed.

However, a closer inspection – especially of the steady-state stage 2 – of all performed magnetomechanically monitored fatigue tests on mat-A, mat-B and mat-C (8 tests are performed on mat-A, 12 tests on mat-B, see figure 6.20, and 6 tests on mat-C) reveal the following typical features that are always observed in such three-stage magnetomechanical behaviour:

1. The first fatigue stage is always characterized by an increase of the magnetomechanical monitoring parameter (ΔM or ΔM_r), in case of mat-A and mat-C (as been mentioned earlier, for mat-B, no first fatigue stage is present, not in the magnetomechanical behaviour and also not in the mechanical behaviour, see figures 6.21 and 6.23).

2. During the second (steady-state) fatigue stage, the magnetomechanical behaviour is quasi-constant, although when looking closer, some finer scale trends can be observed. Concerning the second stage itself, one of three

possible trends are always observed for each of the 26 performed fatigue tests:

- *Second stage, possible trend (a)*: during the second stage first a small increase of the magnetomechanical monitoring parameter $\Delta M_{(r)}$ is observed, followed by a small decrease. In other words, the cycle number n_{max} corresponding to the maximum of the monitoring parameter $\Delta M_{(r)}$, is in between $n_{tr,i}$ and $n_{tr,f}$, which respectively denote the cycle number at the initial transition (from stage 1 to stage 2) and the cycle number of the final transition (from stage 2 to stage 3), see figure 6.19 for a graphical representation of $n_{tr,i}$ and $n_{tr,f}$. A typical example of such a possible trend (a) is shown in figure 6.21: for material mat-A the maximum of ΔM occurs at about 62% of the fatigue lifetime.
- *Second stage, possible trend (b)*: a continuous decrease of the magnetomechanical monitoring parameter $\Delta M_{(r)}$ is observed during the second stage. In other words, the cycle number n_{max} corresponding to the maximum of $\Delta M_{(r)}$ is more or less equal to $n_{tr,i}$. A typical example of such a possible trend (b) is shown in figure 6.19: for material mat-C the maximum of ΔM occurs at about n_{max}/n_f = 13% of the fatigue lifetime, whereas $n_{tr,i}/n_f$ equals 12%.
- *Second stage, possible trend (c)*: a continuous decrease of the magnetomechanical monitoring parameter $\Delta M_{(r)}$ is observed during the second stage, but with a change in slope: first the behaviour is quasi-constant, and at n_s the slope becomes larger. A typical example of such a possible trend (c) is shown in figures 6.23 and 6.24: n_s is about 63% of the fatigue lifetime n_f for mat-A, and 73% for mat-B. Moreover, second stage trend (b) and trend (c) can be both present, a typical example is shown in figure 6.19: n_s is about 85% of the fatigue lifetime n_f.

3. During the final third stage the magnetomechanical monitoring parameter is always sharply decreasing with respect to the cycle number.

The variation of the magnetomechanical monitoring parameters, such as ΔM and ΔM_r, can be used to estimate the remaining life of steel components. The finer-scale features of the magnetomechanical monitoring parameters in the second stage, making use of the four parameters $n_{tr,i}$, n_{max}, n_s and $n_{tr,f}$, as defined above, see for instance figure 6.19(b), show some potential to be used in order to define and evaluate a 'stop' criterion for the cyclic load operation of steel components:

- The most obvious transition to the final fatigue stage is occurring at approximately $n_{tr,f}$ = 97% of the fatigue lifetime, but from a safety point of

view this is rather late in the fatigue lifetime in order to be used as a stop criterion.

- A more defensive stop criterion can be based on the maximum value of the magnetomechanical monitoring parameter, occurring at n_{max}. For the typical result of second stage trend (a) see figure 6.21, n_{max}/n_f equals 62% of the fatigue lifetime, but for the typical result of second stage trend (b), see figure 6.19, n_{max}/n_f equals 13% of the fatigue lifetime.
- A stop criterion based on n_s is also possible, but the actual estimation of it can be somewhat arbitrary in some cases.
- A stop criterion based on $n_{tr,i}$ is not always possible, since for material mat-B for instance, the initial transition stage is not present, and moreover $n_{tr,i}$ occurs at fatigue lifetimes at or sometimes below 10%, which gives rise to a very defensive stop criterion.

Nevertheless, a more detailed experimental study is needed to refine these techniques further towards an actual estimation tool in order to determine a safe moment to stop the operation of cyclicly loaded steel components.

Chapter 7

General conclusions and suggestions for further research

7.1 General conclusions

This Ph.D. research has as general aim the exploration of the possibilities and the sensitivity of the magnetic and magnetomechanical hysteretic characterization to non-destructively evaluate the progression of microstructural degradation phenomena in ferromagnetic materials. The main material degradation processes that are treated in this research work are (1) the hardening and embrittlement phenomena due to neutron irradiation in nuclear reactor pressure vessel steels, and (2) the process of metal fatigue in ferromagnetic materials.

Ferromagnetic behaviour. In order to motivate such an approach of magnetic non-destructive evaluation of material degradation, the fundamental principles dealing with the relation between the magnetization processes and the microstructural features of iron-based materials are elucidated (*chapter 2*). The general aspects, the internal mechanisms and the underlying origin of ferromagnetic behaviour are discussed, with special emphasis on the influence of the microstructural features and the lattice imperfections which are inherent to ferromagnetic materials such as iron and ferritic steels.

To gain an in-depth knowledge about this topic, the micromagnetic theory of competing energy contributions which are the origin for the equilibrium magnetic domain structure, is shown to be very useful. Micromagnetism provides a theoretical framework for the interaction of microstructural defects and inhomogeneities on the one hand and the equilibrium magnetic domain configuration on the other hand, since the defects and inhomogeneities slip into the micromagnetic equations via the magnetoelastic energy term as a residual internal stress distribution.

Making use of the micromagnetic energy concepts, a magnetic domain wall model is derived giving some qualitative results about the influence of defect density and pinning strength on macroscopic magnetic parameters such as coercive field and initial permeability.

The approach of this research work is merely experimental, therefore the development of magnetic characterization methods is a primordial and important issue. Versatile experimental setups and measuring techniques are developed, in combination with advanced analyzing techniques of the experimental data, in order to facilitate and enhance the characterization of the manifold features related to both the magnetic and the magnetomechanical hysteretic behaviour.

Magnetic measurement methods. The experimental approach taken during the performed research is almost entirely based upon the field-metric method (*chapter 3*), under the condition of unidirectional quasi-static excitation, with the specific aim to determine the macroscopic scalar relation between the magnetic field $H(t)$ and the magnetization $M(t)$ of the sample. Of primary interest is the typical hysteretic behaviour present in the constitutive relation $M(H)$ of ferromagnetic materials. The magnetic measurement methods and setups under consideration are deployed to experimentally explore all features of this hysteretic magnetic behaviour.

However, in our experimental investigations on mechanically degraded materials, the sample dimensions are constrained to much smaller dimensions than the dimensions prescribed in international standards for low-frequency magnetic measurements on sheets, strips or rods. To give an idea about the order of magnitude, samples under test can have a length of circa 30 mm, a width of 10 mm and a thickness of 1 mm. Also the sample shape is in many cases constrained to bars with square or circular cross sections.

Even for such samples with constrained size and shape we succeeded in designing modified and miniaturized single sheet tester (SST) configurations, inspired by and as close as possible to the standardized SST, resulting in reasonable accuracy and good repeatability for the magnetic characterization of the different samples under investigation.

When down-sizing the magnetic circuit of the setup in order to suit the samples, the following topics need to be carefully considered. The reluctances of the closing yoke and of the sample-yoke contact needs to be as low as possible compared to the reluctance of the sample under test. Therefore closing yokes are used with much higher permeability than the material under investigation – by using nanocrystalline soft magnetic material yokes – and the contact between the sample and the closing yokes needs to be preserved as good as possible, which becomes more problematic for smaller sample sizes. Nevertheless, for samples with square or circular cross section, the cross section of the yoke becomes of the same order of

magnitude as the cross section of the sample under test, and then it becomes more appropriate to directly measure the magnetic field H. In such cases the extrapolation towards the sample surface of the magnetic field measurements of several Hall sensors placed at several distances as close as possible to the sample surface is utilized in this research work.

Moreover, at EELAB a magnetomechanical experimental setup is designed and constructed, which is in principle the incorporation of a magnetic measurement setup inside a mechanical testing apparatus. This setup has the additional possibility, apart from applying a time-dependent magnetic field to the sample and simultaneously measuring $M(t)$ and $H(t)$, to apply also a time-dependent mechanical stress to the sample (mechanical loading is possible both in tension and in compression), and at the same time to measure both stress $\sigma(t)$ and strain $\varepsilon(t)$. With this setup it becomes possible to investigate the magnetomechanical effect on a macroscopic scale.

Magnetic hysteretic characterization. Magnetic hysteretic characterization methods for non-destructive evaluation (NDE) purposes (*chapter 4*), are in general based on the knowledge that the development of microstructural defects and the variations of the internal micro stress distributions around those defects influence the magnetic domain wall motion, leading to altered macroscopic magnetic hysteretic properties. In principle, we may identify microstructural changes, even before the initiation of cracks, and the deterioration of mechanical properties of ferromagnetic materials in a non-destructive manner by the characterization of the electromagnetic behaviour.

The core issue in relation to magnetic hysteretic NDE techniques is to define magnetic parameters that are sensitive enough to identify the changes of microstructural properties under investigation. As a first step, the classical magnetic hysteresis parameters characterizing the saturation magnetization loop such as coercive field, remanent induction, permeability, can be used for NDE purposes.

In this research work, the magnetic hysteresis non-destructive evaluation method is extended by increasing the input of experimental data for the evaluation technique. This is done by considering a whole set of minor magnetization loops from low to high magnetic induction levels, instead of taking into account only the (major) saturation magnetization loop. In such context a hysteresis model such as the Preisach model that takes the overall magnetic hysteresis behaviour into account is shown to be useful for non-destructive evaluation of microstructural changes.

Effect of microstructural degradation on the magnetic behaviour. Based on a number of experimental case studies for several material degradation processes, carried out during this research inside a laboratory environment, the possibilities and limitations of the field-metric magnetic hysteresis characterization are investigated (*chapter 5*). One of the main topics related to the effect of micro-

structural changes on the magnetic hysteretic behaviour that is investigated in this research work, is the irradiation-induced embrittlement and hardening of iron-based materials. In the nuclear industry this effect can be detrimental for reactor pressure vessel (RPV) steels. The underlying reason of such material degradation process is the formation of nano-size defects during neutron irradiation, i.e. the irradiation-assisted Cu-precipitation accompanied with matrix damage.

Conventionally, the material status concerning embrittlement, hardening and fracture toughness is evaluated destructively on the basis of surveillance specimens (e.g. Charpy impact and tensile test samples), made of exactly the same material as the pressure vessel. In order to cope with extended life times of nuclear power plants and considering the limited number of specimens originally inserted into the reactor in order to perform such destructive mechanical tests, there is a tendency to develop non-destructive evaluation (NDE) techniques. Such NDE techniques can be considered as additional and/or possible replacement techniques to assess the material condition. Their advantage is that the surveillance specimens can be reused, so without losing precious surveillance material.

In this research work, the magnetic hysteretic characterization method is examined as a possible NDE technique. Two related topics are investigated here: the thermal aging (and over-aging) of Fe-Cu model alloys, and the irradiation of Fe, Fe-Cu and ferritic steels.

Firstly, in order to study in detail the hardening and embrittlement processes due to Cu-precipitation, separately from the effects of the irradiation-induced matrix damage, the investigation of the thermal aging of Fe-Cu model alloys is a common and adequate practice, since during thermal aging experiments of Fe-Cu model alloys, one observes hardening processes due to Cu-precipitation, quite similar to the irradiation-enhanced Cu-precipitation hardening.

The formation and growth of Cu-precipitates during the thermal aging process at 500°C leads to variations of the investigated magnetic hysteretic properties, such as remanence, maximum permeability, width and peak value of the local interaction field distribution $Q_m(h_m)$ (which is defined within the frame of the Preisach hysteresis model). Moreover, the regimes that can be indicated in their relation to the aging time correspond with the mechanical hardening and softening regimes, in other words the magnetic parameters fully mimic the yield stress variation.

The hardening regime corresponds to small coherent Cu-precipitates, which obstruct the dislocation motion and the magnetic domain wall movement, whereas the softening regime corresponds to larger and well separated incoherent Cu-precipitates, which are softer obstacles to both dislocations and magnetic domain walls. Furthermore, the extremum values of all investigated magnetic parameters correspond with the mechanical peak hardening, at an aging time of 15h.

Moreover, when compared to the initial case, the peak hardening values of the

magnetic parameters, such as remanence, maximum permeability, width and peak value of the local interaction field distribution, change with approximately 50% or more. This pronounced sensitivity indicates the potential of magnetic NDE for the evaluation of hardening and softening phenomena induced by Cu-precipitation.

Secondly, the actual irradiation-induced embrittlement and hardening is studied. The irradiation-induced microstructural changes not only affect the mechanical behaviour, but also lead to variations in the magnetic hysteretic behaviour for all investigated materials, i.e. nominally pure Fe, Fe-Cu model alloys, and RPV steels, both for a reference quality of RPV steel, 'JRQ' (Japanese Reference Quality), and for the surveillance samples of the reactor pressure vessel of an actual nuclear reactor, 'BSP' (Belgian Surveillance Program).

The main two parameters related to the magnetization loop shape that are investigated are the maximum relative differential permeability, and the peak intensity of the Preisach-based local interaction field distribution. Both parameters decrease with increasing neutron fluence and with increasing yield stress for all investigated materials.

The magnetic behaviour is sensitive to both irradiation-induced hardening mechanisms: a decreasing trend in the above-mentioned magnetic parameters during the mechanical hardening is noticeable, regardless the origin of hardening, which can be either Cu-precipitation (thermal aging of Fe-Cu model alloys), only matrix damage (irradiation of pure Fe), or both mechanisms (irradiation of Fe-Cu model alloys or ferritic RPV steels). These results suggest that the magnetic domain wall movement is hindered by the nano-sized defects induced by irradiation. The change of the magnetic parameters is found to be up to 40%, which indicates the sensitivity and the potential of magnetic hysteretic characterization for the assessment of irradiation-induced material hardening and embrittlement.

Effect of microstructural degradation on the magnetomechanical behaviour. The magnetomechanical behaviour can be considered as the combined effect of elastic mechanical stress and magnetic field on the magnetization (*chapter 6*). Magnetomechanical experiments are conducted for three different material classes (different, concerning their magnetomechanical behaviour), and for different conditions of elastic stress and magnetic field (both as static or dynamic quantities).

For all three investigated material classes (Fe, Ni and Fe-Ni), there is a correspondence in the anhysteretic magnetomechanical behaviour and the anhysteretic magnetostrictive behaviour, which is the outcome of the macroscopic magnetoelastic coupling. Moreover, in case of constant applied magnetic field and cyclic varying mechanical stress, for low-carbon ferritic steels the magnetization-stress behaviour shows hysteretic, asymmetric, non-linear and non-monotonic features. A fair correspondence in the non-linearity of such hysteretic stress-magnetization behaviour and of the anhysteretic stress-magnetization behaviour is observed.

Such an experimental study of the magnetomechanical behaviour is performed in order to better understand the physical mechanisms involved, with the aim to develop magnetic non-destructive evaluation methods for the continuous monitoring of the metal fatigue damage process.

During the service life of constructions or machines the cyclic mechanical loading of steel parts can lead to an accumulation of fatigue damage. To avoid that the fatigue damage process ends in a sudden fracture, it is vital to assess the material degradation, preferably in a non-destructive fashion. In the context of magnetic NDE, typically the change in magnetic hysteresis loop parameters can be determined at several interruptions of the cyclic loading. However, due to the abrupt character of metal fatigue it can be difficult to make predictions about the onset of fatigue failure based on experimental data obtained at only a limited number of load interruptions.

Therefore we explore in this research work the possibility to examine the fatigue process during the cyclic mechanical loading itself, in order to experimentally obtain information for every single mechanical loading cycle. For this purpose the magnetomechanical effect can be exploited: during the cyclic mechanical loading the application of a magnetic field can be considered, and the magnetization variation resulting from both the applied mechanical stress and the enforced magnetic field can be continuously monitored throughout the cyclic mechanical loading test.

Two magnetomechanical examination methods are investigated, differing only in the magnetic field that is continuously applied to the sample during the stress-controlled cyclic mechanical loading: i.e. a constant magnetic field (method H_{stat}) or a time-varying magnetic field (method H_{dyn}), with the magnetic frequency significantly larger than the mechanical frequency. In both methods the magnetization variation $M(\sigma, H)$ during each stress cycle due to the magnetomechanical effect, is continuously measured throughout the complete cyclic mechanical loading test.

Both magnetomechanical methods provide information about the different stages in the fatigue lifetime and also about the final fatigue stage. This is the case for the three investigated ferritic steels. The finer-scale features of the magnetomechanical monitoring parameters in the steady-state stage, show potential to be used in order to define and evaluate a stop criterion for the cyclic load operation of steel components.

This method of continuous monitoring the changes in the magnetomechanical behaviour during the cyclic mechanical loading is validated by comparing with the continuous examination of changes in the mechanical stress-strain behaviour: the different fatigue stages in the inelastic strain-stress behaviour fully mimic the corresponding fatigue stages in the magnetomechanical behaviour.

In conclusion, changes in the microstructural features of the crystal lattice defects influence the dislocation dynamics, but also affect the magnetic domain wall motion in ferromagnetic materials, which lead to altered mechanical and magnetic macroscopic properties, respectively. Although the underlying mechanisms of magnetic and mechanical behaviour are different, there exists a certain interrelation between the macroscopic magnetic behaviour, the macroscopic mechanical behaviour and the underlying microstructural features of the material.

The developed magnetic characterization techniques can be exploited for the non-destructive evaluation of macroscopic mechanical properties, microstructural features and/or localized flaws, aiming for the assessment of ferromagnetic material integrity during their operation or for the quality control during material processing.

Like every other NDE technique, also the magnetic hysteretic characterization is inherently an indirect evaluation method. The microstructure of a polycrystalline iron-based material is a very complex system, and a variety of microstructural features have their influence on the magnetic hysteretic behaviour on the one hand, and on the mechanical behaviour on the other hand. Hence this interrelation between the magnetic properties, the microstructure and the mechanical properties is not a one-on-one relationship.

Due to the always increasing concern for improved safety in industrial environments and engineering structures, but also in the society in general, there remains a continuous need for the development of alternative and improved NDE technologies, which can offer greater capacity when used in combination with already existing non-destructive and destructive techniques. Indeed, the sensitivity of the material integrity assessment can be enhanced by using a combination of multiple methods for the same materials evaluation task, and magnetic hysteretic NDE can certainly play its role to intensify such multi-parameter and multi-method material integrity assessment.

7.2 Collaboration with scientific partners

During the research described in the preceding chapters, especially in chapters 3 to 6, there has been some close and very much appreciated collaboration with other scientific partners. In the following paragraph I give credit to my scientific partners for the work they performed.

Generally speaking, the research treated in this thesis can be divided into three parts, according to the three different developed and applied magnetic NDE methods: (a) magnetic hysteretic NDE, (b) magnetomechanical NDE and (c) magnetic drag force NDE.

(a) Magnetic hysteretic NDE. This method (described in sections 3.1–3.2 and chapter 4) is developed by myself, in more detail both the experimental setup (concept, design, sensors, electronics, hardware, software) and the characterization tools (post-processing of data). Also the application-specific modifications to the method and carrying out the magnetic hysteresis measurements are my work. Four applications of this method are considered: (1) hardening by thermal aging, (2) irradiation-induced embrittlement, (3) plastic deformation by tensile straining and (4) plastic deformation by cold rolling.

For the first two applications (section 5.1) there was close collaboration with the *Belgian nuclear research center SCK·CEN*. They prepared the thermally aged and irradiated samples and performed the mechanical and microstructural characterization. I had the very much appreciated opportunity to perform magnetic hysteretic experiments on irradiated samples inside the hot-cells of the Institute for Nuclear Materials at SCK·CEN. This research resulted so far in a number of joint publications (A1-papers 21 and 25 of my curriculum, see page 255).

Concerning the plastic deformation (section 5.2), the experiments on tensile straining are my work, whereas the cold rolled samples are part of a Round Robin test between different laboratories, executed in the frame of the *"Universal Network for Magnetic Non-Destructive Evaluation"*, an international scientific consortium with academic partners from Japan, UK, USA, Italy, Czech Republic, South Korea, Germany, France, Greece, Hongary, Brazil,... For Belgium, our laboratory EELAB takes part in this consortium. The sample preparation, the mechanical and the microstructural characterization is performed by *Iwate University, Morioka, Japan*. The magnetic measurements are entirely my work.

(b) Magnetomechanical NDE. The method development (section 3.3), the magnetomechanical preliminary study (section 6.1) and the applications towards continuous monitoring of metal fatigue (section 6.2) are entirely my work.

(c) Magnetic drag force NDE. The initial research and development of the magnetic drag force method (section 3.4) is carried out in close collaboration with the R&D companies *Magnova (Pittsfield, MA, USA)* and *MagCanica (San Diego, CA, USA)*. The concept, design and the hardware development is their work, I performed a feasibility study of the concept and did a comparison study between the drag force measurements and magnetic hysteresis measurements. Concerning the application towards localized residual stress, due to cyclic bending (section 5.3), the methodology, the construction of the cyclic bending machine, the sample preparation and the magnetic hysteretic measurements are my work. The drag force measurements on the cyclicly bent samples are performed by Magnova and MagCanica. This collaboration resulted so far in a number of joint publications (A1-papers 15, 18, 22 and 24 of my curriculum, see page 255).

7.3 Suggestions for further research

7.3.1 Applied experimental research

In this research work, we explored and investigated the possibilities, the limitations and the sensitivity of the macroscopic magnetic and magnetomechanical hysteretic characterization of ferromagnetic materials to non-destructively evaluate the progression of microstructural degradation phenomena. The main goal was to deliver a proof of concept of magnetic hysteretic NDE methods by experimental sensitivity studies in a laboratory environment, for several material degradation processes.

Irradiation-induced hardening and embrittlement. Some direct extensions can be made in the research considering the topic of irradiation-induced hardening and embrittlement, by still making use of the present magnetic hysteretic characterization techniques. As shown in figure 5.16, a promising trend is apparent when plotting the investigated magnetic hysteretic parameters against yield stress for instance. However, the number of data points is rather low to draw already strong conclusions. For instance for the Belgian surveillance program (BSP) results, the number of data points is inherently restricted to the number of surveillance capsules that are over the years taken out of the pressure vessel of the nuclear reactor (i.e. for the moment already five capsules).

To investigate in more detail this trend between magnetic and mechanical parameters, and in order to be able to make predictions about the results at future neutron fluence (or dose) values, one of the suggestions is to irradiate already tested (broken) surveillance samples to higher fluence values in an accelerated way by making use of a nuclear test reactor. This opens perspectives to investigate the future trends in the magnetic parameters as a function of neutron fluence or mechanical parameters. However, a disadvantage of such approach can be a possible effect of the higher neutron flux (or dose rate) values when comparing the test reactor with the actual BSP reactor data [Chaouadi2005, Odette2005].

Another suggestion to enlarge the number of points in figures such as 5.16, is to consider so-called post-irradiation annealing (and re-irradiation) [Chaouadi2005, Kryukov1998, Ulbricht2007]. Post-irradiation annealing leads to (partial) recovery of the initial mechanical properties before irradiation-induced degradation. Magnetic hysteretic characterization and mechanical testing experiments can be conducted on post-irradiation annealed (and even re-irradiated) RPV steels in order to see whether such results can also be correlated with the present magnetic versus mechanical parameter trend, which for the moment consists of five data points, in case of the Belgian Surveillance Program (BSP).

The results on irradiated RPV steels are obtained on samples with 10 mm by 1

mm cross section, samples that are cut from broken Charpy specimens. In order to be really non-destructive, the magnetic hysteretic characterization should be conducted on the actual Charpy specimens itself (with preference to the unbroken Charpy specimens). A setup to magnetically measure unbroken Charpy specimen was constructed at EELAB in the frame of a round robin test of the 'Universal Network for Magnetic NDE' (see section 3.2.2 for details about the setup, and section 5.2 for some results). This setup shows promising results when compared to the alternative setups constructed, in the frame of the above-mentioned round robin test, at other magnetic measurement laboratories around the world, but at the moment no measurements on irradiated Charpy samples are performed with it. Magnetic measurements on irradiated non-broken Charpy specimens of model alloys or JRQ steel can be considered as a next step related to this research. However, for the actual surveillance program samples (BSP) such approach is difficult to perform due to the possible unavailability of unbroken samples of earlier surveillance capsules. On the other hand when considering broken Charpy or broken tensile samples, if we can chose between magnetic measurements on the 10 mm by 1 mm by 26 mm samples that are cut from broken Charpy pieces, or magnetic measurements on the broken Charpy piece as a whole, then the first option is preferred.

A next step in this research about the irradiation-induced hardening and embrittlement can be to consider in-situ (in-core) magnetic measurements on closed ring cores made of RPV steels, enclosed in the surveillance capsules inside the reactor pressure vessel, during the operation of the nuclear reactor. By such strategy, the material integrity of the surveillance samples can be monitored non-destructively on a continuous time scale during operation.

On-site magnetic sensor. Another future target is the extension of the research towards practical applications in general. As been said before, the research work of this Ph.D. aims to deliver a proof of concept of magnetic hysteretic NDE methods by experimental sensitivity studies in a laboratory environment, for several material degradation processes. In other words, the aim is to investigate if the sensitivity is sufficient to develop techniques based on the investigated principles that are applicable in the field, concerning material integrity issues in electric power plants, bridges, pipelines and so on.

Hence, in a further stadium, which can be part of future research, the results of the investigations treated in this Ph.D. can serve as the necessary knowledge to develop prototype experimental systems for the in-situ material integrity inspection of critical components of actual engineering structures and industrial installations. The development of a suitable on-site sensor is a prerequisite for such purposes. In a laboratory environment the single sheet tester with two closing yokes above and underneath the sample, and with both excitation coil and measuring coil wound around the sample, is the best choice as magnetic circuit [DeWulf2002]. On site, it can however be impossible to encircle the material under test, but neverthe-

less a suitable sensor can be constructed with both coils around a single yoke for instance.

More applied research is of course necessary to develop such on-site magnetic NDE techniques, and practical considerations shall result in the fact that some of the suggested techniques can be implemented in non-laboratory environments, and others not. Also other application areas (other than the ones that are currently investigated) can be considered, such as creep and thermal fatigue.

7.3.2 Fundamental experimental research

The experimental techniques that are utilized predominantly throughout this research work are based on volumetric field-metric magnetic hysteresis measurements. As an extension, the experience acquired during this research can also be employed to develop two other promising fundamental experimental techniques that can be used for magnetic NDE purposes, i.e. the magnetic (and magnetomechanical) Barkhausen effect and the magnetic relaxation (or magnetic after-effect).

Magnetic and magnetomechanical Barkhausen effect. The Barkhausen effect is related to irreversible magnetization processes: discontinuous magnetic domain wall movements lead to step-like changes in magnetization and such behaviour is detected as stochastic fluctuations in the induced voltage, known as Barkhausen noise, as is also introduced in section 2.4. Such discontinuous domain wall motion is due to temporary pinning of domain walls by the internal micro-stress fields associated with defects. Hence the Barkhausen noise evaluation shows potential for the assessment of microstructural changes. Both applied magnetic field and applied elastic mechanical stress can lead to the motion of magnetic domain walls. Hence Barkhausen noise can be observed both by magnetic excitation (varying magnetic field, static elastic stress) or by mechanical excitation (varying elastic stress, static magnetic field), which is termed as magnetic Barkhausen and magnetomechanical Barkhausen effect, respectively [Augustyniak1995].

In this context a comprehensive study can be carried out on the magnetic and magnetomechanical Barkhausen effect, a study which is by the way an obvious extension of this Ph.D. study on bulk magnetic and magnetomechanical hysteretic behaviour. In such research the development of an experimental setup for the Barkhausen noise acquisition is of course a prerequisite. The concept can be as follows: starting from an appropriately designed sensor to pick up the induced voltage, after band-pass filtering and amplification, the Barkhausen noise signal is further post-processed and analyzed digitally. A study of the Barkhausen-related literature revealed numerous alternatives related to (i) the sensor design and concept, (ii) the excitation waveform, (iii) the frequency window of the band-pass filter, and (iv) the post-processing and the definition of suitable Barkhausen

NDE parameters. Therefore a fundamental study can be carried out to investigate all these aspects. Moreover, we propose to support the interpretation of the Barkhausen experimental data by stochastic modelling of the domain wall dynamics [Alessandro1990]. As possible application of both magnetic and magnetomechanical Barkhausen noise, the metal fatigue and creep material degradation processes are put forward.

Magnetic relaxation or magnetic after-effect. The study of the magnetic relaxation, which is based on the interaction between the magnetic domain walls and the thermal activation of crystal lattice defects such as point defects and dislocations, shows potential for the investigation of the mechanical hardening and embrittlement phenomena due to point defect matrix damage and due to precipitation of e.g. Cu-clusters. Owing to the interaction between magnetic domain walls and crystal lattice defects, the thermally activated motion of such defects leads, after demagnetization, to a reduced domain wall mobility with time and therefore leads to a corresponding time-dependent decrease of the initial permeability. This decrease in initial permeability is the outcome of the magnetic relaxation or magnetic after-effect phenomenon and can be experimentally observed for several fixed temperatures in a broad range to obtain knowledge about the thermally activated relaxations. The characterization of magnetic relaxation shows potential for the investigation of mechanical hardening and embrittlement phenomena in iron-based materials (for a review see [Blythe2000]).

In such research the development of an experimental setup for the magnetic relaxation is of course a prerequisite. The concept can be as follows: an open magnetic circuit (which means without additional means to close the flux path) can be constructed with one pick-up coil and two excitation coils which are located around the bar-shaped sample. After sample demagnetization by using the outer excitation coil, a small alternating magnetic field is applied to the sample by using the inner excitation coil. The resulting induced voltage is measured using the pick-up coil, located closest to the sample. The decay of initial permeability is recorded as a function of time. Such experiment is then repeated for a set of fixed temperatures within the range T = 100 to 500 K. The magnetic relaxation spectrum is determined as the relative permeability change (for a given time) as a function of temperature. As possible application the irradiation-induced embrittlement and hardening is put forward. The magnetic relaxation technique will be utilized for such purpose in close connection with another relaxation technique, namely internal friction. Recently, a joint Ph.D. research program together with SCK·CEN is started to investigate this topic.

7.3.3 Fundamental numerical research

In this research work, building up the qualitative and quantitative relation between microstructural aspects, mechanical properties and macroscopic magnetic behaviour, relied almost exclusively on the experimental research, in some cases supported by a macroscopic magnetic hysteretic model.

On the other hand, dealing with a numerical approach, the computational micromagnetism (see also section 2.3) on a nanometer scale leads to a deeper understanding of magnetic hysteretic effects by visualization of the magnetization reversal process by interacting magnetic dipoles. With present computing capabilities it is nowadays possible to apply the micromagnetic theory for the numerical modelling of three-dimensional ferromagnetic crystals with dimensions of the order of 10 μm [VandeWiele2008a].

Moreover, in the micromagnetic theory, microstructural defects can be taken into account as an internal stress tensor via the magnetoelastic energy term, whereas non-magnetic inhomogeneities can be considered via the magnetostatic energy term in the micromagnetic formalism. Therefore, starting from a predefined microstructural state, the micromagnetic model permits to investigate the macroscopic magnetic behaviour of realistic materials.

In such context, a fundamental and systematic approach is necessary: starting from an acceptable physical description of the phenomena, one must first build up a mathematical model and next develop robust numerical methods, where both tasks have to be validated experimentally and analytically.

Aiming at the micromagnetic computation of macroscopic hysteretic behaviour of polycrystalline material samples (with dimensions in the mm and cm range), in order to investigate the influence of the microstructure on the macroscopic magnetic behaviour, is however very complex and challenging. As a matter of fact the numerical modelling of the experimental phenomena that are determined in this and also earlier Ph.D. research works conducted at EELAB, is actually the subject of two current Ph.D. researchers. Two different approaches are followed, the full-scope micromagnetic numerical approach [VandeWiele2008b], and a so-called mesoscopic approach on the magnetic domain level [VandenBerg2009].

One of the strengths of the numerical micromagnetic approach to investigate macroscopic magnetic behaviour is that it becomes possible to examine in theory the effect of one particular microstructural parameter, which is hard to achieve or to control in case of the experimental determination of the magnetic hysteresis loops on samples with different microstructures.

Appendix A

Tensor notation for elastic stress and strain relations

A.1 Tensor notation: an introduction

A tensor of rank n in a m-dimensional space is a mathematical object that uses n indices to describe its m^n components. Tensors with rank n higher than 2 can be envisaged as multi-dimensional array generalizations of the concepts 'matrix' ($n = 2$), 'vector' ($n = 1$) and 'scalar' ($n = 0$). In general a tensor can be denoted as $u_{i_1 i_2 \ldots i_n}$, with each index i_k ranging from 1 to m. When both its rank and dimension are known, the same tensor can be written down more compactly as $\overline{\mathbf{u}}$.

In this work only Cartesian tensors are considered: these are tensors in a three-dimensional space ($m = 3$) spanned by $\mathbf{e}_i$ $(i = 1...3)$, the unit vectors of a three-dimensional orthogonal (Cartesian) coordinate system. Some examples of Cartesian tensors:

- u_i : tensor of rank 1, with 3^1 scalar components, which can be considered as vector $\mathbf{u} = u_1\mathbf{e}_1 + u_2\mathbf{e}_2 + u_3\mathbf{e}_3$, or as array $[u_1\ u_2\ u_3]^T$.
- u_{ij} : tensor of rank 2, with 3^2 scalar components, which can be considered as (3x3) matrix:

$$u_{ij} = \begin{bmatrix} u_{11} & u_{12} & u_{13} \\ u_{21} & u_{22} & u_{23} \\ u_{31} & u_{32} & u_{33} \end{bmatrix}. \tag{A.1}$$

- u_{ijk} : tensor of rank 3, with 3^3 scalar components.
- u_{ijkl} : tensor of rank 4, with 3^4 scalar components.

Concerning Cartesian tensors, two tensor notation conventions can be introduced:

- when an index occurs in an expression, this index has to be considered from 1 to 3 (unless otherwise indicated);
- *Einstein summation convention*: when an index appears twice in the same term, it implies summation with respect to that index (from 1 to 3, unless otherwise indicated).

As an example, $u = v_i w_i$ corresponds with $u = \sum_{i=1}^{3} v_i w_i = v_1 w_1 + v_2 w_2 + v_3 w_3$, whereas the expression $u_i = v_{ij} w_j$ corresponds with the following three equations:

$$\begin{cases} u_1 = v_{11} w_1 + v_{12} w_2 + v_{13} w_3 \\ u_2 = v_{21} w_1 + v_{22} w_2 + v_{23} w_3 \\ u_3 = v_{31} w_1 + v_{32} w_2 + v_{33} w_3 \end{cases} \tag{A.2}$$

These examples illustrate that expressions and equations can be written into a more concise and compact form by using tensor notation.

A.2 Elastic stress and strain relations in continuum mechanics

In linear elastic continuum mechanics theory, stress and strain can be defined in three-dimensional space as *symmetric* Cartesian tensors of rank two, $\overline{\sigma}$ and $\overline{\varepsilon}$. In matrix notation:

$$\overline{\sigma}(\mathbf{r}) = \begin{bmatrix} \sigma_{11}(\mathbf{r}) & \sigma_{12}(\mathbf{r}) & \sigma_{13}(\mathbf{r}) \\ \sigma_{12}(\mathbf{r}) & \sigma_{22}(\mathbf{r}) & \sigma_{23}(\mathbf{r}) \\ \sigma_{13}(\mathbf{r}) & \sigma_{23}(\mathbf{r}) & \sigma_{33}(\mathbf{r}) \end{bmatrix} \tag{A.3}$$

$$\overline{\varepsilon}(\mathbf{r}) = \begin{bmatrix} \varepsilon_{11}(\mathbf{r}) & \varepsilon_{12}(\mathbf{r}) & \varepsilon_{13}(\mathbf{r}) \\ \varepsilon_{12}(\mathbf{r}) & \varepsilon_{22}(\mathbf{r}) & \varepsilon_{23}(\mathbf{r}) \\ \varepsilon_{13}(\mathbf{r}) & \varepsilon_{23}(\mathbf{r}) & \varepsilon_{33}(\mathbf{r}) \end{bmatrix} \tag{A.4}$$

As a matter of fact, both tensors are defined in each point of space $\mathbf{r}$ and can vary continuously with position. In analogy with vector fields such as for instance electromagnetic fields (magnetic field $\mathbf{H}(\mathbf{r})$, electric field $\mathbf{E}(\mathbf{r})$,...), one could speak here in terms of stress and strain *tensor fields* $\overline{\sigma}(\mathbf{r})$ and $\overline{\varepsilon}(\mathbf{r})$.

More precisely, the strain tensor field $\overline{\varepsilon}$ quantifies the strain in a certain point $\mathbf{r}$ of an object when this object is undergoing a small three-dimensional deformation due to a stress tensor field $\overline{\sigma}(\mathbf{r})$. The three diagonal elements $\varepsilon_{kk} (k = 1...3)$ are the relative changes in length in the direction along $\mathbf{e}_k$, whereas the off-diagonal elements ε_{kl} are the shear strains.

General elastic constitutive law

The general constitutive relation between elastic stress $\overline{\sigma} = \sigma_{ij}$ and elastic strain $\overline{\varepsilon} = \varepsilon_{kl}$, takes into account that the elastic constants of a crystal vary with orientation (i.e. the elasticity of crystals is anisotropic). The constitutive relation of a single-crystal can be envisaged as a generalized Hooke's law, which in tensor notation takes the following form:

$$\overline{\sigma} = \overline{\mathbf{c}} \cdot\cdot \overline{\varepsilon}, \text{ or alternatively: } \sigma_{ij} = c_{ijkl}\varepsilon_{kl} \quad (i,j,k,l = 1...3), \tag{A.5}$$

with $\overline{\mathbf{c}} = c_{ijkl}$ the fourth rank tensor of material dependent elastic constants, the so-called stiffness tensor. Since both stress and strain tensors are symmetric, $\sigma_{ij} = \sigma_{ji}$ and $\varepsilon_{kl} = \varepsilon_{lk}$, see (A.3) and (A.4), also the fourth rank stiffness tensor is symmetric with respect to its first two and last two indices, i.e.

$$c_{ijkl} = c_{jikl} = c_{ijlk} = c_{jilk}. \tag{A.6}$$

Due to these symmetry properties of $\overline{\sigma}$, $\overline{\varepsilon}$ and $\overline{\mathbf{c}}$, the originally nine equations represented by the tensor expression (A.5) reduce to six unique equations. For instance the first equation becomes, when taking into account that $c_{11kl} = c_{11lk}$ and $\varepsilon_{kl} = \varepsilon_{lk}$:

$$\begin{aligned} \sigma_{11} = c_{11kl}\varepsilon_{kl} &= c_{1111}\varepsilon_{11} + c_{1112}(2\varepsilon_{12}) + c_{1113}(2\varepsilon_{13}) \\ &+ c_{1122}\varepsilon_{22} + c_{1123}(2\varepsilon_{23}) + c_{1133}\varepsilon_{33}. \end{aligned} \tag{A.7}$$

In other words, the general elastic stress–strain behaviour can be described by six relations between six independent stress and six independent strain components.

Voigt's contracted notation of symmetric tensors

A useful approach when dealing with symmetric tensors is the so-called Voigt's contracted notation, which in fact is a way to reformulate a *symmetric tensor* by reducing its rank [Mura1987, Dieter1988]:

- a symmetric tensor of rank $n = 2$ and dimension $m = 3$, has 6 unique components, and can be represented by a tensor of rank $n' = 1$ and $m' = 6$, in other words by a (6x1) array.
- a symmetric tensor of rank $n = 4$ and dimension $m = 3$, has 36 unique components, see (A.6), and can be represented by a tensor of rank $n' = 2$ and $m' = 6$, in other words by a (6x6) matrix.

One can see that in the contracted notation of a symmetric tensor the number of indices is reduced, on the condition that the new index should be interpreted from 1 to 6 (instead of from 1 to 3). The relation between the index pair ij of the 'old' tensor component, and the new index i' of the matrix element is unambiguous [Mura1987]:

ij	11	22	33	23	13	12
i'	1	2	3	4	5	6

(A.8)

Elastic constitutive law of b.c.c. iron in Voigt's notation

In Voigt's notation, the six relations between the six stress and six strain components that constitute the generalized Hooke's law (A.5) can then be written as follows:

$$\sigma_i = c_{ij}\varepsilon_j \quad (i,j = 1...6), \tag{A.9}$$

with, when carefully considering (A.7) and (A.8), σ_i and ε_j equal to:

$$\sigma_i = \begin{bmatrix} \sigma_1 \\ \sigma_2 \\ \sigma_3 \\ \sigma_4 \\ \sigma_5 \\ \sigma_6 \end{bmatrix} = \begin{bmatrix} \sigma_{11} \\ \sigma_{22} \\ \sigma_{33} \\ \sigma_{23} \\ \sigma_{13} \\ \sigma_{12} \end{bmatrix}, \text{ and } \varepsilon_j = \begin{bmatrix} \varepsilon_1 \\ \varepsilon_2 \\ \varepsilon_3 \\ \varepsilon_4 \\ \varepsilon_5 \\ \varepsilon_6 \end{bmatrix} = \begin{bmatrix} \varepsilon_{11} \\ \varepsilon_{22} \\ \varepsilon_{33} \\ 2\varepsilon_{23} \\ 2\varepsilon_{13} \\ 2\varepsilon_{12} \end{bmatrix}. \tag{A.10}$$

The relation between the fourth rank stiffness tensor, c_{ijkl} and Voigt's notation by a stiffness matrix, c_{ij}, is described by (A.8).

Moreover, the Voigt's stiffness matrix is also symmetric: $c_{ij} = c_{ji}$ $(i,j = 1...6)$. In other words, to describe the anisotropy of a linear elastic solid in the most general case, the stiffness tensor c_{ij} consists of 21 independent Voigt elastic constants.

For b.c.c. iron however, the number of independent elastic constants reduces to three, as a result of the symmetry conditions of cubic crystals, if the Cartesian coordinate system $\mathbf{e}_i$ is chosen along the crystallographic axes (i.e. the cube edges) [Mura1987]. For b.c.c. iron the values for the three stiffness constants c_{11}, c_{12} and c_{44} are given in table 2.1.

As a conclusion, for b.c.c. iron the relation between the six independent stress tensor components and six independent strain tensor components can be written

in terms of (c_{11}, c_{12}, c_{44}) as follows:

$$\begin{bmatrix} \sigma_{11} \\ \sigma_{22} \\ \sigma_{33} \\ \sigma_{23} \\ \sigma_{13} \\ \sigma_{12} \end{bmatrix} = \begin{bmatrix} c_{11} & c_{12} & c_{12} & 0 & 0 & 0 \\ c_{12} & c_{11} & c_{12} & 0 & 0 & 0 \\ c_{12} & c_{12} & c_{11} & 0 & 0 & 0 \\ 0 & 0 & 0 & c_{44} & 0 & 0 \\ 0 & 0 & 0 & 0 & c_{44} & 0 \\ 0 & 0 & 0 & 0 & 0 & c_{44} \end{bmatrix} \begin{bmatrix} \varepsilon_{11} \\ \varepsilon_{22} \\ \varepsilon_{33} \\ 2\varepsilon_{23} \\ 2\varepsilon_{13} \\ 2\varepsilon_{12} \end{bmatrix}. \tag{A.11}$$

Expression for the elastic energy density of cubic crystals in Voigt's notation

As been said, for cubic crystals $\overline{\mathbf{c}}$ can be described by three independent elastic stiffness constants (c_{11}, c_{12} and c_{44}, in Voigt's notation). Hence, by making use of (A.11), for cubic crystals the general tensor product $\overline{\varepsilon} \cdot\cdot \overline{\mathbf{c}} \cdot\cdot \overline{\varepsilon}$ can be written in the following form:

$$\begin{aligned} \overline{\varepsilon} \cdot\cdot \overline{\mathbf{c}} \cdot\cdot \overline{\varepsilon} &= c_{11}\left(\varepsilon_{11}^2 + \varepsilon_{22}^2 + \varepsilon_{33}^2\right) \\ &+ 2c_{12}\left(\varepsilon_{11}\varepsilon_{33} + \varepsilon_{22}\varepsilon_{33} + \varepsilon_{11}\varepsilon_{22}\right) \\ &+ c_{44}\left((2\varepsilon_{12})^2 + (2\varepsilon_{13})^2 + (2\varepsilon_{23})^2\right). \end{aligned} \tag{A.12}$$

Curriculum
Lode Vandenbossche

Date: March 5, 2009

Publications in peer-reviewed international journals, included in the Web of Science SCI (A1)

1. P. Sergeant, L. Dupré, J. Melkebeek, L. Vandenbossche (2004), "Magnetic field computation for optimized shielding of induction heaters", *Journal of Computational and Applied Mathematics*, vol. 168 (1-2), pp. 437–446.

2. L. Vandenbossche, L. Dupré, M. De Wulf, J. Melkebeek (2004), "Mechanical stress evaluation of steel utilizing its magnetic properties: an inverse problem approach", *Journal of Magnetism and Magnetic Materials*, vol. 272-276, pp. e535–e537.

3. L. Vandenbossche, L. Dupré, J. Melkebeek (2005), "Preisach-based magnetic evaluation of fatigue damage progression", *Journal of Magnetism and Magnetic Materials*, vol. 290-291, pp. 486–489.

4. L. Dupré, L. Vandenbossche, P. Sergeant, Y. Houbaert, R. Van Keer, J. Melkebeek (2005), "Optimisation of a Si-gradient in laminated SiFe alloys", *Journal of Magnetism and Magnetic Materials*, vol. 290-291, pp. 1491–1494.

5. D. Ruiz, T. Ros-Yañez, L. Vandenbossche, L. Dupré, R. E. Vandenberghe, Y. Houbaert (2005), "Influence of atomic order on magnetic properties of Fe-Si alloys", *Journal of Magnetism and Magnetic Materials*, vol. 290-291, pp. 1423–1426.

6. J. Barros, T. Ros-Yañez, L. Vandenbossche, L. Dupré, J. Melkebeek, Y. Houbaert (2005), "The effect of Si and Al concentration gradients on the

mechanical and magnetic properties of electrical steel", *Journal of Magnetism and Magnetic Materials*, vol. 290-291, pp. 1457–1460.

7. L. Vandenbossche, L. Dupré, J. Melkebeek (2005), "Monitoring the fatigue state of steel by evaluating the quasi-static and dynamic magnetic behaviour", *Journal of Applied Physics*, vol. 97 (10), Art. no. 10R307.

8. P. Sergeant, L. Dupré, L. Vandenbossche, M. De Wulf (2005), "Magnetic shielding properties of sheet metal products taking into account hysteresis effects", *Journal of Applied Physics*, vol. 97 (10), Art. No. 10E511.

9. L. Dupré, P. Sergeant, L. Vandenbossche (2005), "Magnetic network model including loss separation and Preisach principles for the evaluation of core losses in devices", *Journal of Applied Physics*, vol. 97 (10), Art. No. 10E515.

10. P. Sergeant, L. Dupré, L. Vandenbossche, J. Melkebeek (2005), "Optimization of multilayered non-linear crystalline alloys for shielding", *Journal of Applied Physics*, vol. 97 (10), Art. No. 10F904.

11. P. Sergeant, L. Dupré, L. Vandenbossche, J. Melkebeek (2005), "Analytical formulation for magnetic shields taking into account hysteresis effects in the Rayleigh region", *COMPEL: International Journal for Computation and Mathematics in Electrical and Electronic Engineering*, vol. 24 (4), pp. 1470–1491.

12. D. Ruiz, T. Ros-Yañez, L. Ortega, L. Sastre, L. Vandenbossche, B. Legendre, L. Dupré, R. Vandenberghe, Y. Houbaert (2005), "Effect of atomic order on the electrical and magnetic properties of $Fe_{100-x}Si_x$ $(6 < x < 14)$ alloys", *IEEE Transactions on magnetics*, vol. 41 (10), pp. 3286–3288.

13. A. Benabou, L. Vandenbossche, J. Gyselinck, S. Clenet, L. Dupré, P. Dular (2006), "Inclusion of a stress-dependent Preisach model in 2D FE calculations", *COMPEL: International Journal for Computation and Mathematics in Electrical and Electronic Engineering*, vol. 25 (1), pp. 81–90.

14. L. Vandenbossche, L. Dupré, J. Melkebeek (2006), "Evaluating material degradation by the inspection of minor loop magnetic behavior using the moving Preisach formalism", *Journal of Applied Physics*, vol. 99 (8). Art. No. 08D907.

15. I. J. Garshelis, S. P. Tollens, R. J. Kari, L. Vandenbossche, L. Dupré (2006), "Drag force measurement: A means for determining hysteresis loss", vol. 99 (8), Art. No. 08D910. *Journal of Applied Physics*,

16. G. Crevecoeur, L. Dupré, L. Vandenbossche, R. Van de Walle (2006), "Reconstruction of local magnetic properties of steel sheets by needle probe

methods using space mapping techniques", *Journal of Applied Physics*, vol. 99 (8), Art. No. 08H905.

17. A. P. Van den Bossche, V. C. Valchev, D. M. Van de Sype, L. P. Vandenbossche (2006), "Ferrite losses of cores with square wave voltage and dc bias", *Journal of Applied Physics*, vol. 99 (8), Art. No. 08M908.

18. L. Vandenbossche, I. Garshelis, S. Tollens, L. Dupré, P. Sergeant (2007), "Magnetic nondestructive evaluation of bending fatigue damage using the drag force method", *IEEE Transactions on magnetics*, vol. 43 (6), pp. 2746–2748.

19. L. Vandenbossche, L. Dupré, J. Melkebeek (2007), "On-line cure monitoring of polyurethane foams by dielectrometric viscosity measurements", *International Journal of Applied Electromagnetics and Mechanics*, vol. 25 (1-4), pp. 589–593.

20. L. Vandenbossche, L. Dupré, J. Melkebeek (2007), "Application of a Preisach type hysteresis model to the magnetic evaluation of material degradation", *International Journal of Applied Electromagnetics and Mechanics*, vol. 25 (1-4), pp. 363–368.

21. L. P. Vandenbossche, M. J. Konstantinović, A. Almazouzi, L. R. Dupré (2007), "Magnetic evaluation of the hardening and softening of thermally aged iron-copper alloys", *Journal of Physics D: Applied Physics*, vol. 40 (14), pp. 4114–4119.

22. I. J. Garshelis, R. J. Kari, S. P. Tollens, P. Sergeant, L. P. Vandenbossche, L. R. Dupré (2008), "Sensing Local Inhomogeneity in Electrical Steels by the Drag Force Method", *Journal of Applied Physics*, vol. 103 (7), Art. No. 07E936.

23. G. Crevecoeur, L. Dupré, L. Vandenbossche, R. Van de Walle (2008), "Local identification of magnetic hysteresis properties near cutting edges of electrical steel sheets", *IEEE Transactions on Magnetics*, vol. 44 (6), pp. 1010–1013.

24. P. Sergeant, L. Dupré, L. Vandenbossche, I. Garshelis, S. Tollens (2008), "Numerical model for the drag force method to evaluate hysteresis loss", *IEEE Transactions on Magnetics*, vol. 44 (6), pp. 842–845.

25. L. Vandenbossche, M. J. Konstantinović, L. Dupré (2008), "Magnetic hysteresis characterization of the irradiation-induced embrittlement of Fe, Fe-Cu model alloys, and reactor pressure vessel steel", *Journal of Magnetism and Magnetic Materials*, vol. 320 (20), pp. e562–e566.

26. G. Crevecoeur, P. Sergeant, L. Dupré, L. Vandenbossche, R. Van de Walle (2008), "Analysis of the local material degradation near cutting edges of electrical steel sheets", *IEEE Transactions on Magnetics*, vol. 44 (11), pp. 3173–3176.

27. L. Vandenbossche, L. Dupré (2009), "Fatigue damage assessment by the continuous examination of the magnetomechanical and mechanical behavior", *Journal of Applied Physics*, vol. 105 (7), Art. No. 07E707.

Publications in peer-reviewed international journals, not included in the Web of Science SCI (A2)

1. L. Vandenbossche, L. Dupré, J. Melkebeek (2005), "Magnetic evaluation of cyclic mechanical loading and fatigue damage progression using the Preisach formalism", *Przeglad Elektrotechniczny (Electrotechnical review)*, ISSN 0033-2097, vol. 81 (5), pp. 14–18.

Publications in conference proceedings (C1)

1. P. Sergeant, L. Dupré, J. Melkebeek, L. Vandenbossche (2002), "Magnetic field computation for shielding of induction heaters", *Proceedings of ACOMEN*, Liège, Belgium, 28–31 May 2002, CD-ROM, 10p.

2. L. Vandenbossche , L. Dupré, M. De Wulf, J. Melkebeek (2004), "A magnetic technique for the evaluation of mechanical deformation and its application to TRIP-steels", *Proceedings of SMM16, 16th Soft Magnetic Materials conference*, Düsseldorf, Germany, 9–12 Sept 2003, (published June 2004, Verlag Stahleisen GmbH, Dusseldorf), pp. 233–237.

3. L. Vandenbossche , L. Dupré, M. De Wulf, J. Melkebeek (2004), "Fatigue damage evaluation of ferromagnetic materials using a magnetic hysteresis technique", *Book of abstracts of the 9th Joint MMM-Intermag Conference*, Anaheim, CA, USA, 5–9 Jan 2004, p. 134.

4. L. Vandenbossche, L. Dupré, J. Melkebeek (2005), "Magnetic evaluation of cyclic mechanical loading and fatigue damage progression using the Preisach formalism", *Proceedings of 8th International Workshop on 1&2-Dimensional magnetic Measurements and Testing*, Ghent, Belgium, 27–28 Sept 2004, CD-ROM.

5. L. Vandenbossche, L. Dupré, J. Melkebeek (2005), "Application of a Preisach type hysteresis model to the magnetic evaluation of material degradation", *Short paper proceedings of ISEM'05, 12th International Symposium on Interdisciplinary Electromagnetic, Mechanic and Biomedical problems*, Bad Gastein, Austria, 12–14 Sept 2005 (Vienna Magnetics Group Reports, ISBN 3-902105-00-1), pp. 296–297.

6. L. Vandenbossche, L. Dupré, J. Melkebeek (2005), "On-line cure monitoring of one component foams by dielectrometric viscosity measurements", *Short paper proceedings of ISEM'05, 12th International Symposium on Interdisciplinary Electromagnetic, Mechanic and Biomedical problems*, Bad Gastein, Austria, 12–14 Sept 2005 (Vienna Magnetics Group Reports, ISBN 3-902105-00-1), pp. 390–391.

7. I. J. Garshelis, S. P. Tollens, L. P. Vandenbossche, L. R. Dupré, R. J. Kari (2006), "Determination of hysteresis loss by drag force measurements with cancelled normal field components", *Book of Technical Digests of the International Magnetics Conference (Intermag 2006)*, San Diego, CA, USA, 8–12 May 2006, p. 593.

8. L. Vandenbossche, L. Dupré, J. Melkebeek (2006), "Evaluation of low cycle fatigue damage accumulation by the online monitoring of magneto-mechanical properties", *Book of abstracts of the 9th International Workshop on 1&2 Dimensional Magnetic Measurements and Testing*, Czestochowa, Poland, 18–19 Sept 2006 (ISBN 83-7193-308-8), pp. 28–29.

9. G. Crevecoeur, L. Dupré, L. Vandenbossche, R. Van de Walle (2006), "Magnetic material characterization using the needle probe method", *Book of abstracts of the 9th International Workshop on 1&2 Dimensional Magnetic Measurements and Testing*, Czestochowa, Poland, 18–19 Sept 2006 (ISBN 83-7193-308-8), pp. 76–77.

10. L. Vandenbossche, M. Konstantinović, L. Dupré, E. van Walle (2007), "Magnetic evaluation of the hardening and softening of thermally aged iron-copper alloys", *Book of abstracts of the 10th Joint MMM-Intermag Conference*, Baltimore, Maryland, USA, 7–11 Jan 2007, p. 348.

Attended conferences/workshops with own presentation

- International Conference on Magnetism (ICM), Rome, Italy, July 2003.
- Soft Magnetic Materials Conference (SMM), Düsseldorf, Germany, Sept 2003.

- Conference on Magnetism and Magnetic Materials (Joint MMM-Intermag), Anaheim, CA, USA, Jan 2004.
- Joint European Magnetics Symposia (JEMS), Dresden, Germany, Sept 2004.
- International Workshop on 1 & 2 Dimensional Magnetic Measurement and Testing (2DM), Ghent, Belgium, Sept 2004.
- Conference on Magnetism and Magnetic Materials (MMM), Jacksonville, FL, USA, Nov 2004.
- International Symposium on Interdisciplinary Electromagnetic, Mechanic & Biomedical Problems (ISEM), Bad Gastein, Austria, Sept 2005.
- Universal Network for Magnetic Non-Destructive Evaluation (UN-MNDE), Vienna, Austria, Sept 2005.
- Conference on Magnetism and Magnetic Materials (MMM), San Jose, CA, USA, Nov 2005.
- International Magnetics Conference (Intermag), San Diego, CA, USA, May 2006.
- Universal Network for Magnetic Non-Destructive Evaluation (UN-MNDE), Prague, Czech Republic, Sept 2006.
- International Workshop on 1 & 2 Dimensional Magnetic Measurement and Testing (2DM), Czestochowa, Poland, Sept 2006.
- Conference on Magnetism and Magnetic Materials (Joint MMM-Intermag), Baltimore, MD, USA, Jan 2007.
- Soft Magnetic Materials Conference (SMM), Cardiff, Wales, UK, Sept 2007.
- Universal Network for Magnetic Non-Destructive Evaluation (UN-MNDE), Cardiff, Wales, UK, Sept 2007.
- Conference on Magnetism and Magnetic Materials (MMM), Austin, TX, USA, Nov 2008.

Bibliography

[Alessandro1990] B. Alessandro, C. Beatrice, G. Bertotti and A. Montorsi. "Domain-wall dynamics and Barkhausen effect in metallic ferromagnetic materials. I. Theory". *Journal of Applied Physics*, 68(6), pp. 2901–2907, 1990.

[Altpeter2001] I. Altpeter, G. Dobmann, K.-H. Katerbau, M. Schick, P. Binkele, P. Kizler and S. Schmauder. "Copper precipitates in 15 NiCuMoNb 5 (WB36) steel: material properties and microstructure, atomistic simulation and micromagnetic NDE techniques". *Nuclear Engineering and Design*, 206(2–3), pp. 337–350, 2001.

[Astié1981] B. Astié, J. Degauque, J. L. Porteseil and R. Vergne. "Influence of the dislocation structures on the magnetic and magnetomechanical properties of high-purity iron". *IEEE Transactions on Magnetics*, 17(6), pp. 2929–2931, 1981.

[Augustyniak1995] B. Augustyniak and J. Degauque. "New approach to hysteresis process investigation using mechanical and magnetic Barkhausen effects". *Journal of Magnetism and Magnetic Materials*, 140, pp. 1837–1838, 1995.

[Barkhausen1919] H. Barkhausen. "Zwei mit Hilfe der neuen Verstarker entdeckte Erscheinungen". *Zeitschrift für Physik*, 20, pp. 401–403, 1919.

[Basso1995] V. Basso, G. Bertotti, A. Infortuna and M. Pasquale. "Preisach model study of the connection between magnetic and microstructural properties of soft magnetic materials". *IEEE Transactions on Magnetics*, 31, pp. 4000–4005, 1995.

[Becker1938] R. Becker and W. Doring. *Ferromagnetismus*. Springer-Verlag, Berlin, Germany, 1938.

[Bertotti1988] G. Bertotti. "General properties of power losses in soft ferromagnetic materials". *IEEE Transactions on Magnetics*, 24(1), pp. 621–630, 1988.

[Bertotti1998] G. Bertotti. *Hysteresis in magnetism*. Academic Press, San Diego, California, USA, 1998.

[Blackstock2001] J. J. Blackstock and G. J. Ackland. "Phase transitions of copper precipitates in Fe-Cu alloys". *Philosophical Magazine A*, 81(9), pp. 2127–2148, 2001.

[Bloch1932] F. Bloch. "Zur Theorie des Austauschproblems und der Remanenzerscheinung der Ferromagnetika". *Zeitschrift für Physik*, 74(5–6), pp. 295–335, 1932.

[Blythe2000] H. J. Blythe, H. Krönmuller, A. Seeger and W. Walz. "A review of the magnetic relaxation and its application to the study of atomic defects in α-iron and its diluted alloys". *Physica Status Solidi A*, 181, pp. 233–345, 2000.

[Bose1986] M. S. C. Bose. "A study of fatigue in ferromagnetic materials using a magnetic hysteresis technique". *NDT International*, 19(2), pp. 83–87, 1986.

[Bozorth1951] R. Bozorth. *Ferromagnetism*. D. Van Nostrand, Toronto–New York–London, 1951.

[Brown1963] W. F. Brown. *Micromagnetics*. Wiley Interscience, New york, 1963.

[Brown1966] W. F. Brown. *Magnetoelastic interactions*. Springer–Verlag, Berlin / Heidelberg, 1966.

[Chaouadi2005] R. Chaouadi and R. Gérard. "Copper precipitate hardening of irradiated RPV materials and implications on the superposition law and re-irradiation kinetics". *Journal of Nuclear Materials*, 345(1), pp. 65–74, 2005.

[Chaouadi2007] R. Chaouadi. "On the (in)adequacy of the Charpy impact test to monitor irradiation effects of ferritic/martensitic steels". *Journal of Nuclear Materials*, 360, pp. 75–91, 2007.

[Charleux1996] M. Charleux, F. Livet, F. Bley, F. Louchet and Y. Brechet. "Thermal aging of an Fe-Cu alloy: Microstructural evolution and precipitation hardening". *Philosophical Magazine A – Physics of Condensed matter, Structure Defects and Mechanical Properties*, 73(4), pp. 883–897, 1996.

[Chi1999] S. H. Chi, K. O. Chang, J. H. Hong, I. H. Kuk and C. O. Kim. "Changes in magnetic parameters of neutron irradiated SA 508 Cl. 3 reactor pressure vessel forging and weld surveillance specimens". *Journal of Applied Physics*, 85(8), pp. 6043–6045, 1999.

[Craik1971] D. Craik and M. Wood. “Magnetization changes induced by stress in a constant field”. *Journal of Physics D: Applied Physics*, 4, pp. 1009–1016, 1971.

[Cui2002] W. Cui. “A state-of-the-art review on fatigue life prediction methods for metal structures”. *Journal of Marine Science and Technology*, 7(1), pp. 43–56, 2002.

[Cullity1972] B. D. Cullity. *Introduction to magnetic materials*. Addison-Wesley Publishing, Reading, MA, USA, 1972.

[Dauwe2004] C. Dauwe. *Elektrische en magnetische eigenschappen van de materie*. Course syllabus, Ghent University, Faculty of Sciences, Department of Subatomic and radiation physics, 2004.

[Davies2002] M. Davies, L. Debarberis, V. Lyssakov, F. Gillemot, F. Sevini, A. Ballesteros. *Nuclear power plant life management in some European countries*, AMES Report (European Network on Ageing Materials Evaluation and Studies), 2002.

[DeWulf2002] M. De Wulf. *Karakterisering en energieverliezen onder unidirectionele magnetisatie in relatie tot de microstructuur van zacht magnetische materialen*, PhD thesis, Ghent University, Gent, Belgium, 2002.

[DeWulf2003] M. De Wulf, D. Makaveev, Y. Houbaert and J. Melkebeek. “Design and calibration aspects of small size single sheet testers”. *Journal of Magnetism and Magnetic Materials*, 254, pp. 70–72, 2003.

[Derese2003] J. Derese. *Sensor voor het magnetisch niet-destructief testen van ferromagnetische materialen*. Master thesis, Ghent University, Gent, Belgium, 2003.

[Deschamps2001] A. Deschamps, M. Militzer and W. J. Poole. “Precipitation kinetics and strengthening of a Fe-0.8wt%Cu alloy”. *ISIJ International (The Iron and Steel Institute of Japan)*, 41(2), pp. 196–205, 2001.

[Devine1992] M. Devine. “The magnetic detection of material properties”. *JOM - Journal of the Minerals, Metals and Materials Society*, 44(10), pp. 24–30, 1992.

[DierickWarlop2005] D. Dierick and B. Warlop. *Ontwerp, constructie en aansturing van een experimentele opstelling voor de cyclische mechanische buigingsbelasting van staalplaat*, Master thesis, Hogeschool Gent / Ghent University, Gent, Belgium, 2005.

[Dieter1988] G. E. Dieter. *Mechanical metallurgy (SI metric edition)*. McGraw-Hill, London, UK, 1988.

[Dupre1995] L. Dupré. *Elektromagnetische karakterisatie van niet-georiënteerd elektroblik*, PhD thesis, Ghent University, Gent, Belgium, 1995.

[Dupré1999] L. Dupré, G. Ban, M. Von Rauch and J. Melkebeek. "Relation between the microstructural properties of electrical steels and the Preisach modelling". *Journal of Magnetism and Magnetic Materials*, 195(1), pp. 233–249, 1999.

[Dupré2002] L. Dupré and M. J. Sablik. "Modelling of microstructural effects on magnetic hysteresis properties". *Journal of Physics D: Applied Physics*, 35, pp. 2086–2090, 2002.

[Everett1955] D. Everett. "A general approach to hysteresis - part 4, An alternative formulation of the domain model". *Transactions Faraday Society*, 51, pp. 1551–1557, 1955.

[Fidler2000] J. Fidler and T. Schrefl. "Micromagnetic modelling – the current state of the art". *Journal of Physics D: Applied Physics*, 33, pp. R135–R156, 2000.

[Fiorillo2004] F. Fiorillo. *Measurement and characterization of magnetic materials*. Elsevier Academic Press, San Diego, California, USA, 2004.

[Fisher1985] S. B. Fisher, J. E. Harbottle and N. Aldridge. "Radiation hardening in Magnox pressure vessel steels". *Philosophical Transactions of the Royal Society of London Series A – Mathematical, Physical and Engineering Sciences*, 315(10), pp. 301–332, 1985.

[Föll2006] H. Föll. *Defects in Crystals*. Course syllabus, University of Kiel, Faculty of Engineering (http://www.tf.uni-kiel.de/matwis/amat/def_en), 2006.

[Forrest1962] P. G. Forrest. *Fatigue of metals*. Pergamon Press, London, UK, 1962.

[Fujii1968] A. Fujii, M. Nemoto, H. Suto and K. Monma. "Precipitation hardening of iron-copper alloys". *Transactions of the Japan Institute of Metals*, S9, pp. 374, 1968.

[Fujita1992] T. Fujita. "Current Progress in Advanced High Cr Ferritic Steels for High-temperature Applications". *ISIJ International (The Iron and Steel Institute of Japan)*, 32(2), pp. 175–181, 1992.

[Garshelis1990] I. J. Garshelis. "Magnetic and magnetoelastic properties of 18% nickel maraging steels". *IEEE Transactions on Magnetics*, 26(5), pp. 1981–1983, 1990.

[Garshelis2006] I. J. Garshelis, S. P. Tollens, R. J. Kari, L. Vandenbossche and L. Dupré. "Drag force measurement: A means for determining hysteresis loss". *Journal of Applied Physics*, 99, Art. No. 08D910, 2006.

[Garshelis2008] I. J. Garshelis, R. J. Kari, S. P. Tollens, P. Sergeant, L. P. Vandenbossche and L. R. Dupré. "Sensing Local Inhomogeneity in Electrical Steels by the Drag Force Method". *Journal of Applied Physics*, 103, Art. No. 07E936, 2008.

[Gottstein2004] G. Gottstein. *Physical foundations of materials science*. Springer-Verlag, Berlin, Germany, 2004.

[Halmshaw1987] R. Halmshaw. *Non-destructive testing*. Edward Arnold Publishers, London, UK, 1987.

[Heisenberg1928] W. Heisenberg. "Zur Theorie des Ferromagnetismus". *Zeitschrift für Physik*, 49, pp. 619–636, 1928.

[Herring1951] C. Herring and C. Kittel. "On the theory of spin waves in ferromagnetic media". *Physical Review*, 81(5), pp. 869–880, 1951.

[Herring1960] C. Herring. "The state of d-electons in transition metals". *Journal of Applied Physics (Suppl.)*, 31, pp. 3S–11S, 1960.

[Herzer1990] G. Herzer. "Grain-size dependence of coercivity and permeability in nanocrystalline ferromagnets". *IEEE Transactions on Magnetics*, 26(5), pp. 1397–1402, 1990.

[Honda1926] H. Honda and S. Kaya. "Magnetization of single crystals of iron". *Scientific reports of Tohoku University*, 15, pp. 721–753, 1926.

[Hu1999] S. Y. Hu, Y. L. Li and K. Watanabe. "Calculation of internal stresses around Cu precipitates in the bcc Fe matrix by atomic simulation". *Modelling and Simulation in Materials Science and Engineering*, 7(4), pp. 641–655, 1999.

[Hubert2008] O. Hubert and K.-J. Rizzo. "Anhysteretic and dynamic piezomagnetic behavior of a low carbon steel". *Journal of Magnetism and Magnetic Materials*, 320(20), pp. e979–e982, 2008.

[IAEA2001] International Atomic Energy Agency (IAEA). "Reference manual on the IAEA JRQ correlation monitor steel for irradiation damage studies". IAEA-TECDOC-1230, *http://www-pub.IAEA.ORG/MTCD/publications/PDF/te_1230_prn.pdf*, ISSN 10114289.

[IEC60404-2] IEC Standard Publication 60404-2. "Methods of measurement of the magnetic properties of electrical steel sheet and strip by means of the Epstein frame". International Electrotechnical Commission, Geneva, Switserland, 1996.

[IEC60404-3] IEC Standard Publication 60404-3. "Methods of measurement of the magnetic properties of magnetic sheet and strip by means of a single sheet tester". International Electrotechnical Commission, Geneva, Switserland, 2000.

[IEC60404-4] IEC Standard Publication 60404-4. "Methods of measurement of d.c. magnetic properties of iron and steel". International Electrotechnical Commission, Geneva, Switserland, 2002.

[Iordache2003] V. E. Iordache, E. Hug and N. Buiron. "Magnetic behaviour versus tensile deformation mechanisms in a non-oriented Fe-(3 wt.%)Si steel". *Materials Science and Engineering A*, 359(1–2), pp. 62–74, 2003.

[Jiles1995] D. C. Jiles. "Theory of the magnetomechanical effect". *Journal of Physics D: Applied Physics*, 28, pp. 1537–1546, 1995.

[Jiles1998] D. C. Jiles. *Introduction to magnetism and magnetic materials (2nd edition)*. Chapman–Hall, London, 1998.

[Jiles2002] D. C. Jiles. "Hysteresis models: non-linear magnetism on length scales from the atomistic to the macroscopic". *Journal of Magnetism and Magnetic Materials*, 242–245, pp. 116–124, 2002.

[Jiles2008] D. C. Jiles. *Introduction to the principles of materials evaluation*. CRC Press, Taylor & Francis Group, Boca Raton, Florida, USA, 2008.

[Kandil2001] F. A. Kandil, J. D. Lord, A. T. Fry and P. V. Grant. *A review of residual stress measurement methods - a guide to technique selection*, NPL report MATC(A)04, National Physical Laboratory, Teddington, Middlesex, UK, 2001.

[Kersten1938] M. Kersten. *Problems of the technical magnetisation curve*. (ed. R. Becker), Springer, Berlin, Germany, 1938.

[Kittel1949] C. Kittel. "Physical theory of ferromagnetic domains". *Rev. Mod. Phys.*, 21(4), pp. 541–583, 1949.

[Konstantinović2007] M. J. Konstantinović, A. Almazouzi, M. Scibetta and E. van Walle. "Tensile properties and internal friction study of dislocation movement in iron-copper system as a function of copper precipitation". *Journal of Nuclear Materials*, 362(2–3), pp. 283–286, 2007.

[Konstantinovic2008] M. J. Konstantinović. “Interplay of dislocation-related relaxation processes in iron-based materials”. *Pysical Review B*, 78, Art. No. 52104, 2008.

[Kronmüller1972] H. Kronmüller. “Magnetic techniques for the study of dislocations in ferromagnetic materials”. *International Journal of Nondestructive Testing*, 3, pp. 315–350, 1972.

[Kronmüller2003] H. Kronmüller and M. Fähnle. *Micromagnetism and the microstructure of ferromagnetic structures*. Cambridge University Press, Cambridge, UK, 2003.

[Kryukov1998] A. M. Kryukov, Y. A. Nikolaev and A. V. Nikolaeva. “Behavior of mechanical properties of nickel-alloyed reactor pressure vessel steel under neutron irradiation and post-irradiation annealing”. *Nuclear Engineering and Design*, 186(3), pp. 353–359, 1998.

[Küpferling2007] M. Küpferling, C. Appino, V. Basso, G. Bertotti, F. Fiorillo and P. Meilland. “Magnetic hysteresis in plastically deformed low-carbon steel laminations”. *Journal of Magnetism and Magnetic Materials*, 316(2), pp. e854–e857, 2007.

[Kuruzar1971] M. Kuruzar and B. Cullity. “The magnetostriction of iron under tensile and compressive stress”. *International Journal on Magnetism*, 1, pp. 323–325, 1971.

[Landau1935] L. D. Landau and E. M. Lifshitz. “On the theory of the dispersion of magnetic permeability in ferromagnetic bodies”. *Phys. Z. Sowjetunion*, 8, pp. 153–169, 1935.

[Landau1960] L. D. Landau and E. M. Lifshitz. *Electrodynamics of Continuous Media*. Pergamon Press, New York (translated from the Russian version by J. B. Sykes and J. S. Bell), 1960.

[Langman1985] R. Langman. “The effect of stress on the magnetization of mild steel at moderate field strengths”. *IEEE Transactions on Magnetics*, 21(4), pp. 1314–1320, 1985.

[Lee1955] E. W. Lee. “Magnetostriction and magnetomechanical effects”. *Reports on Progress in Physics*, 18(1), pp. 184–229, 1955.

[Lo2000] C. C. H. Lo, F. Tang, S. B. Biner and D. C. Jiles. “Effects of fatigue-induced changes in microstructure and stress on domain structure and magnetic properties of Fe-C alloys”. *Journal of Applied Physics*, 87(9), pp. 6520–6522, 2000.

[Lubitz1974] E. Lubitz. “Magnetic studies of dislocation structure of iron single crystals deformed at 295 K”. *Applied Physics*, 4(1), pp. 51–61, 1974.

[Makar1995] J. Makar and D. Atherton. “Effects of isofield uniaxial cyclic stress on the magnetization of 2% Mn pipeline steel – behaviour on near saturation major hysteresis loop”. *IEEE Transactions on Magnetics*, 31(1), pp. 877–884, 1995.

[Makaveev2003] D. Makaveev. *Karakteriseren en neuraal-netwerkgebaseerd modelleren van rotationele magnetisatie in niet-georiënteerd elektrisch staal*, PhD thesis, Ghent University, Gent, Belgium, 2003.

[Matijasevic2008] M. Matijasevic. *Microstructure and mechanical properties of Fe-Cr model alloys and high Cr steels under neutron irradiation*, PhD thesis, Ghent University, Gent, Belgium, 2008.

[Maxwell1873] J. C. Maxwell. “A treatise on electricity and magnetism”. *Trans. R. Soc. Edinburgh*, 26, pp. 1, 1873.

[Mayergoyz2003] I. D. Mayergoyz. *Mathematical Models of Hysteresis and their Applications*. Academic Press, 2003.

[Melikhov2001] Y. Melikhov, D. C. Jiles, I. Tomáš, C. C. H. Lo, O. Perevertov and J. Kadlecova. “Investigation of sensitivity of Preisach analysis for nondestructive testing”. *IEEE Transactions on Magnetics*, 37, pp. 3907–3912, 2001.

[Melikhov2002] Y. Melikhov, C. C. H. Lo, O. Perevertov, J. Kadlecová, D. C. Jiles and I. Tomáš. “Magnetic response to cyclic fatigue of low carbon Fe-based samples”. *Journal of Physics D: Applied Physics*, 35(5), pp. 413–422, 2002.

[Mikheev1981] M. N. Mikheev and E. S. Gorkunov. “Relationship of magnetic properties to the structural condition of a substance - the physical basis of magnetic structure analysis (Review)”. *Sovjet Journal of Nondestructive Testing*, 17(8), pp. 579–592, 1981.

[Mura1987] T. Mura. *Micromechanics of defects in solids (second revised edition)*. Martinus Nijhoff Publishers (Kluwer Academic Publishers), Dordrecht, The Netherlands, 1987.

[Nakata1987] T. Nakata, Y. Kawase and M. Nakano. “Improvement of measuring accuracy of magnetic field strength in single sheet testers by using 2 H-coils”. *IEEE Transactions on Magnetics*, 23(5), pp. 2596–2598, 1987.

[O’Handley2000] R. C. O’Handley. *Modern magnetic materials: principles and applications*. Wiley, New York, USA, 2000.

[Odette1998] G. R. Odette and G. E. Lucas. “Recent progress in understanding reactor pressure vessel steel embrittlement”. *Radiation Effects and defects in Solids*, 144(1–4), pp. 189–231, 1998.

[Odette2005] G. R. Odette, T. Yamamoto and D. Klingensmith. "On the effect of dose rate on the irradiation hardening of RPV steels". *Philosophical Magazine*, 85(4–7), pp. 779–797, 2005.

[Othen1991] P. J. Othen, M. L. Jenkins, G. D. Smith and W. J. Phythian. "Transmission electron microscope investigations of the structure of copper precipitates in thermally aged Fe-Cu and Fe-Cu-Ni". *Philosophical Magazine Letters*, 64(6), pp. 383–391, 1991.

[Othen1994] P. J. Othen, M. L. Jenkins and G. D. W. Smith. "High resolution electron microscopy studies of the structure of Cu precipitates in α-Fe". *Philosophical Magazine A – Physics of Condensed matter, Structure Defects and Mechanical Properties*, 70(1), pp. 1–24, 1994.

[Perevertov2005] O. Perevertov. "Measurement of the surface field on open magnetic samples by the extrapolation method". *Review of Scientific Instruments*, 76, Art. No. 104701, 2005.

[Perez2005] M. Perez, F. Perrard, V. Massardier, X. Kleber, A. Deschamps, H. De Monestrol, P. Pareige and G. Covarel. "Low-temperature solubility of copper in iron: experimental study using thermoelectric power, small angle X-ray scattering and tomographic atom probe". *Philosophical Magazine*, 85(20), pp. 2197–2210, 2005.

[Preisach1935] F. Preisach. "Uber die magnetische Nachwirkung". *Zeitschrift für Physik*, 94, pp. 277–302, 1935.

[Raj2003] B. Raj, V. Moorthy, T. Jayakumar and K. Bhanu Sakara Rao. "Assessment of microstructures and mechanical behaviour of metallic materials through non-destructive characterisation". *International Materials Reviews*, 48(5), pp. 273–325, 2003.

[Russell1972] K. C. Russell and L. M. Brown. "Dispersion strengthening model based on differing elastic moduli applied to iron-copper system". *Acta Metallurgica*, 20(7), pp. 969, 1972.

[Ruuskanen1991] P. Ruuskanen and P. Kettunen. "Reversible component ΔB_r of the stress-induced change in magnetization as a function of magnetic field strength and stress amplitude". *Journal of Magnetism and Magnetic Materials*, 98, pp. 349–358, 1991.

[Sablik1988] M. J. Sablik, G. L. Burkhardt, H. Kwun and D. C. Jiles. "A model for the effect of stress on the low-frequency harmonic content of the magnetic induction in ferromagnetic materials". *Journal of Applied Physics*, 63(8), pp. 3930–3932, 1988.

[Sablik2001] M. J. Sablik. "Modeling the effect of grain size and dislocation density on hysteretic magnetic properties in steels". *Journal of Applied Physics*, 89(10), pp. 5610–5613, 2001.

[Sergeant2008] P. Sergeant, L. Dupré, L. Vandenbossche, I. J. Garshelis and S. P. Tollens. "Numerical model for the drag force method to evaluate hysteresis loss". *IEEE Transactions on Magnetics*, 44(6), pp. 842–845, 2008.

[Sevini2004] F. Sevini, L. Debarberis, K. Törrönen, R. Gérard and L. M. Davies. "Development of the AMES network throughout the 4th and 5th EURATOM framework programmes". *International Journal of Pressure Vessels and Piping*, 81(8), pp. 683–694, 2004.

[Shu2004] Y. C. Shu, M. P. Lin and K. C. Wu. "Micromagnetic modeling of magnetostrictive materials under intrinsic stress". *Mechanics of Materials*, 36, pp. 975–997, 2004.

[Silvester1990] P. P. Silvester and R. L. Ferrari. *Finite elements for electrical engineers*. Cambridge University Press, Cambridge, UK, 1990.

[Slater1930] J. C. Slater. "Atomic shielding constants". *Physical Review*, 36(1), pp. 57–64, 1930.

[Socha2003] G. Socha. "Experimental investigations of fatigue cracks nucleation, growth and coalescence in structural steel". *International Journal of Fatigue*, 25(2), pp. 139–147, 2003.

[Sommerfeld1933] A. Sommerfeld and H. Bethe. "Elektronentheorie der Metalle". *Handbuch der Physik*, 24(2), pp. 595–598, 1933.

[Sternberk1983] J. Sternberk, E. Kratochvilova, J. Hrebik and A. Gemperle. "Coercivity and microstructure of low-alloy Cr-Mo steel". *Physica Status Solidi A - Applied Research*, 79(2), pp. 523–529, 1983.

[Stupakov2006] O. Stupakov. "Investigation of applicability of extrapolation method for sample field determination in single-yoke measuring setup". *Journal of Magnetism and Magnetic Materials*, 307(2), pp. 279–287, 2006.

[Takahashi2006a] S. Takahashi, S. Kobayashi, H. Kikuchi, Y. Kamada and K. Ara. "Analysis of minor hysteresis loops of cold rolled low carbon-steel". *IEEE Transactions on Magnetics*, 42(11), pp. 3782–3784, 2006.

[Takahashi2006b] S. Takahashi, H. Kikuchi, K. Ara, N. Ebine, Y. Kamada, S. Kobayashi and M. Suzuki. "In situ magnetic measurements under neutron radiation in Fe metal and low carbon steel". *Journal of Applied Physics*, 100, Art. No. 023902, 2006.

[Takaki2005] S. Takaki. “Limit of dislocation density and ulta-grain-refining on severe deformation in iron”. *International Journal of ISSI*, 2(1), pp. 21–25, 2005.

[Tomáš2004] I. Tomáš. “Non-destructive magnetic adaptive testing of ferromagnetic materials”. *Journal of Magnetism and Magnetic Materials*, 268, pp. 178–185, 2004.

[UNMNDE] Universal Network for Magnetic Non-destructive Evaluation. “http://www.ndesrc.eng.iwate-u.ac.jp/UniversalNetwork/”.

[Ulbricht2007] A. Ulbricht, F. Bergner, J. Böhmert, M. Valo, M. H. Mathon and A. Heinemann. “SANS response of VVER440-type weld material after neutron irradiation, post-irradiation annealing and reirradiation”. *Philosophical Magazine*, 87(12), pp. 1855–1870, 2007.

[VanOuytsel2000] K. Van Ouytsel, A. Fabry, R. De Batist and R. Schaller. “Determination of the yield strength of nuclear reactor pressure vessel steels by means of amplitude-dependent internal friction”. *Journal of Nuclear Materials*, 279(1), pp. 51–56, 2000.

[VandeWiele2005] B. Van de Wiele. *Beschrijving van macroscopisch magnetisch materiaalgedrag via micromagnetische berekeningen*, Master thesis, Ghent University, Gent, Belgium, 2005.

[VandeWiele2007] B. Van de Wiele, F. Olyslager and L. Dupré. “Fast numerical three-dimensional scheme for the simulation of hysteresis in ferromagnetic grains”. *Journal of Applied Physics*, 101, Art. No. 073909, 2007.

[VandeWiele2008a] B. Van de Wiele, L. Dupré and F. Olyslager. “Memory properties in a 3D micromagnetic model for ferromagnetic samples”. *Physica B*, 403, 342–345, 2008.

[VandeWiele2008b] B. Van de Wiele, F. Olyslager and L. Dupré. “Application of the fast multipole method for the evaluation of magnetostatic fields in micromagnetic computations”. *Journal of Computational Physics*, 227(23), pp. 9913–9932, 2008.

[VandenBerg2009] A. van den Berg, L. Dupré, B. Van de Wiele, and G. Crevecoeur. “Mesohysteresis model for ferromagnetic materials by minimization of the micromagnetic free energy”. *Journal of Applied Physics*, 105(7), Art. No. 07D513, 2009.

[Vandenbossche2005] L. Vandenbossche, L. Dupré and J. Melkebeek. “Monitoring the fatigue state of steel by evaluating the quasistatic and dynamic magnetic behavior”. *Journal of Applied Physics*, 97, Art. No. 10R307, 2005.

[Vandenbossche2006] L. Vandenbossche, L. Dupré and Melkebeek, J. "Evaluating material degradation by the inspection of minor loop magnetic behavior using the moving Preisach formalism". *Journal of Applied Physics*, 99, Art. No. 08D907, 2006.

[Vandenbossche2007a] L. Vandenbossche, I. J. Garshelis, S. P. Tollens, L. Dupré and P. Sergeant. "Magnetic nondestructive evaluation of bending fatigue damage using the drag force method". *IEEE Transactions on Magnetics*, 43(6), pp. 2746–2748, 2007.

[Vandenbossche2007b] L. P. Vandenbossche, M. J. Konstantinović, A. Almazouzi and L. R. Dupré. "Magnetic evaluation of the hardening and softening of thermally aged iron-copper alloys". *Journal of Physics D: Applied Physics*, 40(14), pp. 4114–4119, 2007.

[Verheyen2006] K. Verheyen, M. Jardin and A. Almazouzi. "Coincidence Doppler broadening spectroscopy in Fe, Fe-C and Fe-Cu after neutron irradiation". *Journal of Nuclear Materials*, 351(1–3), pp. 209–215, 2006.

[Vértesy2008] G. Vértesy, I. Tomáš, S. Takahashi, S. Kobayashi, Y. Kamada and H. Kikuchi. "Inspection of steel degradation by magnetic adaptive testing". *NDT & E International*, 41, pp. 252–257, 2008.

[Villari1865] E. Villari. "Change of magnetization by tension and by electric current". *Ann. Phys. Chem. Lpz.*, 126, pp. 87–122, 1865.

[Webster1930] W. Webster. "Magnetostriction and change of resistance in single crystals of iron and nickel". *Proceedings of the Physical Society*, 42, pp. 431–440, 1930.

[Weiss1907] P. Weiss. "L'hypothèse du champ moléculaire et la proprieté ferromagnétique". *Journal de Physique*, 6, pp. 661–690, 1907.

[Withers2007] P. Withers. "Residual stress and its role to failure". *Reports on Progress in Physics*, 70, pp. 2211–2264, 2007.